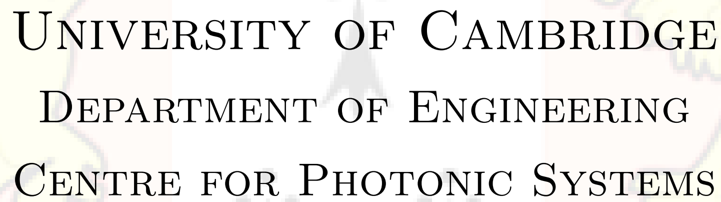

University of Cambridge
Department of Engineering
Centre for Photonic Systems

Monolithic 1.3 μm InAs/GaAs Quantum Dot Lasers on Silicon: Simulation and Experiment

Constanze Hantschmann

Hughes Hall

This dissertation is submitted for the degree of
Doctor of Philosophy

August 2020

To all first-year PhD students

Declaration

This dissertation is the result of my own work and includes nothing which is the outcome of work done in collaboration except as declared in the Preface and specified in the text. It is not substantially the same as any that I have submitted, or, is being concurrently submitted for a degree or diploma or other qualification at the University of Cambridge or any other University or similar institution except as declared in the Preface and specified in the text. I further state that no substantial part of my dissertation has already been submitted, or, is being concurrently submitted for any such degree, diploma or other qualification at the University of Cambridge or any other University or similar institution except as declared in the Preface and specified in the text.

This dissertation does not exceed 65,000 words in length, and it contains less than 150 figures.

Constanze Hantschmann, Hughes Hall

August 2020, Munich

Abstract

1.3 μm quantum dot (QD) lasers epitaxially grown on silicon have attracted great interest as light source for silicon photonics and other optical communication applications. This work focuses on improving the understanding of the physical mechanisms limiting the performance of these devices, and on studying the laser dynamics with respect to data transmission potential through simulation and experiment.

Dislocation-induced carrier loss is a major concern for the performance of QD lasers on silicon. Part of this work aims, therefore, at identifying the processes degrading the laser characteristics as well as on understanding the performance disparity between silicon-based QD and quantum well (QW) devices. By using two specially extended types of rate equation travelling-wave models it is found that enhanced carrier loss at higher dislocation densities leads to a much larger laser threshold increase in QW than in QD lasers. The QD laser's increased tolerance to dislocations can be explained based on efficient and ultrafast carrier capture into the QDs, where high energy barriers prevent them from migrating into defects. The carrier density reduction in the higher energy continuum layers is eventually reflected in a lower current injection efficiency and thus reduced light-current slope, confirming experimentally observed trends of 1.3 μm QD lasers on silicon. In particular, a large minority carrier diffusion length is identified as a key parameter inhibiting laser operation in QW-based devices.

The other part of this work focuses on investigating the QD lasers' dynamics by means of gain switching, small-signal and large-signal modulation. 150 ps short gain-switched pulses, modulation bandwidths of 1.6 GHz to 2.3 GHz, and optical eyes at 1.5 Gb/s are obtained from 2.5 mm long ridge-waveguide lasers grown and fabricated at University College London. Numerical simulations reveal that the observed high-speed limitations are a result of limited gain and a long photon lifetime, whereas suitability for 10 Gb/s operation is predicted in an optimised laser design. It was, furthermore, found that neither dislocation-induced carrier loss nor optical loss limit the modulation characteristics fundamentally. The reduced carrier lifetime is, however, reflected in stronger damping of the small-signal modulation curves. Apart from that, the overall device dynamics remain governed by the QD physics.

Acknowledgements

First and foremost, I would like to thank my supervisor Prof. Richard Penty and my advisor Prof. Ian White for their invaluable support throughout my time in Cambridge. What I have learnt during my PhD has had a strong influence on my plans for the future and I must give Ian and Richard credit for this. Richard, as my primary supervisor, was instrumental in providing regular feedback on projects, papers, and conference talks. Without this, the road down my PhD would have probably been a much bumpier one. Ian taught me to really look at the device physics and to turn challenges into opportunities by focusing on what is special about a new device or technology in order to turn it into an advantage. I have always enjoyed our physics discussions and would like to thank him for his ongoing support even after he had started his new position in Bath.

Special thanks go also to my collaborators at University College London, specifically Prof. Huiyun Liu and Prof. Alwyn Seeds and their group members Siming, Mengya, Mingchu, and Zizhuo, without whom I would not have had any devices to test at all. Huiyun and Alwyn were incredibly supportive over all those years and even organised opportunities for talks and publications for me. I feel very humbled to be part of this world-class research team.

At the Centre for Photonic Systems (CPS), I wish to thank Peter Vasil'ev for extensive support in the lab and Adrian Wonfor for occasionally life-saving advice during my early ventures into the world of computational physics. Apart from that, I want to thank all of my colleagues at CPS for our joint tea times (especially after we found the coffee machine in the Maxwell building).

I would also like to acknowledge my funding partners, in particular Qualcomm Inc. for their generous PhD scholarship and travel funding. I am aware that being able to study at an institution like the University of Cambridge and to travel around the world to meet like-minded photonics enthusiasts puts me in a very privileged position. I will be always grateful for this experience.

For keeping me sane and distracting me from work, I want to thank all of my friends in Cambridge and around the world. More than any other friend, although she might never read this, I would like to acknowledge my dear friend Eleanor Masters. Helping her

to train and rehome rescue horses got me up early in the morning and out of the lab on sunny summer evenings. It gave me energy to spend my days and nights productively and was my lifeline during the more difficult times. For that I will forever be grateful.

Finally, I want to express my gratitude to all those people on my life's journey to Cambridge: Prof. James Lott and Prof. Dieter Bimberg, whose strong support during my bachelor's and master's degree have brought me to Cambridge in the first place. They have taught me positivity and passion, perseverance and dedication. Without their preparation, I might have not embraced the challenges of my PhD research the way I eventually did; My physics teacher Frank Gerhardter, whose enthusiastic way of teaching left me without a spark of doubt that studying physics will be the way to go; My parents Dagmar and Dieter, who have never questioned my decisions to follow my dreams and ambitions out into the world; And finally my husband and soulmate Markus, who has always been there for me. Spending my life with him and exploring the world together is a constant reminder that there is more to life than science.

Contents

List of Publications xv

List of Abbreviations xviii

1 Introduction **1**

1.1 Applications of Monolithic III-V Lasers on Silicon 4

1.1.1 Directly Modulated Standalone Laser 4

1.1.2 Integrated Light Source for Silicon Photonics 5

1.1.3 Other Niche Applications 7

1.2 Organisation and Aim of this Dissertation 8

1.3 Achievements of this Work 10

2 Semiconductor Laser Fundamentals **13**

2.1 Operation Principles 13

2.1.1 The Double Heterostructure 14

2.1.2 Lateral Confinement 16

2.1.3 The Laser Cavity 17

2.2 Active Region Types 19

2.3 Rate Equation Description 23

2.3.1 Static Properties 25

2.3.2 Dynamic Properties: Small-Signal Analysis 27

2.4 Chapter Summary 32

3 Growth of III-V Lasers on Silicon **33**

3.1 The Laser Integration Challenge 33

3.2 Non-Epitaxial Integration Approaches 36

3.2.1 Direct Mounting 36
3.2.2 Bonding-Based Heterogeneous Integration 37
3.2.3 Massive Transfer Printing 39
3.3 Heteroepitaxial III-V Lasers on Silicon 41
3.3.1 Substrate Surface 42
3.3.2 Buffer layers 43
3.3.3 Defect filter layers 45
3.3.4 Thermal Treatments 46
3.3.5 Suitable Active Regions 47
3.4 Static Performance Overview of Monolithic Quantum Dot Lasers on Silicon 49
3.5 Chapter Summary 52

4 Travelling-Wave Rate Equation Quantum Dot Laser Model 55

4.1 Model Introduction 56
4.2 Multi-Level Carrier Rate Equation System 58
4.2.1 Quantum Dot Rate Equation System 59
4.2.2 Quantum Well Rate Equation System 62
4.3 Travelling-Wave Electric Field Equations 63
4.3.1 Numerical Implementation of Propagation in an Amplifying Medium 64
4.3.2 Numerical Implementation of a Digital Spectral Filter 66
4.3.3 Frequency Chirp or Linewidth Enhancement 68
4.4 Modelling Parameters 69
4.4.1 Parameters for InAs QD Lasers on GaAs 70
4.4.2 Parameter Considerations for QD Lasers on Silicon 72
4.5 Numerical Implementation of Simulation Programmes 74
4.5.1 Temporal Evolution 74
4.5.2 Light-Current Simulations 76
4.5.3 Small-Signal Simulations 77
4.6 Model Limitations and Possible Extensions 79
4.7 Chapter Summary 83

5 The Role of Dislocations in III-V Lasers Grown on Silicon 85

5.1 Introduction . . . 85

5.2 Standard Approach Based on Macroscopically Averaged Parameters . . . 87

5.2.1 Numerical Approach: Diffusion-Assisted Carrier Loss . . . 87

5.2.2 Simulation Results . . . 92

5.2.3 Discussion . . . 95

5.3 Spatially Resolved Inclusion of Dislocations . . . 99

5.3.1 Numerical Approach: Implementation of Dislocations . . . 99

5.3.2 Simulation Results . . . 102

5.3.3 Discussion . . . 105

5.4 Chapter Summary . . . 108

6 Gain Switching of Quantum Dot Lasers on Silicon 111

6.1 Dynamic Performance Overview of Monolithic Quantum Dot Lasers on Silicon . . . 112

6.2 Epitaxial Design of the Tested Lasers . . . 116

6.3 Experimental Methods and Results . . . 118

6.4 Simulation Results . . . 123

6.5 Discussion . . . 129

6.6 Chapter Summary . . . 131

7 Direct Modulation of Quantum Dot Lasers on Silicon 133

7.1 Introduction . . . 133

7.2 Experimental Methods . . . 134

7.3 Experimental Results and Analysis . . . 135

7.4 Simulation Results . . . 139

7.4.1 Fitting . . . 139

7.4.2 Bandwidth Optimisation . . . 141

7.5 Discussion: Impact of the Silicon Substrate . . . 145

7.6 Chapter Summary . . . 148

8 Conclusions and Outlook **151**

8.1 Summary 151

8.2 Outlook 156

8.2.1 Integration with Silicon Photonics 156

8.2.2 Directly Modulated Lasers for 10G Passive Optical Networks 159

8.2.3 Materials Research 160

8.2.4 Low-Cost VCSEL Arrays for Sensing Applications 161

Bibliography **163**

List of Publications

Journal Papers:

1. C. Hantschmann, Z. Liu, M.C. Tang, S. Chen, A.J. Seeds, H.Y. Liu, I.H. White, and R.V. Penty, **"Theoretical study on the effects of dislocations in monolithic III-V lasers on silicon,"** *Journal of Lightwave Technology*, vol. 38, no. 17, pp. 4801–4807, 2020.

2. Z. Liu*, C. Hantschmann*, M.C. Tang, Y. Lu, J.-S. Park, M. Liao, S. Pan, A.M. Sanchez, R. Beanland, M. Martin, T. Baron, S. Chen, A.J. Seeds, I.H. White, R.V. Penty, and H.Y. Liu, **"Origin of defect tolerance in InAs/GaAs quantum dot lasers grown on silicon,"** *Journal of Lightwave Technology*, vol. 38, no. 2, pp. 240–248, 2020.
   *Authors contributed equally

3. C. Hantschmann, P.P. Vasil'ev, A. Wonfor, S. Chen, M. Liao, A.J. Seeds, H.Y. Liu, R.V. Penty, and I.H. White, **"Understanding the bandwidth limitations in monolithic** 1.3 **μm InAs/GaAs quantum dot lasers on silicon,"** *Journal of Lightwave Technology*, vol. 37, no. 3, pp. 949–955, 2018.

4. C. Hantschmann, P.P. Vasil'ev, S. Chen, M. Liao, A.J. Seeds, H.Y. Liu, R.V. Penty, and I.H. White, **"Gain switching of monolithic** 1.3 **μm InAs/GaAs quantum dot lasers on silicon,"** *Journal of Lightwave Technology*, vol. 36, no. 19, pp. 3837–3842, 2018.

International Conferences:

(underlined where presenter)

1. C. Hantschmann, Z. Liu, M.C. Tang, A.J. Seeds, H.Y. Liu, I.H. White, and R.V. Penty, **"Impact of dislocations in monolithic III-V lasers on silicon: A theoretical approach,"** *Proc. SPIE Physics and Simulation of Optoelectronic Devices XXVIII*, vol. 11274, San Francisco, CA, USA, 2020, pp. 112740J.

2. R.V. Penty, C. Hantschmann, P.P. Vasil'ev, S. Chen, M. Liao, A.J. Seeds, H.Y. Liu, and I.H. White, **"Dynamics of quantum dot lasers grown on silicon (invited),"** *2nd IEEE British and Irish Conference on Optics and Photonics*, London, UK, 2019, unpublished.

3. Z. Liu, M. Liao, C. Hantschmann, Y. Wang, T. Zhuo, M.C. Tang, J.-S. Park, Z. Zhang, S. Chen, A.J. Seeds, R.V. Penty, I.H. White, S. Yu, and H.Y. Liu, **"Roadmap of 1300-nm InAs/GaAs quantum dot laser grown on silicon for silicon photonics (invited),"** *International Photonics and OptoElectronics Meeting*, Wuhan, China, 2019, p. OTh1C.1.

4. C. Hantschmann, Z. Liu, M.C. Tang, A.J. Seeds, H.Y. Liu, I.H. White, and R.V. Penty, **"Modelling the effect of dislocations in III-V lasers on Si,"** *European Semiconductor Laser Workshop*, Cork, Ireland, 2019, unpublished.

5. C. Hantschmann, P.P. Vasil'ev, S. Chen, M. Liao, A.J. Seeds, H.Y. Liu, R.V. Penty, and I.H. White, **"Dynamics of quantum dot lasers on silicon (invited),"** *Proc. IEEE Photonics Society Summer Topical Meeting Series (SUM)*, Fort Lauderdale, FL, USA, 2019, pp. 1–2.

6. C. Hantschmann, P.P. Vasil'ev, S. Chen, M. Liao, A.J. Seeds, H.Y. Liu, R.V. Penty, and I.H. White, **"Dynamic properties of monolithic 1.3 µm InAs/ GaAs quantum dot lasers on silicon,"** *Proc. IEEE International Semiconductor Laser Conference (ISLC)*, Santa Fe, NM, USA, 2018, pp. 1–2.

7. C. Hantschmann, P.P. Vasil'ev, S. Chen, M. Liao, A.J. Seeds, H.Y. Liu, R.V. Penty, and I.H. White, **"Small-signal modulation of monolithic 1.3 µm InAs/GaAs quantum dot lasers on Silicon,"** *Proc. European Conference on Optical Communication (ECOC)*, 2018, pp. 1–3.

8. P.P. Vasil'ev, C. Hantschmann (Boldt), S. Chen, A.J. Seeds, H.Y. Liu, R.V. Penty, and I.H. White, **"Gain switching of quantum dot lasers on silicon,"** *Proc. Semiconductor and Integrated Opto-Electronics Conference (SIOE)*, Cardiff, Wales, UK, 2018, unpublished.

List of Abbreviations

AC	Alternating current
AR	Anti-reflection
BCB	Benzocyclobutene
BL	Barrier layer
CL	Cathodoluminescence
CMOS	Complementary metal-oxide-semiconductor
cw	Continuous-wave
DC	Direct current
DFB	Distributed feedback
DFL	Defect filter layer
DWELL	Dot-in-a-well
ES	Excited state
FDTD	Finite-difference time domain
FWHM	Full width at half maximum
GaAs	Gallium arsenide
GS	Ground state
HR	High-reflection
InAs, InP	Indium arsenide, phospide
LI	Light-current
NRZ	Non-return-to-zero
RIN	Relative intensity noise
PAM4	Four-level pulse-amplitude modulation
PDMS	Polydimethylsiloxane
PL	Photoluminescence
PON	Passive optical network
QD	Quantum dot
QW	Quantum well
REDR	Recombination-enhanced defect reaction
RF	Radio-frequency
SCH	Separate confinement heterostructure
Si	Silicon
UCL	University College London
UCSB	University of California, Santa Barbara
VCSEL	Vertical-cavity surface-emitting laser
VNA	Vector network analyser
WL	Wetting layer

Chapter 1

Introduction

Bandwidth-thirsty web-based applications have drastically shaped the data communication infrastructure of the twentyfirst century. While online services such as cloud storage, video streaming, and social media are already seamlessly integrated into many people's lives, there are various additional emerging Internet of Things (IoT) technologies whose future impact is hard to estimate yet [1]. Smartphones and other mobile devices sit at the heart of these developments, with mobile and wireless IP traffic having started to exceed

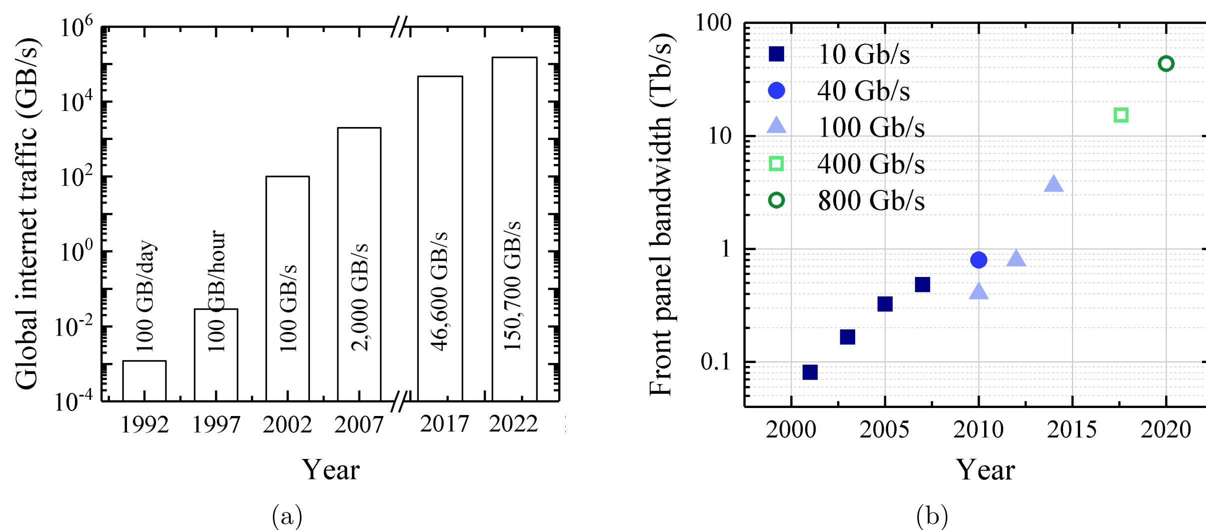

Figure 1.1: (a) Global internet traffic between 1992 and 2017 with estimate for 2022 from Cisco's Visual Networking Index forecast 2017-2022 [1]. (b) Historical view on the aggregated pluggable optics front panel bandwidth using 10 Gb/s, 40 Gb/s, and 100 Gb/s technology as published by Google [2]. 400 Gb/s and 800 Gb/s technology is anticipated to be implemented in the near future.

PC traffic. Specifically smartphones have evolved into the central communication hub for Facebook, Twitter, Youtube etc. as well as into the main interface for a variety of IoT devices ranging from household appliances over medical applications to on-demand video surveillance via the cloud [1].

In the past thirty years, global internet traffic has grown exponentially from an average of only 100 GB per day in 1992, to 100 GB per second in 2002 and to 46,600 GB per second in 2017, as can be seen in Fig. 1.1(a) [1]. It goes without saying that this explosively growing stream of transmitted data places extensive demands on the existing communication networks. Single-lane data rates in fibre optics based optical interconnects have recently been upgraded from 10 Gb/s to 25 Gb/s in state-of-the-art data centres. Combined with multiple parallel optical lanes and higher order modulation schemes, aggregated data rates of 100 Gb/s per interface are currently achieved, whereas even higher rates of 400 Gb/s and 800 Gb/s are envisioned for future generations of data centres and high-performance computers (Fig. 1.1(b)) [2–4]. At present, the trend moves additionally towards building hyperscale data centres to provide higher computational power, although power consumption, heat generation, as well as manufacturing and operation cost place major constraints on the corresponding architecture and technology [5, 6]. The actual networking bottleneck, however, is created at the copper-based electrical interconnects for on-chip and chip-to-chip communications, which approach their limits in providing the demanded bandwidth [7–9].

Silicon photonics, which allows the monolithic integration of data centre interconnect main functionalities including modulating, waveguiding, multiplexing, and light detection on a single silicon die, is believed to be a key enabling technology for meeting next-generation performance requirements at minimised cost per chip [3]. Moving high-speed optical links to the chip level and exploiting their inherent parallelism promises on-chip data rates in the Terabit regime while keeping power consumption and heat generation low [6, 10]. Monolithic silicon photonic integrated circuits hold a further cost advantage compared with traditional components due to reduced processing, packaging, and testing cost with increasing level of integration [3, 11]. Moreover, foundries could take full advantage of the highly mature complementary metal-oxide-semiconductor (CMOS) electronics

infrastructure that enables high-volume manufacturing based on inexpensive large-area silicon wafers [12].

So far, progress on fully monolithic photonic circuits has been quite limited due to the lack of a high-quality silicon-based light source. Silicon is inherently a rather inefficient light emitter due to its indirect bandgap nature, so that integrating high-optical-gain III-V lasers based on GaAs or InP is deemed the most promising approach for meeting performance requirements of practical applications [13]. Due to the large lattice constant and thermal coefficient mismatch to silicon, however, epitaxial III-V growth on silicon substrates results in a high density of threading dislocations propagating into the laser active region and deteriorating the device performance [14]. Off-chip, flip-chip bonded, and wafer-bonded lasers are currently the only commercially available alternatives, despite undermining the high-volume cost advantage due to the costly laser integration process [3, 15].

The first realisation of 1.3 μm InAs/GaAs quantum dot (QD) lasers epitaxially grown on silicon substrate in 2011 was, therefore, a considerable technological breakthrough [16]. Compared with standard bulk or quantum well (QW) active regions, QDs turned out to have an increased tolerance to crystal defects, allowing laser operation at defect densities of four to five orders of magnitude higher than acceptable for commercial GaAs- and InP-based QW devices [17]. In the years to follow, monolithic 1.3 μm QD lasers on silicon evolved rapidly from proof-of-concept lasers operating under pulsed injection only to high-performance devices gaining considerable attention from industry and academia alike [12]. State-of-the-art devices have demonstrated continuous-wave (cw) operation at over 100 °C [18–21], ultralow threshold currents and current densities of 4.8 mA [22] and 62.5 A/cm^2 [13], single-facet maximum output powers of more than 175 mW [23, 24], and extrapolated lifetimes of more than three million hours [23]. These promising early results may eventually open the door for the industrialisation of monolithic III-V lasers on silicon for silicon photonics and beyond in the mid- to longer-term future. Some possible applications will be discussed in the next section.

1.1 Applications of Monolithic III-V Lasers on Silicon

Silicon photonics for high-capacity optical links in data- and computercom was so far the main driver behind developing monolithic III-V lasers on silicon, as co-packaging optics with electronics is believed to be the only way to overcome the electronic bandwidth bottleneck while also reducing power consumption and heat generation. There are, however, multiple applications where III-V gain blocks on silicon may be required and where they may even improve the performance of the original device.

1.1.1 Directly Modulated Standalone Laser

During the process of realising III-V QD lasers grown on silicon, a logical early step is to assess the performance and use of the unintegrated standalone device first. QD lasers have commonly a slower modulation response than QW devices. The advantage of QD lasers on silicon for communication applications beyond silicon photonics will, therefore, be less based on their high-speed properties, but rather on their potential as low-cost emitters in applications where cost rather than performance is decisive. The direct growth on silicon rather than native GaAs or InP substrate should lead to considerable cost savings, as the GaAs and InP substrates price is 14-fold and 38-fold greater than silicon [25]. As a consequence, directly modulated devices grown on GaAs-on-Si virtual substrates have great potential as inexpensive alternatives for new emerging markets such as the 5G mobile network and fibre-to-the-X (FTTX) business or residential optical access [26].

Passive Optical Networks (PONs) can fulfil the respective optical access network requirements of low power and cost, high capacity, and low latency using low-bandwidth optics [27]. 10 Gb/s class optics will be extensively used in the next-generation 10G-PON and show in principle also potential for up- and downstream transmission at $\geq$ 25 Gb/s [28–32]. With millions of optical accesses worldwide and a substantial growth rate [33], PONs are gaining attractivity worldwide, so that there could be a great demand for inexpensive lower-bandwidth lasers such as QD lasers on silicon.

1.1.2 Integrated Light Source for Silicon Photonics

1. Data Centre Optics

Optical interconnects are key in supplying high-speed connectivity in data centres. Fig. 1.2 shows that all interconnections beyond the rack and top of rack level are made optically, as optical links outperform electrical ones at Gigabit data rates ($\geq$ 10 Gb/s) and longer distances $\gtrapprox$ 50 m [34, 35]. For link distances of up to about 100 m to 300 m, 850 nm GaAs-based vertical-cavity surface-emitting lasers (VCSELs) are used in combination with multimode optical fibres [2]. For long reach optics connecting multiple data centre buildings, for example, 1.3 µm InP-based distributed feedback (DFB) lasers and singlemode fibres are used due to limitation of the bandwidth-distance product of multimode fibres [36–38]. Although the optical transceivers interface directly with each server, comparatively long distances have to be spanned by electrical interconnects, as the lasers are only mounted at the edge of the board [39]. Electrical rack-to-rack, board-to-board, and even on-chip communications form here the classical electrical performance bottleneck [35, 40].

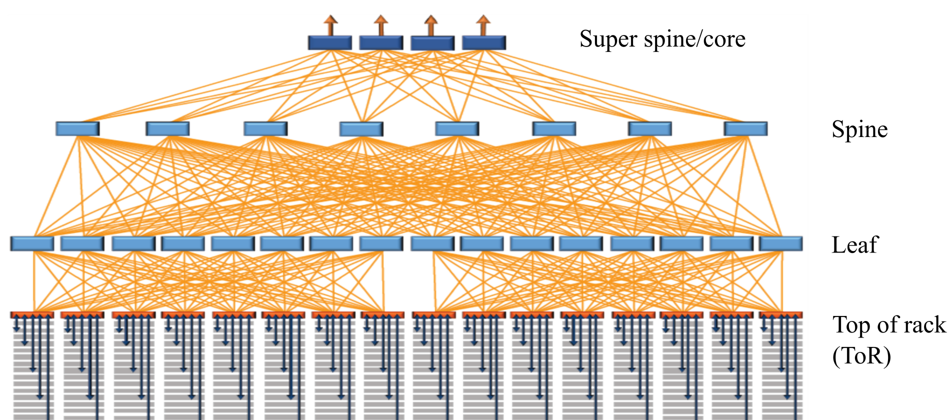

Figure 1.2: Intra data centre network topology with optical interconnects being shown in orange [41].

By moving photonics as closely as possible to the chip level and minimising electrical interconnect distances rather than using standard pluggable optics, higher bandwidths with lower latencies can be provided [39, 42]. A high-performance silicon-based light source is, consequently, integral for data centre silicon photonics. Monolithic 1.3 µm InAs/GaAs QD lasers on silicon hold great promise of overcoming present integration

limitations and show, additionally, many physical properties desirable in optical communication components (further discussed in Chapter 2.2). Since next data centre generations will require single-lane data rates of at least 25 Gb/s, which state-of-the-art QD lasers are unlikely to meet, external rather than direct modulation appears to be the more workable solution in this case.

2. LiDAR

Light detection and ranging (LiDAR) is becoming increasingly popular for 3D sensing in autonomous cars. However, classic LiDAR systems as depicted in Fig. 1.3 tend to be bulky and expensive, as they require beam steering optics or flash illumination with high peak laser power [43]. Silicon photonics has the potential to alleviate many of these system constraints by offering a compact, low-cost, and CMOS-compatible alternative to current approaches [43]. Bhargava *et al.*, for example, have demonstrated an integrated LiDAR system using frequency-modulation continuous-wave (FMCW) detection and a silicon photonic optical phased array for beam steering [44]. FMCW LiDAR offers higher precision than other common detection types such as pulsed LiDAR or amplitude-modulation cw detection [45], while eliminating the need for high-speed electronic circuitry [46]. In a monolithic silicon photonics LiDAR system, the external 1550 nm singlemode laser used in [44] could be replaced by a tunable QD laser grown on silicon as demonstrated in [47].

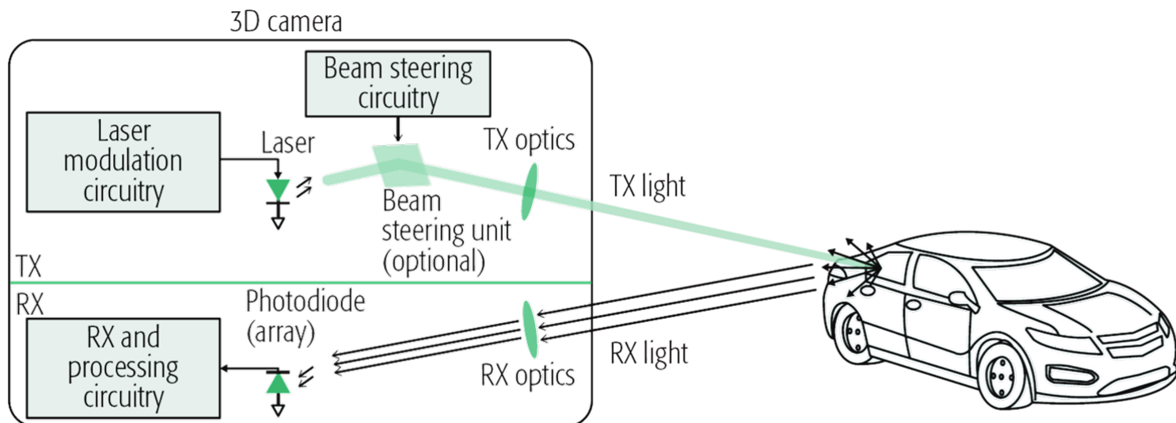

Figure 1.3: Schematic of a basic LiDAR system [45]. Using a silicon photonics platform instead, light could be provided by a tunable QD laser grown on silicon and guided by silicon waveguides and couplers. Optical phased arrays for the transmitted and received light can replace bulky and slow beam steering optics.

Beyond these two examples, there are of course many more applications such as in camera technology [48, 49], metrology [50], and biosensing and medicine [51, 52], for instance, where monolithic silicon photonic integrated circuits have the potential to drastically reduce component or fabrication cost, increase the performance, or enable completely new functionalities [53].

1.1.3 Other Niche Applications

Besides their main application for optical communications, silicon-based 1.3 μm QD lasers offer the possibility of designing optical devices showing enhanced functionality compared with their original, purely III-V-based counterparts. One such example could be a monolithic III-V-on-Si DFB laser with its index grating etched into the passive silicon substrate. As silicon shows a smaller carrier- [54–56] and temperature-induced refractive index change than GaAs and InP [57], this could result in more stable operation. A hybrid version of such a device, has been demonstrated in 2011 by Srinivasan *et al.* [58], for example.

Narrow linewidth lasers are another example showing improved performance when integrated with silicon. Long cavities are required to reduce the laser's emission linewidth [59], and the propagation loss in silicon is one order of magnitude lower than in GaAs or InP [17]. Coupling the photons from the III-V gain region into a long silicon-based ring cavity is, consequently, a promising approach and could find applications in coherent transceivers or LiDAR [60]. The ring configuration provides also an opportunity for wavelength tuning.

Lastly, silicon-based QD lasers show potential as single-mode high-power lasers, for example as pump source for praseodymium-doped (PDFAs) or erbium-doped fibre amplifiers (EDFAs) in O-band and C-band communication systems. Whereas QD active regions are traditionally not deployed in high-power semiconductor devices, QD lasers on silicon have actually a number of properties that would be desirable for applications where not only high power, but also high brightness is required. Poor beam quality resulting from antiguiding effects and irregular contributions of longitudinal and transverse modes due to the carrier density dependence of the refractive index are common issues in

high-power broad-area semiconductor lasers [61, 62]. This coupling between the carrier density and the refractive index is expressed through the antiguiding factor or linewidth enhancement factor α_H, respectively [63]. QD lasers happen to have a near-zero linewidth enhancement factor [64], meaning filamentation issues may be alleviated. Since heat management is a further concern at high pump levels, a moderate high-power QD laser grown on silicon could further benefit from silicon's natural heat sinking resulting from its high thermal conductivity [12]. Although QD lasers suffered traditionally from low power and gain saturation, recent publications of monolithic 1.3 µm QD lasers on silicon reported on front-facet output powers of 185 mW [23], which shows great promise for high-power operation in a suitable laser design. For PDFA pumping, silicon-based lasers could be realised using small InAs/GaAs QDs for emission at 1020 nm [65] or 1047 nm [66], or could be alternatively based on InAs/InP QDs for EDFA pumping at around 1.5 µm [67].

1.2 Organisation and Aim of this Dissertation

The aim of this dissertation is to improve the understanding of the physical mechanisms currently limiting the suitability of InAs/GaAs QD lasers on silicon for commercial applications. At the time this PhD project was conducted, very little was known about the physical properties of this novel kind of laser and about to what extent they might be different from conventional InAs QDs on grown on GaAs. Most publications reported primarily on improvements in semiconductor growth technology in conjunction with improved light-current performance of the mostly very simple laser structures. However, there was a distinct lack of studies looking beyond these basic device characteristics, for instance in the form of theoretical studies investigating the underlying laser parameters responsible for the observed behaviour. In addition, the high-speed data transmission potential of QD lasers on silicon was not addressed at all, despite being one of the key selling points for silicon photonics. This dissertation focuses, therefore, on two main aspects. First, the role of dislocations is investigated theoretically in order to identify how exactly dislocations impair the static performance of QD lasers on silicon, and why lasers with QD active regions are more immune to these effects compared with QWs.

Secondly, the data transmission potential of monolithic 1.3 μm QD lasers on silicon is studied through experiment and simulation.

This dissertation is organised as follows. This first chapter has given an introduction into the underlying motivation and the possible applications driving the progress on photonic integrated circuits and more specifically 1.3 μm InAs/GaAs QD lasers monolithically grown on silicon substrates. Chapter 2 will outline the fundamental operating principles of semiconductor diode lasers, covering the essentials of the double-heterostructure, active region types, and an analytical rate equation description of a semiconductor laser's static and dynamic properties. A detailed introduction into III-V lasers on silicon will be given in chapter 3. After discussing the problems associated with integrating lasers on silicon and introducing the to date main laser integration approaches, the special requirements of epitaxial III-V growth on silicon substrates will be discussed. Finally, a review of recent achievements regarding the static performance of monolithic 1.3 μm QD lasers on silicon will be presented. This is then followed by a detailed explanation of the used theoretical model, on which the results of the following chapters are based, and its numerical implementation in chapter 4. This chapter also touches on common choices of modelling parameters for InAs QD lasers on native substrate, and how these differ for their counterparts on silicon substrate.

Chapters 5 to 7 contain the main experimental and theoretical results of this work. Chapter 5 presents a theoretical study on the role of dislocations in monolithic III-V lasers on silicon. Two approaches are presented here, with the first one based on macroscopically averaged laser parameters describing the performance deterioration with dislocation density, while the second, high resolution approach allows insights into the local phenomena of the optical gain, carrier, and photon density distribution in the presence of dislocations. Both approaches point to the role of carrier migration into defects and explain the superior performance of QD over QW-based active regions. Chapters 6 and 7 investigate the dynamic properties of monolithic QD lasers grown on silicon, beginning by reviewing their so far investigated dynamic properties. The here presented studies on gain switching and small-signal modulation are supported by numerical simulations and aim particularly at understanding the experimentally observed performance limita-

tions, at modelling the fastest achievable modulation speeds in a high-speed optimised laser design, and at studying the potential impact of the silicon substrate. Chapter 8 will finally conclude this dissertation and give an outlook on what is likely to come next for monolithic InAs QD lasers on silicon.

1.3 Achievements of this Work

- The theoretical work of this PhD project has contributed to advancing the knowledge on III-V lasers on silicon by publishing two of the first theoretical studies, thus establishing the first sets of laser parameters available for the simulation of QD optical components on silicon [68, 69]. These first insights into the underlying laser physics served as a valuable starting point to evaluate to what extent the devices are different from their counterparts grown on native substrates, as discussed in chapters 4.4.2, 6, and 7.

- The first theoretical studies considering specifically the impact of threading dislocations in the III-V laser active region were carried out [70, 71]. With the aim of identifying the main mechanisms responsible for the disparity in performance between QD and QW lasers on silicon as well as the origin of the performance degradation observed with increasing dislocation density, the work in chapter 5 presents a novel approach of implementing dislocations in a travelling-wave rate equation model. The simulations allow to identify a large minority carrier diffusion length as a key parameter inhibiting laser operation by enabling carrier migration into dislocations over larger areas, and point also to the issue of locally reduced gain around dislocations, which has to be compensated for in dislocation-free regions. This process could lead to enhanced gain saturation effects in QD lasers on silicon with high dislocation density and limited modal gain [71, 72].

- The experimental results presented in chapters 6 and 7 contribute some of the first studies on the dynamic properties of 1.3 μm QD lasers on silicon. We have reported the first ever gain-switched optical pulses using silicon-based QD lasers [68], and the second ever published results on small-signal modulation [69, 73, 74]. The shortest

optical pulses are 150 ps long, while 3dB modulation bandwidths of 1.6 GHz to 2.3 GHz were measured using 2.5 mm long narrow ridge-waveguide lasers with high-reflection coating [75].

- In contrast to other work, these results are supported by a rigorous theoretical analysis, which can serve as a reference for other researchers who wish to improve their QD devices' high-speed performance. While the high-speed limitations observed in our measurements are largely a result of the laser design, simulations show that data transmission rates of 10 Gb/s may be achievable in an optimised laser layout. They indicate, furthermore, that the overall dynamic properties of QD lasers on silicon seem to be governed by the QD physics, regardless of the substrate type [69]. Based on their increased dislocation-induced nonradiative carrier losses, QD lasers on silicon were, however, identified to show stronger damping in their modulation response. While this in itself does not directly affect the modulation bandwidth, dislocation-induced carrier loss will lead to increased laser thresholds and thus higher power consumption and heating. Locally reduced gain as a result of carrier depleted regions around dislocations may, furthermore, lead to a premature saturation of the modulation bandwidth due to increased gain compression effects.

Chapter 2

Semiconductor Laser Fundamentals

Semiconductor lasers have attracted wide interest for data- and telecommunication applications due to the possibility of transmitting data by modulating the laser's optical output through its drive current. This chapter will give an introduction into the fundamentals of semiconductor laser diodes, covering the operation principles of the double-heterostructure, common active region types, and a theoretical rate equation description of a semiconductor laser's static and dynamic properties.

2.1 Operation Principles

The knowledge about the general concept of lasing, light amplification by stimulated emission of radiation, dates back to as early as 1916, when Albert Einstein first proposed the possibility of stimulated emission of photons in his elaborations on *Quantum Theory of Radiation* [76]. The first experimental demonstration of a laser, a ruby laser realised by Theodore Maiman at the Hughes Research Laboratories, did not take place until 1960 [77, 78], but kickstarted eventually the development of a whole range of laser types - among those the semiconductor laser [79]. All conventional lasers consist of three main building blocks: a gain medium, a laser cavity for optical feedback, and an energy pump exciting electrons into a higher energy level to enable stimulated emission of photons. Analogously, a semiconductor laser in its simplest form is obtained by cleaving a direct semiconductor material (see chapter 3.1 for direct and indirect semiconductors) to obtain

a resonator with the semiconductor itself representing the gain medium [80]. Such a device can be pumped electrically by injecting carriers under forward bias, that means electrons are injected into the conduction band from the n-doped region, while holes are injected into the valence band from the p-doped side. This way, minority carriers accumulate in the p-n depletion region, which increases the probability of radiative recombination of electrons and holes. When an electron and a hole form a pair, which occurs in QWs and QDs (compare section 2.2 for active region types) [81], this quasi-particle is called an exciton. If population inversion is achieved at the band edges, stimulated emission sets in and light amplification is enabled. Lasing is sustained through optical feedback at the partly reflecting semiconductor laser facets perpendicular to the junction plane [82].

2.1.1 The Double Heterostructure

The first ever demonstrated semiconductor diodes lasers in 1962 were formed of a basic p-n GaAs homojunction, as shown in Fig. 2.1(a) [85–88]. Although it is possible to obtain lasing using such a simple configuration, this type of device is rather inefficient, as carriers tend to diffuse away from the junction due to lacking electrical confinement.

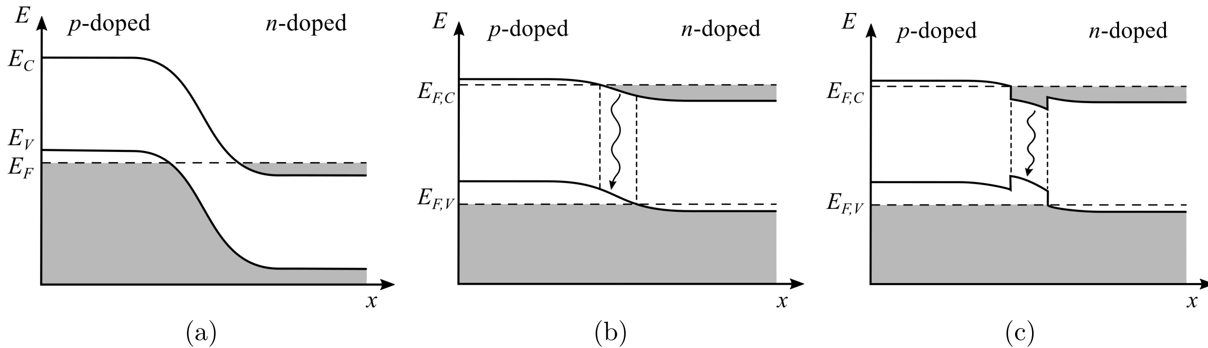

Figure 2.1: (a) Unbiased p-n homojunction with adjusted Fermi level E_F in thermal equilibrium. E_C and E_V denote the conduction band and valence band energy edges. Grey areas represent electrons, while white areas such as those below E_V represent holes. (b) p-n homojunction under forward bias: electrons and holes recombine radiatively in the depletion region. Under these non-equilibrium conditions, the Fermi levels $E_{F,C}$ and $E_{F,V}$ for the conduction band and valence band are separated by about the voltage applied to the junction. (c) Double heterostructure under forward bias with carrier confinement in the active region. The smaller bandgap material is commonly an intrinsic semiconductor with unintentional doping [83]. After [84].

As a consequence, very high current densities of tens of kA/cm^2 were required to obtain lasing [87, 88], while self-absorption in the homojunction is another major issue [83]. These performance limitations restricted the early semiconductor lasers' operation conditions to pulsed and cooled operation only, hence rendering them unsuitable for practical applications [82].

Today's standard semiconductor laser design is, therefore, based on the far more efficient double heterostructure, which is realised using lattice-matched compounds such as AlGaAs or InGaAsP, for example [83, 89]. Having first been realised in 1963 by Alferov, Kayarinov, and Kroemer [90, 91], a double heterostructure distinguishes itself from a *p*-*n* homostructure by sandwiching a material of smaller bandgap in the centre of the junction, as illustrated in Fig. 2.1(c). This kind of configuration provides two essential advantages: carrier confinement and optical confinement. The potential difference between the active region and the cladding layers allows effective localisation of the carriers at the heart of the *p*-*n*-junction. As a consequence of this carrier confinement, population inversion can be reached at comparably low injection densities. Conveniently, a semiconductor's bandgap also scales inversely with its refractive index, so that the smaller bandgap optically active material exhibits a higher index. This optical confinement results in a waveguide effect along the active region by means of total internal reflection at the core-cladding interfaces [82, 83]. State-of-the-art devices with much thinner active regions compared with the 1960s and '70s are still based on this concept, but incorporate slightly more complex waveguide designs confining the optical mode in an intermediate

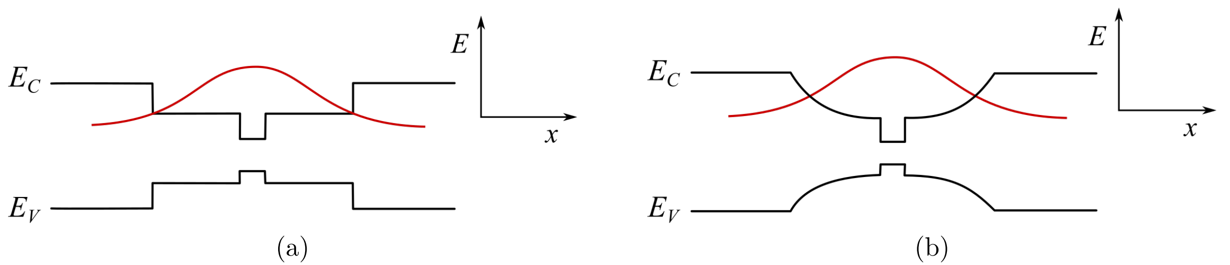

Figure 2.2: Schematic bandgap profile along the epitaxial growth direction of two types of separate-confinement heterostructures (SCHs) along with the optical mode distribution. (a) Step-index SCH. (b) Graded-index SCH (GRINSCH). After [80].

bandgap region around the thin active layers. Fig. 2.2 shows two common examples of such separate-confinement heterostructures (SCHs) [80].The adoption of the double heterostructure allowed quickly for substantial improvements in the device performance, opening the door for low-threshold continuous-wave (cw) operation at room temperature in 1970 [92, 93] and thus making semiconductor diode lasers attractive for a multitude of applications.

2.1.2 Lateral Confinement

Good lateral in-plane confinement of the optical mode along the laser cavity is not only helpful in increasing the overall laser efficiency, but for some applications, such as optical communications, for instance, it is also necessary to ensure high optical fibre coupling efficiency and near single-transverse mode operation [94]. There are two mechanisms through which lateral confinement can be achieved: index guiding and gain guiding. As suggested by the name, the optical mode in a gain-guided laser is primarily confined by restricting the lateral extent of the carrier distribution in the active region, whereas index-guided devices guide the optical wave by embedding the central ridge in a material of lower refractive index [84, 89].

Since gain-guided structures are considerably easier to fabricate than devices with strong index guiding, they are well represented in markets with less stringent operation

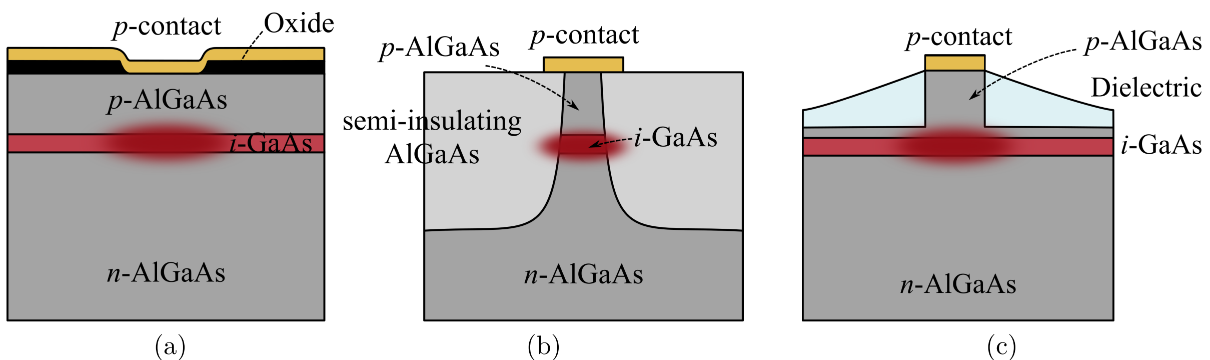

Figure 2.3: Schematic front view of laser structures using different kinds of lateral confinement schemes. (a) Gain-guided oxide-confined laser. (b) Index-guided buried-heterostructure laser. (c) Gain- and partly index-guided narrow ridge-waveguide laser. After [94].

requirements [84]. Gain-guided lasers are fabricated in a straight-forward way by incorporating a current-blocking oxide layer with stripe openings at the wafer surface, for example, as can be seen in Fig. 2.3(a). Hence, current injection is roughly limited to the stripe below the etched oxide opening, although current spreading and carrier diffusion increase the required threshold current. A further problem is that high carrier densities in the central active region can cause anti-guiding of the lateral field profile, as the refractive index decreases with rising carrier density [54, 89]. Since both gain and index guiding are sensitive to changes in the carrier density and the temperature, such devices can show quite complex spatiotemporal dynamics [95].

Index-guided lasers can be divided into strongly guided (refractive index difference $\Delta n \approx 0.2$) and weakly guided devices ($\Delta n \approx 0.01$) [89]. Strong index guiding can be achieved in buried-heterostructure lasers, as shown in Fig. 2.3(b). After defining the optically active ridge, an epitaxial overgrowth step with a lower refractive index semiconductor is required, which makes the realisation of high-performance buried-heterostructure lasers quite demanding [94]. An alternative with more relaxed fabrication conditions is the ridge laser operating based on gain and weak index guiding (Fig. 2.3(c)). Since the edges of the optical field extend into the dielectric coating or planarisation layer, the outside parts of the field experience effectively a lower refractive index, which promotes waveguiding along the narrow ridge [89, 94].

2.1.3 The Laser Cavity

In an ordinary Fabry-Pérot (FP) laser with as-cleaved facets, the reflectivity resulting from the refractive index difference between the semiconductor material and the surrounding medium, which is typically air, provides the necessary optical feedback and direction selectivity to sustain lasing [82]. With GaAs having a refractive index of about 3.5, this yields a reflectivity of

$$R = \left(\frac{n_{GaAs} - n_{air}}{n_{GaAs} + n_{air}}\right)^2 \approx 0.3 \tag{2.1}$$

[96], which is usually sufficient provided that the gain and the amplification length are high and long enough. It lies in the nature of the FP resonator to only provide

constructive feedback at selected wavelengths λ or frequencies ν, respectively, matching the phase condition for the m-th mode

$$\lambda_m = \frac{2n_{eff}L}{m} \quad \Leftrightarrow \quad \nu_m = \frac{mc}{2n_{eff}L} \tag{2.2}$$

[97]. m, n_{eff}, and L are an integer number, the effective refractive index, and the cavity length, respectively. Combined with the semiconductor's broad gain bandwidth, which is around three orders of magnitude wider than that of a helium-neon gas laser [80], this results typically in a highly multimode optical spectrum consisting of equidistant cavity modes (in frequency space), as illustrated in Figs. 2.4(a) and (b).

The lasing condition is fulfilled if the gain balances the losses after one round trip in the cavity [97]. Mathematically, this is the case if the electric field

$$E(z,t) = E_0 \; e^{(\frac{g_{mod}}{2} - \frac{\alpha_i}{2})z} e^{-i(kz-\omega t)} \tag{2.3}$$

reproduces itself in amplitude and phase as

$$E_0 = \left(E_0 \sqrt{R_2} \; e^{(\frac{g^{th}_{mod}}{2} - \frac{\alpha_i}{2})L} e^{-ikL} \right) \left(\sqrt{R_1} \; e^{(\frac{g^{th}_{mod}}{2} - \frac{\alpha_i}{2})(L-0)} e^{-ik(L-0)} \right) \tag{2.4}$$

$$\Leftrightarrow \quad \sqrt{R_1 \; R_2} \; e^{(g^{th}_{mod} - \alpha_i)L} = 1 \tag{2.5}$$

after a propagation of $z = 2L$ and reflection at both facets with reflectivity R_1 and R_2. E_0, k, and ω are the electric field amplitude, the wave number $k = 2\pi/\lambda$ and the angular frequency [94]. The modal gain and optical loss g_{mod} and α_i are scaled with a factor 1/2 as these quantities are defined with respect to the light intensity [98]. In Eq. (2.4) and following, the time dependence $e^{i\omega t}$ is dropped as it occurs in all terms. From Eq. (2.5), one obtains the threshold condition

$$g^{th}_{mod} = \alpha_i + \frac{1}{L} \ln \left(\frac{1}{\sqrt{R_1 R_2}} \right) \tag{2.6}$$

$$\Leftrightarrow \quad g^{th}_{mod} = \alpha_i + \alpha_m \; , \tag{2.7}$$

where the second term is defined as the mirror loss α_m. Since the photon lifetime τ_{ph} is defined as the photon decay rate associated with optical losses in the cavity during propagation and at the mirrors, τ_{ph} is then given via the group velocity $v_{gr} = c/n_{eff}$ as

$$\tau_{ph} = \frac{1}{v_{gr}(\alpha_i + \alpha_m)} \quad [98]. \tag{2.8}$$

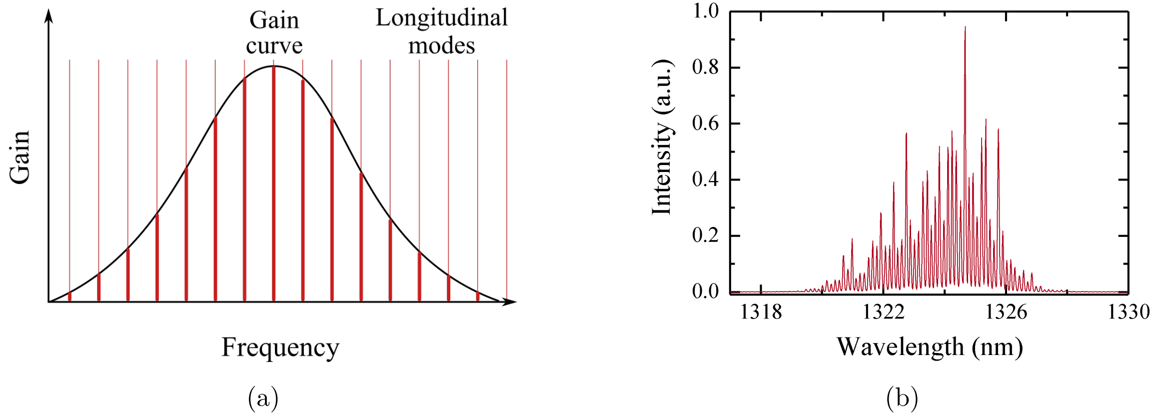

Figure 2.4: (a) Illustration of the longitudinal cavity modes of a broadband gain medium in an FP cavity. (b) Multimode spectrum of a 1.3 µm QD FP laser grown on silicon.

2.2 Active Region Types

The types of active regions deployed in semiconductor lasers evolved with advancing growth technology. For about two decades, semiconductor lasers were based on bulk active regions, i.e. a few hundred nanometres of gain material sandwiched between the cladding layers [83, 89, 99]. These devices were fabricated using liquid phase epitaxy, which did not allow sufficiently accurate layer thickness control, let alone the deposition of thin films at the atomic monolayer level. Semiconductor lasers utilising a bulk active region showed typically high threshold currents due to the large active volume.

The development of vapour-phase epitaxy techniques such as molecular beam epitaxy (MBE) and metal-organic chemical vapour deposition (MOCVD) lead to substantial performance improvements by downscaling the active region thickness to a few nanometres [100, 101]. The reason for this is the onset of quantum effects when electrons and holes are

spatially confined at the length of the de Broglie wavelength (~10 nm) along one or more directions [102, 103]. In QW lasers, the active region thickness of a single QW is reduced to about 7 nm to 10 nm, for example, so that the injected carriers are confined parallel to the growth plane. As a consequence, the density of states is a step function of energy, as can be seen in Fig. 2.5 [104, 105]. QW lasers benefit from reduced threshold currents and higher differential gain and high modulation speeds [106, 107], which makes them to date the preferred active region type in commercially available laser diodes. 850 nm GaAs QWs in AlGaAs cladding layers are the standard material system for VCSELs in short-haul communication systems [36], whereas InGaAsP QWs grown on InP are typically used for in-plane lasers emitting in the low-dispersion O-band (1310 nm) and the low-loss C-band (1550 nm) for telecommunication applications [80]. Although perfectly lattice-matched, unstrained growth was traditionally the goal to achieve almost defect-free structures of high crystalline quality, intentionally strained QWs, such as compressively strained InGaAs/GaAs QWs emitting at 980 nm, yield higher differential gain [108–110]. Additionally, QW lasers contain typically closely stacked multi-quantum well active regions to reduce gain saturation effects [111].

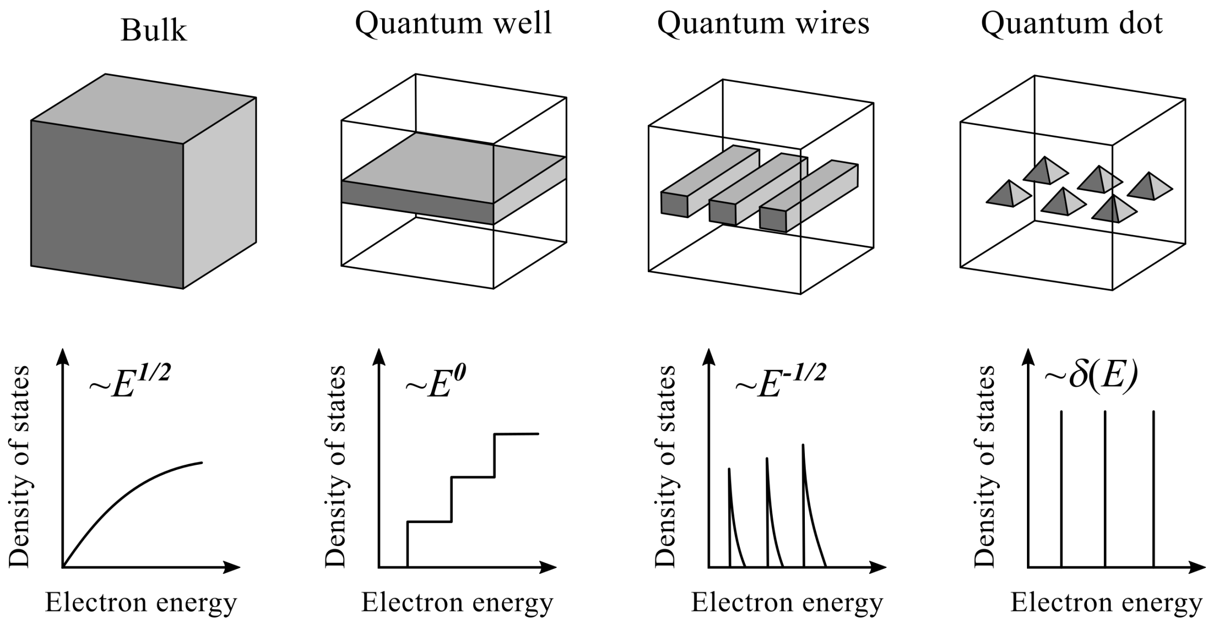

Figure 2.5: Comparison of the electronic density of states of bulk, (single) QW, quantum wire, and QD active regions. After[112].

Fig. 2.5 shows that the degree of carrier confinement can be further increased by growing quantum wires and QDs, which show two- and three-dimensional spatial confinement, respectively. QDs have attracted great academic interest due to their discrete spectrum of energy eigenvalues consisting of a ground state (GS) with twofold degeneracy and often multiple excited states (ES) with fourfold (ES1) and sixfold degeneracies (ES2 and higher) [113, 114], as shown in Fig. 2.6. As a consequence, QD lasers are prime candidates for high differential gain and ultralow threshold currents, as quick filling of the discrete energy states enables population inversion at very low injection levels [112].

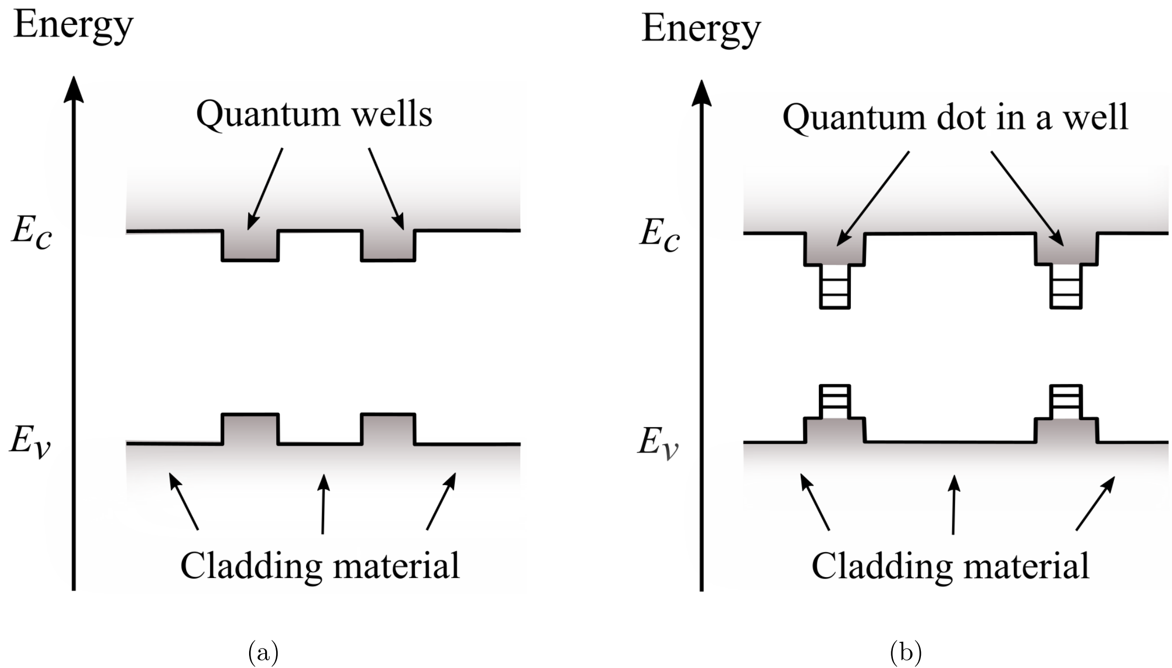

Figure 2.6: Schematic one-dimensional real-space energy band diagrams of (a) a QW active region with a continuum of states and (b) a dot-in-a-well (DWELL) QD active region with two discrete QD states. E_C and E_V depict the conduction band and valence band edge energy.

Compared with quantum wires, QD active regions can conveniently be produced in a self-organised growth process, where a material of larger lattice constant is deposited on a smaller lattice constant substrate, such as InAs on GaAs. The high compressive strain is then released by transitioning into the three-dimensional growth mode and forming QDs [115]. In the case of InAs and GaAs, this offers additionally the advantage of extending

the emission range of the InGaAs system, which is for QWs restricted to wavelengths below about 1.1 μm [116], into the 1.3 μm O-Band. For improved carrier capture and growth conditions, the QD layers are typically embedded in a QW-like wetting layer with intermediate bandgap, such as InGaAs, which results in the coupled electronic system shown in Fig. 2.6 [114].

Although the first InAs/GaAs QD laser was already demonstrated in the 1990s [117], QDs have so far largely remained a subject of academic research, as realistic devices show several shortcomings. Gain saturation due to limited modal gain is one of the central issues. This results in part from the stochastic size and thus energy level distribution of the self-organised QDs, which leads to an inhomogeneously broadened gain function rather than sharp gain peaks at identical energy levels [113, 115]. Growing homogeneously sized QDs is, therefore, important for achieving high peak gain. It is, furthermore, difficult to achieve a high overlap between the optical mode and the active medium due to the limited QD density and thick spacer layers in QD multi-stacks. Up to 50 nm thick buffer layers are needed to compensate for the high strain necessary to form QDs in order to prevent the formation of crystal defects [118, 119], whereas QWs require only a few nanometres [120]. The resulting small confinement factor (0.01% - 0.1% as opposed to a few percent in multi-QWs) reduces, consequently, the modal gain

$$g_{mod} = \Gamma g_{mat}^{max} \; , \tag{2.9}$$

and can lead to premature gain saturation despite intrinsically high QD material gain g_{mat}^{max} [121, 122]. While QWs with their higher modal gain are capable of producing larger output powers as well as faster modulation speeds [123–126], low modal gain in QDs limits the modulation response not only in itself, but additionally also due to the resulting need for long cavity lengths. The QD laser's modulation response is further slowed down by the cascaded carrier transport mechanism into the discrete QD energy states as well as longer carrier transport times through the thicker QD active region [127–129].

Nevertheless, QD lasers show a variety of very interesting properties which might prove extremely useful for certain optical communication applications. Beyond low threshold

currents for reduced power consumption and heat generation [130], they show typically a high characteristic temperature T_0 and exhibit thus high temperature stability for uncooled operation or high component integration density [131, 132], low relative intensity noise for improved signal-to-noise ratios [133, 134], reduced wavelength chirp during direct modulation [64], broadband emission for multi-wavelength sources in wavelength-division multiplexing (WDM) systems [135], and low sensitivity to optical feedback in (integrated) optical systems [136]. With their most recent application as defect-resistant active region type in GaAs- and InP-based lasers grown on silicon, QDs may, for certain niche applications, have actually reached a point though where their unique advantages begin to overcome some of their shortcomings.

2.3 Rate Equation Description

A simple pair of rate equations for the interaction between the carrier density n and photon density S can be formulated to describe the main physical processes in a semiconductor diode laser. A standard one-level rate equation system is given as

$$\frac{dn}{dt} = \frac{\eta I}{eV} - \frac{n}{\tau_{nr}} - \frac{n}{\tau_r} - v_{gr} g(n) S \tag{2.10}$$

$$\frac{dS}{dt} = v_{gr} \Gamma g(n) S + \frac{\beta n}{\tau_r} - \frac{S}{\tau_{ph}} \tag{2.11}$$

[98]. Eq. (2.10) describes the temporal evolution of the carrier density under current injection $\eta I/(eV)$ with efficiency η into the active volume V in the presence of nonradiative carrier loss n/τ_{nr}, spontaneous recombination n/τ_r and lasing $v_{gr} g(n) S$. I, e, τ_{nr}, τ_r, v_{gr}, and $g(n)$ are the electric current, the electronic charge, the nonradiative and radiative carrier lifetime, the group velocity, and the material gain, which is a function of the carrier density. The photon density equation (2.11) contains terms for the lasing process $v_{gr} \Gamma g(n) S$, spontaneous emission $\beta n/\tau_r$, and photon loss S/τ_{ph}, where Γ, β, and τ_{ph} are the optical confinement factor, i.e. the overlap between the active volume and the optical mode volume, the spontaneous emission coupling factor, and the photon lifetime introduced above. The equations assume constant carrier and photon densities over the entire

device, homogeneous current injection, and singlemode operation. Possible extensions, such as the inclusion of temperature effects, are further discussed in chapter 4.6.

The appropriate gain function to use depends on the type of active region to be described. Whereas the bulk gain can be approximated using a linear gain relationship $g(n) = a(n - n_{tr})$ [137, 138], the QW gain function is better calculated using the logarithmic function $g(n) = g_0 \ln(n/n_{tr})$ [81, 139]. a, g_0, and n_{tr} are the differential gain, the nonlinear gain coefficient, and the carrier density at transparency. The QD gain can be parametrised based on the maximum material gain g_{mat}^{max} and the ground state electron and hole occupation probabilities f_{GS}^{e} and f_{GS}^{h} as $g(n) = g_{mat}^{max}(f_{GS}^{e} + f_{GS}^{h} - 1)$ [140, 141]. In order to consider gain saturation effects, a phenomenological factor $(1 + \epsilon S)^{-1}$ containing the gain compression factor ϵ can be multiplied to the gain function [83, 142, 143]. This factor is of special importance for the QD dynamics, as it limits the maximum modulation bandwidth. This will be further explained in section 2.3.2.

Implementing the rate equations (2.10) and (2.11) numerically shows that the interplay of carrier density n and photon density S leads to relaxation oscillations during the laser

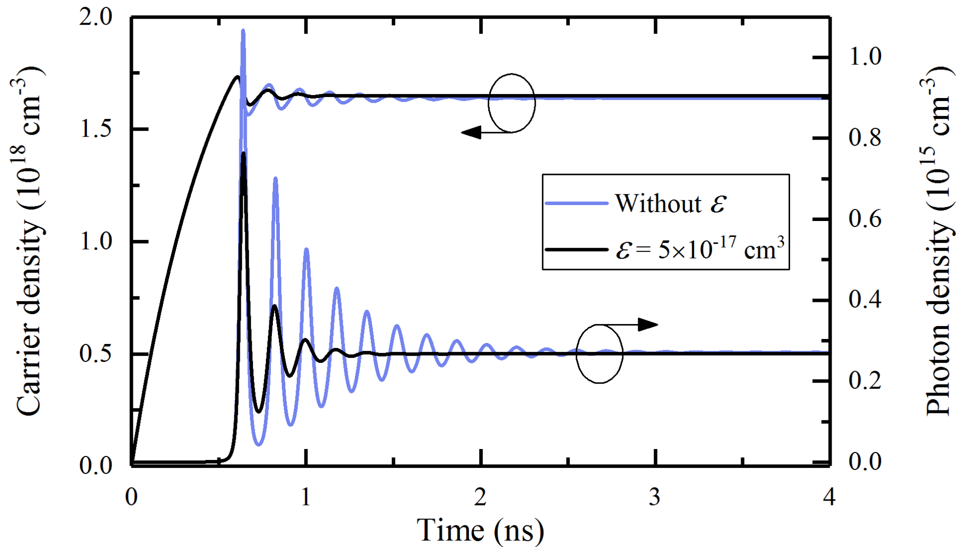

Figure 2.7: Numerical simulation of relaxation oscillations of a QW laser modelled using Eqs. (2.10) and (2.11). The light blue relaxation oscillations have been modelled without gain compression, whereas the black curves have been modelled by including a gain compression factor of 5×10^{-17} cm^3 in the gain function. The result is a substantially higher level of damping.

turn-on process (Fig. 2.7), as n and S oscillate initially around their equilibrium value before the steady state is established [144]. The effect of the gain saturation term on the oscillation dynamics is illustrated as well.

2.3.1 Static Properties

Deriving analytical expressions from the steady-state rate equations offers, despite their strongly simplified form, a useful basis for the straightforward interpretation of experimental light-current characteristics as well as a good starting point for numerical simulations. At steady state, an analytical expression for the threshold current I_{th} can be derived from the carrier rate equation (2.10) by setting $dn/dt = 0$. Under the assumption that spontaneous and stimulated emission can be neglected at this point, Eq. (2.10) yields

$$0 = \frac{\eta I_{th}}{eV} - \frac{n_{th}}{\tau_{nr}} \tag{2.12}$$

$$\Rightarrow \quad I_{th} = \frac{eVn_{th}}{\eta\tau_{nr}} \tag{2.13}$$

Both the material gain g_{th} and the carrier density n_{th} are clamped at threshold, as illustrated in Fig. 2.8(a) and (b) [98]. From Eq. (2.13) it can be seen that the threshold

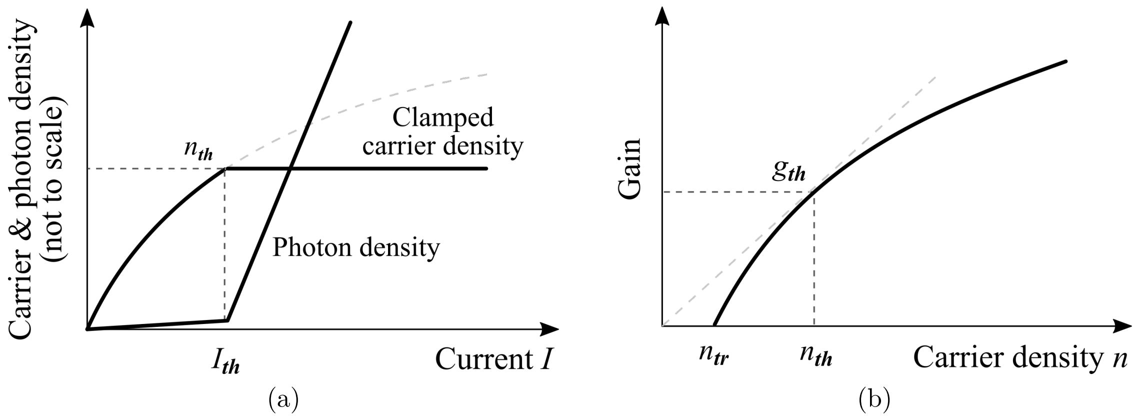

Figure 2.8: (a) Schematic of the static carrier density and photon density behaviour below and above the threshold current. As stimulated emission sets in, the carrier density is clamped at the threshold level. (b) Logarithmic gain against the carrier density. The gain clamps at the threshold (not shown) as a result of the clamped carrier density. After [98].

current depends, among other things, on the pump volume V, the injection efficiency η, and the carrier lifetime τ_{nr}.

An expression for the photon density S above threshold is obtained by equating Eq. (2.12) and the static expression of the carrier rate equation (2.10):

$$\frac{\eta I_{th}}{eV} - \frac{n_{th}}{\tau_{nr}} = \frac{\eta I}{eV} - \frac{n}{\tau_{nr}} - v_{gr} g(n) S \ . \tag{2.14}$$

Since $n = n_{th}$ and $g(n) = g_{th}$ on the right-hand side of the equation, this yields

$$S = \frac{\eta(I - I_{th})}{eV v_{gr} g_{th}} \ . \tag{2.15}$$

This is converted into the actually emitted optical output power P_{out} by multiplying with $h\nu V_{mode}$, to obtain the energy of the optical mode in the cavity, and by dividing by τ_m, which represents the optical loss rate through the cavity facets or mirrors [98].

$$P_{out} = \frac{h\nu V_{mode} S}{\tau_m} \tag{2.16}$$

Using the definition

$$\mathit{\Gamma} = V/V_{mode} \tag{2.17}$$

for the optical confinement factor, the relation

$$\tau_m = \frac{1}{v_{gr}\alpha_m} \tag{2.18}$$

analogously to Eq. (2.8), the threshold condition $\mathit{\Gamma} g_{th} = \alpha_i + \alpha_m$ (Eq. (2.7)), and Eq. (2.15) for the relationship between the photon density S and the current above threshold $(I - I_{th})$ yields

$$P_{out} = \frac{h\nu V_{mode} S}{\tau_m} \tag{2.19}$$

$$= \eta \frac{\alpha_m}{\alpha_i + \alpha_m} \frac{h\nu}{e} (I - I_{th}) \ , \tag{2.20}$$

where $\eta_d = \eta \ \alpha_m/(\alpha_i + \alpha_m)$ is defined as the differential slope efficiency η_d [98]. The

factor $\eta\ \alpha_m/(\alpha_i + \alpha_m) \cdot h\nu/e$ describes the actual slope of the experimental LI curve in W/A, showing that the LI slope depends largely on the injection efficiency η as well as the magnitude of the optical loss α_i.

2.3.2 Dynamic Properties: Small-Signal Analysis

Small-signal modulation is when a laser's frequency response is studied by modulating the drive current I_{DC} with a small, typically sinusoidal signal $\tilde{I}$ with swept frequency ω. Depending on the overall bias level, the modulation amplitude $\tilde{I}$ is typically only a few milliamps, so that the small-signal condition $\tilde{I} \ll I_{DC} - I_{th}$ is fulfilled [145]. Although large-signal modulation schemes are used in actual communication systems, small-signal modulation offers the advantage of analytic solutions to the rate equations (2.10) and (2.11), hence giving insight into the underpinning dynamic laser parameters. From the data transmission point of view, one of the most important quantities is the modulation bandwidth f_{3dB}, defined as the frequency range over which the small-signal response drops by 3 dB compared to its low-frequency or DC value, as it is used to predict a laser's large-signal capabilities [146]. Using complex frequency domain notation, the modulated current, carrier density, and photon density can be expressed as

$$I(t) = I_{DC} + \tilde{I}e^{i\omega t} = I_{DC} + dI \tag{2.21}$$

$$n(t) = n_{DC} + \tilde{n}e^{i\omega t} = n_{DC} + dn \tag{2.22}$$

$$S(t) = S_{DC} + \tilde{S}e^{i\omega t} = S_{DC} + dS\ . \tag{2.23}$$

Since the steady-state solutions dI_{DC}/dt, dn_{DC}/dt, and dS_{DC}/dt cancel out to zero, inserting Eqs. (2.21) – (2.23) into (2.10) and (2.11) and neglecting spontaneous emission yields

$$d\left(\frac{dn}{dt}\right) = \frac{\eta\ dI}{eV} - v_{gr}g\ dS - v_{gr}dgS_{DC} - \frac{dn}{\tau_{nr}} \tag{2.24}$$

$$d\left(\frac{dS}{dt}\right) = \Gamma v_{gr}g\ dS + \Gamma v_{gr}dgS_{DC} - \frac{dS}{\tau_{ph}}\ . \tag{2.25}$$

This can be brought in a more suitable form by considering the gain dependence on the

carrier and the photon density, so that dg expands to

$$dg = \frac{\partial g}{\partial n} dn - \frac{\partial g}{\partial S} dS \tag{2.26}$$

with the differential gain $\partial g/\partial n$ and the gain derivative with respect to the photon density $\partial g/\partial S$, which is related to the gain compression factor ϵ via

$$\frac{\partial g}{\partial S} = \frac{\epsilon g}{1 + \epsilon S} \tag{2.27}$$

[143]. The difference in sign indicates that higher photon densities reduce the available gain due to gain saturation effects [142]. Combining additionally the threshold condition $g_{mod} = \Gamma g = \alpha_i + \alpha_m$ and the photon lifetime $\tau_{ph} = 1/(v_{gr}(\alpha_i + \alpha_m))$ to $g = 1/(\Gamma v_{gr} \tau_{ph})$ allows to write Eqs. 2.24 and 2.25 as

$$d\left(\frac{dn}{dt}\right) = \frac{\eta\, dI}{eV} - \gamma_{nn} dn - \gamma_{nS} dS \tag{2.28}$$

$$d\left(\frac{dS}{dt}\right) = \gamma_{Sn} dn - \gamma_{SS} dS \tag{2.29}$$

$$\Leftrightarrow \quad \frac{d}{dt}\begin{pmatrix} dn \\ dS \end{pmatrix} = \begin{pmatrix} -\gamma_{nn} & -\gamma_{nS} \\ \gamma_{Sn} & -\gamma_{SS} \end{pmatrix} \begin{pmatrix} dn \\ dS \end{pmatrix} + \frac{\eta}{eV} \begin{pmatrix} dI \\ 0 \end{pmatrix} \tag{2.30}$$

$$\text{with} \quad \gamma_{nn} = \frac{1}{\tau_{nr}} + v_{gr} \frac{\partial g}{\partial n} S_{DC} \;, \qquad \gamma_{Sn} = \Gamma v_{gr} \frac{\partial g}{\partial n} S_{DC} \;, \tag{2.31}$$

$$\gamma_{nS} = \frac{1}{\Gamma \tau_{ph}} - v_{gr} \frac{\partial g}{\partial S} S_{DC} \;, \qquad \text{and} \qquad \gamma_{SS} = \Gamma v_{gr} \frac{\partial g}{\partial S} S_{DC} \tag{2.32}$$

[142]. In the case of sinusoidal small-signal modulation, the time derivatives d/dt become $i\omega$ and Eq. (2.30) rearranges to

$$\frac{\eta}{eV} \begin{pmatrix} dI \\ 0 \end{pmatrix} = \underbrace{\begin{pmatrix} \gamma_{nn} + i\omega & \gamma_{nS} \\ -\gamma_{Sn} & \gamma_{SS} + i\omega \end{pmatrix}}_{=:\hat{M}} \begin{pmatrix} dn \\ dS \end{pmatrix}. \tag{2.33}$$

From that and by using $\omega = 2\pi f$, the frequency-dependent two-parameter modulation transfer function $H(f)$ is obtained, whose squared modulus $|H(f)|^2$ is used to fit experimental small-signal modulation curves. A typical example of a set of curves for increasing DC drive current can be seen in Fig. 2.9.

$$H(\omega) = \frac{\omega_R^2}{det(\hat{M})} = \frac{\omega_R^2}{\omega_R^2 - \omega^2 + i\omega\gamma} \tag{2.34}$$

$$\Rightarrow \ H(f) = \frac{f_R^2}{f_R^2 - f^2 + \frac{if\gamma}{2\pi}} \ . \tag{2.35}$$

f_R and γ are the relaxation oscillation frequency shown in Fig. 2.9 and the damping factor. The second term in Eq. (2.36) is usually neglected.

$$\omega_R^2 = \gamma_{nS}\gamma_{Sn} + \gamma_{nn}\gamma_{SS} = \frac{v_{gr}\frac{\partial g}{\partial n}S_{DC}}{\tau_{ph}} + \frac{\Gamma v_{gr}\frac{\partial g}{\partial S}S_{DC}}{\tau_{nr}} \tag{2.36}$$

$$\Rightarrow \quad f_R^2 \approx \frac{1}{4\pi^2}\frac{v_{gr}\frac{\partial g}{\partial n}S_{DC}}{\tau_{ph}} \tag{2.37}$$

$$= \frac{1}{4\pi^2}\frac{v_{gr}\eta\frac{\partial g}{\partial n}}{eV}(I - I_{th}) \tag{2.38}$$

$$\gamma = \gamma_{NN} + \gamma_{SS} \quad = \quad \frac{1}{\tau_{nr}} + v_{gr}\frac{\partial g}{\partial n}S_{DC} + \Gamma v_{gr}\frac{\partial g}{\partial S}S_{DC} \tag{2.39}$$

$$=: \quad K f_R^2 + \gamma_0 \ . \tag{2.40}$$

In many practical cases, a parasitic pole originating from the laser's electrical design and packaging has to be considered as well. This is done by expanding (2.35) to a three-pole function with parasitic pole f_p as

$$H(f) = \frac{f_R^2}{f_R^2 - f^2 + \frac{if\gamma}{2\pi}} \cdot \frac{1}{1 + \frac{if}{f_p}} \tag{2.41}$$

[147, 148]. For devices with thicker active regions such as QD lasers, $f_p = 1/(2\pi\tau_p)$ can also be used to interpret additional time constants resulting from carrier transport effects [149–151]. The equations above define the figures of merit forming the basis of characterising a laser's small-signal modulation response and will be discussed individually in the following.

The relaxation oscillation frequency f_R

As can be seen from Fig. 2.9 and Eq. (2.38), f_R increases with current. At the same time, the damping factor γ, which flattens the response out, increases in proportion to f_R^2. A high relaxation oscillation frequency, which is desirable for high-speed direct modulation, can be achieved through a short photon lifetime, high differential gain, and a high current injection efficiency. Experimentally, f_R is determined by fitting the measured modulation response with Eq. (2.41).

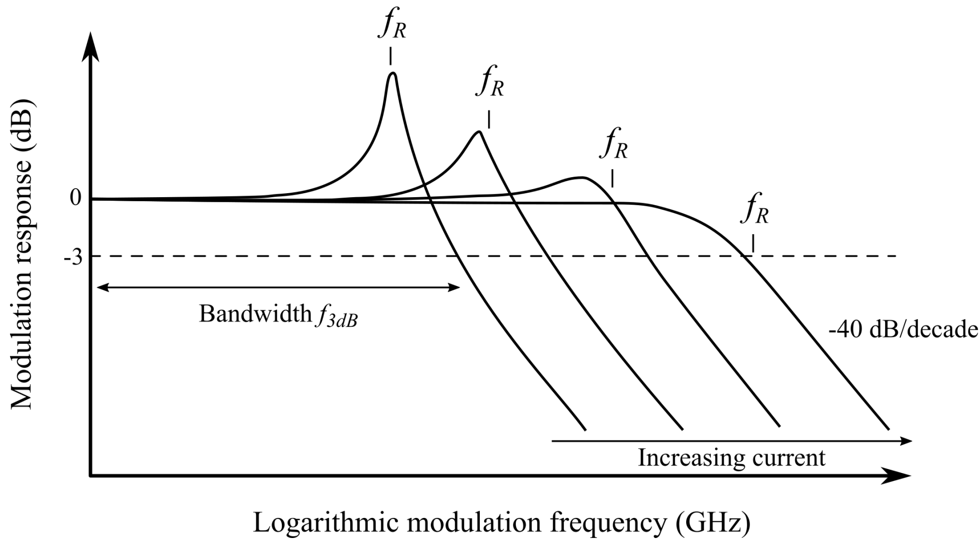

Figure 2.9: Schematic small-signal modulation response for increasing drive currents [142]. The modulation response is flat at low frequencies, where the carriers and photons follow the current modulation linearly, peaks as it approaches the lasers intrinsic relaxation oscillation frequency, and finally drops, as the carriers and photons can no longer respond to the fast current modulation. An increasing level of damping is observed at higher drive current .

The 3dB modulation bandwidth f_{3dB}

The 3dB modulation bandwidth increases with f_R as

$$f_{3dB} \approx \sqrt{1+\sqrt{2}} \cdot f_R \approx 1.55 f_R \qquad \text{– low damping} \tag{2.42}$$

$$f_{3dB}^{max} = \sqrt{2}\,\frac{2\pi}{K} \qquad \text{– damping-limited regime} \tag{2.43}$$

[142]. (2.43) gives the maximum achievable bandwidth in the absence of any thermal limitations or electrical parasitics [152, 153].

The K-factor

Minimising K is of utmost importance for high-bandwidth lasers [154]. K depends on the photon lifetime, the differential gain, and the gain derivative with respect to the photon density (and thus the gain compression factor) as

$$K = 4\pi^2 \tau_{ph} \left(1 + \Gamma \frac{\partial g/\partial S}{\partial g/\partial n}\right) \tag{2.44}$$

A short photon lifetime $\tau_{ph} = 1/(v_{gr}(\alpha_i + \alpha_m))$ through a short cavity, low optical losses, and low facet reflectivities, if possible, is therefore instructive for a high-speed optimised laser design. The implicit dependence on the gain compression factor points, furthermore, out that gain saturation is reflected in a high value of K and thus a strongly damped modulation response. Since excess damping limits the maximum modulation response as it leads to a premature drop of the curve, small values of ϵ are desirable for high-speed modulation. K is experimentally obtained as the slope from the plot of the damping factor γ against f_R^2, as indicated by Eq. (2.40).

The D-factor and modulation current efficiency $MCEF$

The D-factor, or modulation efficiency of f_R, is defined after Eq. (2.38) as

$$f_R = D \cdot \sqrt{I - I_{th}} \tag{2.45}$$

$$\Rightarrow \; D = \frac{1}{2\pi} \sqrt{\frac{v_{gr} \eta \frac{\partial g}{\partial n}}{eV}} \tag{2.46}$$

and indicates the relaxation oscillation frequency increase with current above threshold. D is obtained experimentally from the linear slope of the plot of f_R against the square root of current above threshold $\sqrt{I - I_{th}}$ before the rollover of f_R through increasing damping. Alternatively, the modulation current efficiency $MCEF$ of f_{3dB}

$$f_{3dB} = MCEF \cdot \sqrt{I - I_{th}} \tag{2.47}$$

can be used, as f_{3dB} can be directly read from the modulation response curve and does not require further analysis through fitting [153, 155].

The damping offset γ_0

The y-axis intercept in the linear fit of γ versus f_R^2 is called the damping offset $\gamma_0 = \tau_{nr}^{-1}$ and is a measure of the carrier lifetime. Technically (although often neglected), the derivation outlined above gives here the *differential* carrier lifetime, which is a factor of 2 – 3 shorter than the actual carrier lifetime [142], but in many cases this inverse carrier lifetime is not a quantity of major importance. However, in the case of directly modulated QD lasers of silicon, γ_0 may be an indication of the level of dislocation-induced carrier loss [156], as further discussed in chapter 7.

2.4 Chapter Summary

This chapter has given an introduction into the fundamentals of semiconductor laser physics and devices. It has started by explaining common features regarding the double-heterostructure and the laser design in order to achieve confinement of the injected carriers and the optical mode in the active region. Subsequently, possible active region types were discussed. Typical properties of bulk, QW, and QD lasers were outlined, while a special focus was put on the up- and downsides of QD active regions. Lastly, a one-level rate equation approach for the description of the carrier and photon density in a simplified semiconductor laser was presented. Analytical solutions for the laser threshold and the steady state condition as well as for modulation under small-signal conditions were derived along with common figures of merits used to analyse dynamic laser properties in a practical context. The definitions derived in section 2.3.2 will be of importance for chapter 6 and, more specifically, chapter 7.

Chapter 3

Growth of III-V Lasers on Silicon

3.1 The Laser Integration Challenge

The underlying motivation for integrating III-V lasers with silicon photonic circuits originates from the nature of silicon's energy band structure. Fig. 3.1 shows the energy-momentum diagrams of silicon and GaAs, which indicate the allowed electron and hole

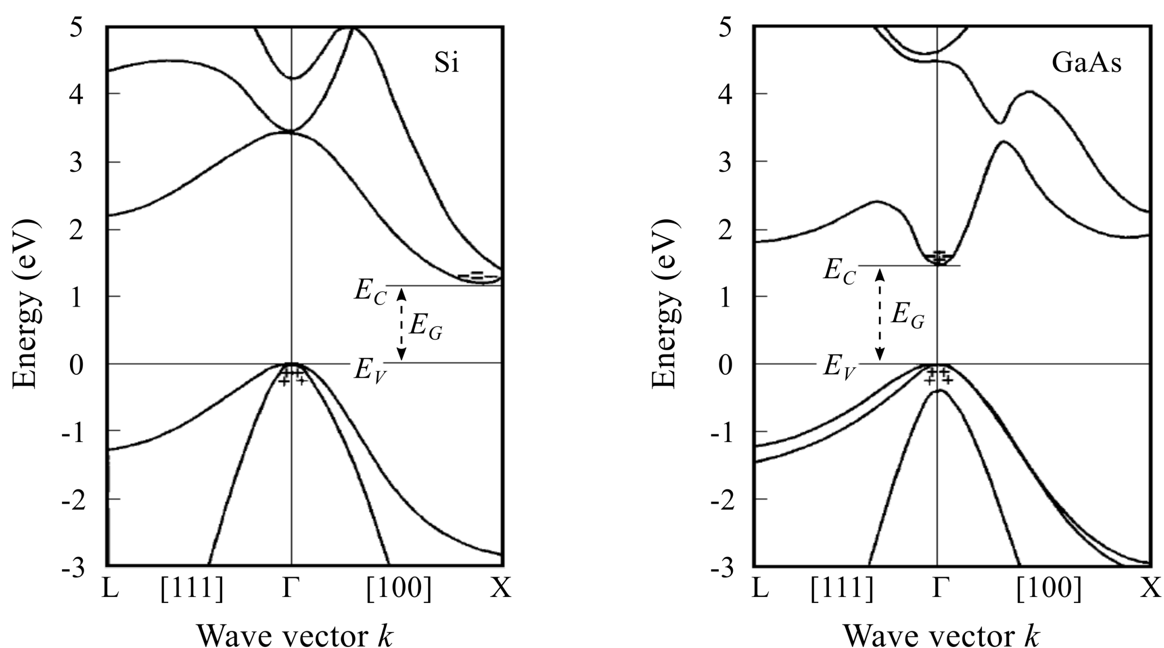

Figure 3.1: *k*-space energy band diagrams of silicon (left) and GaAs (right). An optical transition between the misaligned energy band minima of an indirect semiconductor requires a carrier change in momentum by means of phonon emission or absorption $E_{Photon} = E_G \pm E_{Phonon}$, for example. In direct semiconductors, the momentum or energy conservation rule $E_{Photon} = E_G$ is naturally satisfied. After [104].

energies as a function of their wavevector k. Silicon is an indirect semiconductor, which means that the conduction band minimum and valence band maximum, where minority carriers accumulate under forward bias, do not coincide with each other in k space. Since any kind of electron-photon interaction requires momentum conservation, a stimulated radiative transition between these bands requires a three-particle-process involving not only an electron-hole pair and an incoming photon with its energy approximately equal to the bandgap energy, but also an extra phonon to conserve momentum. This reduces the likelihood of optical transitions in silicon and other indirect semiconductors significantly, making them generally unsuited as light sources because of their poor photon emission efficiency [104, 157].

One of the fundamental challenges of epitaxial III-V laser material growth on silicon is the large crystalline lattice mismatch, as illustrated in Fig. 3.2. Both GaAs and InP exhibit a large lattice constant mismatch of about 4 % and even 8 % compared with silicon, which leads to a very high density of crystal defects and threading dislocations propagating up into the active region, which limits the device performance and lifetime [15, 158, 159]. For comparison, the lattice mismatch between GaAs and AlAs is only 0.0073 Å or 0.13 %, respectively [160]. Among the relevant semiconductor families, the only exception to the lattice constant issue is GaP, which is regrettably not suitable for silicon photonics or other standard communication applications due to its short emission wavelength and thus high absorption in silicon [158, 161, 162] Typical semiconductor laser materials such as GaAs and InP exhibit all direct energy band structures enabling very efficient band-to-band transitions and thus high optical gain [80]. Although it is possible to engineer indirect semiconductors such as silicon to yield stimulated emission with, relatively speaking, higher efficiencies (silicon-based Raman lasers [163–165], nanostructures [166], or strain-engineered Ge or GeSn alloy QWs [7, 167, 168], for instance), the overall light emission efficiencies remain very poor [169]. It is, consequently, deemed the most promising approach to combine ”the best of both worlds” by growing high optical gain III-V materials directly on CMOS-compatible silicon.

Additional challenges to be overcome are the large difference in thermal expansion coefficients and the polar-on-nonpolar compound growth. With semiconductor QD laser

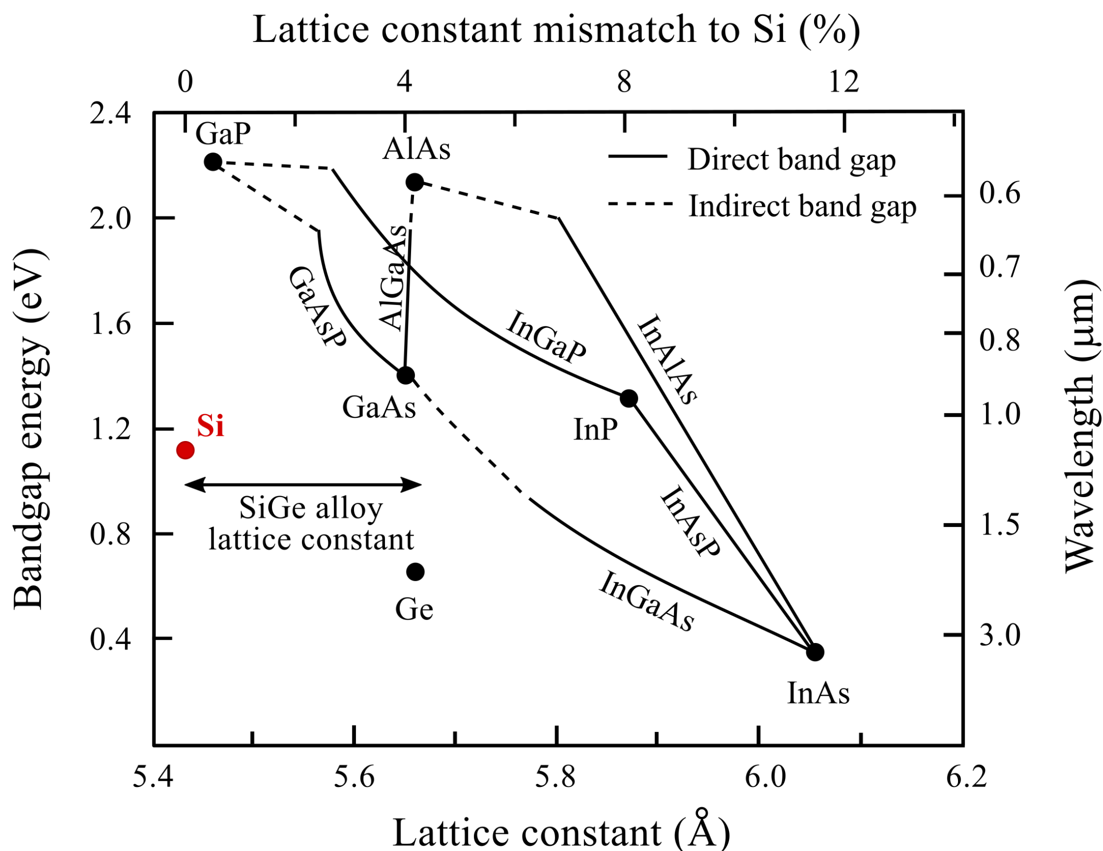

Figure 3.2: Overview of typical III-V semiconductor compounds for lasers in the 0.6 μm to 3.0 μm wavelength range in a bandgap energy/wavelength versus lattice constant graph. The top axis shows the percentage lattice mismatch with respect to silicon. After [80] and [170].

structures being grown at temperatures of 500 °C to 600 °C [13, 23, 171], this is especially an issue during the cooling stage to ambient temperature following the growth process. Since InP and GaAs have a larger coefficient of thermal expansion than silicon, the III-V epilayers contract more than the silicon substrate, inducing wafer bowing, microcracking (Fig. 3.3(a)), and hence generally reduced yield [12, 158, 172]. The large remaining tensile stress has also been observed to contribute to the further formation of dislocations during cool-down [173]. Antiphase domains (APDs) or boundaries (APBs), respectively, resulting from the growth of polar zincblende III-Vs on nonpolar group IV elements such as Ge or Si can, furthermore, lead to a poor surface morphology and reduced carrier lifetime [158]. These boundaries emerge if the occupation of the Ga and As sublattices, for instance, does not remain the same through out the whole crystal [174, 175], as indicated in Fig. 3.3(b).

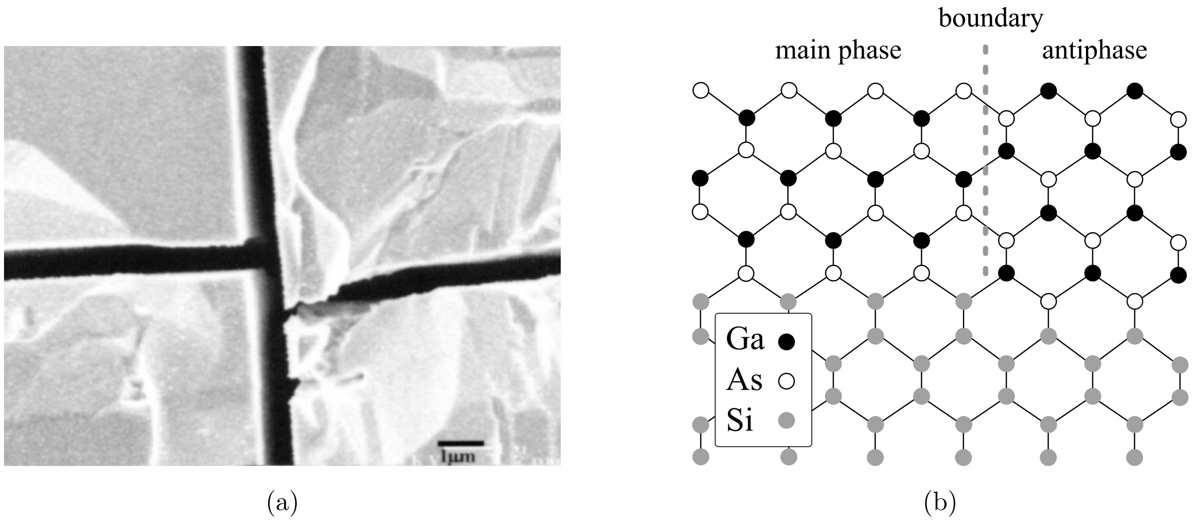

(a) (b)

Figure 3.3: (a) Optical microscope image of a thin, cracked GaAs film grown on a silicon substrate. The cracks occur during the cool-down to ambient temperature after the growth is complete [172]. (b) Schematic of antiphase domain (APD) formation during polar III-V growth on nonpolar group IV elements.

Whereas various techniques have been developed to overcome the challenges of III-V heteroepitaxy on silicon, several alternative approaches have been developed simultaneously. The following sections will first give an introduction into state-of-the-art non-epitaxial ways to co-integrate lasers with silicon, and then discuss epitaxial techniques in more detail in section 3.3.

3.2 Non-Epitaxial Integration Approaches

3.2.1 Direct Mounting

Direct mounting of individual III-V laser dies via pick-and-place technology or flip-chip solder bonding, respectively, is traditionally the preferred industrial approach for laser integration on silicon [35, 47]. This technique benefits primarily from the possibility to pre-test and select suitable lasers enabling optimum performance, while separate packaging of the laser diode ensures good heat dissipation [176]. The drawbacks are, however, that such a configuration yields low light coupling efficiencies and requires sub-micrometre precision alignment, which is difficult to achieve using self-alignment techniques as shown in Fig. 3.4 [177, 178]. Active alignment allows higher precision, but makes the assembly

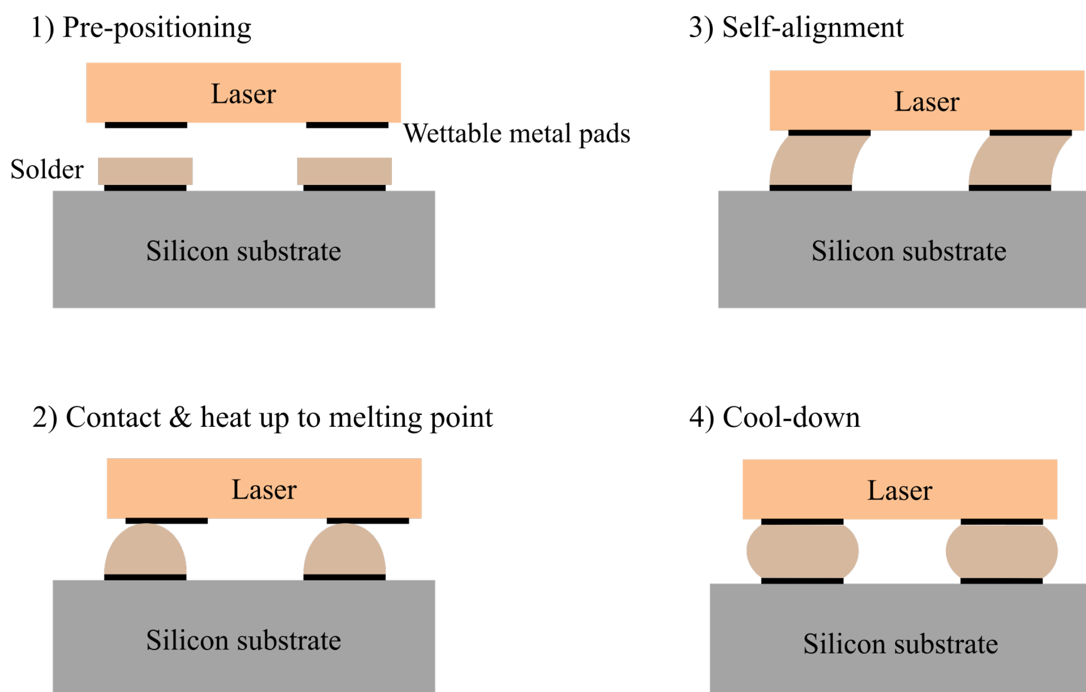

Figure 3.4: Schematic showing a self-alignment-assisted flip-chip bonding process. After the laser is placed in the approximately correct position (1), the laser and the silicon chip are brought in contact and the solder is heated (2). Minimisation of the surface tension on the wettable metal pads defining the solder positions leads to a self-alignment process (3) and a correctly positioned optical device after cool-down (4). After [169] and [177].

process very time consuming and expensive in addition to the high laser packaging cost [169, 179]. The size of the solder bumps limits, furthermore, the possible component integration density, and it is, additionally, often necessary to include optical isolators or other components due to the likelihood of reflections and feedback [176].

3.2.2 Bonding-Based Heterogeneous Integration

Heterogeneous III-V integration by means of die-to-wafer or wafer-to-wafer bonding is currently en route to becoming the as yet most successful approach for commercial integrated photonics mass manufacturing [47, 180]. Bonding approaches can be divided into direct or indirect bonding, depending on if an intermediate layer is required or not. During direct bonding, two perfectly clean and flat wafers or dies with (typically pre-patterned) surfaces smooth to the atom level are brought into contact to form a strong interfacial bond. Alternatively, indirect or adhesive bonding uses a thin polymer layer,

BCB for instance, to bond the wafers together [169, 176, 181]. A simplified version of this process can be seen in Fig. 3.5. The III-V and silicon components are precisely aligned as a result of lithographic alignment, and the light emitted by the heterogeneous laser is coupled vertically into the silicon chip via evanescent coupling with high efficiency (> 90 %) [176, 182].

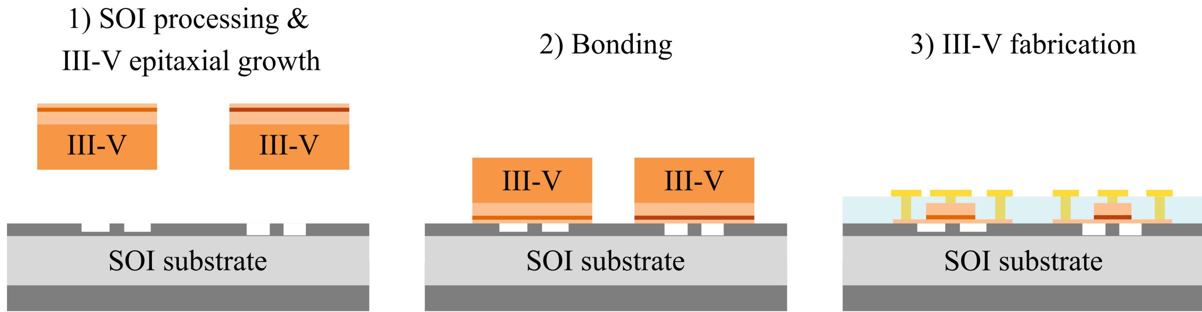

Figure 3.5: Simplified example of a heterogeneous laser integration process flow. Separately grown and diced III-V wafer dies are bonded to a pre-patterned silicon wafer (1 and 2) and subsequently processed together (3). After [183].

A wide range of high-performance heterogeneous (or sometimes called hybrid) devices has been demonstrated, such as modulators [184], mode-locked lasers [185], widely tunable lasers [60], narrow-linewidth lasers [60, 186], DFB lasers [187, 188], and semiconductor optical amplifiers [189]. Besides the benefits from manufacturing at scale as well as the freedom to combine III-V and silicon-based components on a single wafer, the great advantages of heterogeneous rather than epitaxial integration are that it allows to optimise the III-V lasers without any compromises on the choice of materials, the active region type, or the laser epistructure (see section 3.3). This has led to several foundries adopting heterogeneous III-V-on-Si integration in their production lines. Prominent examples are given by Intel [7, 190], Hewlett Packard Enterprise [191, 192], and Juniper Networks [193, 194] [15], while STMicroelectronics, CEA-LETI, and IMEC have also announced their interest to integrate III-V optical materials into their CMOS fabs [12].

Despite extensive years of R&D, the heterogeneous integration approach still brings a number of disadvantages leaving room for further improvements. First of all, the bonding approach itself is rather complex and expensive, as it includes several crucial cleaning and

preparation steps such as the preparation of the silicon wafer (definition and etching of waveguides and planarisation followed by chemical-mechanical polishing and the definition of an outgassing channel [195, 196]), plasma treatment for activation of the wafer surfaces, the low-temperature bonding process, and a final annealing step [8, 197]. This entire process has to be performed under ultra-clean conditions to avoid inclusion of particles. At the same time, the expensive III-V material is not used in the most efficient way, since eventually only the few micrometres of epistructure are of interest for the photonic integrated circuit, while the substrate goes to waste [12]. While this is currently the standard procedure in all commercially available integration approaches, growing the III-V laser directly on inexpensive silicon substrate instead might lead to great cost savings. The ability to bond together two very different semiconductor wafers is also limited by their thermal expansion coefficient mismatch which can give rise to wafer bowing, as with the epitaxial approach [176]. This issue may be circumvented by smaller die rather than full wafer bonding, although this limits high volume fabrication. Additionally, some BCB or other polymer-assisted bonding techniques limit the thermal budget of the subsequent fabrication steps, as they can melt at elevated temperatures. They also contribute optical loss during evanescent light coupling [181, 195]. Finally, despite its substantially increased mass manufacturing capabilities compared with direct mounting, the wafer size mismatch between GaAs/InP (typically 2 inch) and silicon (8 inch to 12 inch) restricts the ability to wafer-bond at scale in order to further reduce the cost per chip [176, 183].

3.2.3 Massive Transfer Printing

Transfer printing may be an alternative to the heterogeneous approach offering a more efficient use of the costly III-V material while maintaining the possibility of large volume fabrication. In this approach, a patterned elastomer polydimethylsiloxane (PDMS) stamp is used to transfer III-V epilayers (coupons) or batches of fabricated devices from their III-V source substrate onto the silicon or silicon-on-insulator (SOI) target substrate [198]. Fig. 3.6 illustrates schematically the main steps of this process. After the growth of the III-V epistructure, III-V coupons (typically on the order of a few hundred by hundred μm^2 [199]) and tethers are defined. A sacrificial etch layer is incorporated into the III-V

stack to create an undercut in preparation for the release process, whose functionality stems from the kinetic-dependent adhesion of the PDMS stamp [200, 201]. Coupons can be picked up by quickly moving up the stamp from the source substrate, whereas they can be printed to the target by releasing the stamp very slowly. After removing the tether resist, the transferred coupon is ready for further processing. Alternatively, it is also possible to transfer batches of fabricated devices directly, although this requires extra care for precise alignment with the silicon-based components [169].

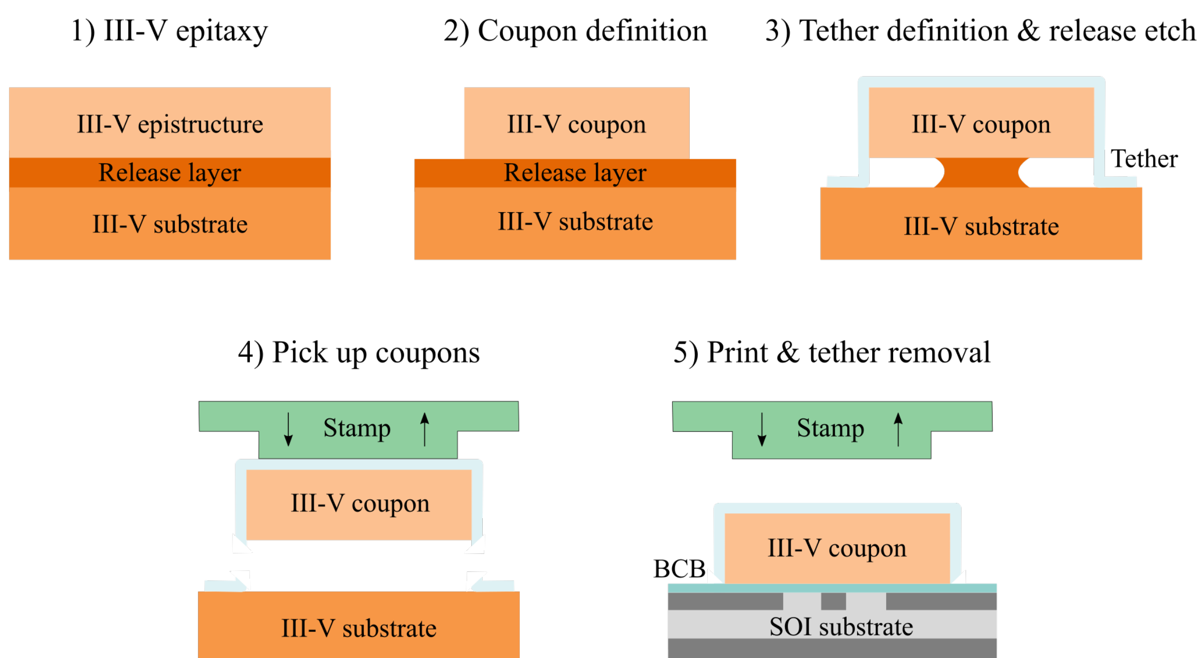

Figure 3.6: Simplified transfer printing process flow after [201].

Being able to transfer print thousands of coupons in parallel, this technique is not only massively scalable, but makes also use of the fact that the area taken by the active components is small compared with the total chip size, so that a single III-V wafer can cater for several large-area silicon substrates [47, 202]. Very high process yields have been demonstrated [198], as transfer printing is more resistant to defects then heterogeneous integration while achieving the same lithographic precision [199]. Lastly, transfer printing leaves in principle also the option to reuse III-V substrates. Although massive transfer printing has great potential to be adopted in CMOS fabs, it should be noted that this

is still a much less mature approach than bonding-assisted heterogeneous integration. In addition, it suffers from similar limitations, as a high-yield process still requires ultra-clean conditions, whereas BCB-assisted printing results also in non-ideal heat dissipation [169].

3.3 Heteroepitaxial III-V Lasers on Silicon

The monolithic integration of III-V optical components on CMOS-compatible silicon wafers by heteroepitaxial growth is still at quite an early stage of academic research, but it remains the ultimately envisioned goal for small-footprint and high-bandwidth-capacity integrated photonic circuits at minimized cost per chip [180]. As mentioned in section 3.1, the main obstacle epitaxial III-V-on-Si growth has to handle is the high density of strain releasing crystalline defects emerging from the lattice-mismatched III-V/Si interface, as can be seen in Fig. 3.7(a). Especially misfit dislocations propagating up into the active region and terminating in the wafer surface (Fig. 3.7(b)), so-called threading dislocations [205, 206], are a major concern for the reliable operation of any kind of semiconductor device [206–208].

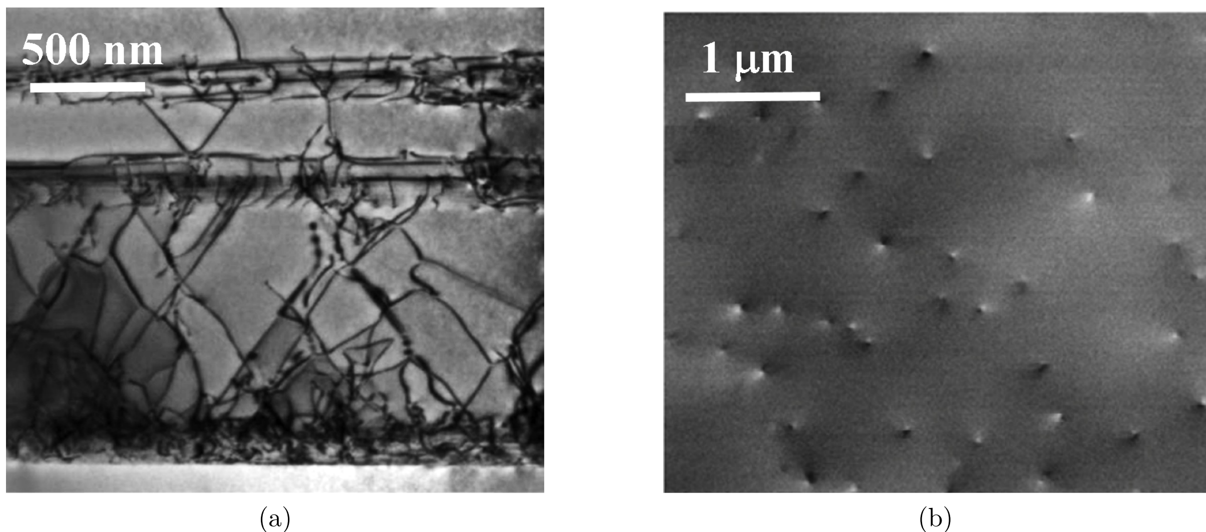

(a) (b)

Figure 3.7: (a) Transmission electron microscope image showing a cross section of GaAs grown on silicon with defect filter layers (see section 3.3.3) [203]. (b) Electron channelling contrast top view image of a germanium buffer layer grown on (001) Si with dislocation density of 3.3×10^8 cm^2 [204].

Dislocations close to the III-V/Si interface can well reach densities of 10^9 cm^{-2} to 10^{10} cm^{-2} [209] , whereas values of the order of 10^4 cm^{-2} to 10^3 cm^{-2} are required in commercially available laser wafers to ensure both high yield and predictable device characteristics [17, 206, 210]. In the literature, it is widely known that dislocations in a laser structure act as nonradiative recombination centres, leading to enhanced carrier loss and thus a reduced minority carrier lifetime [211–213], current leakage [118, 207, 214], and even additional optical losses at high dislocation densities [215, 216]. This degrades not only the laser characteristics, but results also in substantial reliability issues, as recombination-enhanced defect reactions (REDR) under forward bias can create a growing network of dislocations leading ultimately to catastrophic device failure [217–219].

It is, fortunately, possible to significantly reduce the threading dislocation density to about 10^6 cm^{-2} to 10^5 cm^{-2} through carefully optimised growth conditions as well as the inclusion of buffer and filter layers [13, 220]. Very recently, pioneering research reducing the density of dislocations in virtual Ge-on-Si substrate to even 10^4 cm^{-2} by dislocation-selective electrochemical deep etching has been published [221], but this technique has not yet been demonstrated in conjunction with actual optical devices. The following sections will outline well established approaches for the realisation of monolithic III-V and, more specifically, GaAs-based lasers on silicon.

3.3.1 Substrate Surface

The choice of substrate surface is a first starting point to mitigate the effect of the network of misfit dislocations emerging at the strained III-V/Si interface. A common approach for circumventing the formation of APDs is growing the III-V structure on a (001) silicon substrate with a slight miscut towards the [110] or [111] direction [16, 222, 223], for example, as shown in Fig. 3.8(a). The reason for this is that Si atoms at the misoriented crystal surface form preferentially double atomic steps, which reduces the likelihood of APD formation [224, 225]. Over the period from the very first demonstration in 1999 until 2016, all publications on monolithic InAs/GaAs QD lasers on silicon exploited this approach [222, 226–228]. Despite having proven rather useful, III-V laser growth on

intentionally miscut silicon is eventually not the preferred solution, as high-volume CMOS-based manufacturing requires on-axis (001)Si wafers .

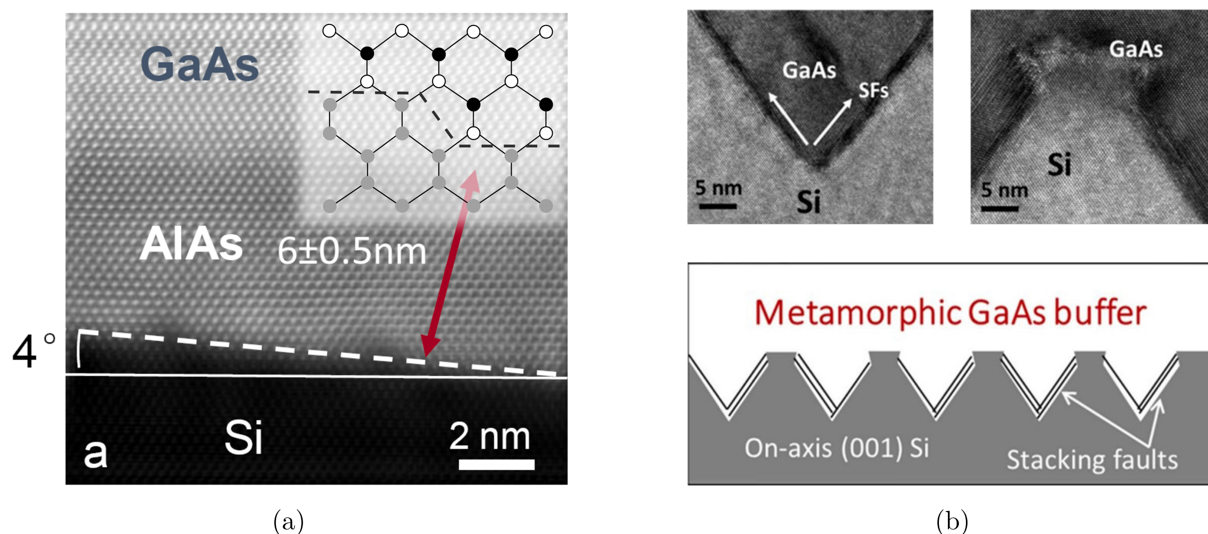

(a) (b)

Figure 3.8: (a) Illustration of an offcut silicon substrate from [220]. The inset illustrates the prevention of APDs through double-atomic steps at the silicon surface. (b) Schematic and cross-sectional transmission electron microscope image showing stacking faults terminating in the V-grooves of a patterned (001)Si substrate [171].

Another possibility to both inhibit APDs and filter dislocations and stacking faults is given by the growth on V-groove pre-patterned silicon substrates, as demonstrated at the University of California, Santa Barbara (UCSB) by Shan *et al.* [171], Wan *et al.* [229], Norman *et al.* [228], and Shi *et al.* [230]. Fig. 3.8(b) shows that the strain releasing layers remain largely confined in the V-grooves with stacking faults being terminated at the (sometimes SiO_2-capped) tip [171], which yields a large-area semiconductor surface of high crystalline quality [231]. This approach is similar to the epitaxial lateral overgrowth (ELO) technique, which is rather common in the GaN community [232], although as yet rarely seen among monolithic In(Ga)As lasers on silicon [233].

3.3.2 Buffer layers

To accommodate the inevitable lattice constant change between the silicon platform and the III-V-based active region, many semiconductor laser growers utilise intermediate buffer

layers bridging the differences in the lattice constant and thermal expansion coefficient [224]. Ge_xSi_{1-x} compound compositional gradings are well-suited for reducing the lattice mismatch to GaAs down to about 0.08 % [234], as illustrated in Fig. 3.2.As a consequence, tensile strain can be relaxed slowly without being released into a high number of dislocations [170, 235, 236]. Germanium (Ge) is, furthermore, compatible with silicon CMOS processes due to its importance as a high-mobility channel in metal-oxide-semiconductor field-effect transistors (MOSFETs) [237, 238]. Even without a compositional GeSi grading, germanium acts still as an effective buffer material that has been incorporated in many of the first monolithic 1.3 μm InAs/GaAs QD lasers on silicon [239–241].

While germanium buffers offer a route to dislocation reduction via a close lattice match with GaAs, an alternative technique is to achieve a close lattice match with the silicon surface using a III-V material first, so that some aspects of the III-V-on-group-IV growth can be solved separately without having to deal with the issue of plastic relaxation [225]. As can be seen in Fig. 3.2, such a pathway is given through the inclusion of a pseudomorphically strained GaP buffer, which has a lattice mismatch of only 0.37 % to silicon and a slightly less pronounced thermal expansion coefficient mismatch (170 % compared with 220 % for GaAs) [224, 242–244]. This approach has produced several high-performance 1.3 μm QD lasers on GaP/(001)Si templates at UCSB [23, 24, 245].

Lastly, it is also possible to simply deposit thick buffers of the target material (i.e. GaAs or InP), as the dislocation density has been found to be inversely proportional to the epitaxial layer thickness (with the exception of $>$ 50 μm GaAs buffers at high dislocation densities $\gtrapprox 10^7$ cm^{-2}) [246, 247]. This allows a reduction in the dislocation density to $< 10^5$ cm^{-2} without the inclusion of intermediate buffer layers or other defect reducing growth techniques. It is not possible to eliminate all crystal defects this way, because threading dislocations can only terminate in a surface or by nucleating with another threading dislocation in a loop [216].

Despite being very effective in reducing the density of dislocations propagating into the active region, all of these approaches and particularly the last one have in common that they result in several micrometre thick buffers to be grown between the silicon platform and the III-V gain blocks. This limits efficient coupling of the optical mode into silicon

waveguides and adds extra absorption, while additionally increasing growth cost and time [25, 204].

3.3.3 Defect filter layers

To bypass the need for thick buffer layers, the epitaxial structure of state-of-the-art QD lasers grown on silicon contains highly strained defect filter layers (DFLs) suppressing the propagation of threading dislocations vertically up into the active region. The concept of these defect filters is based on the fact that strain fields are capable of deflecting threading dislocations, so that compressively strained layers are utilised to bend the dislocations into the growth plane and enhance their lateral motion towards the laser sidewalls [13, 206, 248].

Some of the early monolithic (1.1 µm) QD lasers grown on silicon substrates incorporated defect filter layers based on InAs/GaAs QDs, similar to the ones deployed in the active region [249, 250]. While the three-dimensional islands generate very high strain fields leading to a stronger in-plane force on dislocations than strain-limited films in two-dimensional growth mode [251], the accumulated strain of a multi-stacked QD-based dislocation filter is prone to introducing further defects rather than eliminating them [252]. Strained-layer superlattices have therefore prevailed as the today dominant form of

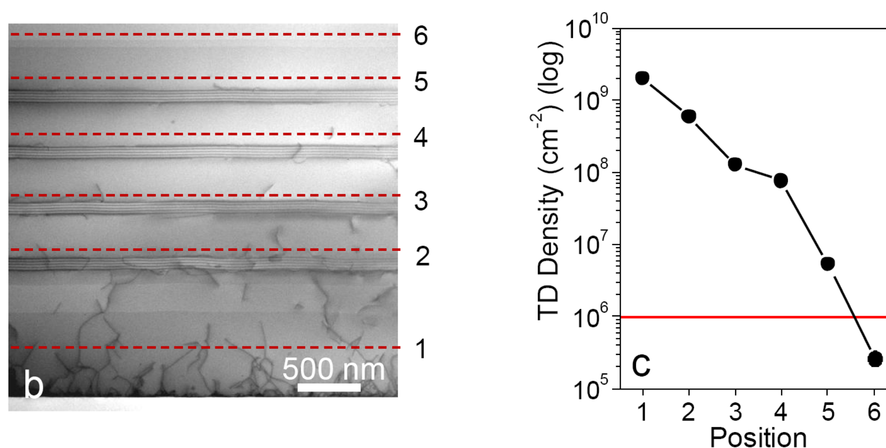

Figure 3.9: Left: Cross-section transmission electron microscope image of InGaAs/GaAs defect filter layers. It can clearly be seen how the dislocations bend over and propagate sidewards. Right: Threading dislocation density measured at the positions marked by the dashed red lines to the left [220].

defect filter layers, with a typical example consisting of five to ten periods of 10 nm InGaAs/10 nm GaAs. The reported InGaAs thicknesses and compositions vary around the values of 10 nm to 20 nm and around an indium content of 0.1 to 0.2 [13, 220, 228, 253]. A very powerful example of defect control through dislocation filters can be seen in Fig. 3.9, where the initial dislocation density of higher than 10^9 cm^{-2} is reduced to about 10^5 cm^{-2} by using five sets of defect filter layers [220].

3.3.4 Thermal Treatments

Two prime examples for highly effective thermal treatments are two-step growth of GaAs buffers and thermal cycling annealing. Two-step GaAs buffer growth is a critical technique for reducing the number of dislocations propagating up into subsequent epitaxial layers. Thereby, the first few tens or hundreds of nanometres are deposited at a low temperature of about 400 °C to 550 °C and a low growth rate (for example about 0.1 μm/h). In case that islanding occurs at the highly strained III-V/Si interface, the low deposition rate leads to the formation of a high density of shallow islands, which eventually coalesce to a smooth surface with most of the dislocations remaining confined in the low-temperature GaAs buffer [224, 248]. Subsequently, the growth rate is raised to a higher temperature (such as 600 °C to 900 °C) to allow an increased dislocation glide velocity, which increases the likelihood of dislocation encounter and annihilation [203, 254].

Thermal cyclic annealing can be performed between the low-temperature and high-temperature buffer growth stages or in conjunction with the deposition of defect filter layers [13]. This growth technique involves the periodic variation of the temperature above and below the original operation point in a range of about 300 °C to 900 °C, for example [254]. This process produces layers of alternating thermal stress, which promotes dislocation glide and hence the probability of dislocation nucleation [216]. Instead of cyclic annealing, a simple high-temperature annealing step can be performed as well, as this by itself leads to the reduction of threading dislocations through a recrystallisation process at high temperatures [255].

3.3.5 Suitable Active Regions

Apart from substantial optimisations in III-V-on-Si growth technology, the recent breakthrough of GaAs-based lasers grown on silicon substrates is largely owed to the utilisation of a suitable active region material. When researchers in the 1980s first started becoming interested in co-integrating optical and electrical components on a common platform, the obvious active region of choice were QWs, since semiconductor lasers with QD active regions were only to be realised about one decade later [117]. To date, however, no reliable, high-performance silicon-based QW laser has been realised.

From the outset, monolithic GaAs-based QW lasers on silicon suffered from high threshold current densities [257–260] and poor lifetimes [235, 260–262], which is suspected to be a result of carrier migration into defects and the associated REDR-based dislocation growth [218, 219]. The integration of QD active regions in lasers on silicon has first been demonstrated at the University of Michigan in 1999 [222], but experienced a revival in the 2010s, having kickstarted the publication of to date more than 100 journal and conference

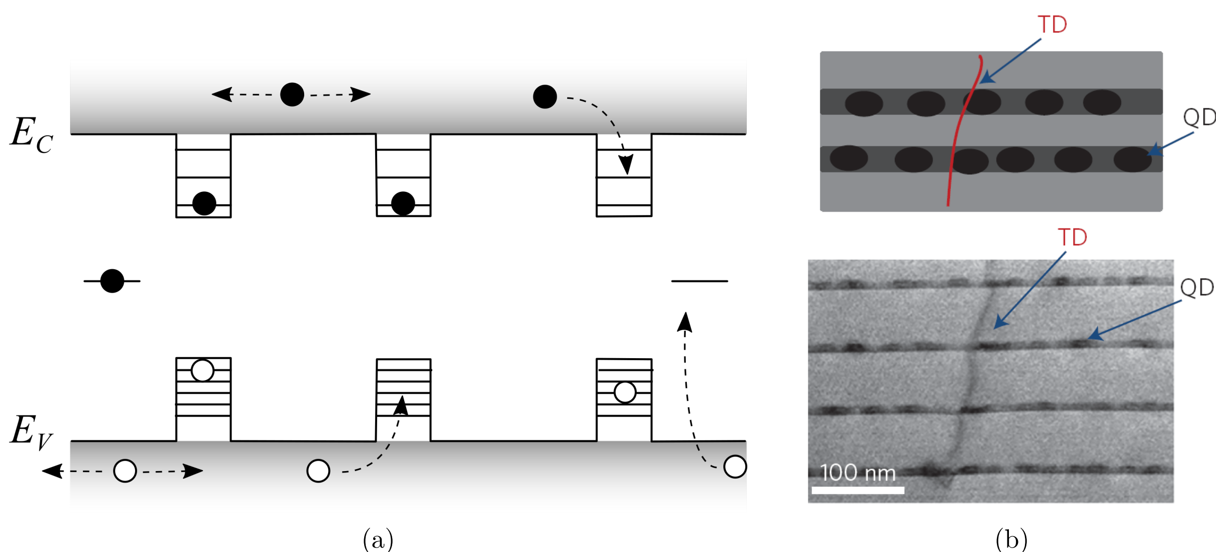

Figure 3.10: (a) Schematic one-dimensional real-space energy band diagram illustrating the functionality of QDs in the presence of dislocations due to effective carrier capture into the dot states reducing the in-plane diffusion length in the continuum states. This concept was patented as early as 1991 [256]. (b) Cross-sectional transmission electron microscope image plus schematic showing how QDs can be spared by dislocations through the high strain field surrounding them [13].

papers on monolithic 1.3 μm InAs/GaAs QD lasers on silicon for photonic integrated circuits. The success of QD active regions, i.e. their obviously higher tolerance to crystal defects, can be traced back to multiple aspects.

There is evidence that lateral carrier migration within the active regions is strongly suppressed in QD active region types, suggesting that efficient, ultrafast carrier capture into the dot states plays a critical role [263, 264], as displayed in Fig. 3.10(a). Compared with QW structures, which have much larger minority carrier diffusion lengths of several micrometres [135], this inhibits the interaction with dislocations substantially, meaning that more carriers are available for the lasing process rather than recombining nonradiatively at dislocation-induced mid-bandgap states [265]. In the QDs, carriers remain spatially confined at discrete energy levels and isolated from dislocations unless they re-thermalise into the continuum states. In addition, the spatial isolation of the dots themselves diminishes the detrimental impact of threading dislocations propagating through the active region, as the majority of QDs remains intact and keeps providing gain even with threading dislocations hitting a few dots. A dislocation density of 10^7 cm^{-2}, for instance, amounts to only 100 threading dislocations in a 2×500 μm^2 narrow ridge-waveguide laser, whereas the number of QDs in a 2×500 μm^2 laser containing five layers is 1,500,000 at a dot density of 3×10 cm^{-2}, for comparison. Hence, even for a generous dot coverage estimate of 10% [121], the number of individual dislocations hitting a QD is negligible. The probability of a dot being hit by a threading dislocation is indeed even smaller considering that the strain field surrounding the QDs will deflect the dislocations, as indicated in Fig. 3.10(b) [266]. Lastly, the DWELL active region leads also to superior device lifetime and reliability as compared with QWs, as it inhibits REDR-induced dislocation-climb and in-plane dislocation glide long the active layers [23, 217, 267]. The exact underlying processes behind the QDs enhanced defect immunity are still subject to research and will be further discussed in chapter 5.

3.4 Static Performance Overview of Monolithic Quantum Dot Lasers on Silicon

The last decade has witnessed considerable progress in the performance of III-V lasers grown on silicon, based on the success of utilising InAs/GaAs QD active regions. The following section will give an overview of the status of monolithic silicon-based 1.3 μm QD lasers with respect to their static performance.

Fig. 3.11 contains an overview of various aspects regarding the *LI* performance of 1.3 μm FP-type InAs/GaAs lasers epitaxially grown on silicon so far published in the literature. The majority of data points has been contributed by Huiyun Liu's group at UCL and John Bowers' group at UCSB, who are to date the main drivers behind the development of monolithic 1.3 μm QD lasers on silicon, although there are also individual publications by Cardiff University and the University of Tokyo. Progress on InP-based 1.5 μm QD lasers has been reported from the University of Hong Kong and from UCSB [268–270].

Fig. 3.11(a) shows a historic view of the development of the absolute threshold current by the silicon substrate and pseudo-substrate type as introduced in sections 3.3.1 and 3.3.2. The distinction between pulsed and cw operation reveals that early devices required pulsed operation to allow lasing under the back then quite high injection currents. From about 2016, III-V QD-on-Si growth technology has improved to producing almost exclusively devices capable of operating under cw conditions. Simultaneously, a reduction of the threshold current towards a level rivalling threshold currents of 1.3 μm InAs/GaAs QDs grown on native substrates has been achieved [271].

The trend shown in Fig. 3.11(a) is, however, in part also a result of the fact that until about 2016 to 2017 predominantly simple broad-area lasers were fabricated, whereas narrow ridge-waveguide lasers with a smaller pump volume, thus smaller absolute threshold values (but slightly higher threshold current densities), and in part also high-reflection coatings dominate the literature from then on. To date, the minimum threshold current of 4.8 mA was demonstrated at UCSB in a 2.5 × 1174 μm^2 99%/60% HR-coated device on GaP/(001)Si substrate with five *p*-modulation doped QD layers [22]. Finally, the

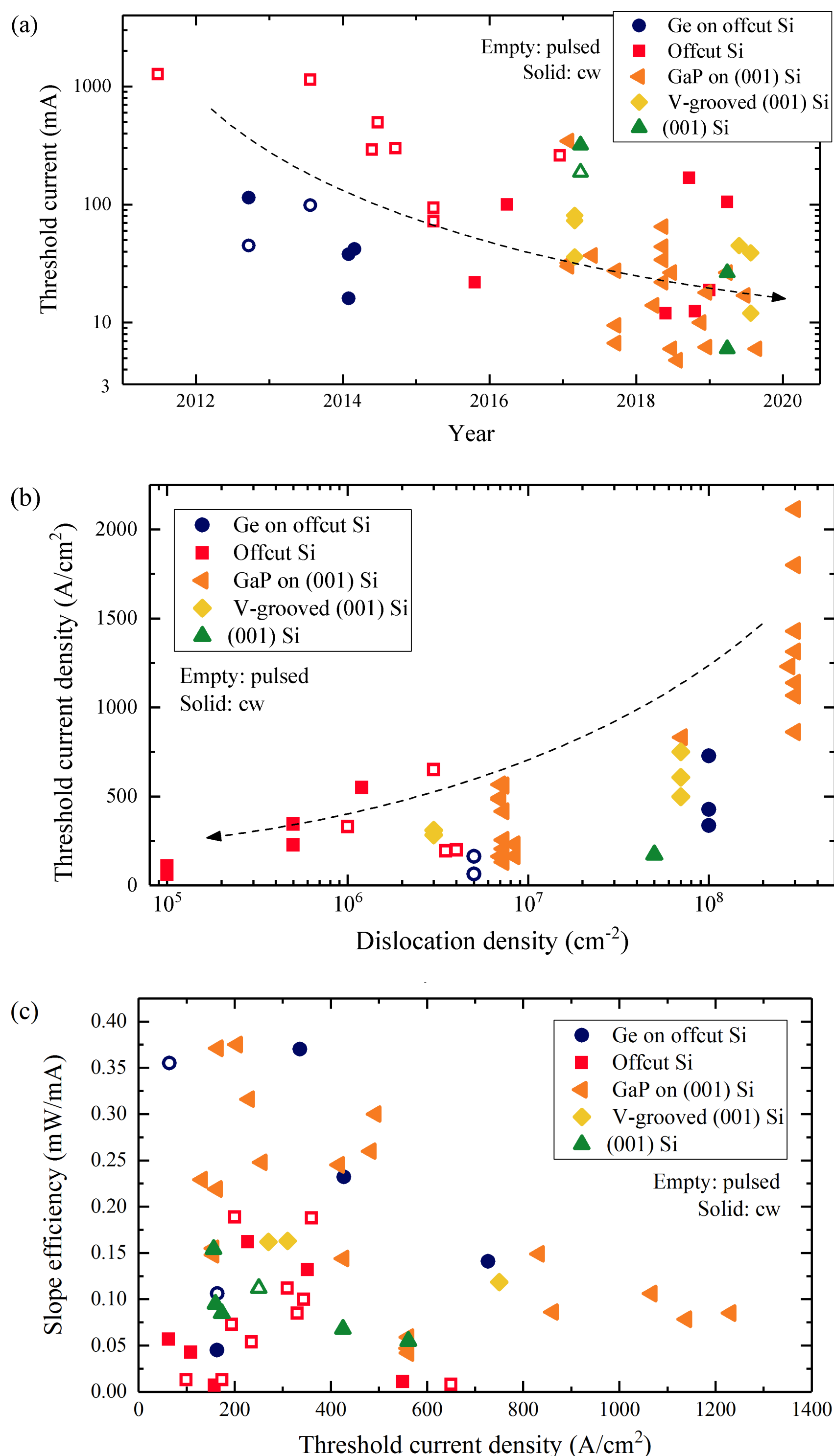

Figure 3.11: *LI* performance overview of 1.3 µm InAs/GaAs FP QD lasers grown on silicon operating at room temperature plotted by substrate type and pulsed/cw operation mode. Arrows indicating trends are included as a guide to the eye. (a) Threshold current against publication year. (b) Threshold current density against dislocation density where stated in the publication. (c) *LI* slope efficiency against the threshold current density. The colour codes are identical in all graphs. Offcut silicon was used at UCL and Cardiff, whereas Ge-on-offcut-Si was both deployed by UCL and UCSB. Data shown for GaP/(001)Si and V-grooved substrates have been produced at UCSB, whereas UCL Tokyo University are engaged in the growth on (001)Si.

development of the substrate type over the years is another interesting feature to note. Whereas early devices exploited offcut silicon (UCL and Cardiff) and Ge-on-Si substrates (UCL and UCSB) to alleviate some of the epitaxial issues at the incompatible III-V/Si interface, the trend of the last years has mainly moved towards direct (UCL and Tokyo University) or GaP buffer- (UCSB) and V-groove-assisted growth (UCSB and Hong Kong University) on CMOS compatible (001) silicon substrates.

Next, it is worth taking a look at the relationship between the threshold current density and dislocation density, as depicted in Fig. 3.11(b). This graph plots the threshold current *density* rather than its absolute current value as above in order to allow a comparison somewhat more normalised with respect to the laser geometry. Thus, it can be seen that there is a correlation between the achievable threshold current density and the dislocation density in the active region. This is consistent with the perception that dislocations act as nonradiative defect centres, which result in higher laser thresholds through increased carrier loss [143]. The highest quality buffer and defect filter layers with a dislocation density reduction to 10^5 cm^{-2} and the lowest threshold density of 62.5 A/cm^2 have been achieved on offcut substrate at UCL [13] (illustrated in red). Significant defect density reductions down to 3×10^6 cm^{-2} on V-grooved substrate [171] (shown in yellow) and 6.7×10^6 cm^{-2} on GaP/(001)Si [272] (shown in orange) have, however, also been achieved at UCSB. It is noteworthy that the highest reported dislocation density of a monolithic 1.3 μm InAs/GaAs QD laser on silicon is 3×10^8 cm^{-2} [226, 273, 274], whereas an even higher value of 5×10^8 cm^{-2} has been reported for QD lasers emitting at 1.225 μm [20]. As with Fig. 3.11(a), the results leading to this trend are again somewhat influenced by the laser geometry and potential facet coatings.

The literature is much less clear with respect to a possible dependence of the *LI* slope efficiency on dislocation density due to the dominant influence of the laser cavity design, facet coatings, and the active region quality. An overview of the slope efficiency plotted against the threshold current density is instead shown in Fig. 3.11(c). Lasers with a high-gain active region, positioned in the top left quarter of the graph, show not only low threshold current densities, but also a higher laser efficiency, hence a steeper slope. This may even be the case at larger dislocation densities, where high gain can

threshold-wise compensate for a reduced minority carrier lifetime. Devices grown at UCSB on GaP/(001)Si and Ge-on-offcut-Si substrates show, despite their higher dislocation densities, very high slope efficiencies (shown in orange and blue). The highest value of 0.375 W/A has been demonstrated with an HR-coated/as-cleaved 3×1090 μm^2 device on GaP/(001)Si, while an uncoated 2.5×1485 μm^2 device showed a slope efficiency of 0.248 W/A [24]. Again, it is important to stress here that different combinations of facet reflectivities have an impact on the performance of individual devices.

There is also a considerable number of devices positioned at the bottom left corner showing very low laser thresholds and low slope efficiencies. This kind of behaviour may occur for longer devices, but also for those with lower gain and a long minority carrier lifetime (i.e. high crystal quality). This would be the case for a laser with lower dislocation density and limited modal gain, for example. It should be noted that the opposite of this scenario – QD lasers on silicon with high threshold current densities and simultaneously high slope efficiency – appears to be less likely and does not exist in Fig. 3.11(c). Since high thresholds tend to be coupled to high dislocation densities, this indicates that a reduced slope efficiency is implicitly coupled to higher dislocation densities. All publications of 1.3 μm QD lasers on silicon with high threshold current densities report also on a lower slope efficiency. In the literature, this trend is confirmed by Orchard *et al.* and Jung and Zhang *et al.*, who have tested comparable laser devices at different dislocation densities, observing rising threshold currents and reduced *LI* slopes [275, 276]. In [275] it is suggested that the slope reduction may be a consequence of increased optical scattering loss at dislocation cores or of a reduced internal quantum efficiency.

3.5 Chapter Summary

This chapter began by highlighting the challenges associated with the integration of III-V lasers on silicon substrates. Since a large mismatch in the lattice constants and the thermal expansion coefficients as well as the different crystal polarities hamper III-V heteroepitaxy on silicon, alternative non-epitaxial integration approaches have been established instead. While direct mounting still tends to be the industrially preferred approach,

many foundries have started adopting bonding-based heterogeneous integration in their fabrication flows. Massive transfer printing is still subject to academic research, but offers possibly increased cost efficiency compared with heterogeneous integration and has the potential to be massively parallelised. While these approaches have all their up- and downsides, none of them really offers the cost advantage of manufacturing at scale yet, which may only be truly achievable through monolithic integration. Subsequently, heteroepitaxial III-V integration on silicon was discussed. In order to inhibit the formation of threading dislocations propagating through the active region, which is known to degrade the laser performance, several epitaxial techniques have been adopted. This chapter has explained how the substrate surface orientation or patterning, buffer layers, defect filter layers, and thermal treatments can be used effectively to block dislocations from propagating upwards into the laser structure. In particular, the importance of incorporating QD rather than QW active regions due to their increased tolerance to defects was discussed. Finally, a literature search reviewing the static performance of 1.3 μm InAs/GaAs QD lasers on silicon was presented. While light-current characteristics rivalling those of QD lasers grown on native substrates have been achieved, keeping the dislocation density low is still of critical importance for low threshold, high efficiency devices.

Chapter 4

Travelling-Wave Rate Equation Quantum Dot Laser Model

Numerical modelling is a valuable tool for gaining insight into the complicated physics of semiconductor devices. Although there are various experimental techniques for the extraction of key laser parameters, numerical simulations are invaluable in allowing the investigation of otherwise inaccessible parameters, or in making design decisions for commercial devices in a cost- and time-effective manner.

Since semiconductor laser modelling can have very different purposes, there are a number of theories available showing various degrees of complexities. A full quantum mechanical treatment, for instance, describes the light-matter interaction at the microscopic level and can explain fundamental coherence properties [277]. A mesoscopic semiclassical laser model, in contrast, is slightly less complex, but still very suitable for describing most physical properties including microscopic material imhomogenities such as dot-to-dot size variations or spatially inhomogeneous light propagation, for example [278, 279]. The complexity and level of physical knowledge required for both of these models, however, renders these approaches unsuitable for most people without a deep background in theoretical and modern physics. Conversely, phenomenological rate equation modelling of the homogeneous carrier and photon density, including the travelling-wave laser model approach with additional spatial resolution, are complexity-wise located at the other end of this spectrum. Compared with the first two approaches, these macroscopic laser mod-

els are the least physical ones, but easiest to implement [277]. The likewise increased computational speed makes them, therefore, an excellent choice for modelling the laser performance in its envisaged operation environment or in a series of varying device designs. Hence the best-suited model for a certain application is not necessarily the most accurate one capturing the full physics, but the one including all relevant aspects while keeping the computational and physical complexity at a reasonable level.

4.1 Model Introduction

The simulations presented in this dissertation are based on a travelling-wave multi-level rate equation model with one-dimensional spatial resolution along the longitudinal direction of the laser. The theoretical framework of this model was originally adopted from work detailed in the dissertations of Thompson [280] and Rae [140]. The laser model was subsequently implemented numerically in MATLAB and extended to meet the needs of modelling monolithic QD lasers on silicon. This chapter focuses mainly on explaining the underlying, standard QD travelling-wave rate equation model, whereas novel work specifically aiming at modelling monolithic QD lasers on silicon will be detailed in chapter 5.

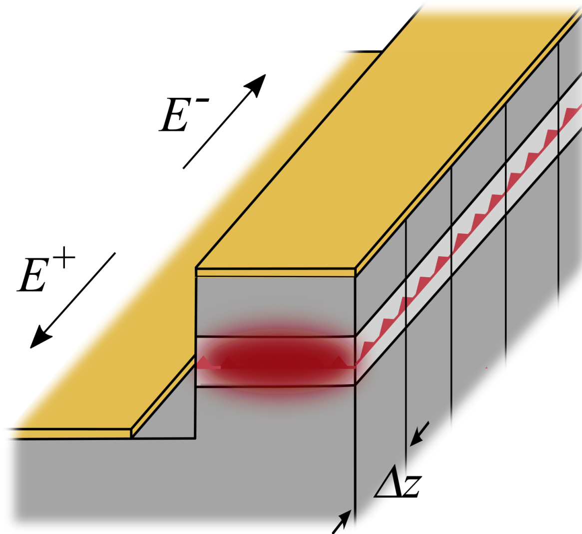

Figure 4.1: Sketch of the laser discretisation along the longitudinal direction. The QDs are not to scale with Δz.

The spatiotemporal evolution of the main simulation variables, such as the gain, the carrier densities, and the photon density, for instance, is described by differential carrier and slowly varying travelling-wave electric field equations, which are explained in more detail in sections 4.2 and 4.3. The travelling-wave method discretises the laser cavity into individual sections $\varDelta z$ along the z axis, as indicated in Fig. 4.1, over which all simulation variables are assumed to be constant. Since $\varDelta z$ is linked to the temporal step $\varDelta t$ via $\varDelta z = v_{gr}\varDelta t$, the maximum possible spatial step size is dictated by the shortest deployed simulation time constants τ, which need to be larger than $\varDelta t$ for the model to converge. Many simulation environments allow comparably low spatial resolutions (~10 μm, for example), which is beneficial for computational speed, as the overall simulation time scales as $\varDelta z^{-2}$ [280]. Compared with a pure rate equation model without spatial resolution, the one-dimensional travelling-wave approach offers increased flexibility in terms of the device types that can be modelled, because individual sections can be assigned either active, waveguiding, grating, or absorber functionalities. It neglects, however, transverse effects, so that it is best suited for modelling narrow ridge-waveguide lasers, where filamentation and the interplay of transverse gain and index guiding are negligible.

All differential equations are solved using the finite difference time domain technique (FDTD). The rate equations are implemented numerically using a first-order forward difference approximation, where the continuous derivative $\partial N/\partial t$ of a variable N is approximated in intervals Δt using

$$\frac{\partial N(t)}{\partial t} = \ ... \quad \longrightarrow \quad \frac{\Delta N(t)}{\Delta t} = \frac{N(t+1) - N(t)}{\Delta t} = \ ... \tag{4.1}$$

[281, 282]. This yields the recursion equation $N(t+1) = N(t) + \Delta t(...)$, where $N(t+1)$ is calculated based on its previous value $N(t)$. The slowly varying complex field envelopes in section 4.3, in contrast are computed based on the central difference method

$$\frac{\Delta N(t)}{\Delta t} = \frac{N(t + 1/2) - N(t - 1/2)}{\Delta t} \tag{4.2}$$

for improved numerical stability [281]. Based on this, the laser model is implemented in MATLAB as illustrated in the flow chart in Fig. 4.2.

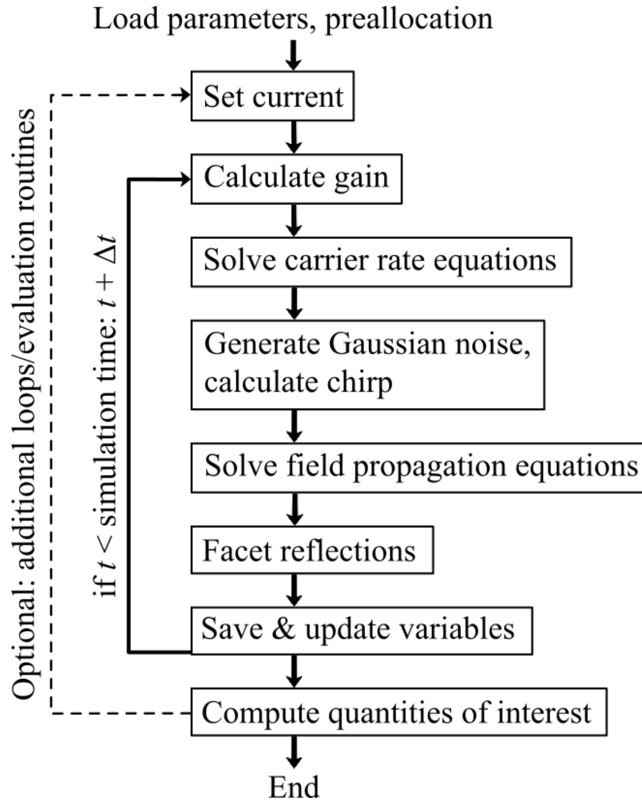

Figure 4.2: Flow diagram outlining the travelling-wave rate equation programme implemented in Matlab.

4.2 Multi-Level Carrier Rate Equation System

The main focus of this work lies on the analysis of monolithic QD lasers on silicon. Yet for comparison, it is very insightful to investigate, for example, the impact of dislocations in QW active regions as well, as will be discussed in chapter 5. Hence, the following sections will give a comprehensive introduction into the multi-level rate equation system used to model QD lasers, followed by a brief overview of the key equations required to simulate QW devices. The rate equation approach presented here is a so-called excitonic model describing the laser diode in terms of electron-hole pairs [143]. Based on the assumption that the internal laser dynamics are limited by the electron population, which shows slower capture and relaxation rates due to the smaller effective mass [283, 284], a separate set of hole rate equations can usually be omitted. This reduces the respective system to the electron equations only and thus increases the computational speed.

4.2.1 Quantum Dot Rate Equation System

The coupled electronic structure of a DWELL QD laser is commonly modelled using a multi-level electron rate equation system, as shown in Fig. 4.3. The simplified electronic system consists of two discrete energy levels for the QD ground state (GS) and excited state (ES) and a wetting layer (WL) representing the QW-like layer in which the QDs are embedded. Strictly speaking, the term wetting layer denotes only the first few atomic monolayers of QW material deposited before the QD material, yet in the QD modelling literature it is quite common to adopt this term for the whole QW-like layer. Additionally, the barrier layers (BLs) from the separate confinement heterostructure (SCH) or multiple excited states can be added to the rate equation system [146, 285]. Section 4.6 will elaborate further on possible model extensions.

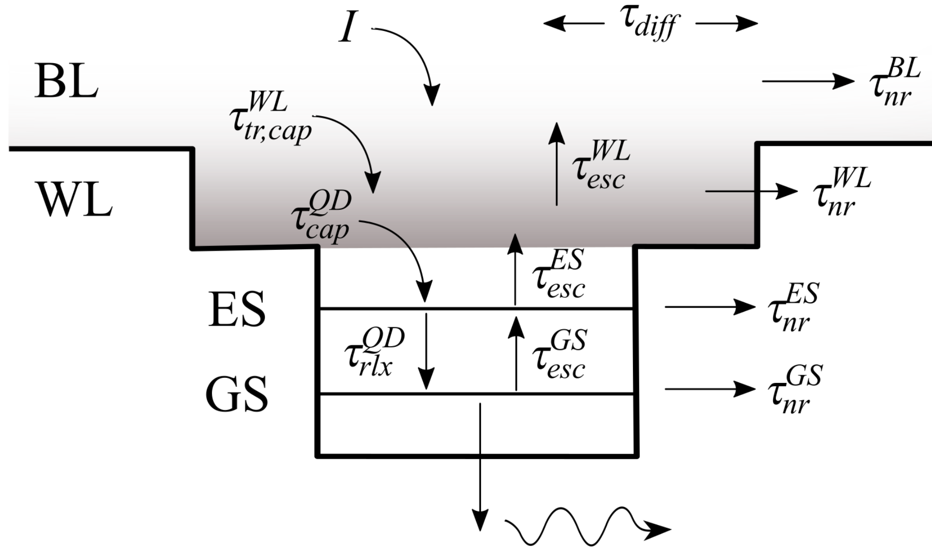

Figure 4.3: Schematic one-dimensional real-space energy band diagram of the electronic system illustrating the dynamics and the energy levels of the QD rate equations. The grey-shaded area represents the continuum of states in the wetting layer and barrier layer.

The various processes illustrated in Fig. 4.3 are described by Eqs. (4.3)-(4.6) [140, 286]. It should be noted that these describe carrier numbers rather than densities, although the respective carrier densities are easily obtained by dividing through the corresponding layer volume per laser section $n_{BL} = N_{BL}/V_{BL} \cdot \Delta z/Ł$ (and analogously for the other levels). An explanation of the simulation variables and parameters can be found in Table 4.1.

$$\frac{\partial N_{BL}}{\partial t} = \frac{\eta I}{e}\frac{\Delta z}{L} - \frac{N_{BL}}{\tau^{WL}_{tr,cap}} + \frac{N_{WL}}{\tau^{WL}_{esc}} - \frac{\Delta N_{BL}}{\tau_{diff}} - \frac{N_{BL}}{\tau^{BL}_{nr}} \tag{4.3}$$

$$\frac{\partial N_{WL}}{\partial t} = \frac{N_{BL}}{\tau^{WL}_{tr,cap}} - \frac{N_{WL} f'_{ES}}{\tau^{QD}_{cap}} - \frac{N_{WL}}{\tau^{WL}_{esc}} + \frac{N_{ES}}{\tau^{ES}_{esc}} - \frac{\Delta N_{WL}}{\tau_{diff}} - \frac{N_{WL}}{\tau^{WL}_{nr}} \tag{4.4}$$

$$\frac{\partial N_{ES}}{\partial t} = \frac{N_{WL} f'_{ES}}{\tau^{QD}_{cap}} - \frac{N_{ES} f'_{GS}}{\tau^{QD}_{rlx}} + \frac{N_{GS} f'_{ES}}{\tau^{GS}_{esc}} - \frac{N_{ES}}{\tau^{ES}_{esc}} - \frac{N_{ES}}{\tau^{ES}_{nr}} \tag{4.5}$$

$$\frac{\partial N_{GS}}{\partial t} = \frac{N_{ES} f'_{GS}}{\tau^{QD}_{rlx}} - \frac{N_{GS} f'_{ES}}{\tau^{GS}_{esc}} - \frac{N_{GS}}{\tau^{GS}_{nr}} - v_{gr} g_{QD} S \frac{\Delta z V_{QD}}{L} \tag{4.6}$$

Carriers are injected into the barrier layer ($\eta I/e \cdot \Delta z/L$), from where they are captured into the wetting layer ($N_{BL}/\tau^{WL}_{tr,cap}$) and relax in a cascaded process via the excited state ($N_{WL} f'_{ES}/\tau^{QD}_{cap}$) into the QD ground state ($N_{ES} f'_{GS}/\tau^{QD}_{rlx}$) [143, 287]. At the same time, nonradiative carrier loss (N/τ_{nr}) takes place in all levels and carriers escape through thermal excitation from the ground state ($N_{GS} f'_{ES}/\tau^{GS}_{esc}$), the excited state ($N_{ES}/\tau^{ES}_{esc}$), and the wetting layer level (N_{WL}/τ^{WL}_{esc}) back into higher energy levels. Lasing ($v_{gr} g_{QD} S \Delta z V_{QD}/L$), where $\Delta z V_{QD}/L$ is a scaling term converting the photon density S into a photon number, is assumed to occur from the ground state only. The photon density S is obtained from the electric field equations, as further explained in section 4.3. Finally, the lateral carrier diffusion term (N/τ_{diff}) in the barrier layers and wetting layer is only relevant for configurations with higher variations in the carrier density, such as mode-locked lasers with an absorber section or those modelled in chapter 5.

The barrier layers and wetting layer are both assumed to be a continuum of states, so that by default no occupation factors f' are included in Eqs. (4.3) and (4.4) [143, 283]. In order to model the QD physics accurately though, it is instructive to consider the two-fold and four-fold degeneracy $p_{GS,ES}$ of the QD ground state and excited state, respectively, and the resulting Pauli blocking by including the electron excited state and ground state occupation probabilities

$$f_{GS,ES} = \frac{N_{GS,ES}}{p_{GS,ES}\,\rho_{QD}\,N_{layers}\,w\,\Delta z} \tag{4.7}$$

Symbol	Description
Common Variables and Parameters for QW and QD Simulations	
N_{BL}, $N_{WL/QW}$, N_{ES}, N_{GS}	BL, WL/QW, ES, and GS carrier number
n_{BL}, $n_{WL/QW}$, n_{ES}, n_{GS}	BL, WL/QW, ES, and GS carrier density
V_{BL}, $V_{WL/QW}$, V_{QDs}	Total BL, WL/QW, and QD volume
S	Photon density
f_{ES}, f_{GS}	QD ES, GS occupation probability
p_{ES}, p_{GS}	QD ES, GS degeneracy
I	Injection current
η	Current injection efficiency
Δz	Spatial step size
L	Cavity length
w	Waveguide width
Γ	Optical confinement factor
ϵ	Gain compression factor
N_{layers}	Number of active layers
$\tau_{tr,cap}^{QW,WL}$	SCH region transport and QW/WL capture time
$\tau_{esc}^{QW,WL}$	QW/WL escape time
τ_{nr}	Nonradiative lifetime (all levels)
τ_{diff}	Diffusion time constant (BL, WL/QW)
v_{gr}	Group velocity
e	Elementary charge
QD-Specific Parameters	
g_{mod}	Modal gain
f_{GS}^{h}	Ground state hole occupation probability
ρ_{QD}	QD density
$p_{GS,ES}$	GS and ES QD degeneracy
τ_{cap}^{QD}	Carrier capture time into QDs
τ_{rlx}^{QD}	Intradot relaxation time
$\tau_{esc}^{GS,ES}$	GS and ES escape time
QW-Specific Parameters	
g_0	Gain constant
n_{tr}	Transparency carrier density

Table 4.1: Simulation variables and parameters used in the QD and QW rate equations (4.3)-(4.6) and (4.8)-(4.9).

[283]. Eq. (4.7) describes the number of carriers in the QD ground or excited state per unit section in relation to the total number of available states per unit section. The terms $f'_{GS,ES} = (1 - f_{GS,ES})$ express, consequently, the probability of finding an unoccupied state in the QD levels, slowing the corresponding transition rates down at high occupation [283]. In the absence of an extra index e or h, the occupation probability or other parameters refer to the corresponding electron parameter by default.

The electronic properties couple with the laser's optical behaviour via the QD gain relationship based on the electron and hole ground state occupation probabilities f^e_{GS} and f^h_{GS}, as introduced in chapter 2.2. Whereas f^e_{GS} is directly calculated from the rate equations, adopting this value for f^h_{GS} should be avoided due to the pronounced desynchronisation of the electron and hole dynamics [288]. This is a result of the large hole effective mass, which has two important effects. First, the discrete QD hole states have a much smaller energy spacing than the electron states, meaning that the hole inversion remains incomplete as the holes thermalise into the excited states. Secondly, hole capture and intradot relaxation is about one order of magnitude faster compared with the electron time scales [143, 283, 284]. For these reasons, a constant value $f^h_{GS} = 0.5$ is chosen in these simulations [140, 283].

4.2.2 Quantum Well Rate Equation System

QW laser diodes can be modelled analogously to QDs as a two-level system consisting of the SCH barrier layers and the QWs. As a consequence, the QW electron rate equations simplify to

$$\frac{\partial N_{BL}}{\partial t} = \frac{\eta I}{e}\frac{\Delta z}{L} - \frac{N_{BL}}{\tau^{QW}_{tr,cap}} + \frac{N_{QW}}{\tau^{QW}_{esc}} - \frac{\Delta N_{BL}}{\tau_{diff}} - \frac{N_{BL}}{\tau^{BL}_{nr}} \tag{4.8}$$

$$\frac{\partial N_{QW}}{\partial t} = \frac{N_{BL}}{\tau^{QW}_{tr,cap}} - \frac{N_{QW}}{\tau^{QW}_{esc}} - \frac{\Delta N_{QW}}{\tau_{diff}} - \frac{N_{QW}}{\tau^{QW}_{nr}} - v_{gr} g_{QW} S \frac{\Delta z V_{QW}}{L} \tag{4.9}$$

[149, 289]. For QWs, the logarithmic gain function introduced in chapter 2.2 is used.

4.3 Travelling-Wave Electric Field Equations

The rate equation travelling-wave model is completed by a pair of time-dependent wave equations derived from Maxwell's equations under the slowly varying amplitude approximation [138, 290].

$$\left(\frac{1}{v_{gr}}\frac{\partial}{\partial t} \pm \frac{\partial}{\partial z}\right) E^{\pm}(z,t) = (\tilde{g}_{mod} - \tilde{\alpha}_i - i\delta)E^{\pm}(z,t) + i^{\pm}_{sp}(z,t) \tag{4.10}$$

describes the slowly varying complex amplitudes of the forward and reverse propagating electric fields $E^{+}(z,t)$ and $E^{-}(z,t)$, whose computation yields the photon density S according to

$$S(z,t) = |E^{+}(z,t)|^2 + |E^{-}(z,t)|^2 \ . \tag{4.11}$$

The electric fields are excited by spontaneous emission noise $i^{\pm}_{sp}$ coupling into the oscillation modes and experience gain $\tilde{g}_{mod} = {}^1\!/\!_2\ g_{mod}$, waveguide loss $\tilde{\alpha}_i = {}^1\!/\!_2\ \alpha_i$,

Symbol	Description
$E^{\pm}$	Forward and backward travelling electric field amplitudes
S	Photon density
$\tilde{g}_{mod}$	1/2 Modal gain g_{mod}
$\tilde{\alpha}_i$	1/2 Optical waveguide loss α_i
δ	Wavelength detuning
$i_{sp\pm}$	Spontaneous noise
β	Spontaneous emission coupling factor
B	Bimolecular recombination coefficient
$\mathcal{G}$	Zero-mean random complex number
$R_{1,2}$	Rear and front facet reflectivity
P_{out}	Front-facet optical output power
$h\nu$	Photon energy at frequency ν
V_{QD}	Total volume of all QDs
h_{QW}	QW thickness

Table 4.2: Simulation variables in the travelling-wave electric field equations.

and phase changes δ [139, 291]. The spontaneous emission noise can be modelled as Gaussian noise

$$i_{sp}^{\pm} = \sqrt{0.5\mathit{\Gamma}\beta B\Delta t}\; n_{GS,QW}\; \mathcal{G} \;, \tag{4.12}$$

where $\mathcal{G}$, β, B and $n_{GS,QW}$ are a zero-mean random complex number, the spontaneous emission coupling factor, the bimolecular recombination coefficient, and the respective QD ground state or QW carrier density [280]. The counter-propagating waves are coupled via facet reflections at the first and the last section of the laser, giving the boundary conditions

$$E^{+}(0,t) = \sqrt{R_1}E^{-}(0,t) \quad \text{and} \quad E^{-}(L,t) = \sqrt{R_2}E^{+}(L,t) \;. \tag{4.13}$$

The calculated photon density is subsequently coupled back into the rate equations, or, if the end of the simulation is reached, converted into optical output power using the relations

$$P_{out}^{QD} = \frac{S(L)\; v_{gr} h\nu\; V_{QD}}{\mathit{\Gamma} L} \cdot (1 - R_2) \quad [140] \tag{4.14}$$

$$P_{out}^{QW} = \frac{S(L)\; v_{gr} h\nu\; N_{layers} h_{QW} w}{\mathit{\Gamma}} \cdot (1 - R_2) \quad [280]. \tag{4.15}$$

These equations describe the case where the output facet is located at facet R_2 ($z = L$). An overview of all simulation variables associated with the travelling-wave electric field equations can be found in Table 4.2. The numerical implementation of the field equations can be easily understood following the central difference-based method, which will be outlined in the following sections.

4.3.1 Numerical Implementation of Propagation in an Amplifying Medium

To begin with, we consider the simplified case of forward propagation in an amplifying medium with gain $\tilde{g}_{mod}$, which is given by the differential equation

$$\frac{1}{v_{gr}}\frac{\partial E^{+}(z,t)}{\partial t} + \frac{\partial E^{+}(z,t)}{\partial z} = \tilde{g}_{mod} E^{+}(z,t) \quad . \tag{4.16}$$

Using the central difference method explained in section 4.1 and the relation $\Delta z = v_{gr}\Delta t$ modifies Eq. (4.16) to

$$\begin{aligned}
&\frac{1}{v_{gr}}\frac{E^+(z,t+\frac{1}{2})-E^+(z,t-\frac{1}{2})}{\Delta t}+\frac{E^+(z+\frac{1}{2},t)-E^+(z-\frac{1}{2},t)}{\Delta z}=\tilde{g}_{mod}E^+(z,t)\\
&\Leftrightarrow\; E^+(z,t+\tfrac{1}{2})-E^+(z,t-\tfrac{1}{2})+E^+(z+\tfrac{1}{2},t)-E^+(z-\tfrac{1}{2},t)=\Delta z\tilde{g}_{mod}E^+(z,t)\;.
\end{aligned} \tag{4.17}$$

This can be further simplified by applying Lax averaging [281], to both sides of Eq. (4.17), yielding Eq. (4.18) for the left-hand side of the equation and Eq. (4.19) for the right-hand side.

$$\begin{aligned}
E^+(z,t+\tfrac{1}{2})&-E^+(z,t-\tfrac{1}{2})+E^+(z+\tfrac{1}{2},t)-E^+(z-\tfrac{1}{2},t) \\
&=\tfrac{1}{2}E^+(z+\tfrac{1}{2},t+\tfrac{1}{2})+\tfrac{1}{2}E^+(z-\tfrac{1}{2},t+\tfrac{1}{2})\\
&+\tfrac{1}{2}E^+(z+\tfrac{1}{2},t-\tfrac{1}{2})+\tfrac{1}{2}E^+(z-\tfrac{1}{2},t-\tfrac{1}{2})\\
&+\tfrac{1}{2}E^+(z+\tfrac{1}{2},t+\tfrac{1}{2})+\tfrac{1}{2}E^+(z+\tfrac{1}{2},t-\tfrac{1}{2})\\
&+\tfrac{1}{2}E^+(z-\tfrac{1}{2},t+\tfrac{1}{2})+\tfrac{1}{2}E^+(z-\tfrac{1}{2},t-\tfrac{1}{2})\\
&=\tfrac{1}{2}E^+(z+\tfrac{1}{2},t+\tfrac{1}{2})-\tfrac{1}{2}E^+(z-\tfrac{1}{2},t-\tfrac{1}{2})
\end{aligned} \tag{4.18}$$

$$\Delta z\tilde{g}_{mod}E^+(z,t)=\Delta z\tilde{g}_{mod}\left(\tfrac{1}{2}E^+(z+\tfrac{1}{2},t+\tfrac{1}{2})+\tfrac{1}{2}E^+(z-\tfrac{1}{2},t-\tfrac{1}{2})\right) \tag{4.19}$$

After shifting Eq. (4.20) by a half space step and rearranging, the result is given as

$$E^+(z+1,t+1)=\frac{1+{}^1\!/_2\;\tilde{g}_{mod}\Delta z}{1-{}^1\!/_2\;\tilde{g}_{mod}\Delta z}\cdot E^+(z,t)\;, \tag{4.20}$$

which is easily numerically implemented [280, 281]. If optical loss and phase detuning are to be included as well, Eq. (4.16) modifies to

$$\frac{1}{v_{gr}}\frac{\partial E^+(z,t)}{\partial t}+\frac{\partial E^+(z,t)}{\partial z}=\left(\tilde{g}_{mod}-\tilde{\alpha}_i-i\delta\right)E^+(z,t)\;. \tag{4.21}$$

While there are different ways to implement this numerically [282, 292], one possible

solution is given by

$$E^{+}(z+1,t+1) = \frac{1 + 1/2\ \tilde{g}_{mod}\Delta z}{1 - 1/2\ \tilde{g}_{mod}\Delta z} \cdot E^{+}(z,t)e^{-\tilde{\alpha}_i \Delta z}e^{-i\delta\Delta z} \quad [280]. \tag{4.22}$$

4.3.2 Numerical Implementation of a Digital Spectral Filter

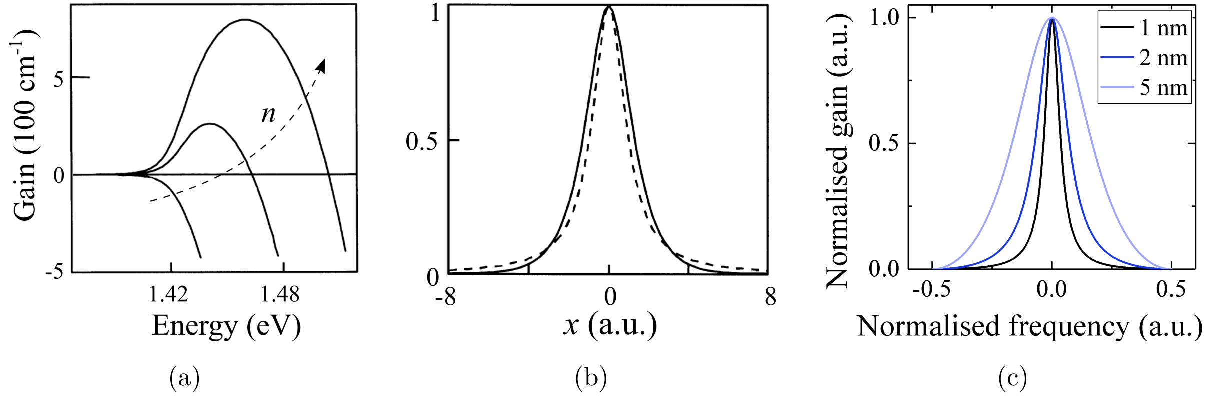

Figure 4.4: (a) Gain spectra of bulk GaAs at different carrier densities n [63]. (b) Examples of functions modelling the spectral shape (dashed: Lorentzian, solid: sec function) [63]. (c) Analytical implementation of the Lorentzian gain filter for different material gain bandwidths.

A digital Lorentzian gain filter with frequency response

$$g(\omega) = \frac{g(\omega_0)}{1 + i\tau\omega} \tag{4.23}$$

as described in [280] and [281] is used to implement the wavelength dependence of the gain as shown in Fig. 4.4(a) and (b). For implementation in the time-domain model, Eq. (4.23) is first Fourier transformed to give

$$\left(1 + \tau\frac{\mathrm{d}}{\mathrm{d}t}\right) y(t) = g(\omega_0)\ x(t)\ , \tag{4.24}$$

where the time constant τ is linked to the material gain bandwidth $\Delta\nu$ via $1/\tau = \Delta\omega = 2\pi\Delta\nu$. Analytical examples of this filter modelled for different material gain bandwidths

can be seen in Fig. 4.4(c). The numerical implementation of Eq. (4.24) is enabled by applying the central difference approximation and Lax averaging, which gives

$$y(t) = \frac{K-1}{K+1}y(t-1) + \frac{g(\omega_0)}{K+1}\,(x(t)+x(t-1)) \quad [280], \tag{4.25}$$

where K is the filter parameter $K = 2\tau/\Delta t = \lambda_0^2/(\pi c \Delta t \Delta\lambda)$ [281]. In order to apply this to the result from the previous section, Eq. (4.20) is rearranged using the substitution

$$E^+(z+1,t+1) = \frac{1+{}^1\!/_2\;\tilde{g}_{mod}\Delta z}{1-{}^1\!/_2\;\tilde{g}_{mod}\Delta z}\;\underbrace{E^+(z,t)e^{-\tilde{\alpha}_i\Delta z}e^{-i\delta\Delta z}}_{=:A(z,t)} \tag{4.26}$$

$$\underbrace{E^+(z+1,t+1) - A(z,t)}_{=:y(t)} = \underbrace{{}^1\!/_2\;\tilde{g}_{mod}\Delta z}_{g(\omega_0)}\underbrace{\left(E^+(z+1,t+1) + A(z,t)\right)}_{x(t)}\;. \tag{4.27}$$

Inserting Eq. (4.27) into Eq. (4.25) yields finally

$$\begin{aligned} E^+(z+1,t+1) =& m_a E^+(z,t)e^{-\tilde{\alpha}_i\Delta z}e^{-i\delta\Delta z} + m_b E^+(z,t-1)e^{-\tilde{\alpha}_i\Delta z}e^{-i\delta\Delta z} \\ &+ m_c E^+(z+1,t) \end{aligned} \tag{4.28}$$

$$m_a = \frac{K+1+{}^1\!/_2\;\tilde{g}_{mod}\Delta z}{K+1-{}^1\!/_2\;\tilde{g}_{mod}\Delta z} \tag{4.29}$$

$$m_b = \frac{-K+1+{}^1\!/_2\;\tilde{g}_{mod}\Delta z}{K+1-{}^1\!/_2\;\tilde{g}_{mod}\Delta z} \tag{4.30}$$

$$m_c = \frac{K-1+{}^1\!/_2\;\tilde{g}_{mod}\Delta z}{K+1-{}^1\!/_2\;\tilde{g}_{mod}\Delta z}\;. \tag{4.31}$$

For the full numerical solution, Gaussian excitation is added to Eq. (4.28). The final result for the counter-propagating electric field amplitudes is, therefore,

$$\begin{aligned} E^+(z+1,t+1) =\;& m_a E^+(z,t)e^{-\tilde{\alpha}_i\Delta z}e^{-i\delta\Delta z} + m_b E^+(z,t-1)e^{-\tilde{\alpha}_i\Delta z}e^{-i\delta\Delta z} + \\ & m_c E^+(z+1,t) \;+\; i_{sp}^+(z,t) \end{aligned} \tag{4.32}$$

$$\begin{aligned} E^-(z_r+1,t+1) =\;& m_a E^-(z_r,t)e^{-\tilde{\alpha}_i\Delta z}e^{-i\delta} + m_b E^-(z_r,t-1)e^{-\tilde{\alpha}_i\Delta z}e^{-i\delta\Delta z} + \\ & m_c E^-(z_r+1,t) \;+\; i_{sp}^-(z_r,t) \end{aligned} \tag{4.33}$$

with z_r being a reverse running spatial variable. Examples of spectra obtained from numerical simulations at different material gain bandwidths can be seen in Fig. 4.5.

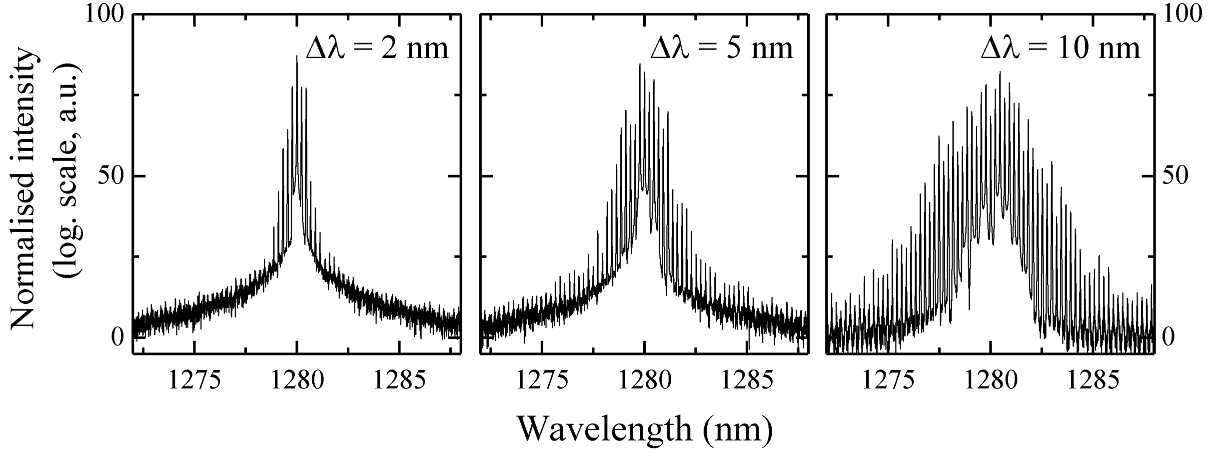

Figure 4.5: Normalised spectral response (absolute square of the Fourier transformed electrical field [280]) obtained from travelling-wave simulations using the digital Lorentzian gain filter and different material gain bandwidths.

4.3.3 Frequency Chirp or Linewidth Enhancement

Variations in the emission wavelength λ or dynamic linewidth broadening during high-bit-rate large-signal modulation and ultrafast pulse generation impose major limitations on the performance of directly modulated semiconductor lasers in long-haul communication systems with dispersive fibres [142, 293, 294]. Physically, this so-called frequency chirping is a result of the Kramers-Kronig relation, which links any changes in the imaginary part of the effective refractive index n_{eff} with changes in its real part [295, 296]. The practical implications of this relation are that gain changes $\partial g/\partial n$ due to carrier density variations are accompanied by a carrier-induced refractive index change $\partial n_{eff}/\partial n$. Note the difference between the refractive index n_{eff} (with index) and the carrier density n (without index). This property of semiconductor lasers is described by the linewidth enhancement factor or Henry's alpha factor

$$\alpha_H = -\frac{4\pi}{\lambda}\frac{\partial n_{eff}/\partial n}{\partial g/\partial n} \tag{4.34}$$

[297], where the minus sign is chosen such that α_H is positive for semiconductor laser wavelengths [296]. Hence in the travelling-wave model, the transient chirp through the carrier-induced refractive index contribution can be modelled in a relatively simple way by calculating the phase as

$$\delta = -\alpha_H \tilde{g}_{mod} \Delta z \tag{4.35}$$

[280]. While the above approach works analogously for QW and QD simulations, it is worthwhile considering a second effect primarily important for QD lasers. Due to the higher number of states available in the QD excited states and the wetting layer continuum, where the carrier densities are not clamped at threshold [286], the free carriers accumulating in these higher energy levels contribute significantly to the refractive index change as well [283, 298]. The refractive index change due to this free carrier plasma effect [299] can be expressed as

$$\Delta n_{plasma} = \frac{e^2}{2\epsilon_0 n_{eff} m_{eff}^e \omega_0^2} \left(\Gamma \Delta n_{ES} + \Gamma_{WL} \Delta n_{WL} \right) \tag{4.36}$$

[283, 286], leading to an additional phase component $\delta_{plasma} = \omega_0 \Delta n_{plasma}/c$. ϵ_0, m_{eff}^e, and ω_0 denote the vacuum permittivity, the effective electron mass, and the centre lasing angular frequency, whereas Γ and Γ_{WL} denote the confinement factors of the active region, i.e. the QDs, and of the wetting layer. Band filling in the barrier layer is here neglected due to the typically low barrier layer occupation.

4.4 Modelling Parameters

The novelty in modelling monolithic QD lasers on silicon lies primarily in evaluating to what extent simulation parameters from InAs/GaAs QDs on native substrates can be adopted and which ones have to be treated with some caution due to the impact of dislocations. This section gives first an overview of common parameters for InAs/GaAs QDs on native substrates and discusses, furthermore, where deviations may exist for devices grown on silicon.

Description & Symbol	Values	References
Current injection efficiency η	0.5 - 0.65	[140, 300, 301]
QW/WL capture time $\tau_{cap}^{QW,WL}$	$1 - 10$ ps	[139, 146, 302, 303]
QD carrier capture time τ_{cap}^{QD}	$0.1 - 10$ ps	[143, 146, 283, 304]
Intradot relaxation time τ_{rlx}^{QD}	$0.1 - 10$ ps	[143, 146, 302, 305]
Nonradiative lifetime τ_{nr}	$1 - 5$ ns	[141, 143, 283, 306]
Modal gain g_{mod}	$10 - 50$ cm^{-1}	[126, 140, 143, 307]
Optical confinement factor Γ	0.0001 - 0.06	[121, 140, 308, 309]
Gain compression factor ϵ	$10^{16} - 10^{15}$ cm^3	[113, 150, 306, 310]
QD density ρ_{dots}	$1 - 6 \times 10^{10}$ cm^{-2}	[154, 306, 311, 312]
GS hole occupation probabilityf_{GS}^h	$0.35 - 0.5$	[140, 283, 313]
Optical loss α_i	$1 - 8$ cm^{-1}	[141, 309, 314, 315]
Linewidth broadening factor α_H	$0 - 2$	[316, 317]
Bimolecular recombination coefficient B	1×10^{-16} m^3/s	[141, 280]
Spontaneous emission coupling factor β	$10^{-6} - 10^{-4}$	[143, 309, 318]

Table 4.3: Typical modelling parameters of InAs/GaAs QD lasers on GaAs.

4.4.1 Parameters for InAs QD Lasers on GaAs

A multitude of experimental and theoretical studies on InAs/GaAs QDs grown on native GaAs substrates exists in the literature. An overview of representative parameters as well as further necessary definitions can be found in and below Table 4.3. With simultaneously growing knowledge on QDs devices and growth technology, a few developments of the recent years should be pointed out though. The performance of a QD laser depends critically on the quality of the active region. Early QD lasers from the late 1990s and early 2000s suffered from low areal QD densities and the difficulties of growing multiple closely stacked QD layers, resulting in a low optical confinement factor and thus low modal gain. Although no magic recipe has been found for solving these underlying challenges, the spectrum of possible parameters has significantly expanded upwards. QD densities of $(5-6) \times 10^{10}$ cm^{-2} are routinely achieved [319], and with the associated increase in Γ,

high modal gains of up to 50 cm^{-1} to 60 cm^{-1} have been demonstrated [126]. It is noteworthy that to date the optical confinement factor is largely a fitting parameter varying over two orders of magnitude in the literature, because the calculation of Γ is associated with many assumption due to the unknown exact QD geometry.

Carrier escape times τ_{esc}

The carrier escape times are calculated based on the QD level degeneracies and energetic barriers as

$$\tau_{esc}^{GS} = \tau_{rlx}^{QD} \frac{p_{GS}}{p_{ES}} \exp\left(\frac{E_{ES} - E_{GS}}{k_B T}\right) \tag{4.37}$$

$$\tau_{esc}^{ES} = \tau_{cap}^{QD} \frac{p_{ES}\rho_{QD}}{p_{WL}} \exp\left(\frac{E_{WL} - E_{ES}}{k_B T}\right) , \tag{4.38}$$

where $E_{GS,ES,WL}$, k_B, T, and p_{WL} are the respective energy levels, Boltzmann's constant, the temperature in Kelvin, and the effective wetting layer density of states per unit area [320]. p_{WL} is given as

$$p_{WL} = \frac{m_{eff}^{e} k_B T}{\pi \hbar^2} , \tag{4.39}$$

with $\hbar$ being Planck's constant [309]. The WL/QW escape time depends on the QW/WL height $h_{QW/WL}$ and the energy barrier $(E_{BL} - E_{WL/QW})$ as

$$\tau_{esc}^{WL/QW} = h_{QW/WL} \sqrt{\frac{2\pi m_{eff}}{k_B T}} \exp\left(\frac{E_{BL} - E_{WL/QW}}{k_B T}\right) \quad [149, 321]. \tag{4.40}$$

Carrier transport time through the active region τ_{tr}

In the excitonic model, the transport time through the active region is calculated as

$$\tau_{tr} = \frac{1}{2}\left(\frac{h_{BL}^2}{2D_e} + \frac{h_{BL}^2}{2D_h}\right) = \frac{\tau_{tr}^{e}}{2} + \frac{\tau_{tr}^{h}}{2} . \tag{4.41}$$

h_{BL} is the thickness of the barrier layers or SCH width, respectively, while D_e and D_h are the electron and hole diffusion constants. The transport time component is added to the

QW/WL capture time $\tau_{cap}^{WL/QW}$ to give

$$\tau_{tr,cap}^{WL/QW} = \tau_{tr}^{WL/QW} + \tau_{cap}^{WL/QW} \ , \tag{4.42}$$

which is used in the rate equations [308].

Calculation of the (active) volume

The total barrier layer, wetting layer, and QW volume $V_{BL,QW,WL}$ are obtained in a straightforward way by multiplying the overall layer thickness with the active area wL. The QD volume V_{QD} is calculated by multiplying the number of dots per layer with the number of active layers N_{layers} and the volume V_{dot} of an individual QD. QDs are assumed to have a pyramidical shape, so that a single QD's volume is accordingly given as

$$V_{dot} = 1/3 \ h_{dot} w_{dot}^2 \tag{4.43}$$

[322]. However using typical QD dimensions such as $h_{dot} = 7$ nm and a dot diameter of 20 nm [13], this tends to lead to early power saturation and smaller active volumes compared with QD volumes stated in other modelling papers [286, 323]. The QD base length w_{dot} as well as the form factor 1/3 can, therefore, be varied, if necessary.

4.4.2 Parameter Considerations for QD Lasers on Silicon

Many laser parameters can remain unchanged in the simulation of monolithic 1.3 µm InAs/GaAs QD lasers on silicon substrates, but special attention will be given to the following ones.

1. Carrier lifetime τ_{nr}

Threading dislocations are known to act as nonradiative recombination centres. In III-V lasers monolithically grown on silicon, it is, therefore, expected that enhanced nonradiative recombination may reduce the minority carrier lifetime into the sub-nanosecond regime [273]. This may affect specifically the continuum barrier layer and wetting layer lifetimes, as carriers in these layers can easily migrate into into nearby defect states.

Carriers confined in the QD states, in contrast, are believed to be less affected by this loss mechanism due to their higher confinement energy preventing them to diffuse into these states.

2. Internal optical loss α_i

Increased optical loss as a result of photon scattering at dislocation cores has been discussed as a second major contributor to degraded laser performance [324]. However, there is so far little experimental evidence supporting this hypothesis quantitatively. Wang *et al.* have calculated waveguide loss of the order of 2.4 cm^{-1} to 5.5 cm^{-1} for the epilayers of III-V QD lasers on silicon [325], whereas Jung *et al.* have measured low internal losses of about 2.5 cm^{-1} [23], which is consistent with values found in the modelling work of this dissertation (see chapters 6 and 7). Shutts *et al.* report an increase of the optical loss from 2.77 cm^{-1} to 3.55 cm^{-1} during laser degradation [326]. Although such a development might be problematic for QD devices with limited modal gain, these values, even if containing a residual dislocation-induced loss component, are still quite small and compare well with the values of devices grown on native substrates shown in Table 4.3. Realizing very low optical losses < 1 cm^{-1} will be interesting for high-power applications though [327, 328].

3. Reduced injection efficiency η

Electrically active threading dislocations may offer alternative recombinations pathways reducing the carrier injection efficiency. While QD lasers on silicon with high slopes, i.e. high injection efficiencies (Eq. (2.20), $\eta_d = \eta\ \alpha_m/(\alpha_i + \alpha_m)$), have been demonstrated as discussed in chapter 3.4, lower slope efficiencies can be linked to higher dislocation densities. The question whether this is a result of a reduced injection efficiency can not be answered clearly in this case, as high carrier losses in the continuum states reduce carrier capture into QDs, which is analytically expressed in a low η rather than a short lifetime.

4. Reduced QD modal gain g_{mod}

Finally, the moderate performance of early monolithic QD lasers on silicon has, furthermore, raised the question whether generally small modal gain may in part be responsible

for the performance limitations. Possible explanations for lower peak gain could be a reduced QD uniformity, where the QD gain spreads over a wider range of energies. This is typically caused by enhanced surface roughness, which is not only an issue for GaAs-on-Si pseudo-substrates [254], but actually also for QD lasers on native ones [118]. Yet specifically for III-V lasers on silicon, the strong tensile strain after post-growth cool-down resulting from the thermal expansion coefficient mismatch can add to the issue of inter-layer QD size variations [329]. Today, monolithic QD lasers on silicon with large modal gain up to 60 cm^{-1} [18, 330] and a very large estimated confinement factor of 0.067 [330] prove that low QD modal gain is no specific problem of QD lasers grown on silicon. For such devices, photoluminescence (PL) spectra with typical full-widths at half-maximum (FWHM) between 28 meV and 30 meV have been reported [13, 24, 331], which is as good as typical PL FWHMs for QDs on GaAs [332].

4.5 Numerical Implementation of Simulation Programmes

4.5.1 Temporal Evolution

Computing the temporal evolution of the laser performance at a drive current I forms the backbone of all other simulations presented in this thesis. While the optical output power is set to be the output variable by default, the programme allows also to monitor other quantities of interest, for example the gain and the different energy levels' carrier densities, by saving the respective variable $X(t)$ in each iteration to a preallocated vector $X(t) = \underbrace{(0,0,0,...)}_{\#\ time\ steps}$. Alternatively, it is also possible to view the longitudinal dependencies of spatially varying variables by saving snapshots $X(z)$ at a time t to an optionally preallocated vector $X(z) = \underbrace{(0,0,0,...)}_{\#\ laser\ sections}$. Examples of the QD simulation variables' temporal evolution can be found in Figs. 4.6(a) and (b), while the spatial variation of the photon density versus the longitudinal position at different currents can be seen in Fig. 4.7.

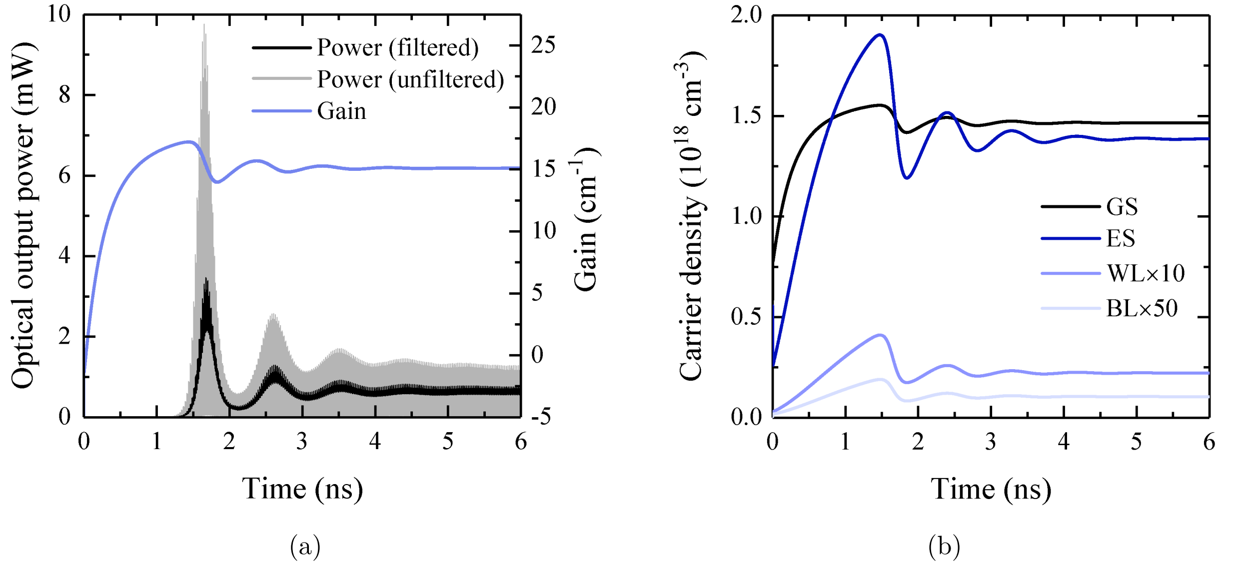

Figure 4.6: Modelled temporal evolution of (a) the optical output power, the gain, and (b) the carrier density in the QD ground state, excited state, wetting layer, and barrier layer at an input current of 10 mA. The unfiltered (i.e. as calculated) optical output in Fig. 4.6(a) shows pronounced beating of the longitudinal modes and is, consequently, low-pass-filtered with a bandwidth of 20 GHz to mimic realistic experimental output at the instruments.

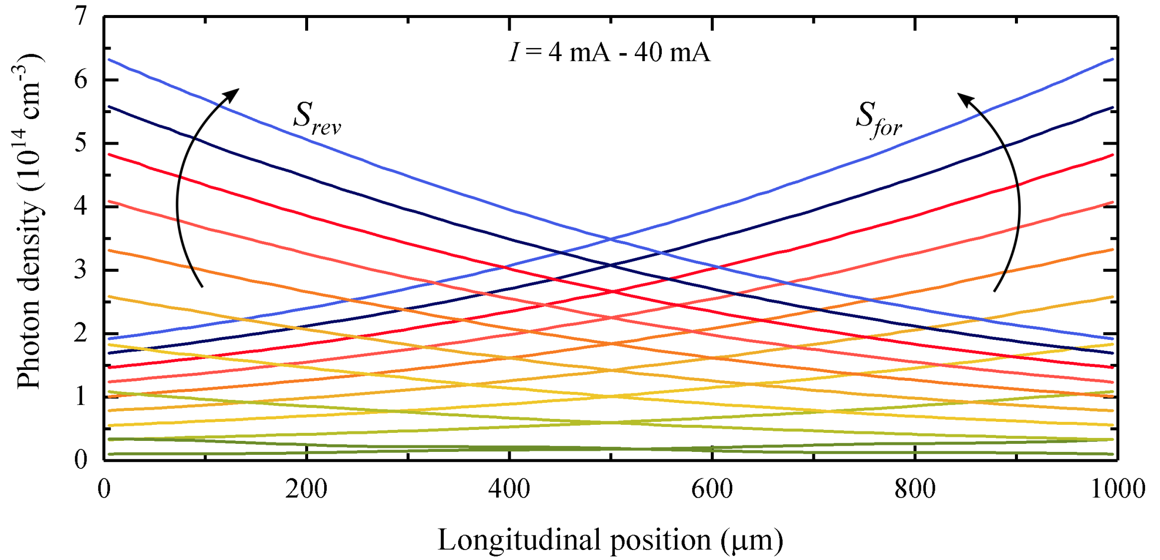

Figure 4.7: Forward and reverse propagating photon densities against the longitudinal laser position at different injection currents. The arrows indicate the rising photon density from 4 mA to 40 mA. The shown dependencies are the average of ten snapshots recorded over the duration of 1 ns after 9 ns warm-up time.

4.5.2 Light-Current Simulations

In order to obtain the typical light-current laser characteristics, the travelling-wave rate equations computing the temporal evolution of the simulation variables are implemented in a loop and are run i times in accordance with the number i of current steps. If input currents of increasing amplitudes are to be used, it is convenient to store the spatial dependencies of the simulation variables at the last current step in order to re-use these as start values in the next iteration. This process is illustrated in Fig. 4.8, where the optical output power at each new current is given by its value at the end of the previous iteration. The settled time-dependent output is then averaged over a pre-defined range of time steps (in this case 2.5 ns, indicated by the grey shaded area) to yield the steady-state data point $L(I)$, as shown in Fig. 4.9(a). This procedure can be performed with all variables of interest, for instance the carrier densities or occupation probabilities and the optical gain (Figs. 4.9(b) and (c)). The respective output values can be saved to a preallocated vector $X(I) = \underbrace{(0, 0, 0, ...)}_{\#\ current\ steps}$ (convenient for subsequent operations) or they can be saved to disk, which is usually the preferred option for more comprehensive programmes performing numerous iterations under different simulation environments.

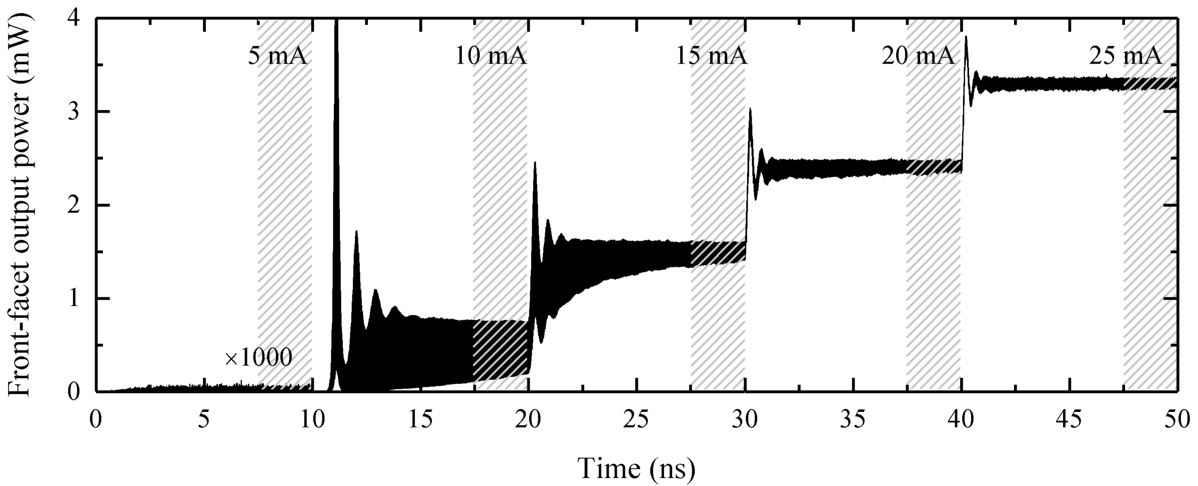

Figure 4.8: Illustration of the numerical implementation of light-current simulations. In this example, the physical simulation time per iteration is 10 ns with a 2.5 ns output average range (grey shaded area). Suitable simulation times and average time spans depend on the exact operation conditions.

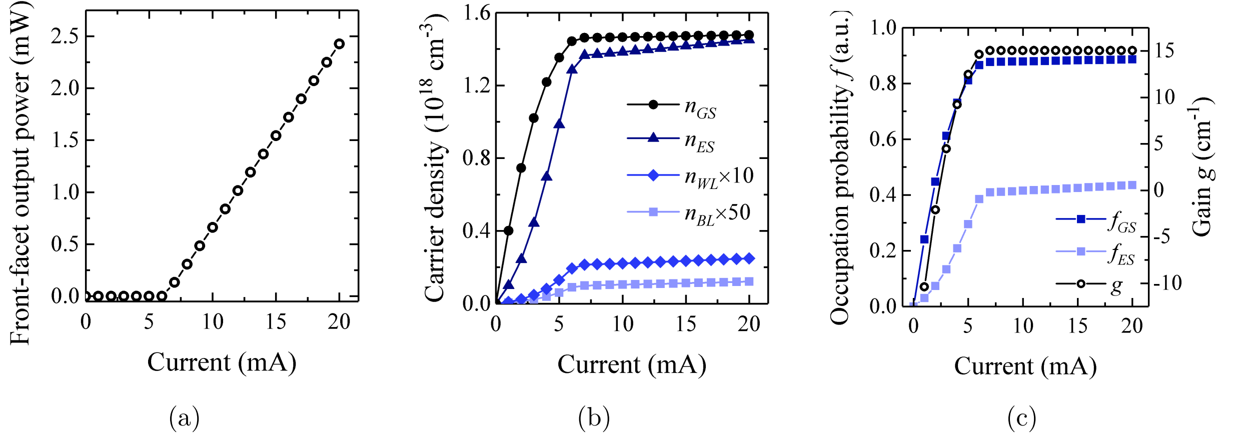

Figure 4.9: Results of light-current simulations as explained above. While (a) shows the classic LI laser characteristic, (b) and (c) allow also to view the evolution of the carrier densities/occupation probabilities and the gain with current. It can be seen that the ground state carrier density or occupation probability and thus also the gain are clamped at threshold, whereas the carrier numbers in the other energy levels can continue to increase. This is more pronounced at simulations up to higher currents (200 mA, for example).

In some cases, parallelisation can be used to speed up the overall runtime. This requires typically a slightly longer physical simulation time per iteration to account for the laser's turn-on delay and relaxation oscillations, because simulation start values based on the next smaller current magnitude are not always available in that case. Otherwise, irregularities caused by the relaxation oscillations can occur.

4.5.3 Small-Signal Simulations

A laser's small-signal modulation response can be simulated numerically by converting the input current I, usually a constant, into time-dependent input by superimposing a sinusoidal modulation of small amplitude (a few percent of the DC current, for example). The frequency response to the modulation frequency f is obtained by taking the Fourier transform of the optical output power at the front facet. The resulting spectrum is complex and needs to be multiplied with its complex conjugate and a factor of 2 to yield the real, power-conserved RF spectrum. The maximum range of frequencies f_{max} is

dictated by the temporal resolution Δt as

$$f_{max} = \frac{1}{2\Delta t} , \tag{4.44}$$

although the more limiting factor here is rather the frequency resolution Δf, which is given by the inverse of the physical simulation time [280, 281]. Since a pronounced DC peak at 0 GHz overshadows the signal to be extracted, the Fourier spectrum calculated under DC operation conditions is subtracted from the respective AC Fourier spectrum. The peak at the position f is then extracted by integrating over the area beneath it and its neighbouring points. This method is computationally more stable than simply extracting the response value at f, because the used fast Fourier transform algorithm requires exactly 2^M data points, with M integer, for a precise representation of the modulation response in the frequency domain [281]. If this condition is not fulfilled by the number of simulation time steps, small oscillations can occur in the high-frequency regime, where the modulation response drops steeply. Repeating this procedure for a range of frequencies allows to calculate the entire modulation response curve as illustrated below.

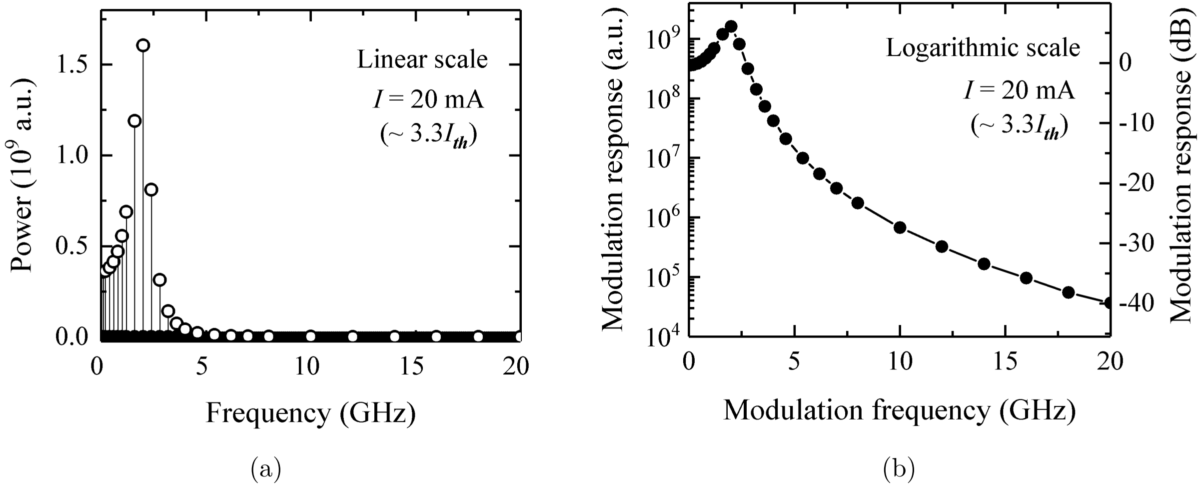

Figure 4.10: Examples illustrating the numerical calculation of a laser's small-signal response curve. (a) Calculated Fourier spectrum, where the empty symbols represent the response values at their respective current modulation frequencies (linear scale). (b) Small-signal response values from (a) versus modulation frequency on a logarithmic scale. The typical shape of a small-signal response curve is observed.

The calculated Fourier spectrum in Fig. 4.10(a) shows that on a linear scale, the modulation response peaks only differentiate themselves from the noise floor up to around 5 GHz at the chosen settings. Plotting the extracted response values on a logarithmic scale though (Fig. 4.10(b)) reveals the typical shape of a laser's small-signal modulation curve. The y axis in this kind of plot is usually given in dB using

$$P_{dB} = 10 \log_{10} \left(\frac{P_{a.u.}}{P_0} \right) , \tag{4.45}$$

where P_0 is here a low-frequency, almost DC reference value. The slower the laser's intrinsic modulation response, the longer the simulation has to run in order to retrieve enough energy in the respective modulation frequency. For a faster laser with modulation bandwidths of around 10 GHz, run times of 10 ns to 20 ns per frequency might be sufficient, whereas a slower 1 GHz laser may require run times in the range of 50 ns to 100 ns to obtain high-quality small-signal simulation results.

4.6 Model Limitations and Possible Extensions

To facilitate the application-oriented calculations as outlined in the previous sections, it is necessary to keep the computational complexity relatively low in order to obtain simulation results in a reasonable amount of time. A physics-based tool for high-power broad-area lasers, for example, can take as much as 2 hours for a physical simulation time of 1 ns if not highly parallelised [333], which would not be acceptable for the calculation of a set of small-signal response curves at different currents. This section will discuss the limitations of the here used numerical approach as well as some possible model extensions.

Separate electron-hole equations

While the rate equations presented in this chapter follow an excitonic approach, it is possible to explicitly include separate hole rate equations. This can, for example, be done in order to investigate the desynchronisation of the electron and hole dynamics resulting from the different carrier capture dynamics [283, 288, 334]. In chapter 5.2, separate electron and hole rate equations are used to model how their different diffusion constants

impact the performance of monolithic QD lasers on silicon through carrier migration into defect states.

Multiple excited states

It is good practice to reduce the QD electronic structure to two discrete states only, as the higher excited states do not have a significant impact on the QD static and dynamic properties [143]. It can, however, be useful to include these specifically, for example when studying intradot relaxation dynamics [313] or the impact of carrier re-emission into higher energy levels and the associated dislocation-induced carrier loss in lasers on silicon, as will also be discussed in chapter 5.2.

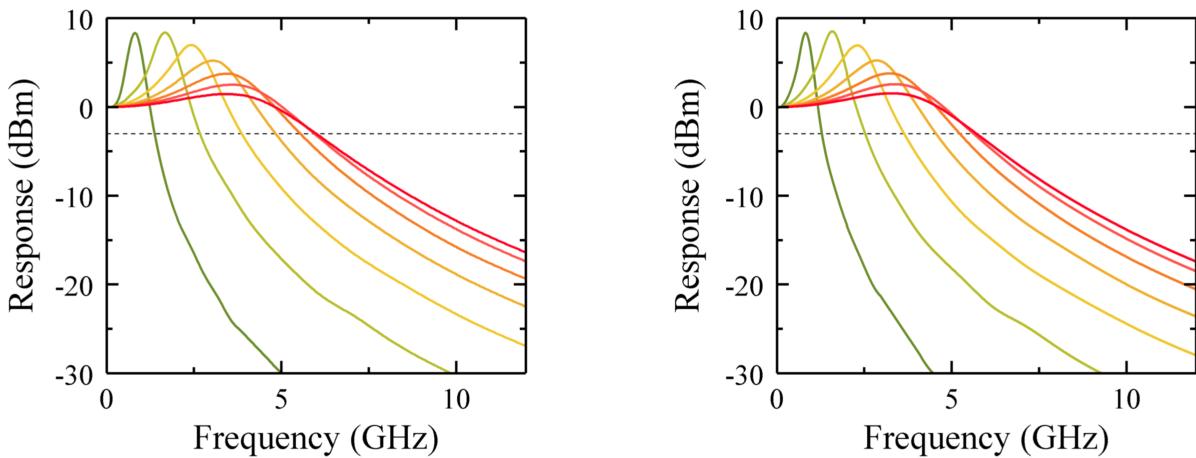

Figure 4.11: Examples of small-signal modulation curves including (left) one excited state and (right) two excited states. The laser dynamics remain fundamentally unchanged.

Quantum dot ensemble

The model presented in this chapter treats the QD active region as an ensemble of identical, noninteracting QDs, projecting the energy levels of all QDs in the active region onto the very same energies. The size and thus energy distribution of the QD ensemble can be modelled realistically by subdividing the QD rate equations into N groups, each receiving a proportion of the injected carriers scaled with the QD group existence probability, as shown in Fig. 4.12. Such an approach can be advantageous to model explicitly the shape of the inhomogeneously broadened QD gain distribution and its relation to the linewidth enhancement factor in order to investigate the frequency chirp of directly modulated QD

lasers [113, 283]. However, it also increases the computational complexity significantly, so that the inclusion of the digital Lorentzian gain filter as introduced in section 4.3.2 is a viable alternative in cases where the QD ensemble properties are of subordinate importance.

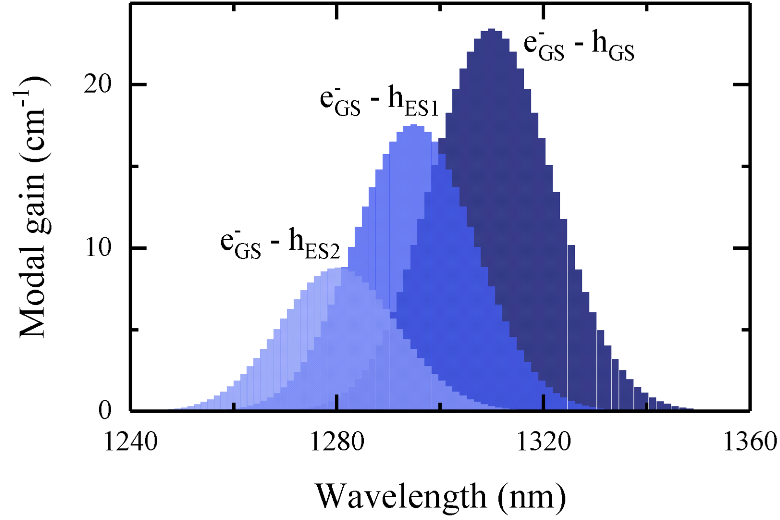

Figure 4.12: Modelled example of the gain distribution for transitions from the electron ground state to the hole ground state and first and second excited state using a QD ensemble with Gaussian distribution.

Thermal effects

Thermal effects have a large impact on the performance of a semiconductor laser, especially at high injection levels. Yet in many simulation approaches with low- to medium-level complexity they are neglected, as they are difficult to implement in a self-consistent manner and are computationally very time-consuming [335]. This is mainly because thermal effects take place on a fundamentally different time scale than optical effects (micro- to milliseconds as opposed to nanoseconds), meaning that unfeasibly long physical simulation times would be required in standard time-domain models.

Li *et al.* have presented a simplified approach for simulating temperature-dependent QW *LI* curves by deploying a temperature-dependent gain function, where the gain coefficient g_0 and the transparency carrier density n_{tr} depend on the internal temperature. These are coupled to a heat transfer equation, in which the ambient or heat sink temperature and the injection current act as heat source, while light output enables laser cooling.

The equations are solved iteratively until the simulations converge [335, 336]. Fig. 4.13 shows an example of simulated *LI* curves at various heat sink temperatures together with the evolution of the transparency carrier density and the nonlinear gain coefficient. Whereas this approach is tailored for QW lasers, it would certainly also offer a route for implementing thermal effects in QD laser simulations. In the simulations presented in the following chapters, thermal effects are omitted, because a significant number of iterations is required for the calculation of each data point.

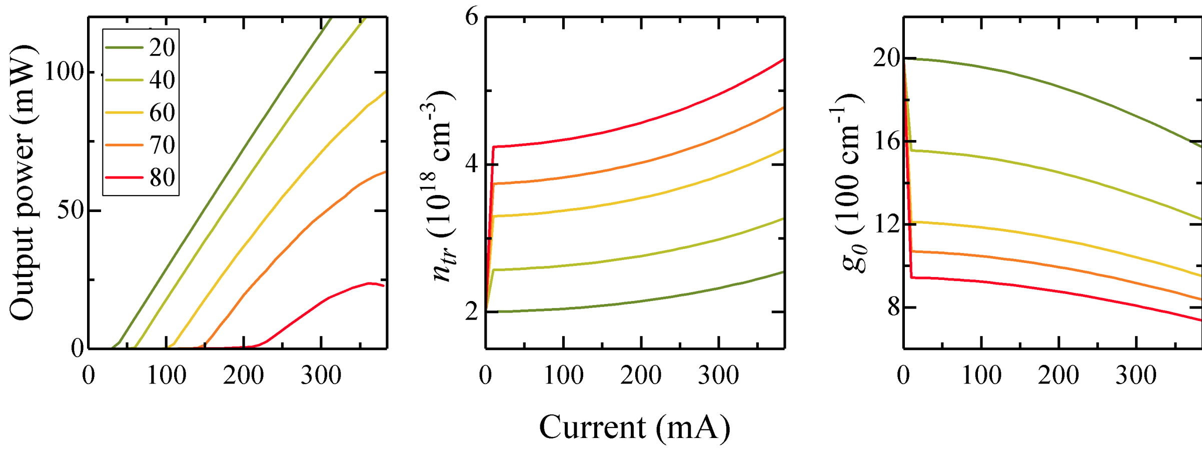

Figure 4.13: QW *LI* simulations at different heat sink temperatures in °C calculated using the model in [335] (left). The temperature-dependent transparency carrier density and gain coefficient are shown in the middle and to the right.

Two-dimensional resolution

The travelling-wave model used in this work is a multi-longitudinal, but single-transverse-mode model neglecting any lateral effects with respect to the carrier distribution or the optical mode profile [290]. For narrow ridge-waveguide lasers or broad-area lasers at low injection regimes, this is usually an acceptable simplification. Expanding the simulations into a more complex two-dimensional system can be useful though for designing and modelling high-power lasers, for example, where it is critical to account for filamentation effects and the respective impact on the optical output power and the beam quality.

Beyond the aspects mentioned in this section, there are still various other possible extensions, such as the inclusion of the polarisation [113], splitting of the nonradiative time constant into its *ABC* components (nonradiative, radiative, and Auger recombination)

[139] as well as inhomogeneous current injection. The simulation of QD lasers and similar low-dimensional active structures is a topic of ongoing research and might gain greater importance with QD devices becoming increasingly attractive for commercial applications.

4.7 Chapter Summary

This chapter started with an introduction into modelling of semiconductor diode lasers and into the numerical implementation of differential equations using the FDTD technique. A system of multi-level carrier QD rate equations including the SCH barrier layers, the wetting layers and two equations for the QD energy levels were presented, followed by a short section on QW carrier rate equations. Subsequently, the numerical implementation of travelling-wave electric field equations for calculation of the photon density was explained in detail, containing explicit derivations of the used equations for the scenarios of light propagation in an amplifying medium and for a digital spectral filter, which can be used to model the wavelength dependence of the QD or QW gain function. In this context, the inclusion of wavelength detuning or frequency chirping, respectively, based on the linewidth enhancement factor and the free carrier plasma effect was discussed as well. Next, an overview of common modelling parameters of 1.3 μm InAs/GaAs QD lasers grown on native substrates was shown, combined with a discussion on parameter considerations for the simulation of monolithic QD lasers on silicon. While the role of dislocation-induced nonradiative carrier loss, optical loss, and a potentially reduced injection efficiency and modal gain in these devices was reviewed, only the nonradiative carrier lifetime and possibly also the injection efficiency were found to be significantly affected by dislocations in the active region. Finally, the numerical implementation of temporal evolution, light-current, and small-signal modulation programmes was explained, which was followed by a section discussing the model limitations as well as possible model extensions.

Chapter 5

The Role of Dislocations in III-V Lasers Grown on Silicon

5.1 Introduction

Dislocation-induced performance degradation has been a major concern for semiconductor researchers ever since the early days of semiconductor injection lasers in the 1970s [210, 337, 338]. Although the reliability issues then concerned primarily semiconductor lasers on native substrates for communications, the problem today remains fundamentally the same for QD lasers on silicon with high dislocation densities. In order for QD lasers on silicon to become attractive for commercial applications, there is an urgent need to better understand the role of dislocations in the laser active region. At the time of writing, the superior performance of QDs compared with QW active regions on silicon is only understood at a rather qualitative level. It is a general consensus that efficient carrier capture into QDs and high electronic confinement prevents carrier migration into defect states, allowing good performance in the first place and substantially slowing down REDR-based dislocation growth in the longer term [120].

Over the course of 2018 and 2019, a handful of experimental studies has become available. Jung *et al.* and Orchard *et al.* have published experimental studies comparing *LI* characteristics of QD lasers on silicon with different dislocation densities, as discussed in chapter 3.4 [275, 276]. Huang *et al.* have measured a defect level activation energy

of 0.4 eV in InAs/GaAs QD photodetectors on silicon, which corresponds to a classic mid-bandgap state serving as a nonradiative recombination centre [265], whereas Buffolo *et al.* found increased forward current leakage with dislocation growth combined with a reduced current injection efficiency due to carrier loss in the InGaAs wetting layer [339, 340]. Lastly, Selvidge *et al.* have presented temperature-dependent cathodoluminescence measurements showing reduced QD emission characteristics in the vicinity of dislocations in late 2019 [211].

To develop a consistent theory, it is necessary to tie these experiments up with numerical simulations reproducing the existing performance trends. The objective of the theoretical studies presented in this chapter is, therefore, to identify the main mechanisms responsible for the drop in performance typically observed at dislocation densities $\rho_{dis} \geq 10^6$ cm^2 for monolithic InAs QD lasers on silicon. A special focus will also be on understanding the performance discrepancies observed between QD and QW active regions on silicon, with the aim of ultimately taking the learnings from QD lasers on silicon and applying them to engineering workable solutions for QWs.

This chapter consists of two parts. In section 5.2, a conventional travelling-wave rate equation approach as introduced in chapter 4 incorporating a dislocation density-dependent nonradiative carrier lifetime is used to model the LI characteristics of QW and QD laser on silicon as a function of dislocation density. In section 5.3, an alternative high-resolution approach allowing the inclusion of individual, spatially resolved dislocations along the laser cavity is used to gain insight into local phenomena of the optical gain, photon, and carrier density distribution in the vicinity of dislocations. It will be shown that the results of this chapter, building on the results published in [275] and [276], are confirmed by some of the findings reported in [211, 339, 340].

5.2 Standard Approach Based on Macroscopically Averaged Parameters

5.2.1 Numerical Approach: Diffusion-Assisted Carrier Loss

In a simplified model, the impact of threading dislocations can be described as follows. Carriers in the vicinity of dislocations can migrate into defect states, where they are likely to recombine nonradiatively. As illustrated in Fig. 5.1, this process affects primarily the continuum layers such as the barrier layers, QWs, and to some extent also the wetting layers embedding the QDs. The QDs themselves are assumed to be safe from nonradiative

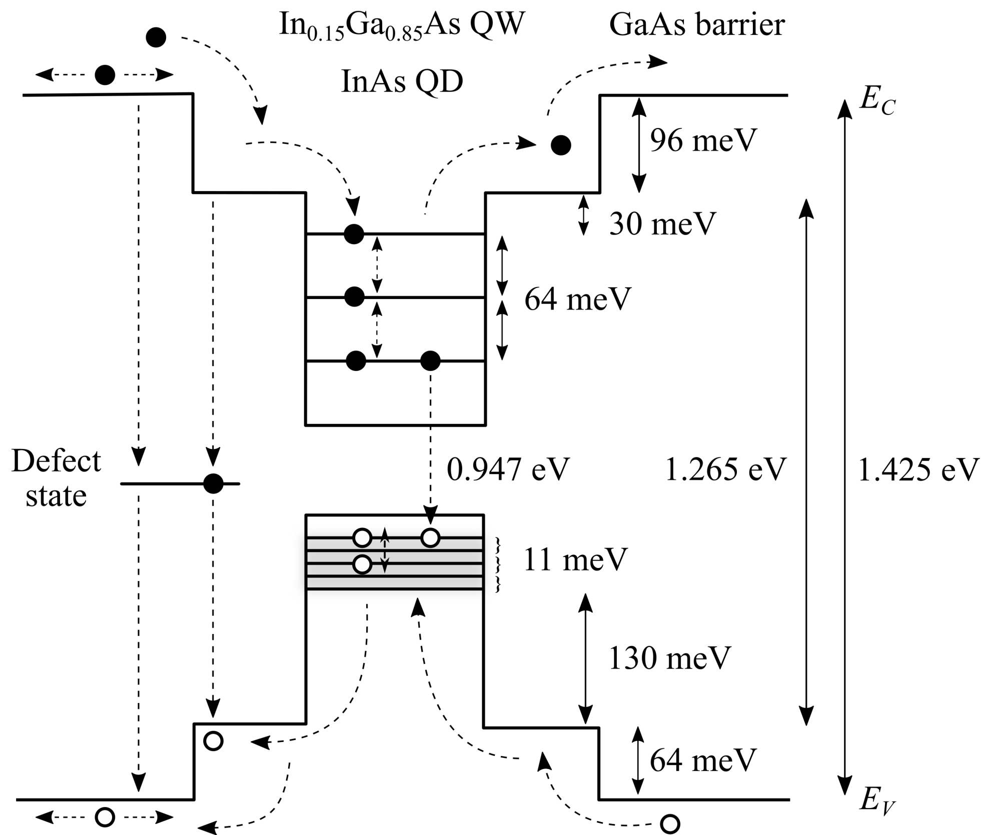

Figure 5.1: Schematic one-dimensional real-space energy band diagram of an In(Ga)As DWELL QD laser [120, 285]. The InGaAs QW energy band diagram does not contain the discrete QD levels, but can otherwise be regarded as analogous. Nonradiative recombination processes via dislocation-induced mid-bandgap defect centres take place from the barrier layer and wetting layer/QW only. Carriers confined in the QDs are not affected unless they thermalise out of the QD states.

recombination, as captured carriers cannot directly diffuse into defect states unless they thermalise back up into the continuum layers [264]. The amount of QDs directly hit by a threading dislocation is ignored due to the typically negligible number of dislocations compared with the number of QDs, as discussed in chapter 3.3.5. Shallow traps in thermal equilibrium with the conduction and valence band are also ignored as well as carrier re-emission from the defect states.

Considering the effect of dislocation-induced carrier loss, the total carrier lifetime is written as a combination of a background carrier lifetime τ_{nr} in the absence of threading dislocations and a component τ_{dis} representing enhanced nonradiative recombination as a function of dislocation density ρ_{dis}:

$$\tau_{nr,tot}^{-1} = \tau_{nr}^{-1} + \tau_{dis}^{-1} \tag{5.1}$$

[212, 341]. In order to estimate the dislocation-induced loss time constant τ_{dis}, we consider the average spacing d_{dis} between two dislocations, which can be estimated as

$$d_{dis} = \frac{2}{\sqrt{\pi \rho_{dis}}} = L_{diff}^{dis} \tag{5.2}$$

[213, 342] and corresponds to an average dislocation-limited diffusion length. The respective dislocation-dependent carrier lifetime is then given over the relationship to the diffusion constant D as

$$L_{diff} = \sqrt{D\tau_{nr}} \quad [337] \tag{5.3}$$

$$\Leftrightarrow \tau_{dis} = \frac{(L_{diff}^{dis})^2}{D} \; . \tag{5.4}$$

Fig. 5.2(a) shows a plot of the total electron and hole lifetimes as a function of dislocation density. The respective values of τ_{dis} differ slightly, which is a result of the different electron and hole diffusion constants, as pointed out by Andre *et al.* [212]. Using Eq. (5.4) and a nonradiative background carrier lifetime of 1 ns, the dislocation-limited electron lifetime begins dropping into the sub-nanosecond regime for densities between about 10^6 cm^{-2} and 10^7 cm^{-2}, which can affect the laser performance quite seriously. For holes, in contrast, this is only the case from about 10^7 cm^{-2} to 10^8 cm^{-2}. This is a result of the faster interaction between electrons and dislocations due to the high electron mobility

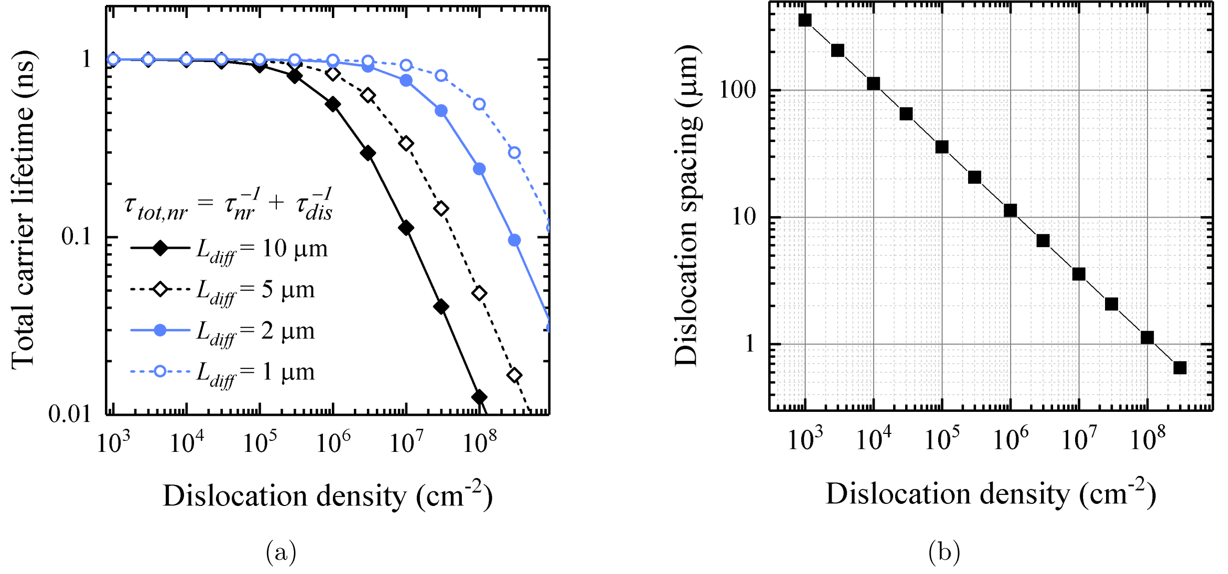

Figure 5.2: (a) Total nonradiative carrier lifetime as a function of dislocation density calculated for different background diffusion lengths (i.e. in the absence of dislocations). Plots in black and blue indicate realistic values for electrons and holes, respectively. The nonradiative background component τ_{nr} is set to 1 ns. (b) Average dislocation spacing versus dislocation density, estimated using Eq. (5.2).

and thus longer diffusion length, which is in agreement with the short electron lifetimes that have been measured in epitaxial GaAs on non-native substrates [212]. Fig. 5.2(b) illustrates that these dislocation density ranges coincide approximately with dislocation spacings of about 1 µm to 10 µm. With typical (In)GaAs hole diffusion lengths of 1 µm to a few micrometres [213, 343, 344] and electron diffusion lengths reaching up to 10 µm [213, 264, 345], $\rho_{dis} = 10^6$ cm^{-2} – 10^8 cm^{-2} marks the range where the average dislocation spacing starts falling below the intrinsic carrier diffusion length, which has been identified in [337] as the starting point of serious laser performance degradation.

Lastly, it is also considered that dislocation-induced carrier loss can saturate due to population of the defect states as higher carrier densities are reached [118, 240]. τ_{dis} is, therefore, multiplied with a phenomenological saturation term $(1 + n/n_{sat})$, where n is the respective wetting layer/QW or barrier layer carrier density and the reference value n_{sat} is chosen to be 10^{18} cm^{-3}. Since the nature of the defect states formed by threading dislocations in III-V structures on silicon has not been investigated more closely yet, it is currently not known if those defects behave as acceptor-like or donor-like and

thus if the electron or hole time component is more dominant in the dislocation carrier capture process. This will certainly affect the respective capture dynamics and can explain potential discrepancies between experiment and theory. It is also worth pointing out that various equations have been developed to describe the dependence of the overall nonradiative carrier lifetime on dislocation density [210, 342, 346]. However, all of them follow the approximate trend shown in Fig. 5.2(a).

In order to consider the effects of different electron and hole diffusion constants as well as the likelihood of carrier re-emission from the QD confined states back into the continuum layers, the rate equation model introduced in chapter 4.2.1 is expanded with a set of hole equations to match the electronic system shown in Fig. 5.1. Since the carrier escape time constants depend on the electronic barrier height (Eq. (4.37) and following in chapter 4.4.1), the QD state equations are for this purpose only expanded to include a second excited state (ES2) as well, whereas the QD hole states are formed of five closely spaced levels [267, 285]. Dislocation-induced carrier loss using $-N/\tau_{nr,tot} = -N/\tau_{nr} - N/\tau_{dis}$ is only included in the barrier layer and wetting layer, where carrier migration into dislocations is possible, while the carrier loss term $-N/\tau_{nr}$ in the QD state equations remains unchanged.

The hole barrier layer and wetting layer equations are modelled analogously to the barrier layer and wetting layer electron equations, whereas the hole QD levels are modelled via one joint equation, as the holes tend to thermalise among the various confined states due to their small energy spacing [283]:

$$\frac{\partial N_{QD}^{h}}{\partial t} = \frac{N_{WL}^{h} f_{QD}^{h'}}{\tau_{cap}^{QD,h}} - \frac{N_{QD}^{h}}{\tau_{esc}^{QD,h}} - \frac{N_{QD}^{h}}{\tau_{nr}^{QD}} - v_{gr} g_{QD} S \cdot \frac{V_{AR} \Delta z}{L} \quad . \tag{5.5}$$

The QW model is directly adapted from chapter 4.2.2 with identical electron and hole equations and the new dislocation-induced carrier loss term included in both the barrier and the QW level. An overview of the used simulation parameters can be seen in Table 5.1. The QW laser parameters are based on those in [280], whereas the QD parameters are chosen based on values presented in Table 4.3 to represent a high-quality QD device in the absence of dislocations.

SHARED QD & QW SIMULATIONS PARAMETERS CHAPTER 5.2	
$\Delta z = 10$ µm	Spatial step size
$L = 500$ µm	Cavity length
$w = 2$ µm	Waveguide width
$h_{BL} = 65$ nm, 250 nm	Total QW/QD barrier layer thickness
$h_{QW/WL} = 7.5$ nm, 8 nm	InGaAs QW/WL thickness
$N_{layers} = 5$	Number of active layers
$R_{1,2} = 0.95$, 0.30	Rear and front facet reflectivity
$\lambda = 980$ nm, 1300 nm	QW/QD emission wavelength
$\Gamma = 0.05$, 0.005	QW/QD confinement factor
$\epsilon = 10^{-17}$ cm^3, 10^{-16} cm^3	QW/QD gain compression factor
$\alpha_i = 5$ cm^{-1}	Optical waveguide loss
$\eta = 0.55$	Current injection efficiency
$\tau_{cap}^{QW/WL,e} = 3.0$ ps, 3.4 ps	Electron transport & capture time into QW/WL
$\tau_{cap}^{QW/WL,h} = 1.0$ ps, 8.9 ps	Hole transport & capture time into QW/WL
$\tau_{esc}^{QW/WL,e} = 2.5$ ps	Electron QW/WL escape time
$\tau_{esc}^{QW/WL,h} = 1.9$ ps	Hole QW/WL escape time
$\tau_{nr} = 1$ ns	Nonradiative lifetime (all levels)
$L_{diff}^{e/h} = 10$ µm, 2 µm	Electron/hole BL and QW/WL diffusion length
QW-SPECIFIC PARAMETERS	
$g_0 = 3000$ cm^{-1}	QW gain constant
$n_{tr} = 1 \times 10^{18}$ cm^{-3}	Transparency carrier density
QD-SPECIFIC PARAMETERS	
$g_{mod} = 50$ cm^{-1}	QD modal gain
$\rho_{dots} = 6\times10^{10}$ cm^{-2}	QD density
$\tau_{cap}^{QD,e/h} = 3$ ps, 0.5 ps	Electron/hole carrier capture time into QDs
$\tau_{rlx}^{QD,e} = 0.25$ ps	Electron intradot relaxation time
$\tau_{esc}^{GS/ES1/ES2,e} =$ 1.3 ps, 1.8 ps, 2.4 ps	Electron GS, ES1, ES2 escape time
$\tau_{esc}^{QD,h} = 10.9$ ps	Hole QD escape time

Table 5.1: Overview of the used simulation parameters.

5.2.2 Simulation Results

The *LI* characteristics of QD and QW lasers are modelled as a function of dislocation density using the dislocation-dependent carrier lifetime as described in section 5.2.1. From Fig. 5.3(a) it can be seen that excellent QD lasing characteristics are obtained for threading dislocation densities between 10^4 cm^{-2} and about 10^8 cm^{-2} using the parameters for a high-gain QD laser as shown in Table 5.1. Particularly for dislocation densities around 10^6 cm^{-2} – 10^7 cm^{-2}, which are common values for III-V lasers grown on silicon, the modelled *LI* characteristics are almost unaffected by the additional carrier loss component. This finding agrees with publications of high-performance InAs QD laser on silicon at dislocation densities of 7×10^6 cm^{-2} by Jung *et al.* [23, 24]. Although the modelled threshold current here more than doubles for densities from 10^4 cm^{-2} to 10^8 cm^{-2}, the absolute shift from 11.7 mA to 27.6 mA still results in a relatively low threshold laser. While the slope efficiency drops also by 26 %, the slope of 0.18 W/A is indeed still acceptable for a QD laser. This sort of behaviour at a high dislocation density of 10^8 cm^{-2} is in agreement with the experimental performance observed in [240] and [241]. $\rho_{dis} = 3 \times 10^8$ cm^{-2} is the maximum dislocation density reported for any 1.3 µm InAs QD laser on silicon, which is consistent with the sharp drop in performance obtained in the simulations.

Fig. 5.3(b) reveals that a lower-gain QD laser ($g_{mod} = 25$ cm^{-1} rather than 50 cm^{-1}) suffers much more from enhanced dislocation-induced carrier loss at increasing dislocation densities. For densities from 10^4 cm^{-2} to 10^8 cm^{-2}, the laser experiences an almost fourfold increase in threshold current. Lasing at 3×10^8 cm^{-2} is realistically unlikely to be achieved, as in a practical device Joule heating (which is not considered in these simulations) will play a significant role at these high injection levels and will lead to additional loss mechanisms [347, 348]. In this context, it should, furthermore, be noted that the here presented calculations do not consider device degradation due to dislocation climb, which is known to be a a common failure mechanism in III-V QW lasers grown on silicon and native substrates [218, 219].

The dislocation-dependent QD *LI* simulations confirm the experimental trends discussed in chapter 3.4 and can be interpreted in a quite straight-forward way. With rising

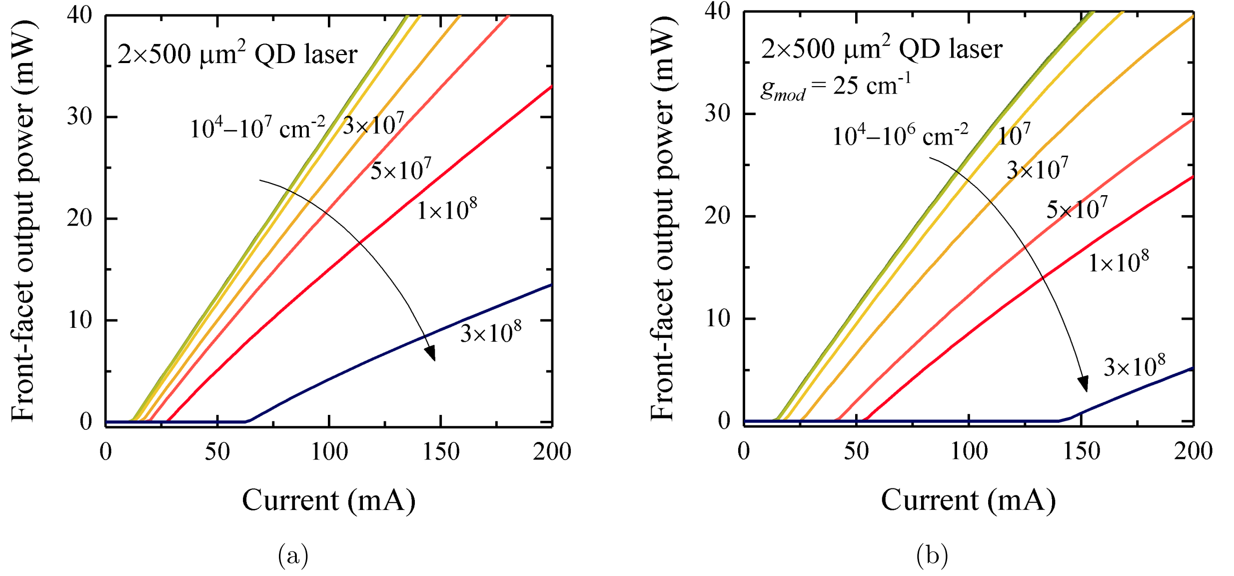

Figure 5.3: (a) QD *LI* curves calculated as a function of dislocation density using the laser parameters of Table 5.1 and the introduced dislocation loss term. (b) Analogous simulations for a lower-gain QD laser ($g_{mod} = 25$ cm^{-1}, $\Gamma = 0.0025$, $\rho_{dots} = 3\times10^{10}$ cm^{-2}).

dislocation density, the total nonradiative carrier lifetime $\tau_{nr,tot}$ shortens due to the enhanced dislocation-induced carrier loss component τ_{dis}. Although this affects primarily the barrier layer and wetting layer lifetimes and is alleviated by the unchanged lifetime in the QDs, it is ultimately reflected in the overall carrier lifetime of the entire system. Since increased carrier loss requires higher injection levels to achieve occupation inversion, this leads to a rise of the threshold current [143], as can be seen in Fig. 5.3(a) and (b). The earlier drop of the electron loss time constant indicates, furthermore, that electron migration into dislocations poses the limiting factor for the performance of bipolar devices on silicon [212]. Despite the drop of the barrier layer and wetting layer lifetimes to 100 ps – 10 ps at high dislocation density though, the fast capture of carriers into the confined QD states allows lasing up to large ρ_{dis}. In the case of QD lasers, dislocation-induced carrier loss in the continuum layers manifests itself, therefore, eventually in a reduced carrier injection efficiency η and is reflected in the *LI* slope reduction, as previously discussed in chapter 4.4.2.

Dislocation density-dependent simulations of an equivalent QW laser using the parameters of Table 5.1 can be seen in Fig. 5.4(a). From this and the overview graph

in Fig. 5.4(b) it becomes immediately evident that a QW laser without QD energy level that is safe from dislocation-induced carrier loss is more seriously affected by an increasing number of dislocations. While the current required to pump a QW-based active region is naturally higher compared with low-volume QDs, the laser threshold increases drastically from $\rho_{dis} > 1 \times 10^6$ cm^{-2}. As carriers accumulate in the QWs, where they can migrate into nearby dislocations rather than being captured into QDs, dislocation-induced carrier loss is here of much greater importance, making it increasingly difficult to attain a population inversion in the presence of many dislocations. It takes, therefore, only a relatively low dislocation density of 5×10^6 cm^{-2} to shift the laser threshold above 100 mA, where thermal effects are likely to degrade the performance even further. It is interesting to note that the slope efficiency of the dislocation-dependent QW *LI* curves is almost independent of dislocation density. This is probably as the barrier layer losses alone have a small impact on the carrier injection efficiency into the QWs compared with the combined effect of barrier layer and wetting layer losses in the case of a QD laser.

GaAs-based QW lasers grown on silicon have experimentally only been demonstrated in the comparably low dislocation density range of 2×10^6 cm^{-2} to 10^7 cm^{-2} [233, 257,

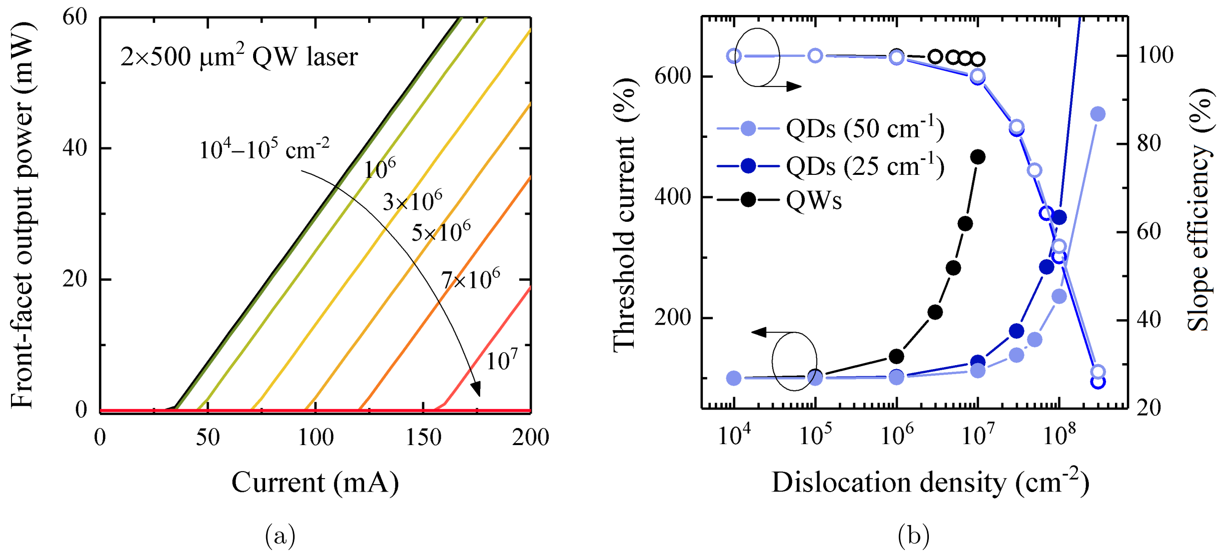

Figure 5.4: (a) QW *LI* curves calculated as a function of dislocation density using the laser parameters of Table 5.1 and the introduced dislocation loss term. (b) Overview of the threshold current increase and the slope reduction of the modelled QW and QD lasers against dislocation density, calculated with respect to the values at 10^4 cm^{-2}.

258, 349, 350], which makes these data insufficient for the identification of meaningful performance trends. On top of that, the unreliable performance of III-V QW lasers grown on silicon substrates did not allow any systematic studies comparing similar devices at varying dislocation. However, the simulations in Fig. 5.4(a) confirm the tendency of QW lasers on silicon to have high threshold currents [257–260] and correlate well with the approximate dislocation densities for which it is realistic to obtain lasing with QW-based active regions.

5.2.3 Discussion

In order to investigate the hypothesis that the defect tolerance of monolithic QDs lasers on silicon originates from the unique properties of QDs, efficient carrier capture and high carrier confinement, further simulations are performed to study the impact of the minority carrier diffusion length, the capture time into QDs, and the QD electronic barrier height.

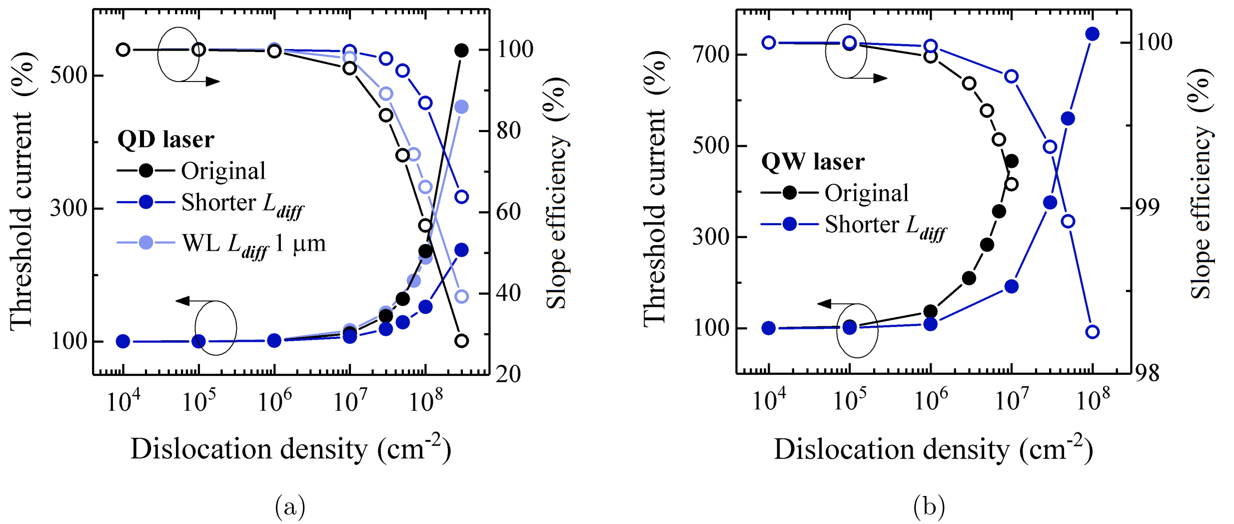

Figure 5.5: Overview of the threshold current increase and the slope efficiency reduction of LI curves as a function of dislocation density. (a) QD laser results comparing the original performance (black) with simulations using shorter electron and hole diffusion lengths of 5 µm and 1 µm (dark blue), and unchanged barrier layer diffusion parameters, but a reduced electron and hole diffusion length of 1 µm (light blue). (b) QW laser results comparing the original performance (black) with the shorter diffusion length simulation results (5 µm and 1 µm, dark blue).

Figs. 5.5(a) and (b) show overviews of the threshold current increase and slope reduction of QD and QW devices modelled at different diffusion settings. Whereas the original simulations (black) were performed using large electron and hole diffusion lengths of 10 μm and 2 μm, respectively, the results of sets with shorter diffusion lengths of $L^e_{diff} = 5$ μm and $L^h_{diff} = 1$ μm are here shown as well (dark blue). From both graphs it becomes obvious that a shorter minority carrier diffusion length at the same original carrier lifetime is beneficial for the operation of a laser in the presence of a high dislocation density, as carriers are less likely to diffuse into defects, which increases the overall carrier lifetime and thus reduces the threshold current increase compared with the original results in black. The performance improvements are particularly pronounced for the QW simulations in Fig. 5.5(b) and actually appear to overestimate the expected performance. At a dislocation density of 10^7 cm^{-2}, this simulation approach predicts a threshold current increase of about 100 % from 34 mA to 65 mA, which might be slightly too optimistic for a QW-based laser in the presence of many dislocations.

In Fig. 5.5(a), additional simulation results are also shown for unchanged barrier layer diffusion lengths ($L^{e,h}_{diff} = 10$ μm, 2 μm), but a reduced electron and hole wetting layer diffusion length of 1 μm. This scenario is investigated, because it has been shown experimentally that lateral carrier diffusion is strongly suppressed in DWELL active regions due to dominant carrier capture into the closely spaced (about 50 nm) QDs [263, 264]. Fig. 5.5(a) illustrates, however, that modelling this explicitly results only in moderate performance improvements as fast carrier capture is modelled here naturally by setting the QD electron and hole capture times to 3 ps and 0.5 ps, respectively.

Further insights into the physics of QD lasers on silicon can be obtained from Fig. 5.6(a), showing LI simulations at threefold increased carrier capture time constants, and Fig. 5.6(b), showing a set calculated for reduced (factor 2) electronic barrier heights between the QD and the wetting layer as well as between the QD states themselves. Interestingly, both simulation sets point out very different features. In the first case, carriers linger in the wetting layer for a longer time and experience stronger carrier loss through nonradiative recombination at defect centres. This results effectively in fewer carriers relaxing into the QD ground state and is hence reflected in a a reduced current injection efficiency, i.e. a

more greatly reduced QD LI slope at high dislocation densities. Whereas the LI slopes of the original QD simulations illustrated in Fig. 5.3(a) are reduced to 57 % (10^8 cm^{-2}) and 28 % (3×10^8 cm^{-2}) of their original slope at 10^4 cm^{-2}, for example, the LI curves modelled under slower carrier capture show a much stronger slope reduction down to 35 % (10^8 cm^{-2}) and 14 % (3×10^8 cm^{-2}), respectively. Since the overall carrier lifetime remains unchanged, no substantial threshold current increase is observed compared with the original carrier capture parameters.

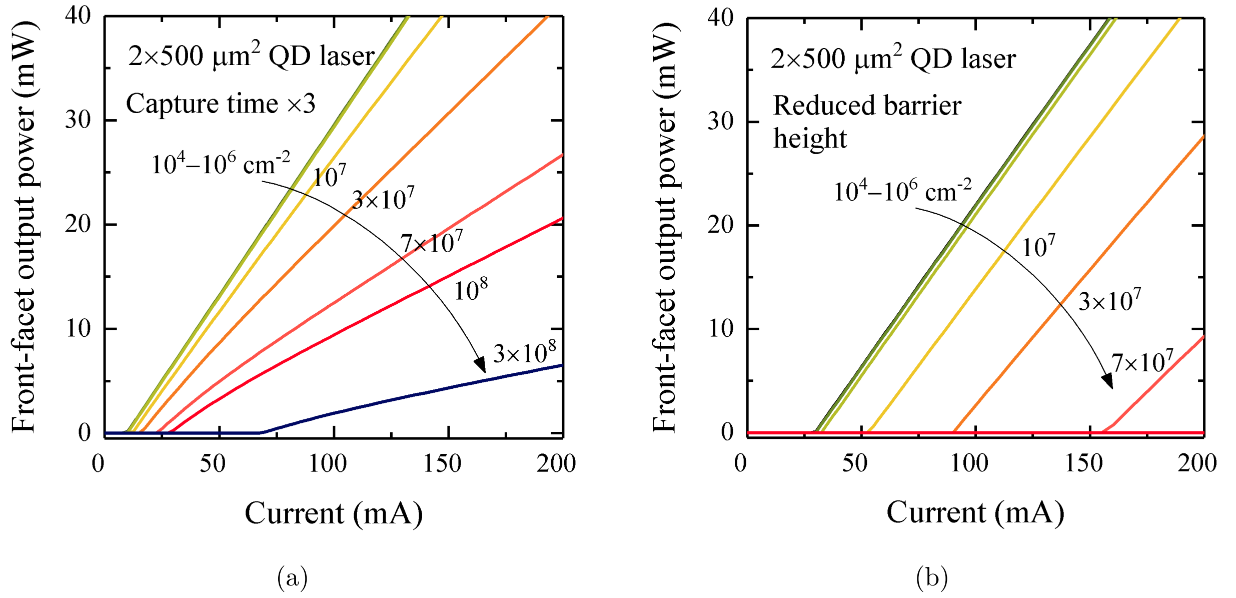

Figure 5.6: Remodelled QD LI curves as a function of dislocation density using (a) threefold increased carrier capture times ($\tau_{cap}^{QD,e} = 3$ ps $\rightarrow$ 9 ps, $\tau_{cap}^{QD,h} = 0.5$ ps $\rightarrow$ 1.5 ps) and (b) halved QD energy barriers and QD state spacings ($\Delta E_{GS,ES1}^{e} = 64$ meV $\rightarrow$ 32 meV, $\Delta E_{ES1,ES2}^{e} = 64$ meV $\rightarrow$ 32 meV, $\Delta E_{ES2,WL}^{e} = 30$ meV $\rightarrow$ 15 meV, $\Delta E_{QD,WL}^{h} =$ 130 meV $\rightarrow$ 65 meV).

Fig. 5.6(b), in contrast, shows the opposite trend. Using a hypothetical energy structure with halved QD barrier heights and discrete state energy spacings yields faster carrier escape according to Eqs. (4.37) and (4.38). Although escaped carriers can in principle directly relax back into the QDs, a certain proportion might instead recombine nonradiatively at a dislocation. This process translates effectively into a reduced QD carrier lifetime, which is manifested in a clearly visible threshold current increase but a nearly unaffected slope efficiency compared with Fig. 5.3(a). At $\rho_{dis} = 3 \times 10^7$ cm^{-2}, for instance,

the QD laser threshold with lower energy barriers is increased to 90 mA compared with only 16 mA using the original barrier heights. The underlying physical behaviour is confirmed by a temperature-dependent cathodoluminescence (CL) study of InAs QD lasers on silicon by Selvidge *et al.*, as can be seen in Fig. 5.7, where a clear reduction of CL intensity is observed due to increased likelihood of QD carrier re-emission at higher temperatures.

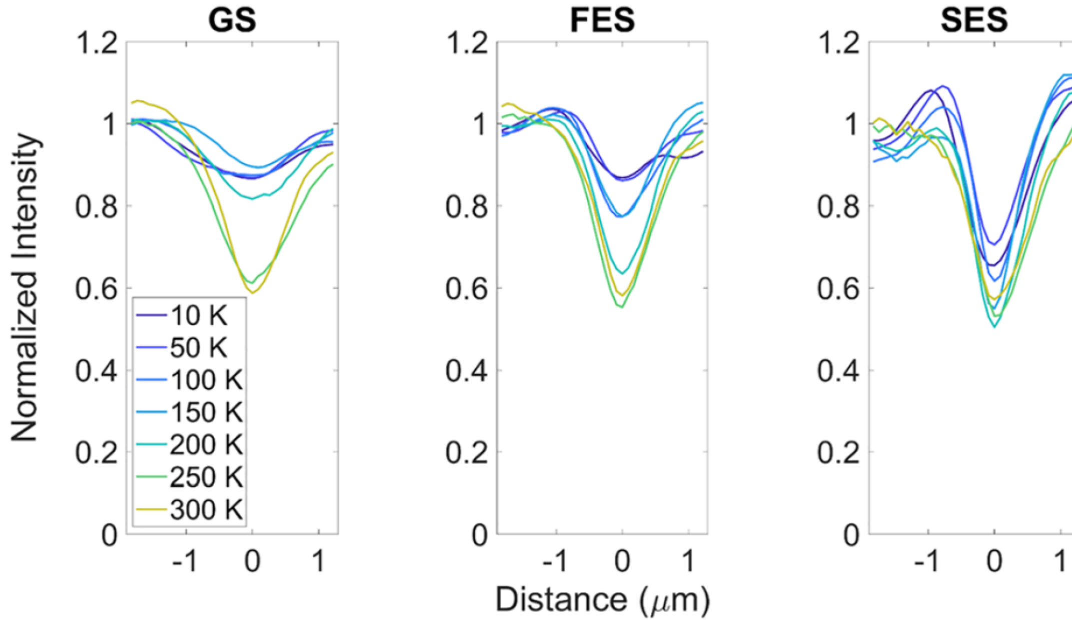

Figure 5.7: Temperature-dependent CL line scans of the ground state (left), first excited state (middle), and second excited state (right) across a dislocation in a monolithic InAs/GaAs QD laser on silicon [211].

So, based on the dislocation-dependent carrier loss time constant inferred from the average dislocation-limited diffusion length in the barrier layers and the QWs/ wetting layers, the presented simulations are capable of reproducing experimental performance trends of silicon-based In(Ga)As QD and QW lasers published in the literature. The results allow to explain the superior performance that is obtained with QD active regions and confirm that fast QD carrier capture and sufficiently high energy barriers prevent the captured carriers from migrating into defect states. However, since dislocations are local phenomena which might not only affect carrier density, but also gain and optical loss, it is quite likely that this kind of approach is not fully capable of describing the physics

of monolithic QD lasers on silicon accurately. This issue will be addressed in the next section of this chapter.

5.3 Spatially Resolved Inclusion of Dislocations

This study aims at taking the simulations from the previous section one step further in order to explore an alternative approach on how to describe the physics of monolithic III-V lasers on silicon in a more suitable way.

5.3.1 Numerical Approach: Implementation of Dislocations

In section 5.2, it was found that nonradiative recombination of electrons at dislocations is likely to pose the performance-limiting factor in bipolar monolithic devices on silicon due to their higher diffusivity and thus faster interaction with dislocations. While the electronic QD barrier height was shown to have an impact on the QD laser performance in the presence of high dislocation density, resolving the exact electronic QD structure does not appear to be crucial for understanding local phenomena around dislocations in III-V lasers on silicon. For these reasons, this section utilises the standard excitonic rate equation travelling-wave model for QWs and QDs as presented in chapter 4.2. Contrary to the previous simulations, which had to be conducted using averaged, effective laser parameters such as the overall reduced nonradiative recombination to account for an increased number of dislocations, in these simulations Δz is reduced to the sub-micrometre level in order to enable the explicit inclusion of individual nonradiative defect centres in the active region. All simulation parameters used remain the same as shown in Table 5.1, except $\Delta z = 500$ nm, $f^h_{GS} = 0.5$, and $\tau^{QD}_{rlx} = 500$ ps, because the number of excited states is reduced to one again. As in the previous section, dislocation-induced carrier loss and lateral carrier diffusion is considered in the continuum layers, i.e. the barrier layers and wetting layers or QWs, respectively, only. It should be noted that τ_{dis} is a vector inducing carrier loss at predefined dislocation positions only rather than being an effective laser parameter, as discussed in the following.

In order to study the effects of threading dislocations in GaAs-based laser active regions, nonradiative recombination centres are placed on a regular grid along the laser cavity, as illustrated in Fig. 5.8. The advantage of a regular dislocation arrangement compared with a more realistic, random dislocation distribution is discussed further below. The dislocations are modelled as sections with ultrafast carrier loss at rate τ_{dis}^{-1} to represent fast carrier capture into mid-bandgap defect states [265]. Since the exact dislocation carrier capture time is not known, a capture time of the order of a few picoseconds is assumed, comparable with the one into QD states [302, 304]. For Δz = 500 nm, a dislocation capture time τ_{dis} = 10 ps is chosen, whereas τ_{dis} is set to infinity in dislocation-free regions. A further factor influencing the magnitude of τ_{dis} is the assumed dislocation core diameter and carrier capture length in conjunction with the chosen Δz. A variety of values has been published for the physical size of actual dislocation cores, ranging from below 1 nm [351] over a few tens of nanometres [352, 353] up to 1 µm [341]. The choice of Δz = 500 nm is, accordingly, a trade-off between physical accuracy and computational feasibility. τ_{dis} is hence both a fitting parameter for modelling realistic performance trends with growing dislocation density as well as a way to compensate for larger Δz, which overestimate the dislocation size slightly. Selvidge *et al.* have recently reported a carrier capture length of 500 nm for InAs/GaAs QD lasers on silicon [211], which supports our choice of spatial resolution.

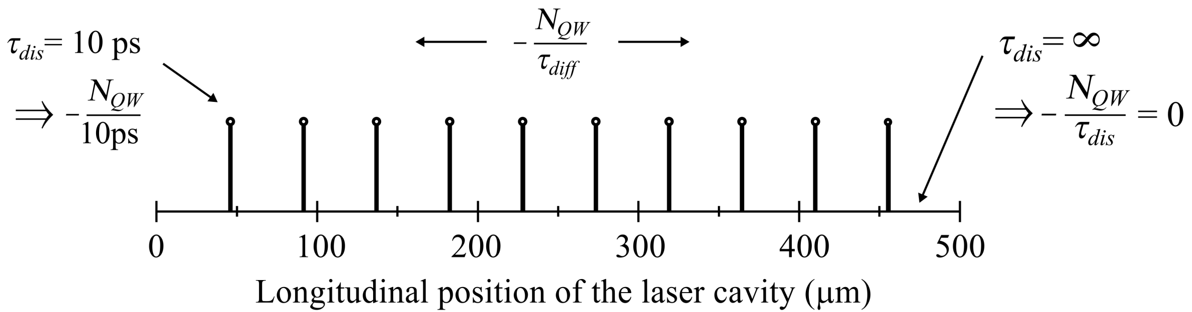

Figure 5.8: Schematic of the implementation of dislocation-induced carrier loss using the example of the QW layers based on a vector τ_{dis} with predefined dislocation positions given by the modelled dislocation density ρ_{dis}.

It should be noted that a series of assumptions and simplifications is made in the present approach. First of all, the travelling-wave approach neglects radial, i.e. two-dimensional carrier migration into dislocations, thus projecting this process onto a one-dimensional plane, as indicated in Fig. 5.9. Since this leads to an overestimation of the impact of dislocations on the laser performance, especially for QDs with their reduced effective diffusion length [263, 264], the waveguide width of the modelled devices is set to a narrow value of 2 μm. This is additionally to ensure single-transverse mode operation. Secondly, while a regular arrangement of dislocations in the active region is best for the reproducibility of simulation results, it tends to be the worst case scenario in terms of laser performance [342], as the number of carriers affected by diffusion-assisted carrier loss is thereby maximised. A realistic III-V laser grown on silicon has a random dislocation distribution allowing for variations in the laser performance, where slightly better than average performance is obtained from devices with large dislocation-free regions. Lastly, here too dislocation-induced carrier loss in the QD levels is ignored due to the small ratio between the dislocation number and the QD number, as explained in chapter 3.3.5. From the computational point of view, it is important to consider that shrinking Δz and Δt may ultimately lead to computational errors. Numerical stability is thus ensured by checking that the Courant Friedrichs Lewy condition is equal to 1 (rather than 0.99999, for example) [354].

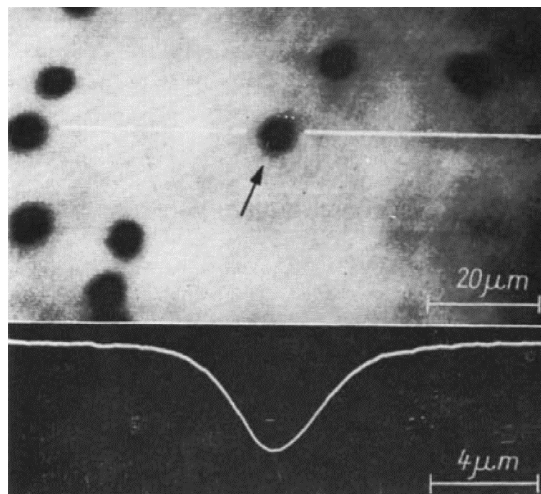

Figure 5.9: CL image (top) plus respective intensity line scan across a dislocation in a GaP substrate [355] .

5.3.2 Simulation Results

Fig. 5.10(a) shows an example of the QW carrier density distribution at twice the laser threshold obtained for a dislocation density of 10^6 cm^{-2}, equating to ten dislocations in a 2×500 μm^2 laser, as well as the carrier density distribution at the same output power level in the absence of dislocations. The threshold carrier density shows a slight curvature in dependence of the cavity position due to the growth of the forward propagating photon density towards the output facet at $L = 500$ μm. This leads to a slightly higher depletion of the carrier density and thus to a reduction of the gain. This effect is more pronounced at $L = 500$ μm, since the photon round-trip from there includes reflection at the HR coating, whereas the round-trip starting from $L = 0$ μm encompasses higher photon loss at the as-cleaved facet after one cavity length.

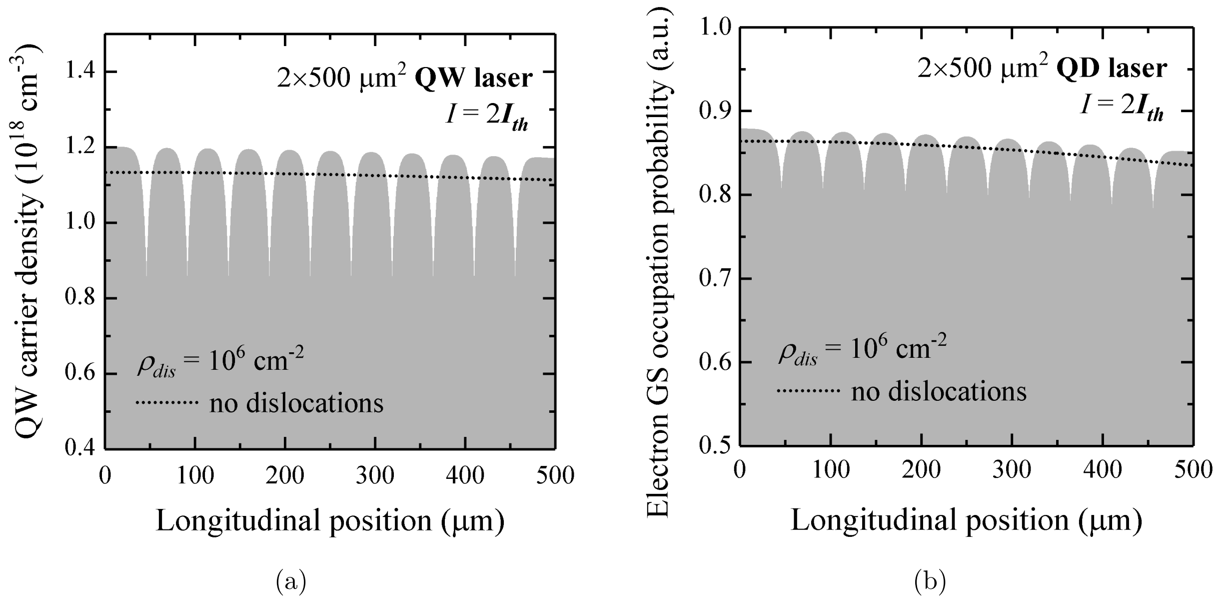

Figure 5.10: (a) QW carrier density and (b) QD ground state occupation probability of 2×500 μm^2 devices at about $2I_{th}$ against the longitudinal position in the presence of ten dislocations. The black dotted lines shows the QW carrier density or QD ground state occupation, respectively, without dislocations at the same optical output power level in comparison.

It can clearly be seen that the influence of carrier loss at the only 500 nm long dislocation positions is intensified by carrier diffusion, which causes the carrier density over several micrometres to fall below the threshold value. The large electron diffusion length

in GaAs-based III-Vs, which remains set to 10 μm, contributes therefore to an increased sensitivity to defects [212]. The carrier density in dislocation-free regions must, consequently, be increased in order to attain the required cavity threshold gain. The comparison with the QD ground state occupation probability against the longitudinal position, depicted in Fig. 5.10(b), highlights that the magnitude of the QD carrier occupation dips is actually relatively small. This is because ultrafast carrier capture into QDs [120] helps maintaining a high overall ground state occupation probability, even at reduced carrier densities in the vicinity of dislocations in higher energy levels.

These behaviours are directly reflected in the gain profiles against longitudinal position, as shown in Fig. 5.11(a) and (b). The QW local gain profile (Fig. 5.11(a)) reveals that carrier depleted areas around dislocations become highly absorptive due to the logarithmic nature of the QW gain function. To still be able to meet the cavity threshold gain and enable lasing, these gain dips have to be compensated for in dislocation-free regions,

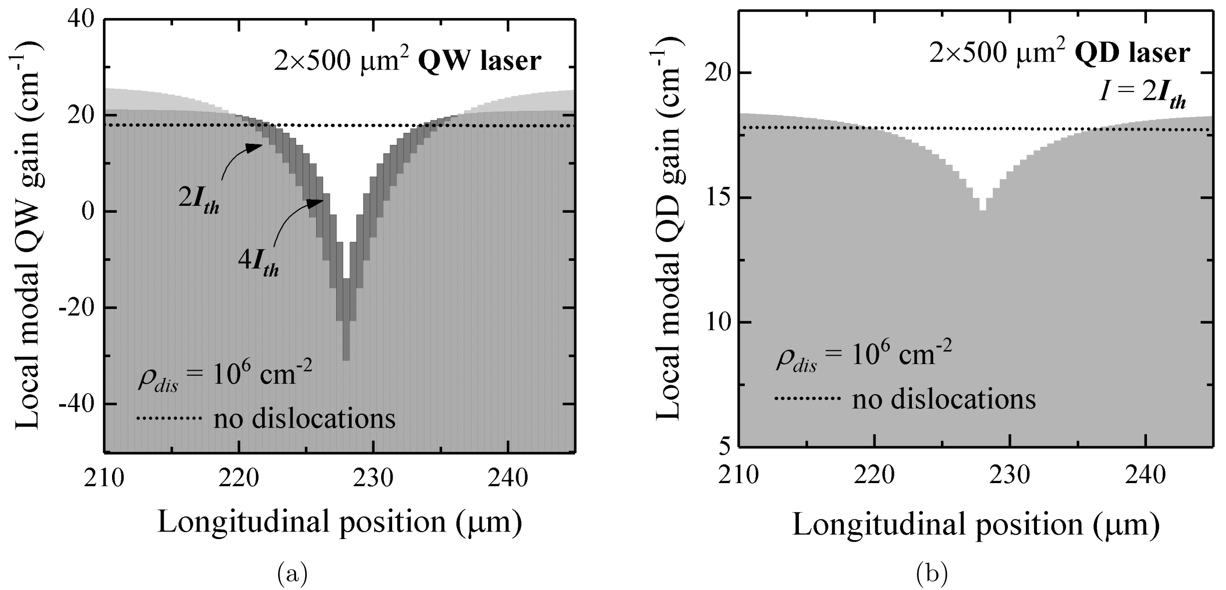

Figure 5.11: (a) QW and (b) QD gain function around a dislocation corresponding to the carrier levels shown in Fig. 5.10 compared with the average cavity threshold gain in the absence of dislocations. It should be noted that at the centre of the dislocation core (i.e. the mid-bandgap energy level acting as nonradiative recombination centre) there is technically no energy level providing gain at the QW and QD lasing wavelengths of 980 nm and 1.3 μm, respectively. Due to the small dimensions of the crystal dislocation itself, this effect is, however, neglected.

where the gain has to rise above the average gain in the absence of dislocations. It is only at higher current injection levels that defect states become populated, as indicated in darker grey, so that diffusion-assisted carrier loss becomes less severe [118, 240]. This is also reflected in the gain level between dislocations, allowing the gain to settle closer to the average threshold gain.

The QD gain profile depicted in Fig. 5.11(b), on the other hand, reflects the comparably high QD ground state occupation in the vicinity of dislocations shown in Fig. 5.10(b). It can be seen that the gain dip extends around the dislocation position itself and is of a similar shape as the QW gain dip in Fig. 5.11(a), which correlates very well with the recent finding by Selvidge *et al.* that the impact radius of nonradiative recombination at a dislocation is larger than that of a single dot and may be affected by the wetting layer loss dynamics [211]. Since the ground state occupation drops only by about 10 % in these regions, the gain dip is substantially less pronounced, so that QDs around dislocations are still capable of providing a positive gain contribution in these simulations.

Figs. 5.12(a) and (b) show results of simulated QD and QW LI curves for device dimensions of 2×500 µm^2 at different ρ_{dis}. This alternative approach reproduces the ex-

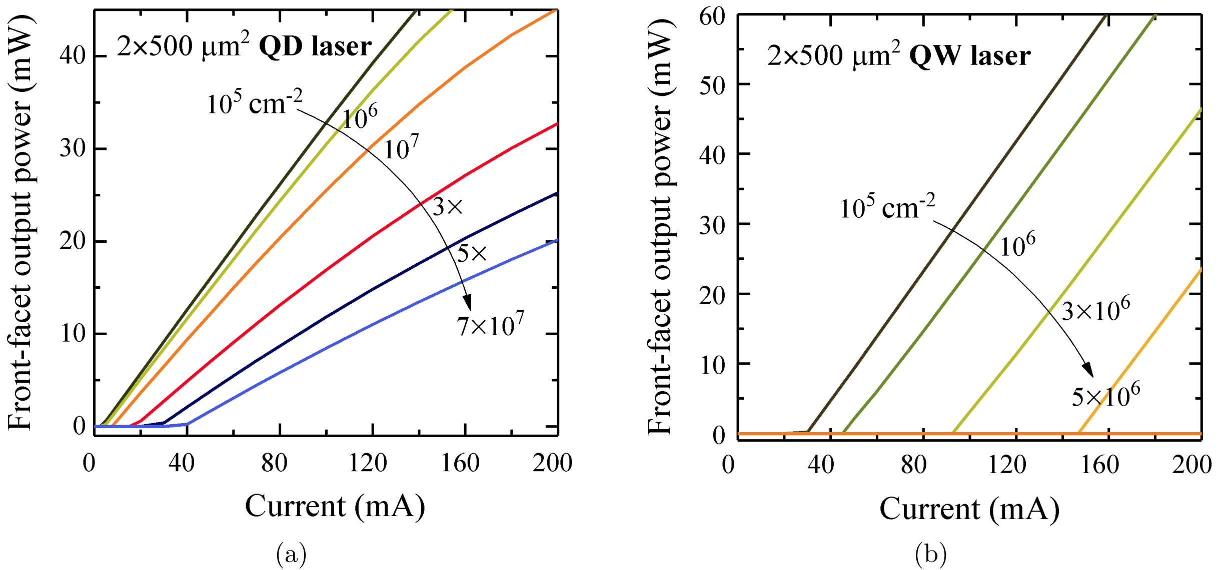

Figure 5.12: Simulated (a) QD laser and (b) QW laser LI characteristics for various dislocation densities ρ_{dis} using the parameters shown in Table 5.1 and the dislocation carrier loss vector τ_{dis} introducing nonradiative recombination centres at defined positions only.

perimentally observed trends [275, 276] very well and is, apart from minor deviations, also in qualitative agreement with the results from section 5.2. Compared with the previous *LI* simulations in Fig. 5.3(a) and Fig. 5.4(a), the dislocation range has to be kept slightly lower here (below $\sim 10^8$ cm^{-2}), as a 500 μm long laser with 1,000 laser sections of 500 nm allows only the introduction of a certain number of dislocation sections if the resolution is not to be further increased. In direct comparison, the threshold of both QW and QD laser in the high resolution approach increases faster compared with the effective simulation approach of section 5.2. The slope efficiency decrease is very similar though for this set of modelling parameters. This slightly different behaviour is not completely unexpected, as the high resolution simulation approach is capable of capturing local phenomena in the gain, carrier, and photon distribution that cannot be taken into account in the effective simulation approach with large Δz.

5.3.3 Discussion

Different from the simulations shown in section 5.2, where the reduced slope efficiency with higher dislocation density was solely a result of high carrier loss and thus a reduced injection efficiency, the *LI* slope reduction can here be explained as a result of two mechanisms.

The first one is the reduction in local gain around dislocations, since the photon density building up while propagating along the laser cavity experiences a slight drop in these regions. Hence, it can be understood intuitively that photons travelling along a laser cavity with many dislocations experience less amplification than photons in the presence of only a few dislocation-induced absorptive regions. This effect is primarily prevalent in QWs with their highly absorptive regions around dislocations, but it can largely be compensated by high gain in dislocation-free regions and is practically overshadowed by the rapid threshold current increase. Although this effect is not observed in QDs due to the still positive gain contribution around dislocations (Fig. 5.11(b)), it should be noted that QDs with their lower modal gain may be less able to compensate for locally reduced gain. From a slightly different view point, it is also worth noting that the threshold gain moving closer to the maximum ground state gain in dislocation-free regions may

introduce additional gain compression effects [310]. This might contribute to the damped character observed in directly modulated QD lasers on silicon [73, 356], which will be further discussed in the next two chapters.

The other contribution to the slope efficiency reduction is effectively the reduced current injection efficiency due to excess dislocation-induced carrier loss in the continuum states. As shown in Fig. 5.12(a), the QD *LI* slope begins to decrease substantially from $\rho_{dis} \gtrapprox 10^7$ cm^{-2}, where the barrier layer and wetting layer carrier densities have started to decrease to a level that makes sufficient carrier capture into the QDs problematic. This effect is more dominant in QD lasers, which allow lasing at higher dislocation densities in the first place, and is consistent with the results of section 5.2.

The second typical feature, the threshold current increase, can be explained by the overall carrier lifetime reduction, which is a well-known origin of a linearly shifted *LI* curve towards higher currents [143]. This is again in agreement with the results shown in the first half of this chapter. But whereas the performance dependence of monolithic III-V lasers on silicon on carrier diffusivity was the underlying assumption in section 5.2 and led thus naturally to a performance improvement by decreasing L_{diff}, this hypothesis can explicitly be confirmed in the high-resolution approach. Varying L_{diff} shows that lateral carrier diffusion is the key factor decreasing the QW performance by allowing diffusion-assisted barrier layer and QW carrier loss within a radius of several micrometres around a dislocation. It can be shown indeed that the QW laser performance is affected very little by dislocation-induced carrier loss if lateral carrier diffusion is 'switched off' completely. As already illustrated in Fig. 5.11(b), the detrimental impact of carrier diffusion in QD active regions, in contrast, is naturally much reduced due to rapid carrier capture into QDs, where the carriers are laterally confined and remain isolated from nearby dislocations [211]. For this reason, QD lasers require a much higher dislocation density than QWs to reduce the overall carrier density to a critical level where dislocation-induced carrier loss starts competing with QD carrier capture and thus increases the laser threshold more significantly.

The hypothesis that diffusion-assisted carrier loss in originally defect free regions is a major problem for QW lasers at elevated dislocation densities, even in the theoreti-

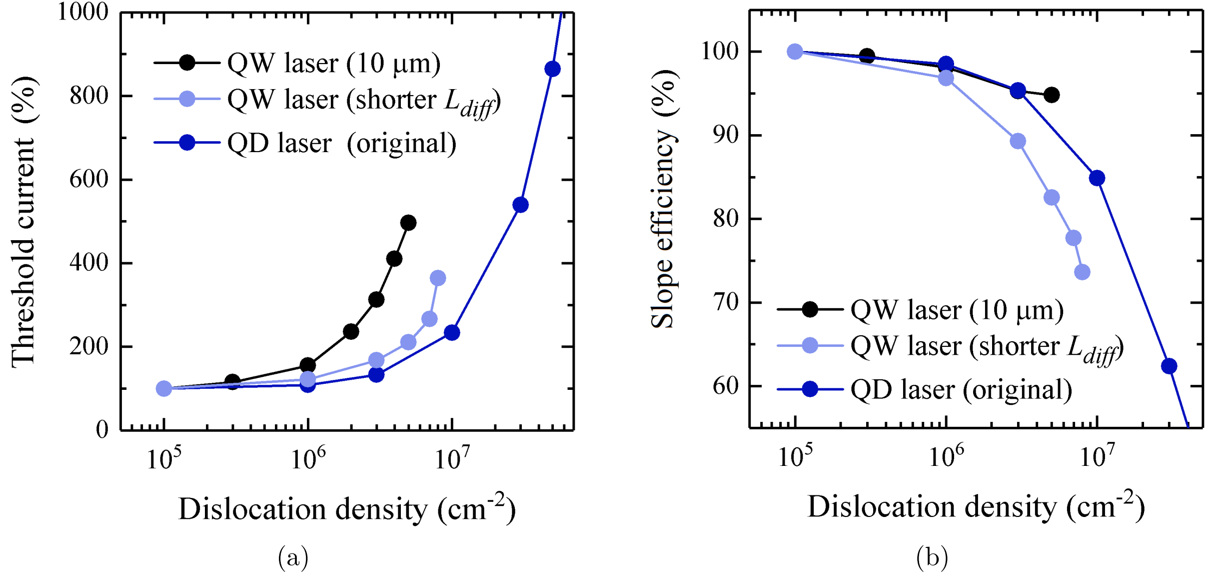

Figure 5.13: (a) Threshold current increase and (b) slope efficiency reduction against dislocation density. The original QW (black) and QD (dark blue) simulations are compared with QW calculations at $L_{diff}^{BL} = 5$ μm, $L_{diff}^{QW} = 1$ μm (light blue).

cal absence of dislocation climb, is supported by modelling QW structures at different diffusion lengths. As shown in Fig. 5.13(a), the QW threshold current increase with dislocation density is substantially reduced using shorter diffusion lengths of $L_{diff}^{BL} = 5$ μm and $L_{diff}^{QW} = 1$ μm, respectively, similar to what could be expected for the barrier layers and wetting layers in a QD laser, because fewer carriers are affected by dislocation-induced carrier loss. This observation is in agreement with early observations comparing the defect sensitivity of LEDs of different III-V compounds [337, 357] and with the performance demonstrated by GaN optical devices, for example, where the short minority carrier diffusion length is believed to play a key role in enabling high light emission efficiencies despite dislocation densities of up to 10^{10} cm^{-2} [352]. The calculations indicate that the point where the threshold current increases above 100 mA can be shifted from $\rho_{dis} \approx (3–4) \times 10^6$ cm^{-2} at the original diffusion length settings to about 8×10^6 cm^{-2} using the shorter diffusion lengths (compared with about 2×10^7 cm^{-2} in section 5.2), which may be sufficient for state-of-the-art III-V-on-Si growth technology. The modelled performance improvement is here somewhat smaller compared with what is shown in Fig. 5.5(b): a result of the different simulation approaches. The simulations indicate further that the smaller thresholds come at the expense of a higher slope reduction (Fig. 5.13(b)). This

is as carrier loss taking place in a more concentrated region seems to introduce a sharper drop in the local gain, which requires higher gain in dislocation-free regions, i.e. more carriers and thus a higher injection current to compensate for this.

One possible approach for reduced in-plane diffusion could be offered by utilising InP-based active regions, which exhibit reduced carrier diffusion and have traditionally shown longer lifetimes than GaAs-based QW lasers on silicon. The growth of InP on silicon is, however, also associated with a larger lattice constant mismatch [158, 159, 358]. Indeed, Shi *et al.* demonstrated recently room temperature cw lasing with 1.55 μm broad-area QW lasers grown on (001)Si. Although the devices had relatively high threshold current densities of around 2 kA/cm^{-2}, they still showed lasing operation at comparably high dislocation densities of $> 10^8$ cm^{-2} [359–361]. Another option worth exploring are gain-coupled DFB QW lasers [292], where a gain grating etched into the QWs might have a similar effect in terms of restricting carrier diffusion into defects just like QDs. For a first order gain grating with period $\Lambda = 137$ nm, the escape time component of carriers re-emitted from QW gain sections and subsequently migrating into dislocations could decrease the effective diffusion length to about 1 μm to 2 μm.

5.4 Chapter Summary

Two different approaches for modelling the impact of dislocations on the *LI* performance of III-V QW and QD lasers on silicon were presented. Both approaches, an effective one using a dislocation-dependent nonradiative lifetime averaged for the whole device as well as a high-resolution approach allowing the implementation of individual dislocations along the laser cavity, are capable of reproducing the experimental trends of increasing laser thresholds and decreasing slope efficiencies with rising dislocation density observed for QDs, and the tendency of high threshold currents in the case of QW-based lasers on silicon. The results point out that diffusion-assisted carrier migration into defects plays a major role in the functionality of QW and QD devices, affecting QW active regions more strongly than their QD counterparts. The first approach suggests a QW threshold current increase of more than 400 % from $\rho_{dis} = 10^4$ cm^{-2} to 10^7 cm^{-2}, whereas the QD

laser threshold rises insignificantly in this range. A more pronounced QD laser threshold increase is only observed from about $\rho_{dis} = 10^7$ cm^{-2}, which is, however, accompanied by a substantial reduction of the QD *LI* slope efficiency down to about 30 % of its original value at $\rho_{dis} = 10^4$ cm^{-2}. Additional simulations confirm that fast QD carrier capture and high energy barriers preventing carrier re-emission promote the QD laser's resilience to dislocation-induced carrier loss. The underlying assumptions leading to the results reported in this chapter are in agreement with recent findings by Buffolo *et al.*, who interpret a reduced current injection efficiency during dislocation growth as a result of enhanced carrier loss in the InGaAs wetting layer [339, 340].

The second approach confirms these trends, but produces a faster threshold current increase compared with the first approach: the QD laser threshold in section 5.2, for example, doubles only in the dislocation range from 10^6 cm^{-2} to 10^8 cm^{-2}, while in section 5.3 it already doubles from 10^6 cm^{-2} to 10^7 cm^{-2}, which appears to model experimental trends more realistically. While the effective approach in section 5.2 benefits from increased computational speed due to larger spatial steps Δz, the high-resolution approach of section 5.3 allows to investigate local phenomena in the gain, photon, and carrier distribution around dislocations, hence giving insight into mechanisms that are not observable using constant laser parameters averaged over the entire device. In particular, the finding that structures with short minority carrier diffusion lengths show a higher resilience to dislocations is used to identify InP-based devices with lower diffusivity or gain-coupled QW DFB lasers with reduced defect sensitivity as potential candidates to pave the way towards monolithically integrated high-gain QW lasers on silicon.

Chapter 6

Gain Switching of Quantum Dot Lasers on Silicon

As progress is being made minimising the impact of threading dislocations on the performance of heteroepitxial III-V QD lasers on silicon, research has begun to focus increasingly on demonstrating high-performance devices of greater relevance for industrial purposes. Data centre providers are scaling up their single-lane speeds from 25 Gb/s NRZ modulation to 40 Gb/s and 100 Gb/s PAM-4 modulation [2] and future PONs envision shared data rates of up to 50 Gb/s [362, 363]. So, the viability of QD lasers on silicon for such high-speed data transmission applications depends critically on their high-speed potential, whereas cost rather than performance might be the more dominant criterion in other types of communication links. In order to identify suitable application areas for heteroepitaxial 1.3 µm InAs/GaAs QD lasers on silicon, especially against the background that bandwidth capacity is one of the main selling points of silicon photonics, the logical consequence is to also investigate the high-frequency performance of 1.3 µm QD lasers on silicon.

This chapter will first review the present status of QD lasers on silicon in terms of their dynamic properties and then present the first results of gain-switched optical pulses generated using monolithic 1.3 µm InAs/GaAs QD lasers on silicon. Since the first studies on the modulation characteristics of such devices only became available in 2018 and theoretical studies are still sparse, the here presented results form the first part of

a rigorous analysis of the high-speed characteristics of monolithic QD lasers on silicon substrates through experiment and numerical simulations. Chapter 7 will then focus on the lasers' small-signal modulation characteristics.

6.1 Dynamic Performance Overview of Monolithic Quantum Dot Lasers on Silicon

Studies reporting on the dynamics of 1.3 μm QD lasers on silicon can be categorised into the fields of small-signal and large-signal modulation and optical pulse generation by means of gain switching and mode locking. Further research with respect to the laser dynamics concerns feedback sensitivity, linewidth enhancement, and relative intensity noise (RIN).

Gain switching

Gain switching is a simple technique for generating ultrafast optical pulses by modulating the optical gain through short, high-amplitude current pulses. The physical mechanism behind this is illustrated in Fig. 6.1, showing that the input electrical pulse (top) is timed in a manner that the carrier density does not reach the threshold level a second time after the damped periodic oscillation during the turn-on process have set in (middle). Stimulated emission of light is, consequently, stopped right after the first relaxation oscillation peak (bottom) [364, 365]. The advantage with respect to short optical pulse generation is that picosecond-short optical pulses can be achieved using nanosecond-long electrical input pulses. Typical optical pulse durations correspond to a few times the round-trip time in the cavity (such as a few 10 ps in a short cavity, for instance) and peak powers of tens to hundreds of Milliwatts [366].

Gain-switched optical pulses have a large frequency chirp as a result of the non-equilibrium current injection conditions [296, 364]. Although these chirped pulses offer potential for extra pulse compression [366–368] or optical frequency comb generation [369], they are not commonly used as directly modulated pulsed light source. Compared with other optical pulse generation mechanisms though, such as mode-locking or Q-switching,

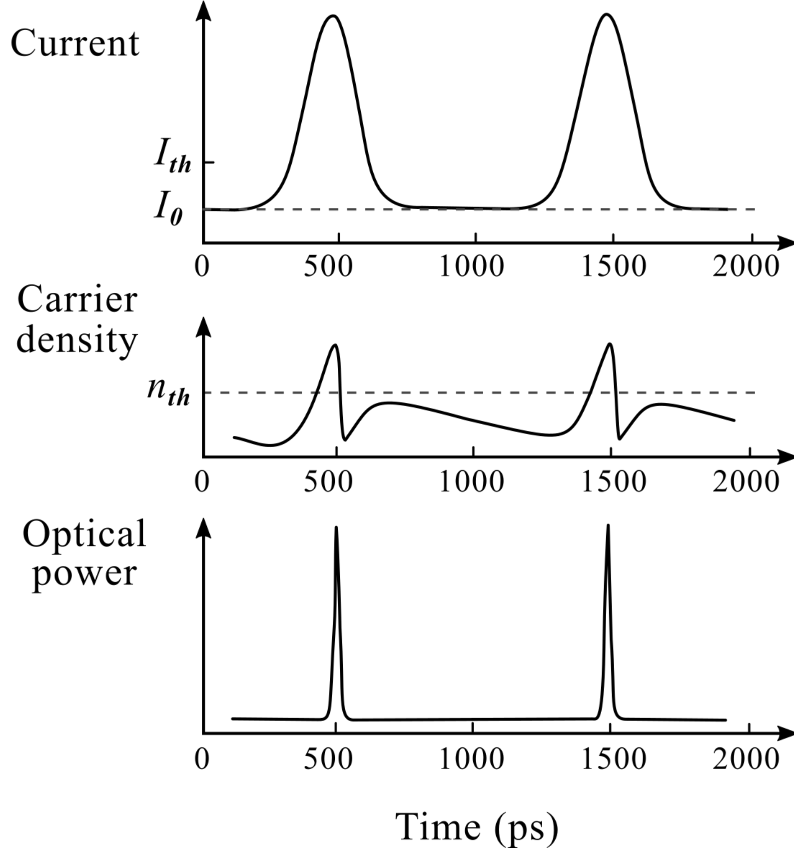

Figure 6.1: Temporal evolution of the carrier density (middle) and optical output power (bottom) under gain-switching current modulation (top) [364].

the benefit of gain switching lies in the simplicity of the approach, which allows to produce optical pulses with any kind of laser at variable repetition rates dictated by the current drive [370]. As a consequence, it finds also widespread interest outside communication applications, such as in time-resolved fluorescence spectroscopy and biological imaging [371, 372] or in seed lasers for high-power laser material processing [373, 374].

In the context of this dissertation, gain switching is, therefore, a very convenient means for obtaining first insights into the dynamics of a semiconductor laser under relaxed experimental conditions. The gain-switched pulses shown in this chapter are the first ones reported for monolithic 1.3 µm QD lasers on silicon [68, 75]. The shortest obtained pulses have durations of 150 ps and 175 ps with maximum peak powers of about 20 mW and 66 mW, respectively, and were measured using a 2.5 mm long narrow ridge-waveguide and a 3.1 mm long broad-area laser device. In 2019, Xue *et al.* at Hong Kong University have measured 50 ns long gain-switched pulses with 6 mW peak power using an uncoated

8×500 μm^2 1.3 μm InAs/InAlGaAs QD laser grown on InP/V-grooved (001)Si substrate, where the pulse width was limited by the electrical pulse generator [269]. Section 6.3 will further discuss how this compares to the results obtained in this work.

Mode-locking

Optical pulses generated by mode-locking offer the advantage of being independent of the relatively slow carrier injection dynamics of the QD active region. Mode-locked 1.3 μm QD lasers on silicon are, consequently, envisioned to be used as pulsed optical sources for next-generation high-capacity communication systems. The first mode-locked laser of this kind was reported in 2018 by Liu *et al.*, showing 1.3 ps short pulses and an 80 kHz narrow RF linewidth at a repetition rate of 9.1 GHz using a 4.5 mm long two-section device. [331]. Auth *et al.* have analysed the pulse time and amplitude jitter of a similar device, reporting ultra-stable operation with a minimum time jitter of 9 fs and a broad emission range where the amplitude jitter is below 1 % [375, 376]. Furthermore, self-mode-locking with 490 fs short pulses and a 100 kHz narrow RF linewidth at a repetition rate of 31 GHz was produced by a 1.33 mm short single-section device [272].

More recently, high-performance devices have been tested with a focus on their data transmission potential. Liu and Wu *et al.* have demonstrated a total data transmission capacity of 0.9 Tb/s using eight channels of a 100 GHz fifth harmonic mode-locked laser in a WDM system, where each line is PAM-4-modulated to carry 112 Gb/s of data in a back-to-back configuration [377]. They have further improved these results towards 4.1 Tb/s data transmission using 64 lines of a high-channel-count 20 GHz passively mode-locked laser. In addition, they also measure a very low RF linewidth of 1.8 kHz [245]. At this still early stage of research, QD lasers on silicon compare very well with the best results achieved on native substrates, a pulse width of 360 fs [378] and an RF linewidth of 500 kHz [379], and show great potential for the data- and telecommunication market.

Except in [380], where Chow has presented an analysis of the 490 fs self-mode-locked pulses at the 2019 IEEE Summer Topical Meetings Series, none of the above results have been analysed theoretically yet. Similar work on mode-locked QD lasers on silicon is known to be in progress at UCL as well.

Small-signal and large-signal modulation

Besides the results presented in this thesis and published in [69] and [75], the only results of modulation experiments at the time of writing have been reported by Inoue *et al.* from the Tokyo Institute of Technology in collaboration with UCSB [381, 382] and Shang *et al.* from UCSB [171]. The so far maximum reported 3dB bandwidth of 6.5 GHz has been achieved using an HR-coated 580 µm long device with *p*-modulation-doped active region for higher gain [381], while $f_{3dB} = 5.8$ GHz was realised using an as-cleaved 1.45 mm long undoped device with optimised probing pads [171]. Back-to-back NRZ data transmission of 12.5 Gb/s and PAM-4 modulation of 25 Gb/s have also been demonstrated using short *p*-doped lasers [381, 382]. Fig. 6.2 shows an overview of 3dB modulation bandwidths of 1.3 µm InAs/GaAs QD lasers grown on native substrates for comparison. The values are plotted against the cavity length L to account for the fact that $f_{3dB} \propto 1/K \propto 1/\tau_{ph}$,

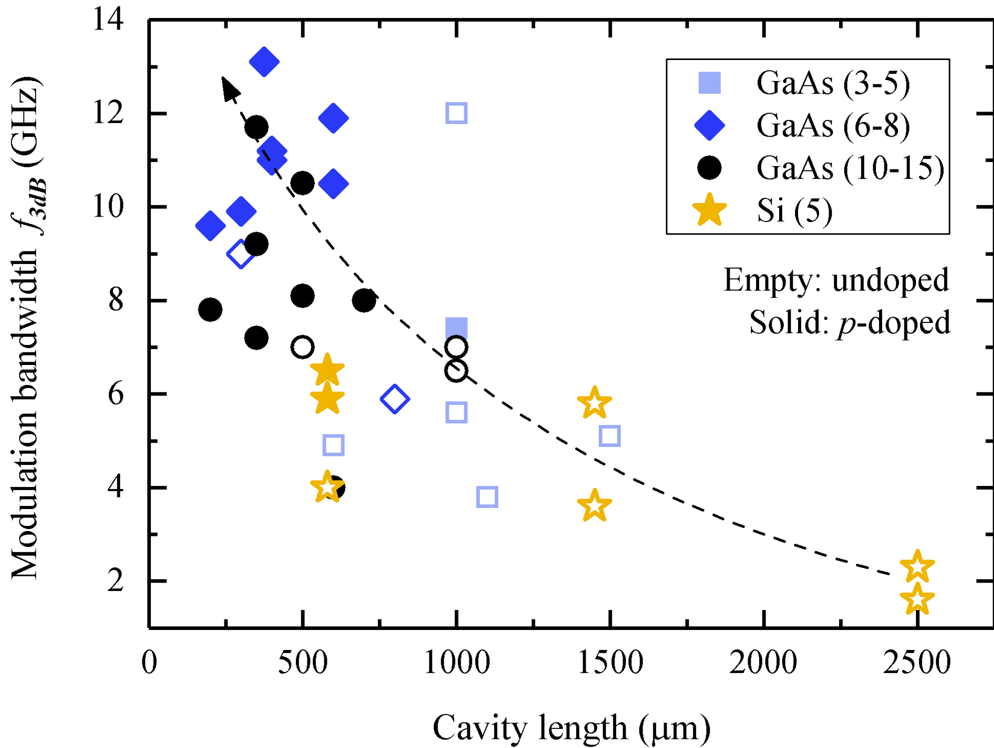

Figure 6.2: Overview of the small-signal modulation performance of 1.3 µm FP-type InAs/GaAs QD lasers operating under cw mode at room temperature. Devices operating based on tunnel injection are not included. QD lasers grown on GaAs substrate are shown in light blue to black by the number of active QD layers. The fastest bandwidth achieved with such a type of laser is 13.1 GHz [128]. QD lasers grown on silicon are shown in yellow and have all five QD layers.

where the photon lifetime τ_{ph} depends on L through the mirror loss $\alpha_m \propto 1/L$, as outlined in chapter 2. It can be seen that directly modulated 1.3 μm QD lasers on silicon have clearly not reached their full potential yet, as there is plenty of room for improvements in terms of the cavity length and the number of QD layer design. A more detailed discussion on the direct modulation properties will follow in chapter 7.

Feedback sensitivity and linewidth enhancement

Based on their low linewidth enhancement factor, strongly damped relaxation oscillations, and higher K-factors, QD lasers are predicted to exhibit a higher critical feedback level than QWs. For QD lasers on silicon, this was first investigated by Liu *et al.* at UCSB, who obtained a 20 dB reduced sensitivity to optical feedback compared with a heterogeneous QW device [274]. A near-zero linewidth enhancement factor of 1.3 μm QD lasers on silicon has been reported in [293, 383–385]. Researchers at the Institut Polytechnique de Paris who have performed measurements on devices from UCSB stress further that the reduced carrier lifetime due to the high number of dislocations in the active region contributes additionally to the increased feedback tolerance. [273, 385, 386]. In this context, Duan *et al.* have also measured an exceptionally high K-factor of 4.7 ns [356], whereas K-factors of comparable InAs/GaAs QD lasers on native substrate are typically around 1 ns [381].

Relative intensity noise

Very low RIN of < 150 dB/Hz has been reported by Liao *et al.* at UCL using a 2.5 mm long QD laser on silicon. This is a promising result indicating suitability as externally modulated light source in communication systems. They also extract strongly damped relaxation oscillation frequencies between 1 GHz and 3 GHz from their RIN data [133]. Duan *et al.* show a maximum resonance frequency of about 2.7 GHz in their RIN data analysis in [356] using a 1.1 mm long device.

6.2 Epitaxial Design of the Tested Lasers

The InAs/GaAs QD laser structures used for the experiments presented in this dissertation are grown on (001)Si substrates with 4° misorientation towards the [011] plane to avoid

the formation of APDs. Initially, a thin AlAs nucleation layer is grown to prevent the formation of three-dimensional islands at the strained interface [224]. This is followed by a 1 µm thick GaAs buffer grown in a multi-temperature-step process and a set of defect filter layers consisting of four sets of InGaAs/GaAs strained-layer superlattices, each containing five repeats of 10 nm $In_{0.18}Ga_{0.82}As$/10 nm GaAs strained-layer superlattices and 300 nm GaAs spacers. The resulting GaAs pseudo-substrate has a dislocation density of the order of 10^5 cm^{-2}.

The III-V laser structure comprises 1.4 µm *n*- and *p*-doped GaAs cladding layers sandwiching the undoped active region. The active layers are embedded in the middle of a 140 nm GaAs waveguide, consisting of five DWELL layers with the InAs QDs embedded in 8 nm thick $In_{0.15}Ga_{0.85}As$ QWs and spaced by 45 nm (narrow ridge-waveguide devices) or 50 nm thick GaAs barrier layers (broad-area devices). The dot density is approximately 3×10^{10} cm^{-2}. A 300 nm highly *p*-doped contact layer completes the epitaxial structure.

Two different types of devices are investigated. The first one is a basic broad-area design as shown in Fig. 6.3(a) from one of the earlier device generations (∼2015) with a

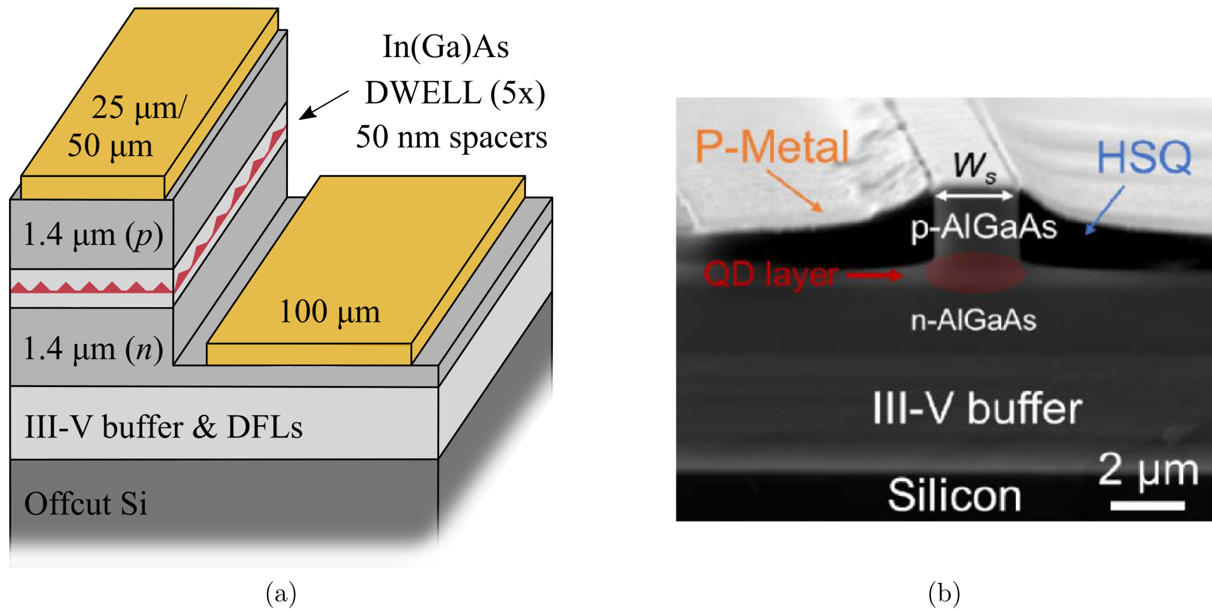

Figure 6.3: (a) Schematic epitaxial structure of the 1.3 µm InAs/GaAs QD lasers on silicon substrate in a broad-area laser design. (b) Scanning electron microscope image showing the side view of a QD laser on silicon in a narrow ridge-waveguide design with as-cleaved front facet [133].

cavity length of 3.1 mm and a waveguide width of 50 µm. The *p* and *n*-type electrical contacts are made from a titanium/platinum/gold and a nickel/gold-germanium/gold composition, respectively. The mirror-like semiconductor facets are left as-cleaved. The laser bar is thinned to about 120 µm to facilitate cleaving into bars and is mounted on a copper heatsink as well as contacted using wire bonds. Top view optical microscope images of the fabricated devices can be seen in Fig. 6.4(a) and (b). The second device type is a 2.2 µm narrow ridge-waveguide Fabry-Pérot laser with cavity length of 2.5 mm, as shown in Fig. 6.3(b), obtained at a later point. Apart from the laser design, the main differences to the first laser type are only the additional high-reflection (HR) coating at the rear facet and that the laser is probed directly rather than via bonding pads (Fig. 6.4(c)). Further information on the growth conditions and the device design can be found in [13] and [133].

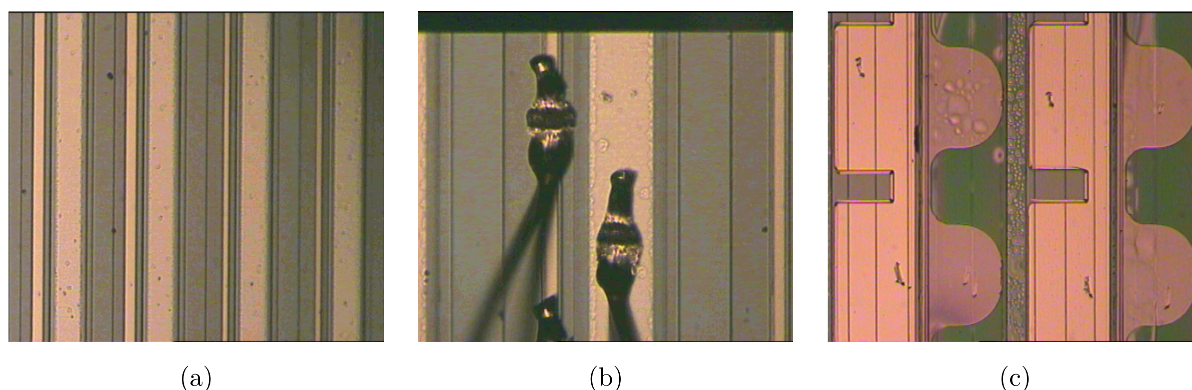

(a) (b) (c)

Figure 6.4: Optical microscope images of the broad-area and narrow ridge-waveguide lasers shown in Fig. 6.3. (a) Top view of the broad-area device (Fig. 6.3(a)). The broad stripes are the 100 µm *n* contacts, whereas the narrower stripes to its left are 25 µm or 50 µm *p* contacts. (b) Example of a wire-bonded broad-area device. (c) Top view of narrow ridge-waveguide lasers (Fig. 6.3(b)) with rectangular *n*-type pads to the left and round *p*-type pads to the right.

6.3 Experimental Methods and Results

For the static characterization, the lasers are operated under cw current injection at room temperature with the heat sink temperature set to 15 °C or 18 °C, respectively. The *LI* curves of both devices can be seen in Figs. 6.5(a) and (b). Under these conditions, the

broad-area laser shows a threshold current of 168 mA (108.4 A/cm^2) and a low forward resistance of 2.5 Ω. The low threshold current density in a broad-area design without any current confinement is an indication of the high epitaxial material quality [89]. The narrow ridge-waveguide laser shows a lower absolute threshold current of 15 mA (272.7 A/cm^2) due to the smaller pump area and a doubled slope efficiency due to the higher optical feedback at the rear facet. The forward resistance is about ten times that of the broad-area laser (21.3 Ω), although ideally no major changes in R_S should be observed. The multimode spectra of both devices are shown in Figs. 6.5(c) and (d).

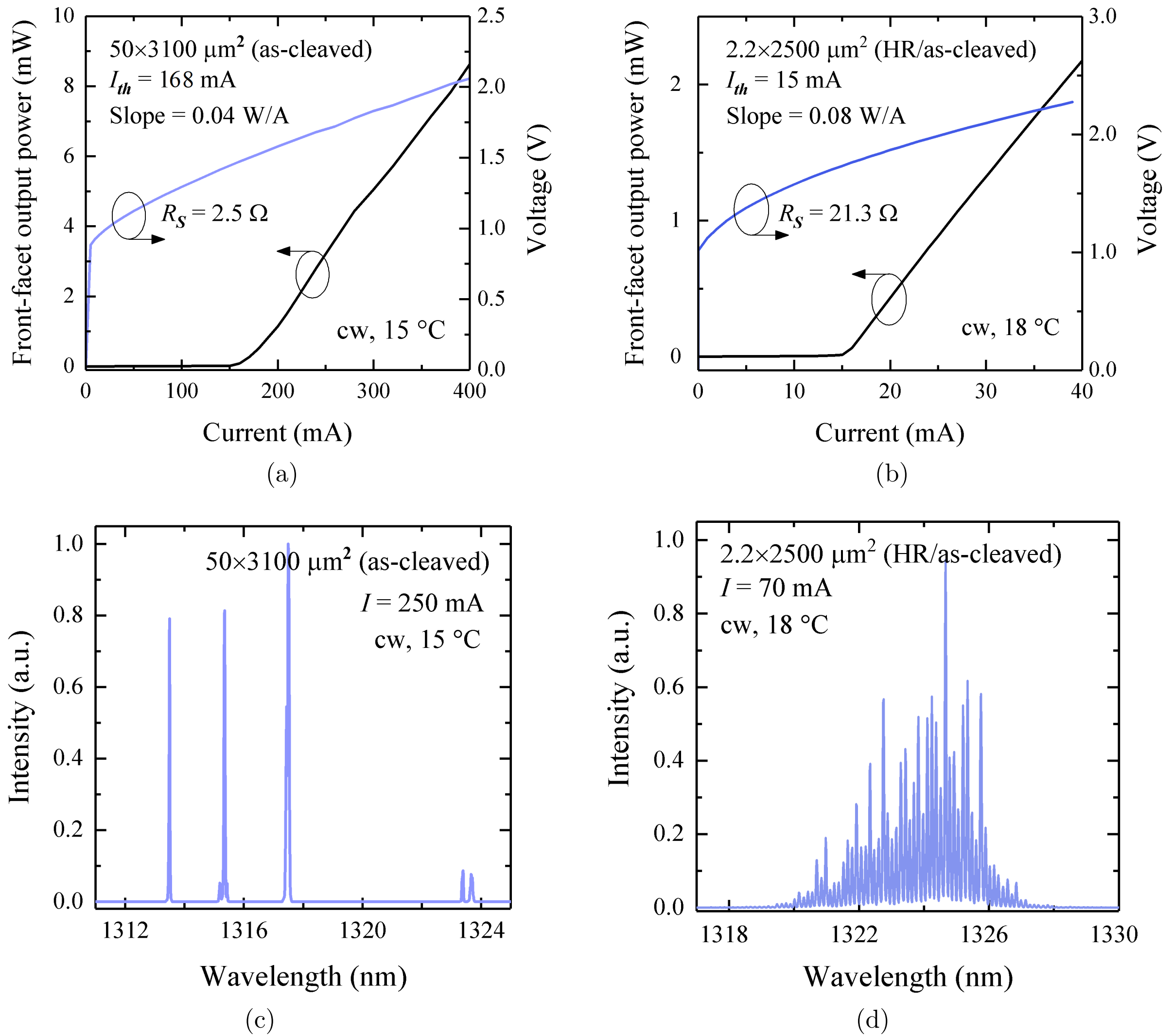

Figure 6.5: *LI* characteristics of the (a) 50 μm × 3.1 mm QD broad-area laser and (b) 2.2 μm × 2.5 mm narrow ridge-waveguide QD laser on silicon operated under cw conditions at heat sink temperatures of 15 °C and 18 °C, respectively. (c) Multimode laser spectra of the broad-area and (d) narrow ridge-waveguide laser, respectively.

The gain switching experiments are performed using a circuit producing a nanosecond long electrical pulse of variable amplitude and duration without prebias to drive the QD laser at a frequency of 100 kHz or 1 MHz. The exact amplitude and pulse duration can be adjusted to generate the shortest possible optical pulse, which is then observed on an

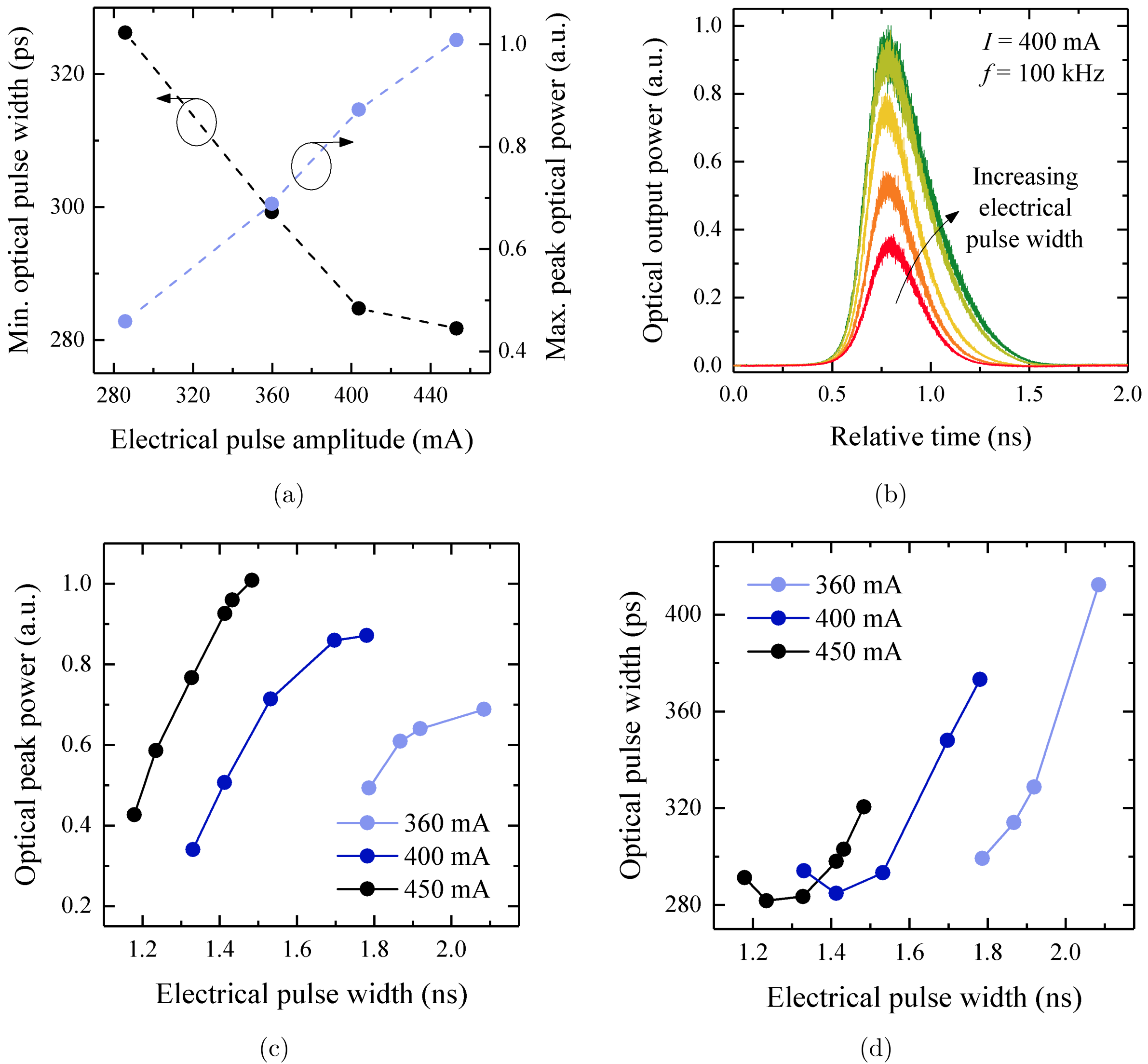

Figure 6.6: Gain switching characteristics of the 50 × 3100 μm^2 broad-area laser at 100 kHz. (a) Minimum optical pulse width and maximum peak optical power against the drive pulse amplitude. (b) Series of gain-switched optical pulses obtained for increasing electrical pulse widths. (c) Peak optical power against current pulse width for three different current amplitudes. (d) Optical pulse width against current pulse width for the same three current amplitudes. The experiments are performed at lower currents than those in Fig. 6.7(a) as the then available probe included a 50 Ω resistor, which restricted the current pulse magnitude.

oscilloscope. A study on the dependence of the optical pulse power and duration on the electrical pulse amplitude and duration, performed using the broad-area device, confirms the behaviour that would be expected for a gain-switched semiconductor laser. Fig. 6.6(a) shows that the shortest optical pulse duration is achieved as the electrical pulse amplitude increases, while the optical power increases with rising electrical pulse amplitude. The peak optical power can be maximised by increasing the current pulse width for a given peak current, as illustrated in Figs. 6.6(b) and (c). Conversely, the optical pulse duration tends to be shortest for shorter electrical input pulses, but depends on the exact operation point of the laser, as can be seen in Fig. 6.6(d). A too narrow drive pulse does not contain sufficient carriers to switch on the laser powerfully enough to obtain a sharp gain-switched pulse, whereas an excessively long drive pulse results in a broadening of the gain-switched pulse due to surplus carrier injection.

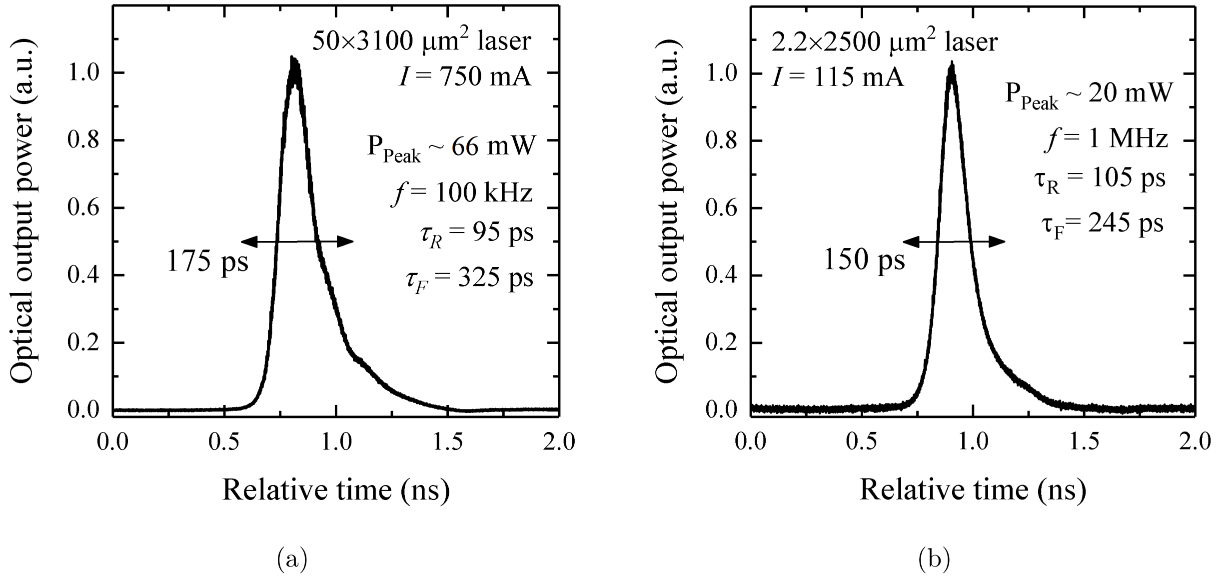

Figure 6.7: Shortest gain-switched optical pulses generated by the (a) 50 × 3100 μm² broad-area laser and the (b) 2.2 × 2500 μm² narrow ridge-waveguide laser.

For the broad-area device, the shortest optical pulse FWHM (from here on denoted as pulse width or duration $\Delta\tau$) of 175 ps is obtained using a high current amplitude of 750 mA. An example of the measured pulse is shown in Fig. 6.7(a). From the measurement of the average optical power P_{av} of the signal using a large-area detector, a peak optical

power P_{peak} of about 66 mW is estimated using

$$\frac{T}{\Delta\tau} P_{av} = P_{peak} \ , \tag{6.1}$$

where $\Delta\tau$ is the gain-switched pulse width and $T = 1/f$ is the duration inferred from the inverse pulse repetition rate. While the pulse rise times τ_R, defined as the duration from 10 % to 90 % of the optical power and vice versa for the fall time, of the shortest obtained pulses are about 95 ps to 140 ps, their longer fall times τ_F of typically 300 ps to 340 ps limit the pulse width. These sorts of exponential trailing edges are quite common for gain-switched pulses [364, 387]. For the 3.1 mm laser length and a resulting round-trip time of approximately 74 ps, the shortest measured pulse width corresponds to a about two and a half cavity round-trip times.

The narrow ridge-waveguide laser, in comparison, tends to show slightly shorter pulse durations ($\Delta\tau_{min}$ = 150 ps) and fall times, but the general pulse dynamics remain unchanged. Physically, the slightly better performance of the narrow ridge-waveguide laser is not unexpected, because of the better electrical and optical confinement in the single-transverse mode ridge-waveguide. In the 50 μm broad-area waveguide, in contrast, contributions from individual transverse modes are unlikely to build up simultaneously, which leads to a pulse broadening and a lengthening of the trailing edge. The narrow ridge-waveguide laser's gain-switched peak power of about 20 mW, almost one third of what has been achieved for the much larger broad-area laser despite the smaller area (2.2×2500 μm^2 versus 50×3100 μm^2), is also a strong indication of the higher efficiency of the narrow ridge-waveguide laser structure.

Compared with the pulse widths of shorter high-gain QW or bulk lasers of 10 ps to 15 ps [366, 387, 388], the pulses produced by the monolithic QD lasers on silicon substrates are one order of magnitude longer, which is assumed to be a result of lower gain and the longer cavity necessary to compensate for that. Xue *et al.*'s 50 ns gain-switched pulses of 1.3 μm InAs/InP QD lasers on silicon do not allow a fair comparison here due to the current pulse limitation (T_P^{min} = 100 ns) of the drive circuit. However, gain-switched pulse durations of 1.5 ns (i.e. a factor of 10 longer than the shortest pulses presented in

this work) were reported in early 2020 using 10×500 μm^2 InP-based 1.55 μm QW lasers without any facet coatings prebiased at 100 mA [361]. Considering the principally higher QW gain and the shorter photon lifetime, which is estimated to be about 12 ps, this shows that silicon-based InGa/GaAs QD are already relatively well developed compared with other types of III-V lasers grown on silicon. No laser design optimisation has been performed with the devices in this dissertation, so it is also expected to measure shorter pulses by increasing the number of active layers and optimizing the cavity layout for operation at a shorter length [366].

6.4 Simulation Results

In order to gain insight into the underlying physics of the dynamic properties of monolithic QD lasers on silicon substrates, the travelling-wave rate equation model from chapter 4 is used to simulate the experiments. The model was originally used as a three-level model only (i.e. excluding the barrier layer carriers, as shown below), which is a common simplification due to the negligible impact of the barrier layer dynamics, especially considering the potentially high epitaxial material quality of the tested QD lasers on silicon.

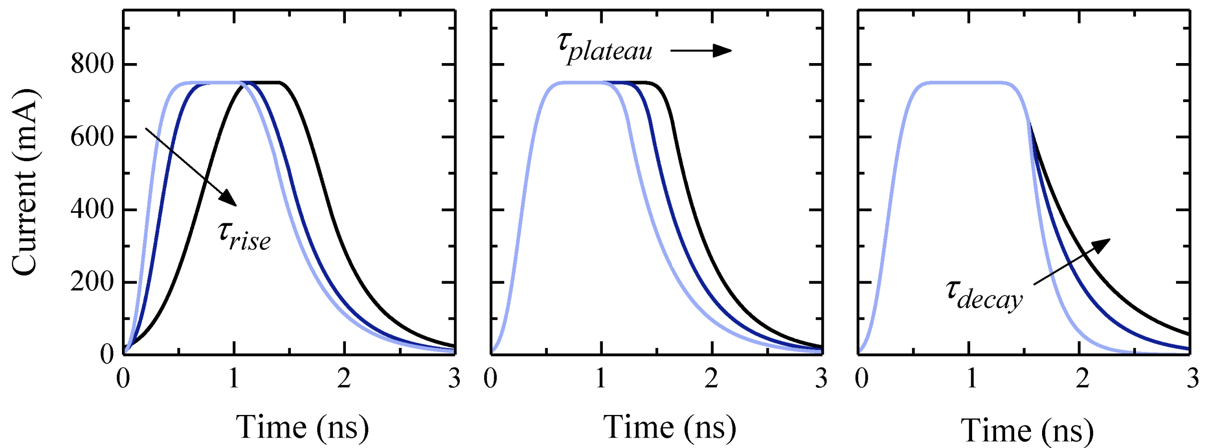

Figure 6.8: Examples of simulated super-Gaussian current pulses with varying current pulse rise times (left, tailored via the curvature of the super-Gaussian pulse), plateau lengths (middle), and exponential decay times (right).

$$\frac{\partial N_{WL}}{\partial t} = \frac{\eta I_P(t)}{e}\frac{\Delta z}{L} - \frac{N_{WL} f'_{ES}}{\tau^{QD}_{cap}} + \frac{N_{ES}}{\tau^{ES}_{esc}} - \frac{N_{WL}}{\tau^{WL}_{nr}} \tag{6.2}$$

$$\frac{\partial N_{ES}}{\partial t} = \frac{N_{WL} f'_{ES}}{\tau^{QD}_{cap}} - \frac{N_{ES} f'_{GS}}{\tau^{QD}_{rlx}} + \frac{N_{GS} f'_{ES}}{\tau^{GS}_{esc}} - \frac{N_{ES}}{\tau^{ES}_{esc}} - \frac{N_{ES}}{\tau^{ES}_{nr}} \tag{6.3}$$

$$\frac{\partial N_{GS}}{\partial t} = \frac{N_{ES} f'_{GS}}{\tau^{QD}_{rlx}} - \frac{N_{GS} f'_{ES}}{\tau^{GS}_{esc}} - \frac{N_{GS}}{\tau^{GS}_{nr}} - v_{gr} g_{QD} S \frac{\Delta z V_{QD}}{L} \tag{6.4}$$

A super-Gaussian current pulse

$$I_P(t) = I \exp\left(-\frac{t}{T_p}\right)^{2m} \quad , \tag{6.5}$$

where I, T_p, and m are the current pulse amplitude, the current pulse duration, and a parameter defining the curvature of the pulse, can be used to model a realistic input source [144]. Fig. 6.8 illustrates how the simulation input pulse can be adjusted to account for various electrical pulse shapes. Additional features can be implemented, so that it is possible to vary m separately for the rising edge (Fig. 6.8(a)), to adjust the pulse duration by

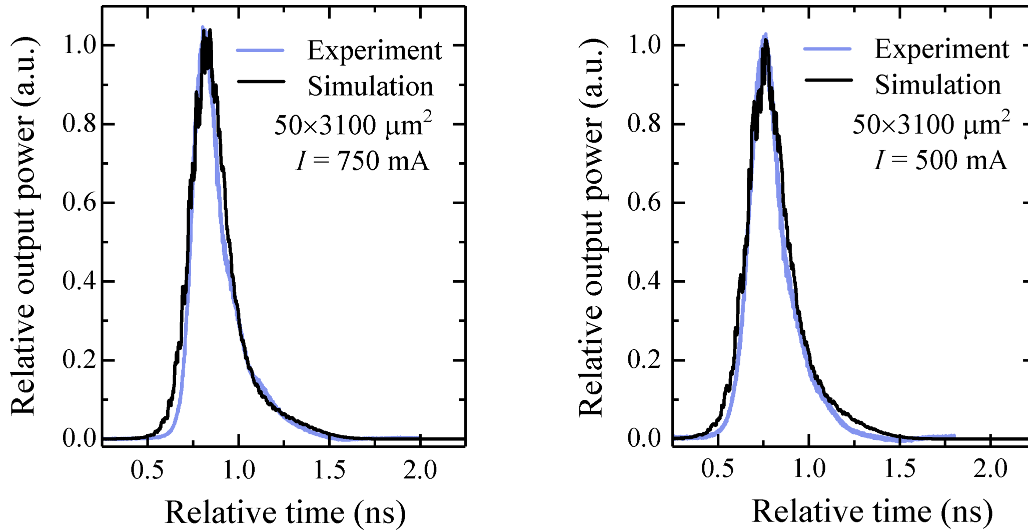

Figure 6.9: Modelled gain-switched pulses (black) using the parameters shown in Table 6.1 in comparison to experimental pulses (light blue) obtained at 750 mA (left) and 500 mA (right). Super-Gaussian current pulses with an exponentially decaying trailing edge are used to account for the imperfections of a realistic input source.

including a pulse plateau of variable time (Fig. 6.8(b)), and to elongate the pulse fall time using an exponentially decaying trailing edge (Fig. 6.8(c)). The simulation programme is then run multiple times in a loop to calculate averaged gain-switched pulses, similarly to what can be observed on the oscilloscope. Using MATLAB's loop parallelisation option, 16 pulses, for instance, can be calculated and averaged at only fourfold increased computational time.

Fig. 6.9 shows simulations of the broad-area laser's gain-switched pulses at current pulse amplitudes of 500 mA and 750 mA in comparison with the experimentally obtained pulses. At both current settings, the modelled pulses model the dynamics of their experimental counterparts well. The fitting parameters, which are summarised in Table 6.1, reproduce also the dependencies of optical peak power on the electrical pulse duration (Fig. 6.10(a)) and on the electrical current pulse amplitude (Fig. 6.10(b)). In Fig. 6.10(c) it can be seen that when varying the current pulse amplitude under fixed current pulse durations, the optical pulse power falls to only 3 mW at $I = 450$ mW, as the number of injected carriers is not sufficient to reach peak maximum power. Fig. 6.10(d) illustrates the extra duration necessary for each input current to achieve its maximum gain-switched peak power, which is in agreement with the experimental trend from Fig. 6.6(c) showing that lower injection currents require longer electrical pulse widths. The dependence of the optical pulse duration on the width of the electrical input pulse can also be modelled qualitatively, although the model tends to underestimate the optical pulse duration, as extra carriers from electrical back reflections at connectors because of a possible impedance mismatch are not considered in the simulations [389]. While the fitting parameters generally resemble those of standard InAs/GaAs QD lasers on native substrates, it is worth pointing out the following parameter findings.

1. The injection efficiency $\eta = 0.25$ is unusually low. Despite what would be expected for a QD laser on silicon with low dislocation density of 10^5 cm^{-2}, this could be a result of dislocation-induced carrier loss, translated into the reduced injection efficiency. Practically, however, this could also be the result of non-ideal metal contacts, inhomogeneous pumping, or filamentation in the broad-area structure.
2. The modelled carrier lifetimes are only slightly shorter than average values (~1 ns).

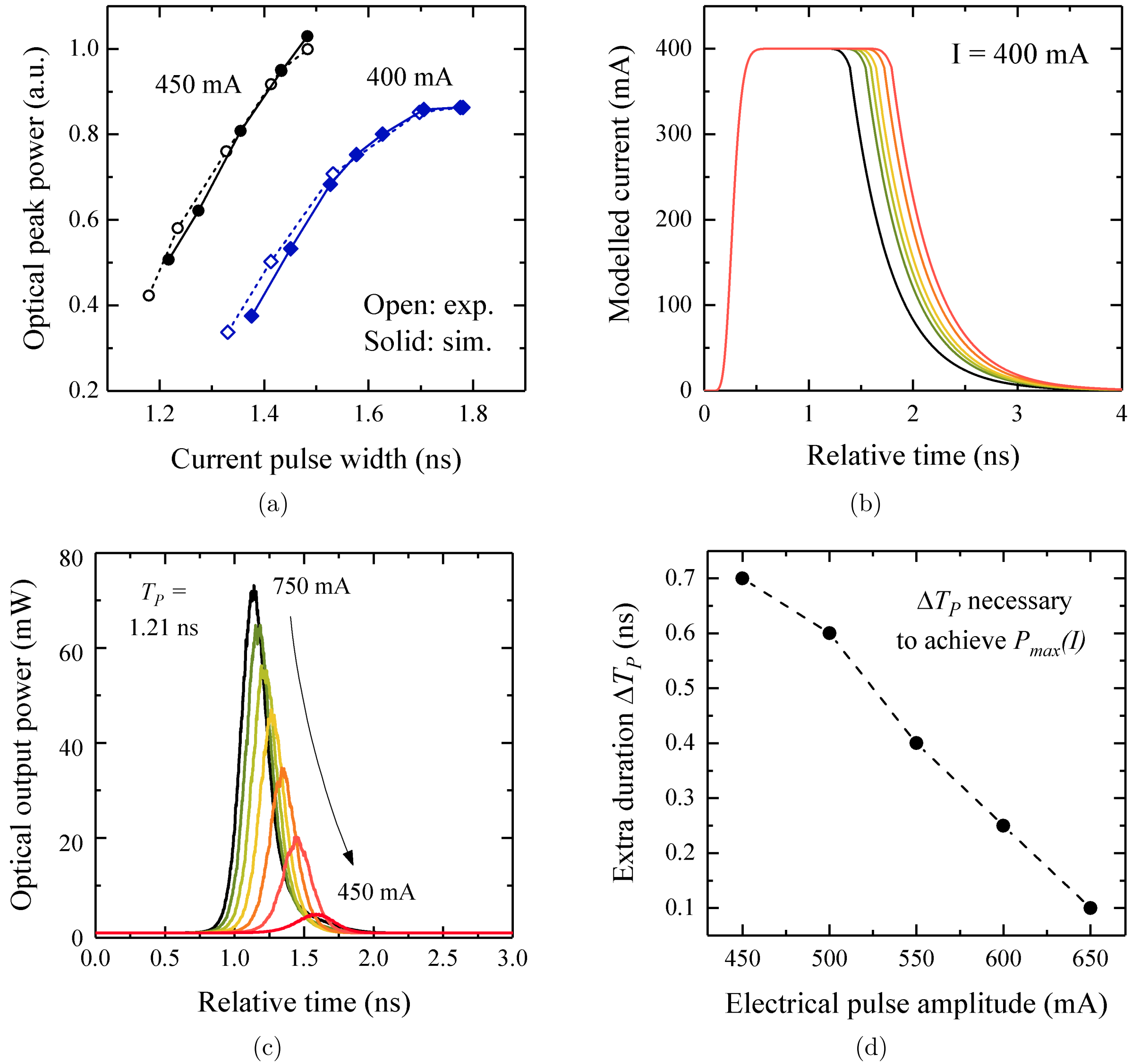

Figure 6.10: (a) Simulations of the dependence of the optical peak power on the current pulse duration using the examples of input currents of 400 mA and 450 mA. (b) Example of the simulation current input pulses at 400 mA used in Fig. 6.10(a). (c) Modelled pulses illustrating the dependence of the gain-switched pulse amplitude on the electrical input pulse amplitude. For an unchanged current pulse duration, the optical peak falls approximately linearly with decreasing electrical pulse amplitude. (d) Additional electrical pulse length required to achieve maximum pulse power at the current pulse amplitudes from Fig. 6.10(c).

3. The optical loss $\alpha_i = 3$ cm^{-1} is actually quite low, contrary to what was initially expected for monolithic QD lasers on silicon.

4. The gain compression factor $\epsilon = 9{\times}10^{-16}$ cm^3 is very high, even for a QD laser. This will be discussed below in more detail.

5. The exact QD carrier dynamics such as the QD carrier capture time τ_{cap}^{QD} and the relaxation time τ_{rlx}^{QD} are insignificant at the time scales investigated in this and the following chapter.

The fact that hardly any of these parameters have been investigated for silicon-based QD lasers highlights the importance of performing detailed measurements supported by numerical modelling for laser parameter extraction.

$L = 3.1$ mm	Cavity length
$w = 50$ µm	Waveguide width
$\Delta z = 10$ µm	Spatial step size
$N_{layers} = 5$	Number of active layers
$R_{1,2} = 0.33$	Rear and front facet reflectivity
$h_{WL} = 8$ nm	WL thickness
$\rho_{dots} = 2.5\times10^{10}$ cm^{-2}	QD density
$\Gamma = 0.0005$	Confinement factor
$g_{mod} = 20.5$ cm^{-1}	Modal gain
$f_{GS}^{h} = 0.5$	GS hole occupation probability
$\epsilon = 9\times10^{-16}$ cm^{3}	Gain compression factor
$\alpha_i = 3$ cm^{-1}	Optical waveguide loss
$\eta = 0.25$	Current injection efficiency
$\tau_{nr}^{GS,ES} = 0.8$ ns, 0.8 ns	GS, ES nonradiative lifetime
$\tau_{nr}^{GS,ES,WL} = 0.5$ ns	WL nonradiative lifetime
$\tau_{cap}^{QD} = 1$ ps	Carrier capture time into QDs
$\tau_{rlx}^{QD} = 0.5$ ps	Intradot relaxation time

Table 6.1: Overview of the used simulation parameters to model the broad-area laser gain-switched pulses.

In seeking to fit the theory to experimental measurement, two key parameters have been found to be particularly important. Specifically, a lower modal gain g_{mod} and a very high gain compression factor ϵ are the parameters that principally contribute to

a slower pulse rise time and a longer pulse duration. These also limit the high-speed performance of QD lasers in general. In particular, the high gain compression factor $\epsilon = 9 \times 10^{-16}$ cm^3 causes a broadening of the pulse and a slowly decaying trailing edge, reflecting gain saturation and carrier transport effects as well as contributions from multi-transverse and multi-longitudinal mode operation [143, 390, 391]. ϵ is here not only more than one order of magnitude higher than typical QW gain compression factors [390], but would be very high for conventional QD lasers on native substrates as well. Although QD gain compression factors in the wide range of 1×10^{-16} cm^3 to 5×10^{-15} cm^3 have been reported [392], most QD devices' gain compression factors take on values between around $(1-5) \times 10^{-16}$ cm^3 [150, 310, 392, 393]. The broadening of the gain-switched pulse is illustrated in Fig. 6.11(a), where a simulated optical pulse is plotted for two different values of ϵ.

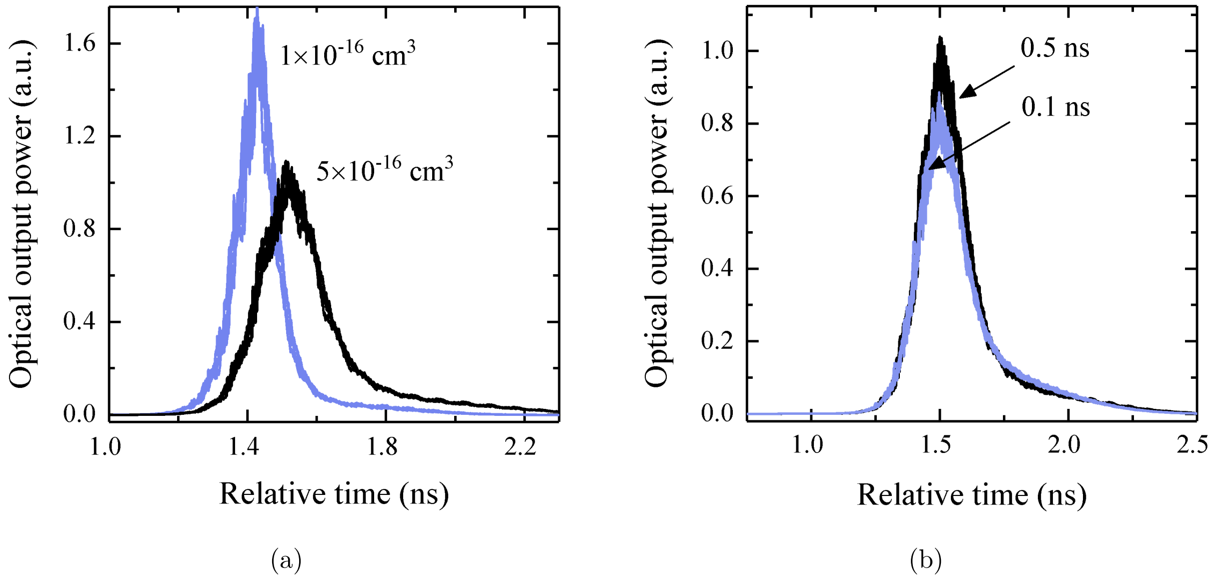

Figure 6.11: Simulations of gain-switched pulses demonstrating the impact of (a) the gain compression factor ϵ and (b) the wetting layer lifetime τ_{nr}^{WL} on the pulse dynamics. Besides reducing the pulse power, high gain compression also lengthens the transient time constants significantly (for example, a 70 % longer pulse duration, a 50 % longer rise time, and a 100 % longer fall time).

For the simulation of the broad-area laser's *LI* curve under cw injection, a lower modal gain of about 14 cm^{-1} yields a good match with the experimental result. However, a higher value is required when modelling the laser performance in pulsed operation. To

simulate the measured gain-switched pulses, a modal gain of the order of 20 cm^{-1} is needed to reproduce the experimental pulse rise times. However, it is important to bear in mind that the transverse variations occurring over the width of the 50 μm waveguides in the local gain, the carrier density, and the photon density, may allow for substantial variations in the observed device performance, and thus in the associated simulation parameters [279, 394].

6.5 Discussion

While some laser parameters are very difficult to influence, for instance gain compression effects resulting from carrier transport through the thick (and sometimes undoped) active region or the moderate QD density of the large InAs dots required for emission at 1.3 μm [395], others are more readily tailored through changes in the laser design or the growth technique.

A first practical means of shortening the optical pulse duration and its peak amplitude is applying a DC prebias I_{DC} or prebias pulse. The prebias level needs to be optimised with respect to the laser threshold and the electrical pulse amplitude to be superimposed [370]. For $I_{DC} > I_{th}$, the optical peak power can degrade as the gain and the carriers are clamped at threshold and it is difficult to achieve a high carrier overshoot for the rapid onset of stimulated emission at this point [387]. The largest improvements are usually observed for sub-threshold values of I_{DC} [370], although amplified spontaneous emission can likewise be undesired, for instance when deploying gain-switched laser diodes as high-power seed lasers [396]. The fact that no prebias has been applied in the here shown experiments is not a major issue for the analysis in this chapter though, since the absence or existence of pre-injected carriers is easily taken into account in the numerical model and does not affect the conclusions drawn from the simulations.

Similar to the modulation bandwidth measured in small-signal modulation experiments, gain-switched pulses can also be sped up by reducing the photon lifetime $\tau_{ph} = 1/(v_{gr}(\alpha_i + \alpha_m))$. Since the mirror loss α_m is a function of both cavity length L and facet reflectivity $R_{1,2}$, there is a trade-off between keeping the photon lifetime short (i.e.

low facet reflectivities) and enabling short cavities, which in turn requires higher optical feedback or higher gain [364]. In the case of the tested devices, the long cavity is currently crucial for maintaining low-threshold laser operation of the uncoated broad-area laser.

Higher modal gain and thus more flexibility to shorten the cavity can be achieved by a number of methods. The most straight-forward way is the incorporation of a higher number of QD layers for a direct increase of the modal gain. A recent demonstration of conventional InAs QD high-speed lasers on GaAs, for instance, incorporates ten QD layers in the active region [397]. Other possibilities are further reducing the optical losses, optimisation of the QD growth so that a higher dot density, higher uniformity, and narrower gain bandwidth are achieved, p-doping of the active region to enhance the carrier transport and to increase the ground state hole occupation probability and thus the gain [18, 398], or optimisation of the carrier transport into the active region through narrower spacer layers [128]. The high gain compression factor used in the simulations suggests that especially improving the carrier transport in the thick QD active region could be a key factor in developing silicon-based QD lasers which are more suitable for optical communications. Fig. 6.12 indicates that the pulse duration of the narrow ridge-waveguide

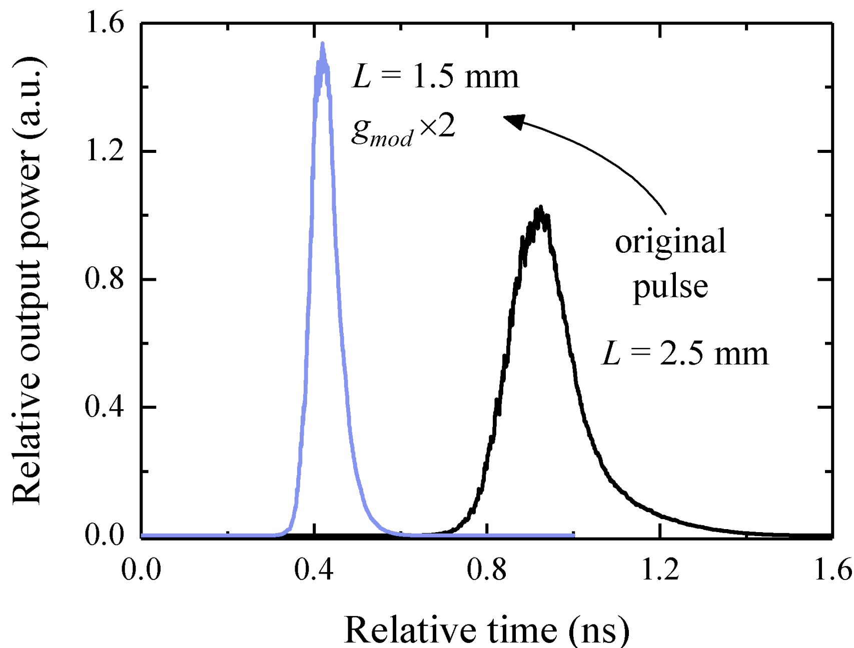

Figure 6.12: Modelled performance improvement ($\Delta\tau$ = 70 ps) of the narrow ridge-waveguide laser with doubled modal gain in a 1.5 mm short cavity.

laser, for example, could be reduced to about 70 ps by doubling the modal gain ($\rho_{QD} \times 1.5$, $\Gamma \times 1.5$ and assuming *p*-modulation doping) and shortening the cavity to 1.5 mm.

A last factor to be discussed is the potential influence of the silicon substrate with respect to the impact of dislocation-induced nonradiative recombination on the pulse dynamics. Fig. 6.11(b) shows two gain-switched pulses modelled at different wetting layer lifetimes of 0.1 ns and 0.5 ns at the same point above the threshold. It can be seen that higher continuum state losses induce slightly higher damping compared with the longer carrier lifetime, while leaving the dynamics otherwise the same. Although this would be in general agreement with the behaviour that has been reported from then on [273], the gain switching experiment leaves far to many free variables (predominantly the current pulse settings) to trace this effect back to dislocation-induced carrier loss.

6.6 Chapter Summary

In conclusion, this chapter contained the first experimental and theoretical study of gain-switched optical pulses generated by monolithic 1.3 μm InAs/GaAs QD broad-area and narrow ridge-waveguide lasers grown on silicon. The shortest obtained pulses generated by the 50×3100 μm^2 broad-area laser have a duration of 175 ps with a maximum peak power of up to 66 mW. Slightly shorter pulses of 150 ps duration with about 20 mW peak output power were obtained using an HR-coated 2.2×2500 μm^2 narrow ridge-waveguide laser. Systematic measurements show that optical pulses with higher power and shorter durations are achieved by increasing the drive pulse amplitudes, whereas there is a trade-off between maximising the optical power and minimising the respective pulse width for the electrical pulse width.

By simulating the experimental performance using the travelling-wave rate equation model of chapter 4, it was possible to obtain a set of laser parameters that is able to model the behaviour of these lasers, forming the foundation of all simulations performed from then on. In general, a good agreement between experiment and theory is found. The results show that, despite the great advances in the performance of silicon-based QD lasers over the last years, significant improvements can be made with these specific devices

in order to optimise the dynamic properties for high-speed communication applications. While the dynamic performance of GaAs-based InAs QD lasers is inherently limited by strong gain compression, monolithic InAs QD lasers on silicon suffer additionally from the defects introduced at the GaAs/Si interface. The extent to which these influence the performance of the gain-switched optical pulses does not become entirely clear from the simulations, but it is indicated that enhanced nonradiative recombination through dislocations induces a damped character to the modelled pulses. The primary concern should be providing higher gain and reducing the large gain compression factor, which is most likely achievable by using more active layers, reducing the spacer layer thickness, increasing the QD density, and by *p*-doping the active region.

Chapter 7

Direct Modulation of Quantum Dot Lasers on Silicon

7.1 Introduction

A laser's small-signal modulation response is of great relevance to assess its high-speed data transmission potential in a practical communication system. However, as pointed out in the beginning of the previous chapter, the information at hand regarding small-signal modulation of QD lasers on silicon are still quite limited, since there are only three other publications from 2018 and 2019 reporting on the small-signal modulation properties of Fabry-Pérot-type 1.3 µm QD lasers on silicon [171, 381, 382] apart from the results reported in this work and published in [69, 75]. Although one might easily assume that the modulation characteristics of InAs/GaAs QD lasers on silicon will be identical to their counterparts grown on native substrates, this might not automatically be the case due to the relatively unexplored role of dislocations for the laser dynamics.

The previous chapter has already presented insights into the intrinsic physical processes in QD lasers on silicon and the potential impact of the silicon substrate. Compared with the simulations in chapter 6, measuring and modelling the small-signal performance of silicon-based QD lasers offers a more robust way to extract the underlying laser parameters of interest with greater confidence, as it eliminates the free parameters induced by the current input pulse. In this chapter, narrow ridge-waveguide devices are, there-

fore, tested under small-signal conditions and the obtained experimental data are used as a template for theoretical simulations. Building on the findings from chapter 6, the simulations will focus particularly on understanding the bandwidth limitations observed in these data, and on investigating the potential impact of the silicon substrate on the modulation response.

7.2 Experimental Methods

Three nominally identical 2.2×2500 μm^2 HR-coated QD narrow ridge-waveguide lasers grown on silicon substrates with epitaxial structure as detailed in chapter 6.2 are tested. Two of these lasers are on the same bar and have laser thresholds around 19 mA, as shown in Fig. 7.1(a). An example of the multimode optical spectrum just above threshold is shown in Fig. 7.1(b). The third laser is the narrow ridge-waveguide laser tested in chapter 6. The small-signal response of the QD lasers is measured by imposing a swept frequency -5 dBm RF power signal between 50 MHz and 4 GHz – 6 GHz to the DC drive current. The modulated light output is collected with a singlemode fibre connected to a

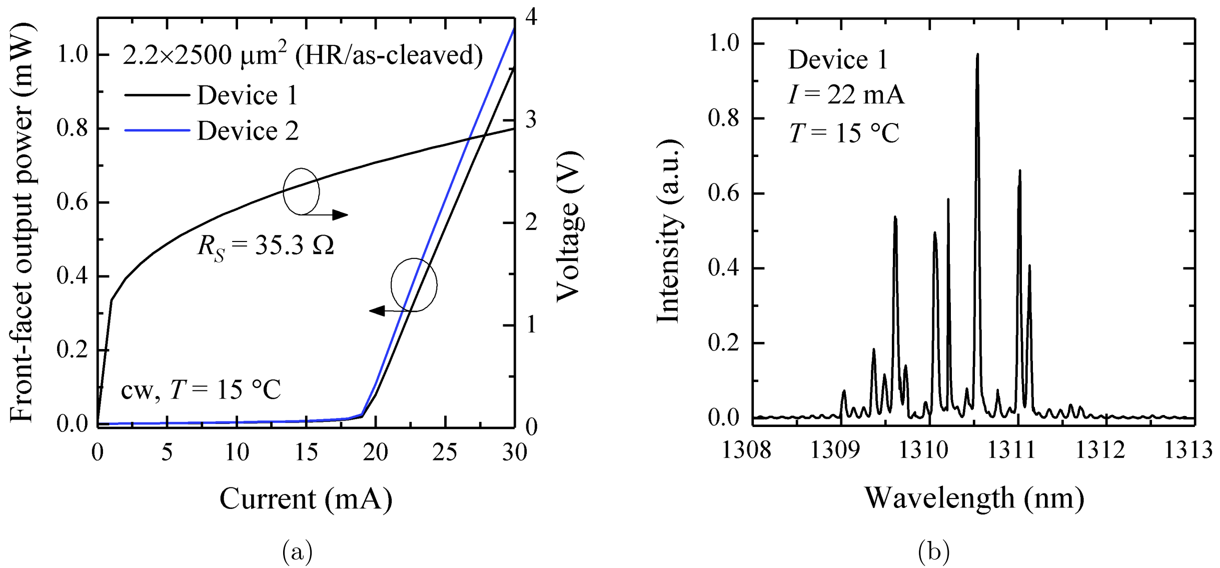

Figure 7.1: (a) CW LI characteristics of the two 2.2×2500 μm^2 QD lasers on the same laser bar showing threshold currents of 19.1 mA (device 1) and 18.9 mA (device 2) at 15 °C. The slope efficiencies are 0.09 W/A and 0.1 W/A, respectively. The voltage-current characteristic with forward resistance of 35.3 Ω is shown for device 1. (b) Multimode laser spectrum of device 1 measured at a drive current of 22 mA.

vector network analyser (VNA), where the small-signal modulation response is computed. Optical eye diagrams are measured by modulating the laser with an NRZ signal from a random bit pattern generator and by recording the eye diagrams using an oscilloscope.

7.3 Experimental Results and Analysis

Fig. 7.2 shows the normalised modulation response curves of device 1 and 2 with both devices demonstrating a maximum 3dB modulation bandwidth of 1.6 GHz. The curves are fitted using the standard three-pole transfer function

$$H(f) = \frac{f_R^2}{f_R^2 - f^2 + \frac{if\gamma}{2\pi}} \frac{1}{1 + \frac{if}{f_p}} \tag{7.1}$$

as introduced in chapter 2.3.2. The respective eye diagrams of device 1 can be seen in Fig. 7.3. Clear eyes are obtained at 1.0 Gb/s and 1.5 Gb/s, whereas the eye at 2.0 Gb/s is closed (not shown).

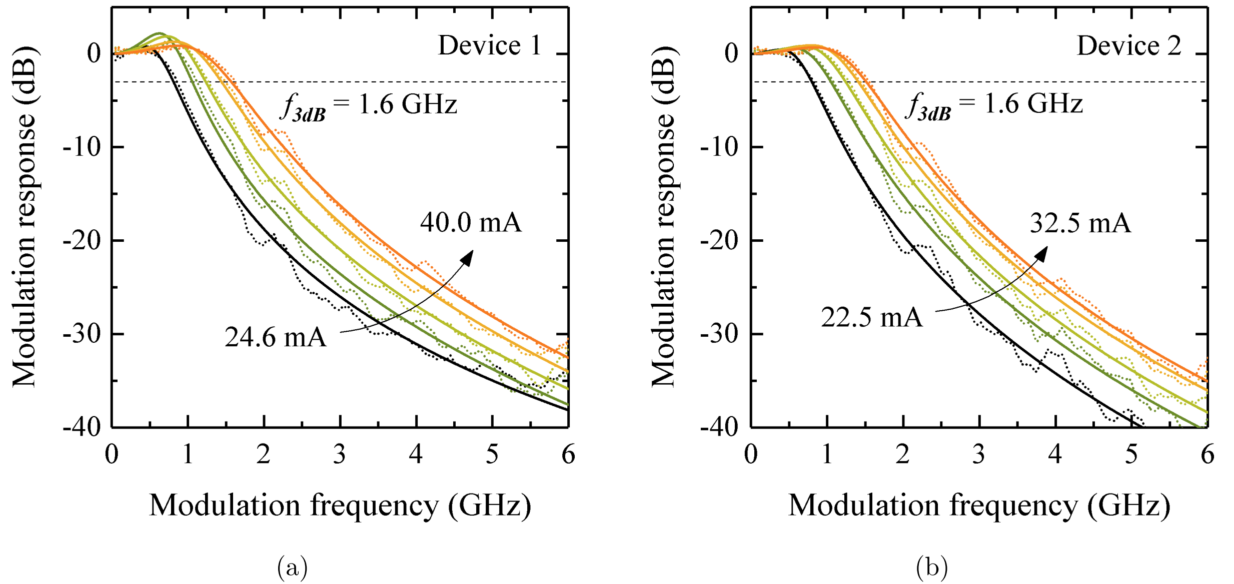

Figure 7.2: Normalised and smoothed small-signal modulation response curves of the 2.2×2500 μm^2 QD lasers on silicon on the same laser bar, measured at 15 °C. The curves are fitted by the three-pole transfer function for further analysis.

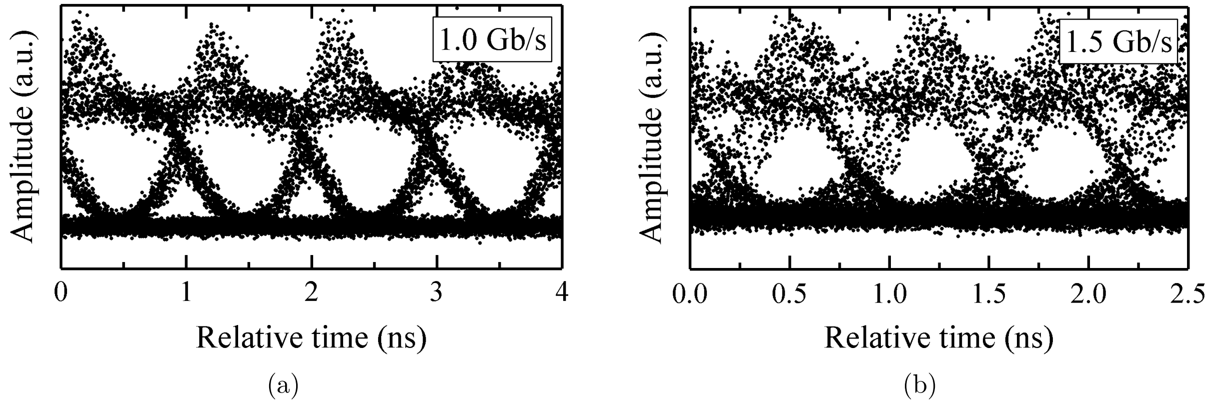

Figure 7.3: NRZ modulation optical eye patterns at data rates of (a) 1.0 Gb/s and (b) 1.5 Gb/s with the laser biased close to the threshold.

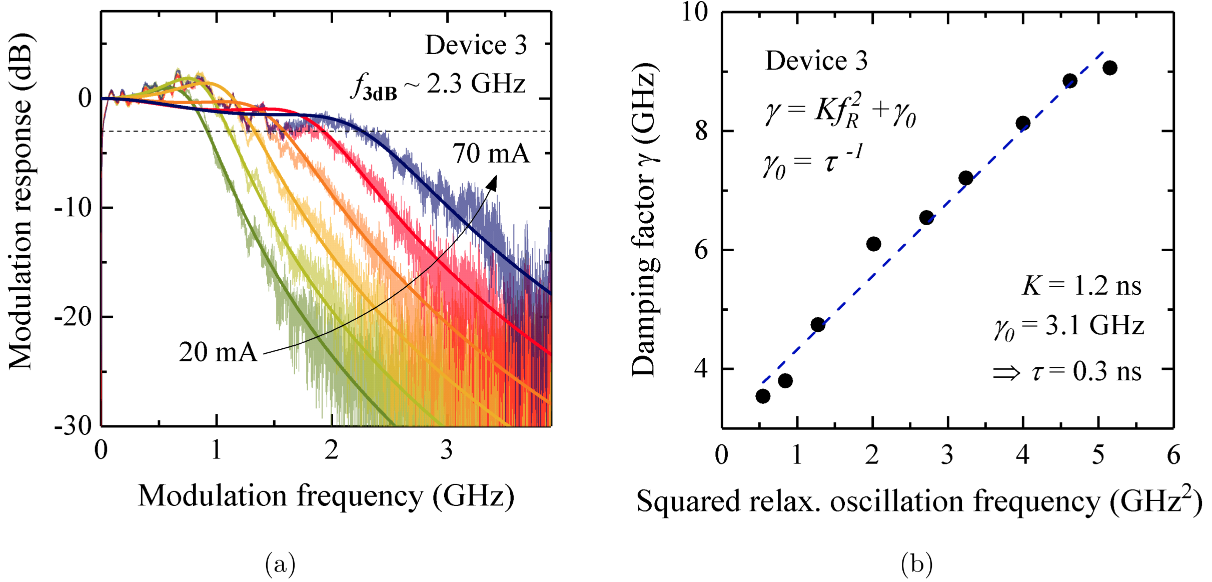

Figure 7.4: (a) Normalised and fitted small-signal modulation response curves of the third device tested at a later point at 18 °C. The different appearance compared with the curves in Fig. 7.2 is a result of the different VNA settings during this measurement. (b) Damping versus squared relaxation oscillation frequency with linear fit yielding a K-factor of 1.2 ns and a damping offset $\gamma_0 = 3.1$ GHz, corresponding to a differential carrier lifetime of 0.3 ns.

The small-signal modulation response measured for device 3 is shown in Fig. 7.4(a). Although a slightly higher 3dB bandwidth of 2.3 GHz is measured, these curves are not considered for further simulations as the pronounced pole at around 1.5 GHz hinders the analytic and numerical analysis of these curves. The parasitic pole might origin from the probe or the electrical contact pads, which are not specially designed for high-frequency

operation. Shang *et al.* have recently improved the 3dB bandwidth of 1.45 mm long 1.3 μm QD lasers on V-grooved silicon substrate from 3.6 GHz to 5.8 GHz without any changes in the epitaxial structure [171], showing that optimising the contact pad design can have a large impact on the demonstrated device bandwidth. Since the small-signal response of the undoped, 580 μm short InAs QD laser on silicon tested in [381] exhibits similar features, this could also be a result of carrier transport issues through the thick and undoped active region [149]. The following analysis builds, therefore, mainly on the two tested devices 1 and 2 from the same bar, where this is less of a problem.

The damping factors γ, which are extracted from the small-signal response fits of device 1 and 2, are subsequently plotted against the respective squared relaxation oscillation frequencies f_R^2, which is displayed in Fig. 7.5(a). The linear fits allow extraction of the K-factors, yielding 3.7 ns and 2.4 ns for device 1 and device 2, respectively. According to $f_{3dB}^{max} \approx 2\pi\sqrt{2}/K$ (Eq. (2.43)), maximum bandwidths of 2.4 GHz and 3.7 GHz are estimated for the tested devices. This order of magnitude is in approximate agreement with the relaxation oscillation frequencies of ∼1 GHz – 3 GHz, which have been reported

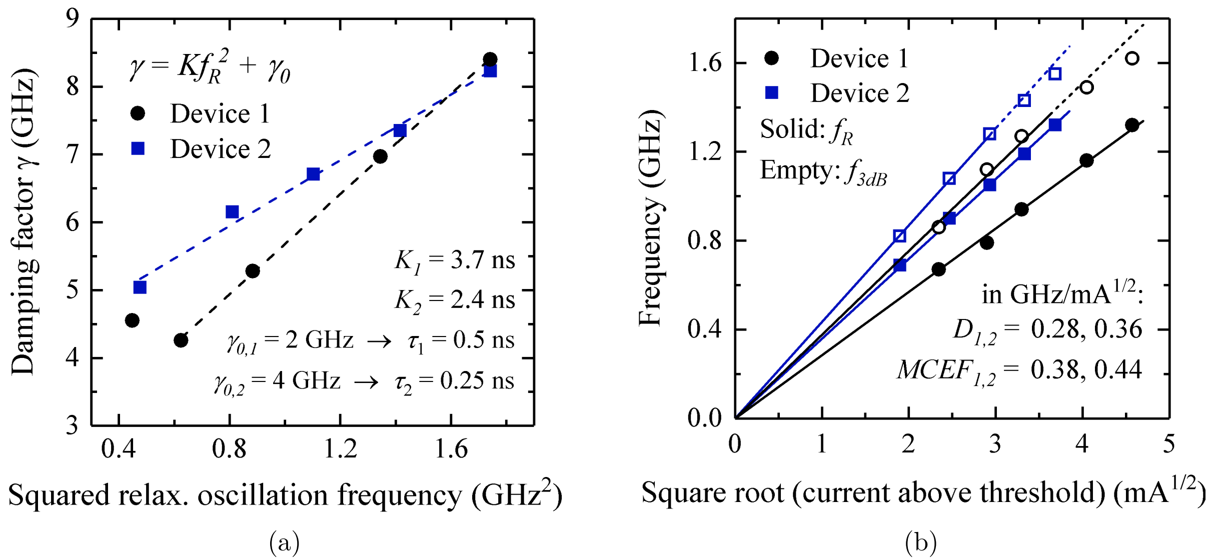

Figure 7.5: (a) Damping versus squared relaxation oscillation frequency for device 1 (black) and 2 (blue) with linear fits. (b) Resonance frequencies (solid) and 3dB frequencies (empty) versus the square root of the current above threshold with linear fits. The sublinear trends of the 3dB frequencies towards high currents (dashed) indicate that strong damping begins to limit the modulation bandwidth.

in [133] using a similar 2.5 mm long QD device on silicon. Typical K-factors of InAs QD lasers on GaAs are of the order of 1 ns [126, 381, 397]. While similar values of 0.92 ns and 1.3 ns have been published for 580 μm short p-doped and undoped silicon-based QD lasers grown at UCSB [381], an even larger K-factor of 4.7 ns has been calculated for a 1.1 mm long 1.3 μm QD laser on silicon [356].

The large K-factors extracted here express that the measured small-signal curves are strongly damping limited. Traditionally, this is in part a result of the K-factor's proportionality to the photon lifetime τ_{ph}, where both the long cavity and the HR-coated rear facet contribute to a long photon lifetime of about 22 ps [364]. Lasers designed for higher speed, in contrast, tend to have short cavities of a few hundred micrometres [128, 397, 399, 400], as discussed in chapter 2.3.2 and 6.1, in order to keep the photon lifetime and thus the K-factor small. Apart from that, the K-factor depends, furthermore, on the differential gain and the gain compression factor [126, 143]. Since a smaller K-factor of 1.2 ns is derived for device 3 with its photon lifetime nominally identical to that of device 1 and 2 (Fig. 7.4(b)), this indicates that τ_{ph} is not the sole factor influencing the magnitude of K. The simulations shown in section 7.4 will show indeed that both quantities, i.e. $\partial g/\partial n$ and ϵ, add to the bandwidth limitations observed in Fig. 7.2.

It is noteworthy that the high K-factors reported particularly for silicon-based QD lasers raise the question whether this is a feature unique to III-V lasers grown on silicon under the influence of high dislocation densities. In that context, it would also be interesting to see if there is a correlation between a high damping offset γ_0 and dislocation density. Since the inverse damping offset $\gamma_0^{-1} = \tau_{nr}$ is a measure of the differential carrier lifetime, which is a factor of 2–3 shorter than the standard lifetime [142], one might expect shorter lifetimes, i.e. higher damping offsets, for QD lasers on silicon with higher dislocation densities. However, more clarity on this will probably only be brought once publications on the direct modulation of silicon-based QD lasers from a variety of research groups are available.

Fig. 7.5(b) shows f_R and f_{3dB} plotted against the square root of the current above threshold with linear fits for extraction of the D-factor and the modulation current efficiency of f_{3dB} ($MCEF$). It can be seen that the D-factor and the $MCEF$ take on values

between about 0.3 GHz/mA$^{1/2}$ and 0.4 GHz/mA$^{1/2}$, which is slightly smaller than the values of about 0.7 GHz/mA$^{1/2}$ and 1.1 GHz/mA$^{1/2}$ reported in [381], but comparable with values in [171] and those that have been obtained during the earlier work on InAs QD lasers grown on GaAs [401, 402]. As $D \propto \sqrt{\eta\, \partial g/\partial n}$ (Eq. (2.46)), this suggests that increasing the current injection efficiency η and the differential gain $\partial g/\partial n$ might help to achieve higher modulation efficiencies in the future.

7.4 Simulation Results

7.4.1 Fitting

In order to identify the origin of the bandwidth limitations observed in the tested devices, the measured cw *LI* characteristic and small-signal response curves of device 1 are used as a fitting template for numerical modelling. The same travelling-wave model though without the barrier layer carrier equation is used for the following analysis, as in the previous chapter. The simulations are largely performed based on the parameter set obtained in chapter 6, which needs only slight adjustment to reproduce a good fit of the *LI* and small-signal fitting templates.

The QD carrier lifetime is used to reproduce the experimental laser threshold precisely. It turns out that slightly shorter ground and excited state lifetimes of 0.52 ns yield a better fit to the small signal curves than the lifetime of 0.56 ns that allows an accurate fit of the initially measured *LI* threshold. This could indicate that the laser may have degraded marginally in the course of performing the experiments. The wetting layer lifetime is set to 0.2 ns to account for potential dislocation-induced carrier loss. The current injection efficiency $\eta = 0.25$ is derived from the *LI* slope (Eq. (2.20)) and agrees well with what has been used in the previous chapter. The low value implies either that the quality of the electrical contact needs to be improved, or that a high level of carrier loss in the barrier layer is present, which would be manifested in a reduced injection efficiency, as discussed in chapter 5. Since the dislocation density in the devices under test is small ($\sim 10^5$ cm^{-2}), it is assumed that the first is primarily the case.

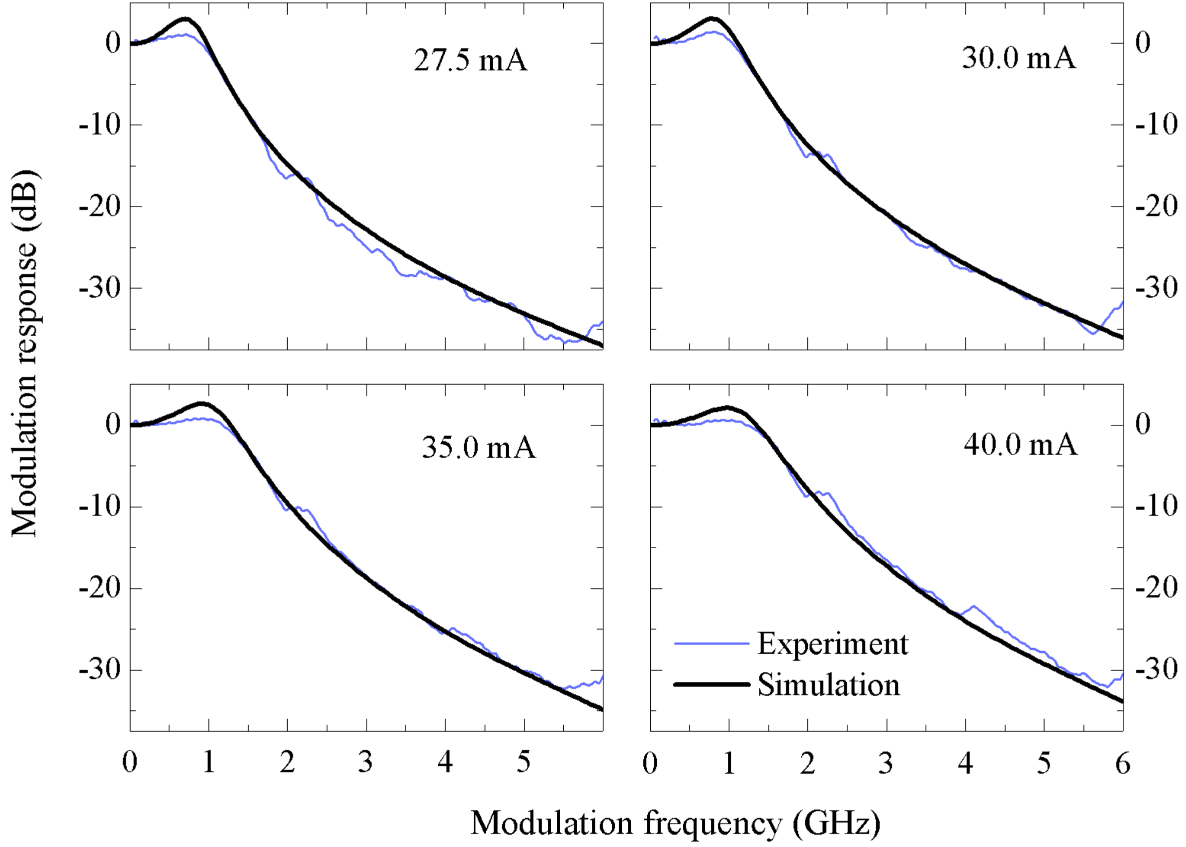

Figure 7.6: Modelled (black) small-signal modulation curves of laser 1 (blue) using a three-level rate equation travelling-wave model based on the parameters displayed in Table 7.1.

The modal gain g_{mod} and the gain compression factor ϵ are important quantities for fitting the current-dependent small-signal modulation trends and adjusting the modulation bandwidth. High modal gain results in a larger modulation bandwidth and a more strongly pronounced resonance, whereas gain compression describes the premature sublinear trend of the 3dB frequency towards higher currents. Although a larger gain compression factor of the order of 10^{15} cm^3 would reproduce the strong damping of the measured response curves somewhat better, it leads to early power saturation of the modelled LI curve, so that a value of $\epsilon = 5 \times 10^{-16}$ cm^3 is chosen as a trade-off. In the context of a feedback sensitivity study, it has been reported that the damped character of monolithic QD lasers on silicon can be explained by the carrier lifetime [273], which will be further discussed in section 7.5. Since this does not fundamentally change the modulation behaviour in terms of the 3dB bandwidth, which will also be shown in section 7.5, the fitting of the resonance shape is not of critical importance here. The result of the

small-signal simulations is displayed in Fig. 7.6. Apart from the slightly overestimated resonance peak, the laser parameter set presented in Table 7.1 yields an excellent fit.

$L = 2.5$ mm	Cavity length
$w = 2.2$ µm	Waveguide width
$\Delta z = 10$ µm	Spatial step size
$N_{layers} = 5$	Number of active layers
$R_{1,2} = 0.99, 0.30$	Rear and front facet reflectivity
$\rho_{dots} = 2.5\times10^{10}$ cm^{-2}	QD density
$\Gamma = 7.5\times10^{-4}$	Confinement factor
$g_{mod} = 14.7$ cm^{-1}	Modal gain
$f^h_{GS} = 0.5$	GS hole occupation probability
$\epsilon = 5\times10^{-16}$ cm^3	Gain compression factor
$\alpha_i = 3$ cm^{-1}	Optical waveguide loss
$\eta = 0.25$	Current injection efficiency
$\tau^{GS,ES}_{nr} = 0.52$ ns, 0.52 ns	GS, ES nonradiative lifetime
$\tau^{WL}_{nr} = 0.2$ ns	WL nonradiative lifetime
$\tau^{QD}_{cap} = 1$ ps	Carrier capture time into QDs
$\tau^{QD}_{rlx} = 0.15$ ps	Intradot relaxation time

Table 7.1: Overview of the used small-signal modulation modelling parameters.

7.4.2 Bandwidth Optimisation

To investigate the potential for monolithic III-V QD lasers on silicon substrates for direct-modulation applications, the previously fitted small-signal modulation response is remodelled for various laser lengths with reflectivity configurations of 0.99/0.30, 0.99/0.05, and 0.99/0.60, corresponding to HR/as-cleaved, HR/AR, and HR/HR-coated facets. In addition, the impact of higher modal gain with twice the number of active layers is simulated.

The result of simulations with an unchanged number of QD layers can be seen in Figs. 7.7(a) and (b). At first glance, the presented trends look slightly atypical, as the

modulation response increases with increasing cavity length and facet reflectivity, contrary to what is implied by the inverse dependence of f_R and f_{3dB} on τ_{ph}. The modulation bandwidth increases for cavity lengths of up to 3.0 mm and 1.75 mm for the HR/as-cleaved and the HR/HR combination, respectively. Beyond these lengths, the 3dB frequency starts to decrease again (not shown).

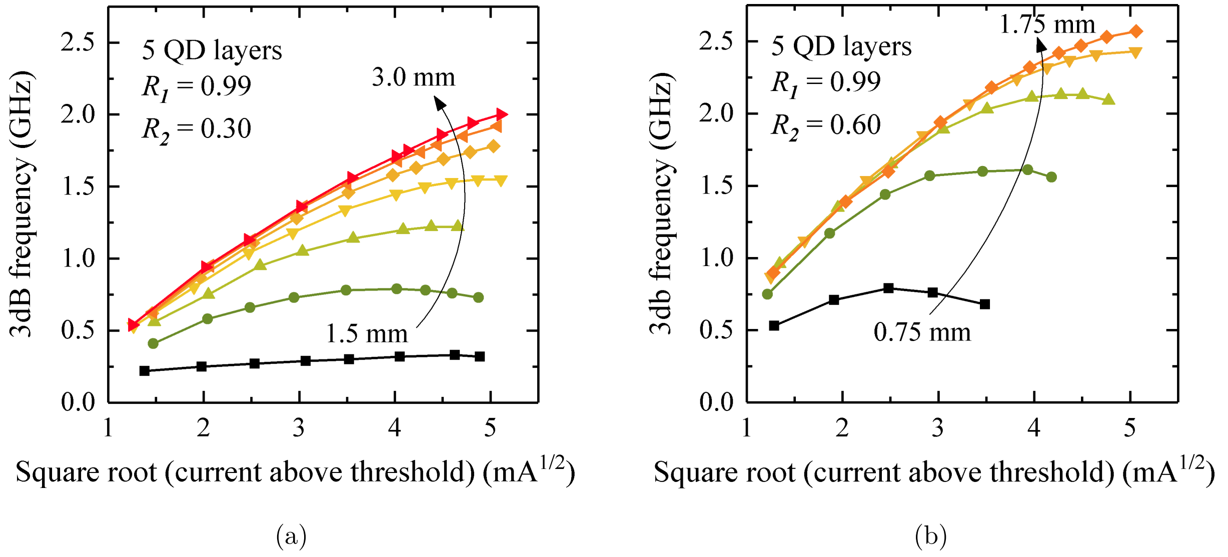

Figure 7.7: 3dB frequency versus the square root of current above threshold modelled for various cavity lengths with (a) HR/as-cleaved facets ($MCEF_{max} = 0.49$ GHz/mA$^{1/2}$) and (b) HR/HR facets ($MCEF_{max} = 0.67$ GHz/mA$^{1/2}$). Simulations with HR/AR configuration did not yield laser operation within the tested cavity lengths up to 4 mm.

For these scenarios, two effects come into play. Whereas both an increased laser length and higher mirror reflectivities lead to a longer photon lifetime (Fig. 7.8(a)), the improved optical feedback as well as the larger gain volume contribute to enhancing the photon density (Fig. 7.8(b)). So depending on the operation point of the laser, the net ratio of $\sqrt{S/\tau_{ph}} \propto f_R$ (see Eq. (2.37)) can increase with increasing laser length or facet reflectivity despite the longer photon lifetime. The second effect is that the simulated lasers seem to be operated in a strongly gain saturated regime, which often is not fully accounted for in standard analytical expressions. If insufficient gain is provided within the structure and the ratio between maximum modal gain and threshold gain is small, the effects of gain compression on the modulation response are even more pronounced [310].

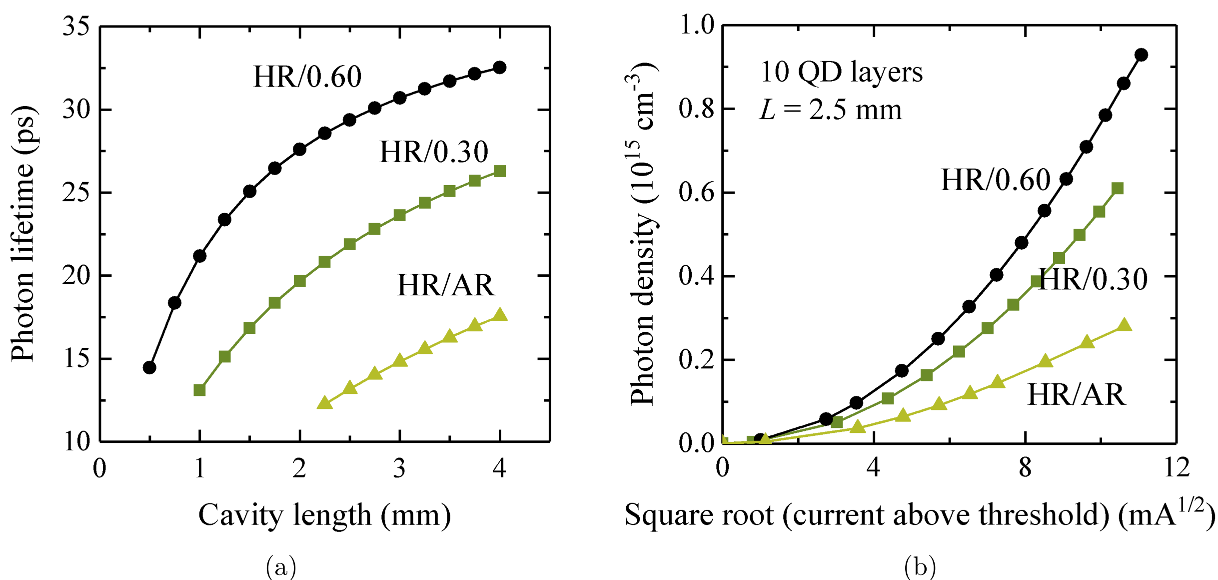

Figure 7.8: (a) Photon lifetime versus cavity length calculated for three facet reflectivity combinations. (b) Modelled photon density against the square root of the current above threshold for a 2.5 mm long laser with ten active layers, illustrating the possibility of attaining higher photon densities through HR facet coatings.

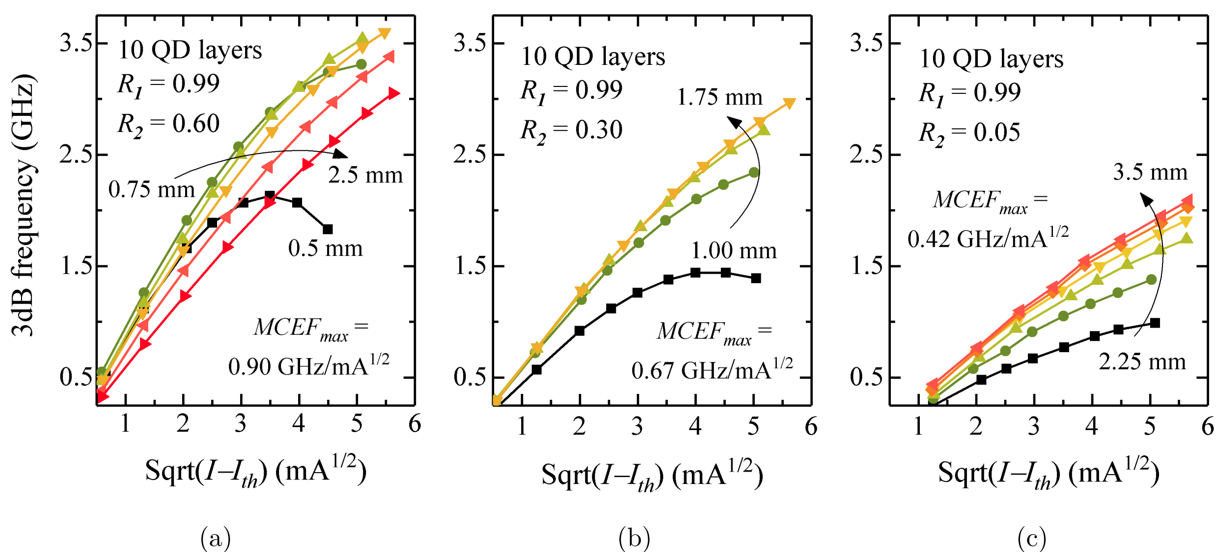

Figure 7.9: 3dB frequency versus the square root of current above threshold modelled for various cavity lengths and facet reflectivity combinations. (a) HR/HR, (b) HR/as-cleaved, and (c) HR/AR.

The HR/HR configuration with the higher modal gain from ten QD layers yields optimum performance for the given laser parameters with the respective results being

shown in Fig. 7.9(a). For the 0.75 mm cavity, the $MCEF$ is increased to 0.90 GHz/mA$^{1/2}$ and 3dB bandwidths of 3.0 GHz to 3.5 GHz are obtained. Small-signal simulations of lasers in HR/as-cleaved and HR/AR configuration as shown in Figs. 7.9(b) and (c) yield lower maximum bandwidths of about 3.0 GHz and (2 – 2.5) GHz, respectively, with the highest $MCEF$s obtained at 1.75 mm (0.67 GHz/mA$^{1/2}$) and 3.5 mm (0.42 GHz/mA$^{1/2}$). In the case of shorter cavities, the modulation bandwidth is limited by insufficient gain, while the photon lifetime is the limiting factor for longer laser lengths.

Since an increased number of QD layers usually results in a higher saturation power, the results obtained for the laser structure with ten QD layers in HR/HR configuration are remodelled for two lower gain compression values, as illustrated in Figs. 7.10(a) and (b). These results suggest that modulation bandwidths of 5 GHz to 7 GHz, which are typical modulation bandwidths of InAs/GaAs QD lasers on their native substrate [124, 397, 402–404], may thus be achievable on the basis of the available growth template. Monolithic QD lasers on silicon show, therefore, promise for low-cost 10 Gb/s applications

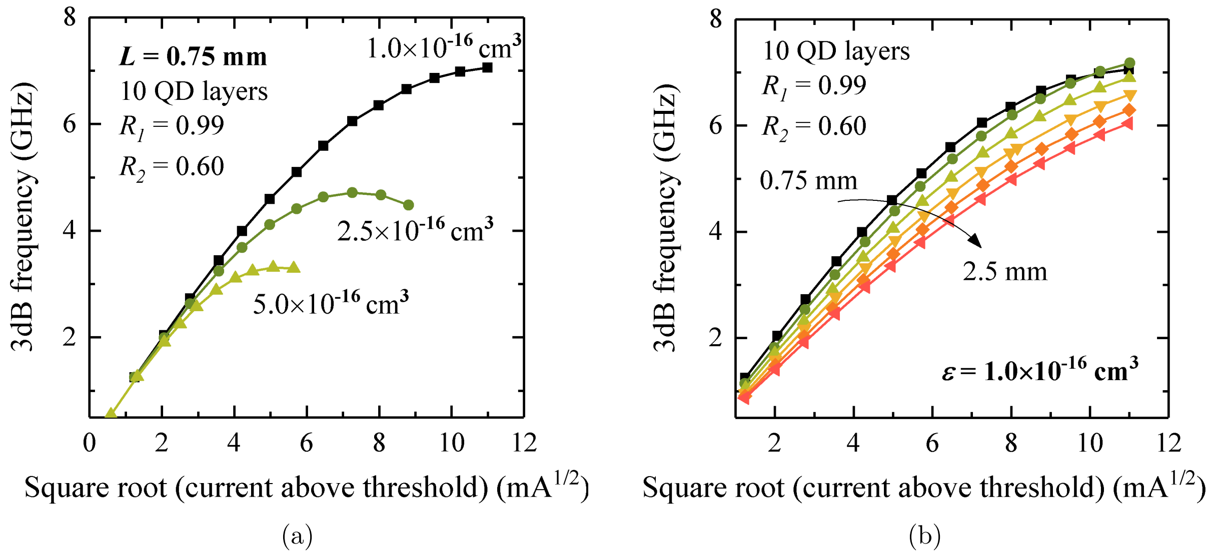

Figure 7.10: (a) 3dB bandwidth against the square root of current above threshold modelled for $L = 0.75$ mm using ten QD layers and HR/HR-coated facets showing possible modulation bandwidths at lower gain compression factors. The confinement factor is increased by 50 % for these simulations to achieve the higher gain. (b) Example of the performance of a 0.75 mm short HR/HR-coated device with ten QD layers at various cavity lengths at a lower gain compression factor of $\epsilon = 10^{-16}$ cm^3.

as discussed in the introduction of this work [146]. The technological challenge is now to combine the growth techniques of high quality GaAs on silicon with these required for high-performance QD active regions, although the excellent modal gain of almost 60 cm^{-1} reported in [330] proves that this does not appear to be an insurmountable hurdle.

7.5 Discussion: Impact of the Silicon Substrate

While QD lasers in general are known to have a limited modulation response compared with QW lasers, due to their lower modal gain and cascaded carrier transport via wetting layer and the individual quantum dot states [146], one of the key questions with respect to the future of monolithic QD lasers on silicon is whether the high density of threading dislocations resulting from the mismatched III-V-on-Si growth impairs the dynamic properties of silicon-based QD lasers in a fundamental way. The two main points of concern are here enhanced dislocation-induced nonradiative recombination and optical loss through scattering at dislocation cores.

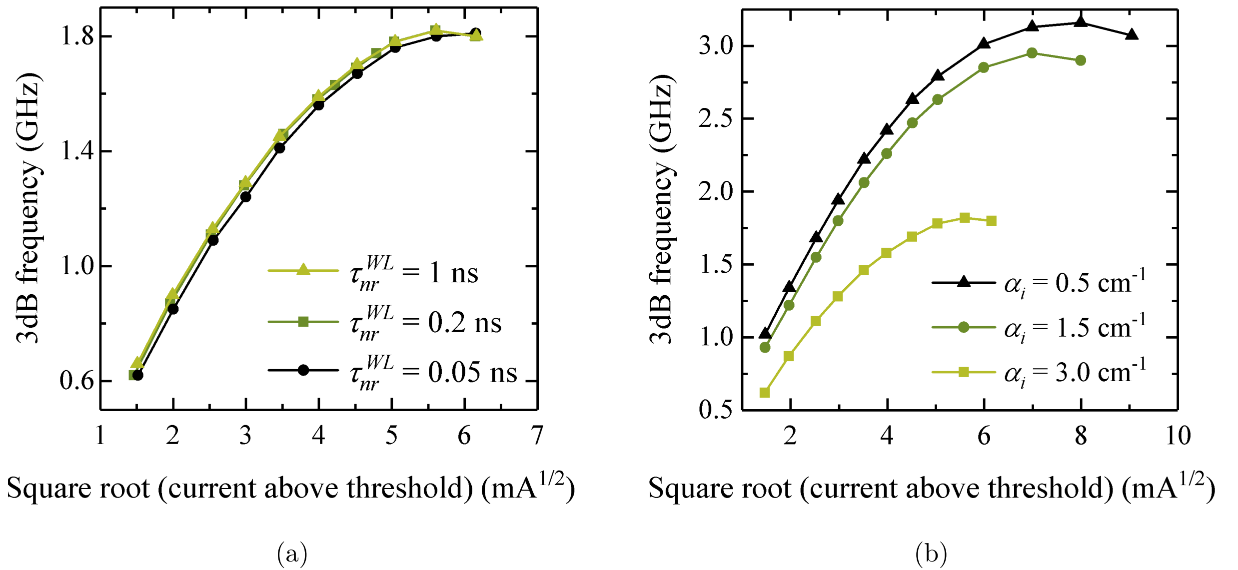

Figure 7.11: 3dB frequency versus the square root of current above threshold: Impact of (a) nonradiative recombination in the wetting layer and (b) optical loss on the modulation response of a QD laser on silicon.

The implications of dislocation-induced carrier loss on the laser bandwidth are investigated qualitatively by setting the wetting layer lifetime τ_{nr}^{WL} to a short value of 0.05 ns, representing the situation with a dislocation density much higher than in our tested lasers, and to 1.0 ns, corresponding to the situation in a typical GaAs-based laser, where carrier lifetimes can be of the order of several nanoseconds [273]. The results, displayed in Fig. 7.11(a), indicate that within the modelled range of values, the QD laser's 3dB bandwidth is almost independent of the continuum layer lifetime, with only a marginal drop observable for the $\tau_{nr}^{WL} = 0.05$ ns scenario. Although high wetting layer (and barrier layer) carrier loss increases the QD laser's threshold and reduces the current injection efficiency and thus the *LI* slope, excess carrier loss at dislocations appears to be only of subordinate importance with respect to the dynamic performance as long as sufficient carriers are supplied to the QDs. Practically though, a drastic increase of nonradiative wetting layer recombination will require higher injection currents, which increases power consumption and leads to undesired device heating, which in turn would degrade the modulation bandwidth again [405].

Fig. 7.12 shows that a reduction in carrier lifetime is also associated with a considerable amount of damping in the curves, as first pointed out in [273]. Fig. 7.12(b) shows simulations fitting the small-signal curves obtained by Inoue *et al.* using the 580 µm short QD laser on silicon with a dislocation density of 7×10^6 cm^{-2}. An overall carrier lifetime of 0.1 ns yields a very good fit to the measured curves. Repeating these calculations with a longer overall carrier lifetime of 1 ns while leaving all other parameters unchanged results in a much more strongly pronounced resonance frequency, as illustrated in Fig. 7.12(c). Interestingly, fitting these curves with the three-pole transfer function and plotting the extracted damping factors γ against the squared relaxation oscillation frequency f_R^2 gives exactly these lifetimes, 0.1 ns and 1 ns, as the differential lifetimes calculated from the damping offsets 10 GHz and 1 GHz. According to the analytical theory, it would be expected that the differential carrier lifetime obtained from the damping offset γ_0 is a factor of 2–3 shorter than the normal carrier lifetime deployed in the model [142]. This is obviously not the case in the numerical model and explains the overestimated resonances in the fitted curves in Fig. 7.6, where it has been attempted to fit the cw *LI* threshold and

the small-signal modulation curves based on a common set of carrier lifetimes. A moderate amount of damping does not lead to a reduction of the 3dB bandwidth, as demonstrated in Fig. 7.11(a), and can in fact even be advantageous for a laser's large-signal transmission capabilities [146, 406, 407].

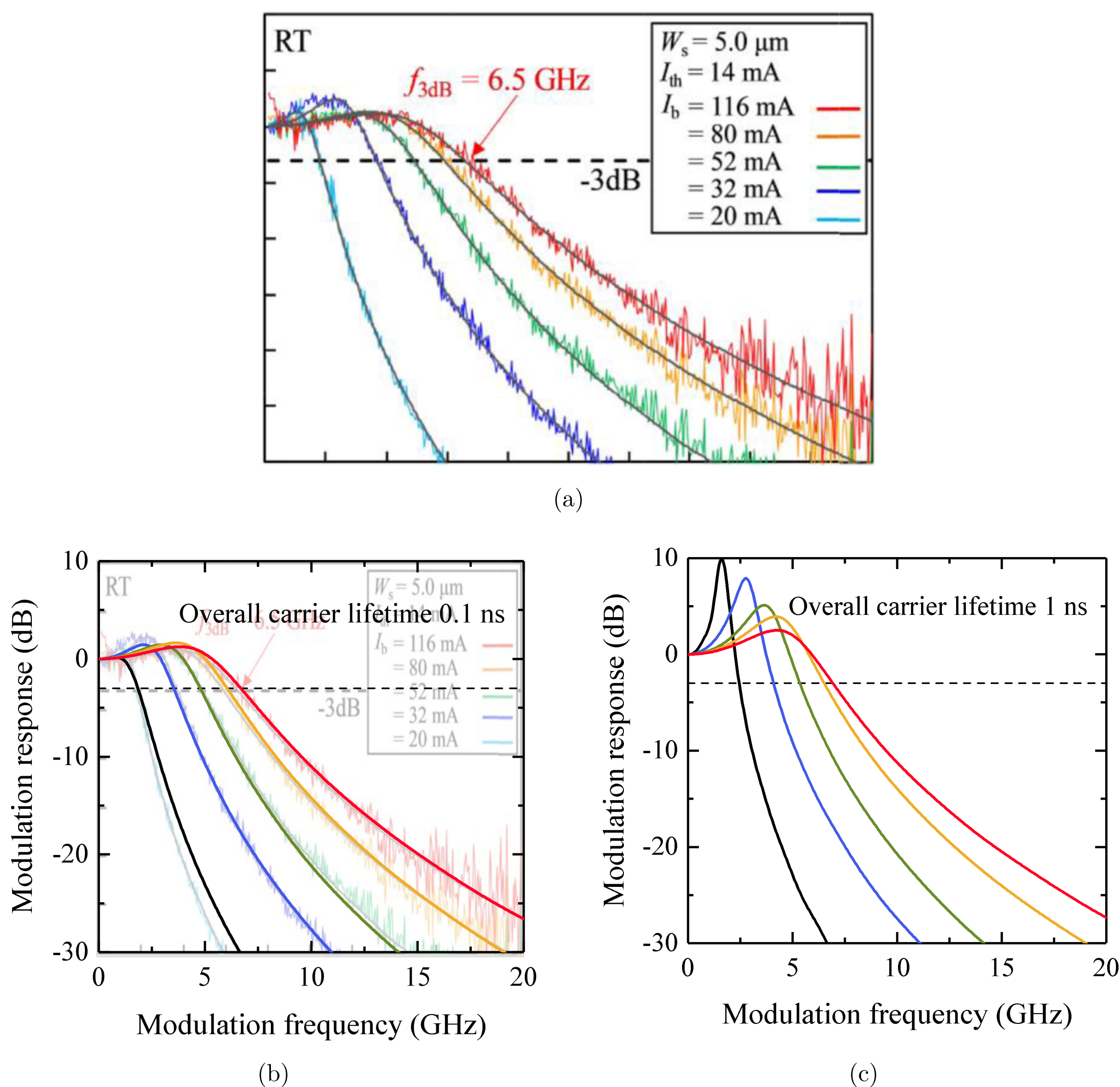

Figure 7.12: Impact of the overall carrier lifetime on the shape of small-signal modulation response curves. (a) Originally measured small-signal modulation curves from Inoue *et al.* [381]. (b) The damped small-signal curves from [381] can be fitted well using an overall carrier lifetime of 0.1 ns. (c) Repeated simulations using a carrier lifetime of 1 ns.

In addition to nonradiative recombination, the internal optical loss caused by dislocation-induced absorption and optical scattering can compromise the performance of QD lasers on silicon [325] – especially with respect to the modulation speed, as optical loss effectively reduces the available gain. In chapter 4.4.2 it has been discussed that the low optical losses reported for monolithic QD lasers on silicon are unlikely to limit their performance in a fundamental way. Even though reducing the optical loss in this structure further to 1.5 cm^{-1} or 0.5 cm^{-1} may almost double the modulation bandwidth for the here tested structures (Fig. 7.11(b)), this effect is likely to be less pronounced in QD lasers on silicon with higher gain.

7.6 Chapter Summary

A study on the high-speed modulation characteristics of monolithic 1.3 μm InAs QD lasers on silicon substrate was presented. Small-signal modulation experiments revealed maximum 3dB bandwidths of 1.6 GHz with D-factors of about 0.3 GHz/mA$^{1/2}$, modulation current efficiencies of 0.4 GHz/mA$^{1/2}$, and K-factors between 2.4 ns and 3.7 ns for two 2.2×2500 μm^2 HR-coated narrow ridge-waveguide lasers from the same laser bar. A third, nominally identical device showed a higher modulation bandwidth of 2.3 GHz with a lower K-factor of 1.3 ns. However, this device was less suitable for further analysis and simulations due to a pronounced parasitic pole in the modulation response.

Given that the tested devices are not designed specifically for high modulation bandwidths, the measured results were modelled numerically to identify the mechanisms limiting the modulation response and to to predict trends for geometrical configurations yielding the fastest possible modulation response. The simulations indicate that the small-signal response is currently not only limited by the long photon lifetime, but also by low gain and high gain compression. These limitations could be overcome by increasing the number of active QD layers to ten, and by using 99 % and 60 % high-reflectivity coatings to allow for lasing at shorter cavity lengths. In this configuration, the simulations predict 3dB modulation bandwidths comparable with InAs/GaAs QD lasers on native substrates of up to 5 GHz to 7 GHz, which indicates suitability for 10 Gb/s oper-

ation and places silicon-based QD lasers almost on a par with QD lasers grown on GaAs. The state-of-the-art dynamic performance of QD lasers can, however, not match that of QWs, so that QW devices are unlikely to be replaced by QD lasers on silicon in high-end direct-modulation applications.

Additional simulations investigating the impact of dislocations on the modulation speed reveal that neither increased nonradiative recombination through carrier migration into defects nor dislocation-induced optical loss appear to limit the modulation characteristics in a fundamental way. Although a shortened carrier lifetime due to dislocation-induced carrier loss was shown to lead to a stronger damping in the modulation response, which might be a characteristic of QD lasers on silicon in the presence of many dislocations, the overall dynamic properties of these devices still seem to be governed by the QD physics, regardless of the substrate type.

Chapter 8

Conclusions and Outlook

InAs/GaAs 1.3 μm QD lasers epitaxially grown on silicon substrate have become a promising candidate as a low-cost, silicon-based light source for silicon photonics and other applications. This thesis was aimed at advancing the knowledge of monolithic III-V lasers on silicon through simulation and experiment, placing its main focus on two specific aspects. First, the impact of threading dislocations on the laser performance was investigated by means of numerical simulations, and secondly, based on the envisioned applications in high-bandwidth-capacity silicon photonic circuits or other optical communication links, the QD laser dynamics were studied in order to identify their potential for optical data transmission. The main contents and findings of this dissertation are summarised below, followed by an outlook on possible future work.

8.1 Summary

This thesis has begun by giving an introduction to the need for silicon-based light sources in chapter 1. The steadily increasing demand for higher data rates in data centres and high-performance computing systems creates a bandwidth bottleneck at electronics-based servers, which is hoped to be alleviated by moving photonics closer to the electrical chip level. Silicon photonics is envisioned to be a game-changer technology providing increased bandwidth capacity at further reduced cost and power consumption, yet progress on all-epitaxial silicon photonic circuits was hampered by the lack of a suitable laser. The availability of monolithically grown III-V QD lasers on silicon might change this, opening

up doors for applications in optical access systems, data centres, LiDAR, or other fields, where certain performance or cost specifications may only be achieved through smart combinations of III-V and SOI technology.

Chapter 2 provided a summary of the semiconductor laser physics relevant for the understanding of the investigated Fabry-Pérot-type QD lasers on silicon. Basic operation principles such as the double heterostructure, lateral confinement schemes, and the lasing condition inside a Fabry-Pérot cavity were covered. The differences of common active region types, i.e. bulk active region, QWs and QDs, were explained. Although lacking behind QWs in terms of gain, optical output, and modulation bandwidth, QDs show a number of interesting properties, such as low threshold currents and relative intensity noise, higher temperature stability, a wide gain bandwidth, and reduced sensitivity to optical feedback, which renders them attractive for specific device types. Their newly discovered immunity to crystal defects is now adding to that list. Rate equations can be used to provide analytical insights to the behaviour of the semiconductor laser carrier and photon densities under static and dynamic operation. In particular, an analytical solution of the rate equations under small-signal modulation conditions was presented, including expressions for the three-pole transfer function $H(f)$ and for important figures of merit such as the relaxation oscillation and 3dB frequency f_R and f_{3dB}, the D-factor and the modulation current efficiency $MCEF$, the K-factor, and the damping offset γ_0.

The issue of realising a high-performance silicon-based light source and ways how to overcome this were discussed in chapter 3. While silicon itself is a rather inefficient light emitter as a result of its indirect bandgap electronic structure, the monolithic growth of high-optical-gain GaAs- or InP-based lasers directly on silicon substrates is impeded by their substantial crystal dissimilarities. Hence, various non-epitaxial integration schemes, such as direct mounting, large-scale so-called heterogeneous integration via wafer bonding, or massive transfer printing (in decreasing order of maturity) have been developed instead. Through the implementation of more defect-resistant QD rather than QW active regions and the development of several techniques for the elimination of threading dislocations propagating from the highly strained III-V/Si interface up into the laser structure, however, epitaxial integration of III-V QD lasers on silicon has also become a competitive

approach in recent years. With the help of pre-patterned substrates, buffer layers, efficient defect filter layers as well as thermal treatments, low dislocation densities of the order of 10^5 cm^{-2} to 10^6 cm^{-2} have been realised. The light-current performance characteristics of monolithic 1.3 µm QD lasers on silicon substrate available in the literature at the time of writing were summarised in a comprehensive overview graph, illustrating how a low dislocation density is linked to low threshold current densities and in turn to higher slope efficiencies.

At the beginning of this research project, little was known about the physical properties and the underpinning laser parameters of monolithic QD lasers grown on silicon under the influence of high dislocation densities. To obtain a better understanding of the underlying device physics limiting their performance compared with lasers on native substrate, a travelling-wave-based rate equation model was implemented and explained in chapter 4 in order to simulate the experimentally obtained results. Several aspects of the model were discussed, including the equations behind the simulation of QW and QD lasers, typical modelling parameters of 1.3 µm InAs/GaAs QD lasers on GaAs, examples of the numerical implementation of the core simulation programmes, and possible model extensions.

Whereas it was initially not known to what extent the modelling parameters of devices grown on silicon would vary from those on native substrate, the theoretical work performed over the course of this project revealed that most parameters can be adopted without any changes. Laser parameters that were found to potentially differ from their counterparts on native substrates are the nonradiative carrier lifetime τ_{nr} and the current injection efficiency η. τ_{nr} can be strongly reduced below 1 ns as a result of enhanced dislocation-induced carrier loss at high defect densities. A reduction of η below standard values of about 0.5 could also be observed in a three-level rate equation model containing energy levels for two QD states and the wetting layer, while the same outcome was produced by high barrier layer losses instead in a four-level model including the separate confinement-heterostructure GaAs barrier layers as well. Although high optical loss α_i and reduced modal gain g_{mod} were initially a concern for monolithic QD lasers on silicon, α_i was not found to be significantly increased in the tested devices ($\alpha_i \approx 3$ cm^{-1}) or in other publications. Similarly, studies at UCSB demonstrated that very high modal gain of

the order of 60 cm^{-1} can be realised [18, 330]. An important point to bear in mind is, therefore, that QD growth technology has considerably advanced compared with earlier generations of InAs/GaAs QDs on GaAs substrate. For this reason, care has to be taken when utilising some QD modelling parameters, such as the modal gain g_{mod} or the optical confinement factor Γ, published in earlier studies.

Based on the implemented model and the consequently obtained parameters, a comprehensive study on the impact of crystal dislocations on the performance of monolithic QD lasers on silicon was conducted and presented in chapter 5. Since the high density of threading dislocations is the main difference to conventional QD lasers on native substrate, two simulation approaches were developed to consider the dislocation density specifically as a modelling parameter. The first approach in chapter 5.2 was based on standard parameters averaged for the whole device using a dislocation-dependent nonradiative lifetime inferred from the average dislocation-limited diffusion length in the barrier layers and QWs or QD wetting layers, respectively, whereas the second one in chapter 5.3 was a high-resolution approach allowing the implementation of individual, locally resolved dislocations along the laser cavity.

In both approaches it was theoretically shown that enhanced carrier loss at higher dislocation densities leads to an increase of the laser threshold in QW and QD devices, although to a much greater extent in QWs, where the threshold current increased fourfold in the dislocation density range between 10^4 cm^{-2} and 10^7 cm^{-2}. For the QD laser, it was found that the eventual reduction of the barrier layer and wetting layer carrier density from $\rho_{dis} \gtrsim 10^7$ cm^{-2} manifested itself in a degraded injection efficiency, which in turn resulted in a reduced *LI* slope efficiency. The overall findings were in good agreement with the *LI* performance trends so far published for GaAs-based QW and QD lasers epitaxially grown on silicon and highlighted the performance disparity between QD and QW devices in the presence of many dislocations. The simulations further revealed that this discrepancy can be explained based on efficient and ultrafast carrier capture into the QDs, where high energy barriers prevent carriers from migrating into defects. In particular, the novel high-resolution simulation approach allowed to identify a large minority carrier diffusion length of several micrometres as a key parameter inhibiting laser operation by enabling carrier

migration into dislocations over larger areas. This simulation approach pointed also to the issue of locally reduced gain around dislocations, which had to be compensated for in dislocation-free regions. This process could lead to enhanced gain saturation effects in QD lasers on silicon with high dislocation densities and limited modal gain.

The dynamic properties of monolithic QD lasers on silicon were investigated by means of gain switching and small-signal modulation in chapter 6 and 7, respectively. Gain-switched optical pulses, the first ever reported ones using monolithic III-V QD lasers on silicon, were generated by monolithic 1.3 μm InAs/GaAs QD broad-area and narrow ridge-waveguide lasers grown on silicon. Systematic measurements studying the relationship between the electrical drive pulse width and amplitude and the respective optical output pulse power and duration were performed. The shortest obtained pulses had durations of 175 ps and 150 ps for an as-cleaved 50×3100 μm^2 broad-area laser and a high-reflection-coated 2.2×2500 μm^2 narrow ridge-waveguide laser with a maximum peak power of about 66 mW and 20 mW, respectively. The supporting numerical simulations in chapter 6 showed that the high-speed limitations observed in these measurements were largely a result of the laser design in terms of limited gain and a long photon lifetime. They indicated that significant improvements can be made by providing higher optical feedback to allow a shorter cavity and by reducing the large gain compression factor, which is most likely achievable by using more active layers, reducing the spacer layer thickness, increasing the QD density, and by *p*-doping the active region.

Small-signal and large-signal modulation experiments were performed to test the data transmission potential of monolithic 1.3 μm QD lasers on silicon. 3dB modulation bandwidths of 1.6 GHz to 2.3 GHz and optical eyes at 1.5 Gb/s were measured, as shown in chapter 7, using the 2.5 mm long narrow ridge-waveguide lasers with high-reflection coating. Small-signal analysis as outlined in chapter 2.3 allowed to extract D-factors of about 0.3 GHz/mA$^{1/2}$, modulation current efficiencies of 0.4 GHz/mA$^{1/2}$, and K-factors between 1.3 ns and 3.7 ns. These values, which are similar to early demonstrations of 1.3 μm InAs/GaAs QD lasers on GaAs substrate, indicated the same sort of underlying performance constraints as observed during the gain switching experiments. In a theoretical optimisation study it was, therefore, found that these limitations could be overcome

and 10 Gb/s operation could be achieved through the incorporation of ten QD layers into a 0.75 mm short cavity with 99 %/60 % high-reflectivity coatings. Although this is likely not sufficient for directly modulated data centre optical links, it suggests suitability for use as low-cost, low-chirp laser in 10G-PONs, for example. Whereas the effect of dislocations on the dynamic performance of QD lasers on silicon did not become clear from gain switching simulations due to the additional free parameter induced by the drive pulse, in chapter 7 it was, furthermore, found that neither dislocation-induced carrier loss through carrier migration into defects nor optical loss limited the modulation characteristics in a fundamental way. The reduced carrier lifetime though was reflected in a more strongly damped modulation response. Apart from that, the overall device dynamics remained governed by the QD physics regardless of the substrate type. These results are an important finding, as they demonstrate that monolithic 1.3 μm QD lasers on silicon have indeed the potential to be adopted in certain commercial systems in the longer term.

8.2 Outlook

8.2.1 Integration with Silicon Photonics

Within the past decade, QD lasers monolithically grown on silicon have evolved from basic proof-of-concept devices to reliable high-performance lasers with low-power threshold currents of 4.8 mA [22], optical output power of more than 175 mW [23, 24], extrapolated lifetimes of longer than three million hours [23], with potential for 10 Gb/s direct modulation in a simple Fabry-Pérot layout [69, 381, 382] and 4.1 Tb/s bandwidth capacity in a more advanced high-channel-count device [245] with suitability for > 100 °C operation [18–21], positioning these devices right on the edge of commercialisation [408]. Now that major hurdles of growing III-V lasers on silicon have been overcome, the next steps on the agenda should without a doubt be demonstrating more advanced integration architectures proving the viability of silicon-based QD lasers in high-bandwidth-capacity (for instance $\gg 1$ Tb/s [9, 10, 409]) all-epitaxial silicon photonic circuits containing functionalities such as integrated modulation, waveguides, multiplexers and demultiplexers as well as detection.

Fig. 8.1 presents three possible approaches to integrate a monolithic III-V-on-Si laser on a silicon or SOI substrate using evanescent coupling (Fig. 8.1(a)), butt-coupling (Fig. 8.1(b)), or a monolithic III-V waveguide layer (Fig. 8.1(c)). In the first approach in Fig. 8.1(a), the laser is grown on a pre-patterned SOI wafer in a way that the cavity mode couples into the silicon waveguide below the active region. Evanescent coupling is a standard procedure for bonded devices and benefits from the possibility of very high coupling efficiencies > 90 % as discussed in chapter 3.2.2 [182]. It also enables the integration of an index grating in the silicon waveguide, so that singlemode operation and precise tuning to wavelengths required by communication standards are conveniently achieved [4]. With respect to epitaxial rather than heterogeneous integration, the major roadblock for monolithic III-V-on-Si lasers is that a very thin n-layer between active region and waveguide is required to obtain efficient coupling [176]. This remains a critical issue as long as the available defect buffer and filter layers presented in chapter 3.3 are still based on several micrometre thick epitaxial layers. This approach may also require current injection through the highly defective buffer layers close to the III-V/Si interface, which could degrade the laser's lifetime through the formation of alternative recombination pathways as well as degrade its electrical characteristics [15].

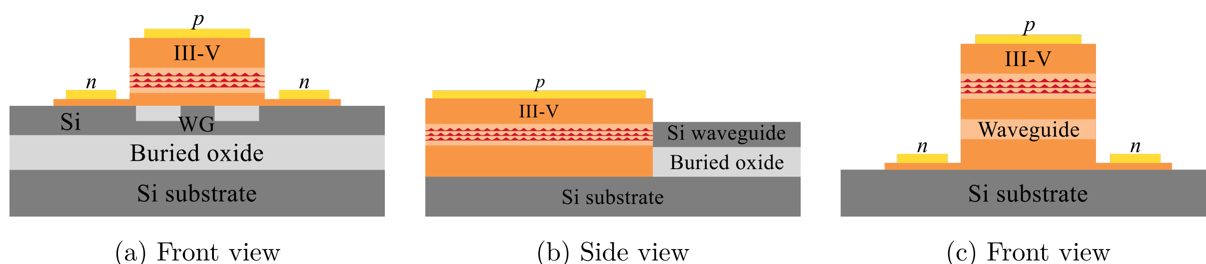

(a) Front view (b) Side view (c) Front view

Figure 8.1: Three possible approaches for integrating a monolithic QD laser on silicon with a waveguide on a common silicon platform. (a) Evanescent coupling, based on [410]. (b) Butt-coupling, based on [411]. (c) Evanescent coupling with all III-V functionalities, based on [15].

In the butt-coupling approach shown in Fig. 8.1(b), the QD laser is grown directly on the silicon handle wafer in a manner that its active region is aligned with the top silicon layer of an SOI substrate, which acts as a waveguide. In principle, a surface grating could

be realised on the silicon waveguide as well [412]. For this architecture, the buffer layer thickness is not quite that critical, however there will be a certain amount of coupling loss at the waveguide interface between the active region and the waveguide. Lastly, the option of evanescent coupling with all photonic circuit technologies integrated in the III-V material is shown in Fig. 8.1(c). This case exploits simply the silicon substrate as low-cost alternative to standard III-V substrates, while otherwise being similar to InP-based photonic integrated circuit technology [15, 413]. Some problems arising from the first two approaches can thus be avoided, although this comes at the expense of not actually using any silicon photonics components.

With respect to integration architectures that cannot offer full monolithity, QD-based devices are in an advantageous position compared with reflection-sensitive heterogeneous QW lasers on silicon, as their enhanced tolerance to optical feedback due to the near-zero linewidth enhancement factor and strongly damped relaxation oscillations can likely enable isolator-free integration into the photonic circuit [310]. This will be an important advantage due to the current lack of high-performance all-silicon isolators [414, 415]. A further factor working to the advantage of QD lasers on silicon for silicon photonics aimed at data centres is that typical data centre operation temperatures can vary from as much as −40 °C to 85 °C [182], hence requiring high temperature stability of the optical transmitter. Although suitability of monolithic QD lasers on silicon for this wide range of temperatures will need to be verified, the commonly more temperature-stable QDs are here expected to be in a favourable position compared with their QW counterparts [405, 416, 417]. Lastly, it should be noted that modulation speed requirements in current and future data centres will make it also necessary to switch to external modulation of the QD light source. Although this does not pose a fundamental issue for the integration of QD lasers on silicon into data centre silicon photonics, it has to be considered that an externally modulated laser (for example with integrated electro-absorption modulator) adds slightly higher cost, complexity, and power consumption compared with low-cost directly modulated VCSELs or DFB lasers [418, 419].

8.2.2 Directly Modulated Lasers for 10G Passive Optical Networks

The potential of monolithic 1.3 µm III-V QD lasers on silicon extends beyond silicon photonics, so it would be very insightful to see studies on improving the bandwidth performance by using thinner barrier layers, more QD layers, and an optimum photon lifetime [128, 300] to explore the market for low-cost 10 Gb/s applications. Next-generation PONs offering shared downstream data rates of 10 Gb/s, and possibly even 25 Gb/s or 50 Gb/s [421], will increasingly be incorporated into future telecommunication systems. Although the latter two would likely require optical transmitters operating at $\geq$ 25 Gb/s under NRZ modulation (rather than 10 Gb/s in combination with higher order modulation schemes) [422], there could be a real market for directly modulated 10 Gb/s QD lasers on silicon, which are not only cheaper than their QW O-Band or C-Band counterpart on InP, but

Figure 8.2: Schematic 10G-PON architecture. Data at the optical line termination (OLT, left) are sent via the medium access control (MAC) logic from the network-to-network input/output interface (NNI data I/O) to the optical transmitter (Tx). Using 10 Gb/s direct modulation, the data are transmitted through an optical fibre and distributed to the various users, where they are detected by the receiver (Rx) at the optical network unit (ONU, right) [33, 420]. Existing wavelength standards may require using InP- rather than GaAs-based QD lasers. Based on [420].

exhibit also a much lower chirp. Since PONs have to cover much longer distances than data centres (typically about 20 km), the issue of wavelength chirping under large-signal current modulation and the respective bit rate penalty caused by fibre dispersion becomes a much more critical one in telecommunications [33, 421]. Although one configuration for chirp control is available in the form of narrow-band optical filters [423, 424], for instance, the use of low-chirp, low-cost 10 Gb/s QD lasers on silicon could significantly simplify the system architecture as well as improve the optical power budget and overall component cost [425]. An example illustrating 10G-PON-based data transmission (also known as XG-PON) for optical access such as fibre-to-the-home can be seen in Fig. 8.2.

8.2.3 Materials Research

While the demonstration of reliable, high-performance InAs/GaAs QD lasers monolithically grown on silicon is a true milestone for the future of optoelectronic integrated circuits, there is still plenty more to learn about III-V lasers grown on silicon in general. More investigations could, for instance, go into the nature of defect states in order to develop a better understanding of the nonradiative loss mechanism induced by threading dislocations. In GaN-based devices, for example, it is known that certain kinds of dislocations behave as acceptor-like, so that GaN's natural background n-doping acts favourably on alleviating the impact of defect states. Indeed it was found that a higher doping level in general helped to improve the light emission efficiency by reducing carrier diffusivity [351, 426]. With carrier migration into nearby dislocations being one of the key factors inhibiting high performance of InP- and GaAs-based QW lasers grown on silicon, similar studies on these III-V materials grown on silicon might offer a route to improving the performance of silicon-based III-V QW lasers.

Other than that, there are various other possible approaches such as lower-diffusivity InP-based devices, gain-coupled QW DFB lasers with laterally structured active region (Fig. 8.3), or thinner QWs, where diffusivity is reduced [211], that could also remedy the situation. Although QD active regions are at the time of writing the only workable solution for monolithic III-V laser growth on silicon, research on growing III-V QWs on silicon should remain a relevant topic and continue in order to address the need for silicon-

based lasers that can offer high direct-modulation speeds through high gain and a short cavity as well as higher power.

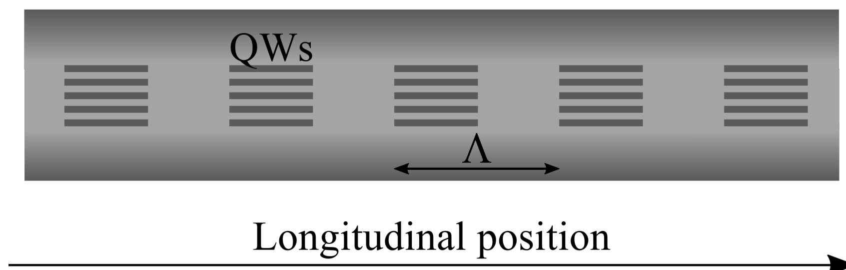

Figure 8.3: Schematic showing the longitudinal active region cross section of a gain-coupled QW DFB laser. Instead of an index grating, a gain grating with period Λ is etched into the QWs, resulting in a complex coupling coefficient κ.

8.2.4 Low-Cost VCSEL Arrays for Sensing Applications

Reducing the dislocation density in monolithic silicon-based QD lasers has been instructive for improving their overall performance. Further improvements in the dislocation density reduction to $< 10^5$ cm^{-2} may lead to entirely dislocation-free active regions in small-area devices such as short high-speed QW lasers (with areas of 2×200 µm^2, for instance) or VCSELs with typical active region diameters of about 5 µm – 10 µm. Especially VCSELs with QD active regions have traditionally been difficult to realise, as the short overlap length of typically only about one material wavelength with the active region requires very high gain, high facet reflectivities, and minimised optical losses [115]. QDs suffer in that respect not only from their lower modal gain due to the limited dot coverage, but additionally from the need for thick spacer layers, which prevents dense stacking of multiple active layers per electric field node as it would be the case with QWs [427–429]. While there are no comprehensive studies yet on the effect of dislocations in QD VCSELs grown on silicon, epitaxial defects in standard AlGaAs VCSELs lead easily to device failure [430, 431]. However, there is currently tremendous demand for VCSEL arrays for sensing applications, where failure of individual devices is insignificant. As a consequence, there could be immense market potential for inexpensive VCSELs grown

on silicon if devices with QW active region could be realised. In the context of higher-power VCSEL array configurations, silicon's improved heat dissipation properties might give these devices an additional edge over conventional VCSEL arrays on GaAs substrate.

To conclude, it can be said that the recent years of research on monolithic 1.3 μm InAs/GaAs QD lasers grown on silicon have greatly improved the prospect of demonstrating all-monolithic photonic integrated circuits. These heteroepitaxial QD devices hold great promise to fulfil the demand of monolithic silicon-based light sources in the longer term and may ultimately open the door for to date impossible photonic integration schemes or other types of devices with improved performance or functionality.

Bibliography

[1] "Cisco Visual Networking Index: Forecast and trends, 2017–2022," *White paper, Cisco public*, 2019.

[2] X. Zhuo, H. Liu, and R. Urata, "Data center optics: Requirements, technologies, and trends," *Chinese Optics Letters*, vol. 15, no. 5, pp. 120 008–1–4, 2017.

[3] Z. Zhou, C. R, X. Li, and T. Li, "Development trends in silicon photonics for data centers," *Optical Fiber Technology*, vol. 44, pp. 13–23, 2018.

[4] J. B. Driscoll, P. Doussiere, S. Islam, R. Narayan, W. Lin, and H. Menhalingam, "First 400G 8-channel CWDM silicon photonic integrated transmitter," in *Proc. 2018 IEEE 15th International Conference on Group IV Photonics*, Cancun, Mexico, 2018, pp. 1–2.

[5] "Cisco Global Cloud Index: Forecast and methodology, 2016–2021," *White paper, Cisco public*, 2018.

[6] J. Williamson, "Silicon Photonics passes the tipping point," *Optical Connection News*, vol. 11, no. Q4, pp. 28–29, 2017.

[7] M. Hudait, M. Clavel, L. Lester, D. Saladukha, T. Ochalski, and F. Murphy-Armando, "Heterogeneously grown tunable group-IV laser on silicon," in *Proc. SPIE, Quantum, Sensing, and Nano Electronics and Photonics XIII*, vol. 9755, San Francisco, CA, USA, 2016, p. 97550Y.

[8] G. Roelkens, L. Liu, D. Liang, A. Fang, B. Koch, and J. Bowers, "III-V/silicon photonics for on-chip and inter-chip optical interconnects," *Laser & Photonics Reviews*, vol. 4, no. 6, pp. 751–779, 2010.

[9] D. A. B. Miller, "Device requirements for optical interconnects to silicon chips," *Proceedings of the IEEE*, vol. 97, no. 7, pp. 1166–1185, 2009.

[10] M. Ashgari and A. V. Krishnamoorthy, "Silicon photonics: Energy-efficient communication," *Nature Photonics*, vol. 5, no. 5, pp. 260–270, 2011.

[11] T. Nagatsuma and G. Carpintero, "Recent progress and future prospect of photonics-enabled Terahertz communications research," *IEICE Transactions on Electronics*, vol. E98, no. 12, pp. 1060–1070, 2015.

[12] A. Y. Liu and J. E. Bowers, "Photonic integration with epitaxial III-V on silicon," *IEEE Journal of Selected Topics in Quantum Electronics*, vol. 24, no. 6, p. 6000412, 2018.

[13] S. Chen, W. Li, J. Wu, Q. Jiang, M. Tang, S. Shutts *et al.*, “Electrically pumped continuous-wave III-V quantum dot lasers on silicon,” *Nature Photonics*, vol. 10, pp. 307–311, 2016.

[14] H. Kawanami, “Heteroepitaxial technologies of III-V on Si,” *Solar Energy Materials and Solar Cells*, vol. 66, no. 1-4, pp. 479–486, 2001.

[15] J. C. Norman, D. Jung, Y. Wan, and J. E. Bowers, “Perspective: The future of quantum dot photonic integrated circuits,” *APL Photonics*, vol. 3, no. 3, pp. 030 901–1–030 901–20, 2018.

[16] T. Wang, H. Liu, A. Lee, F. Pozzi, and A. Seeds, “1.3-μm InAs/GaAs quantum-dot lasers monolithically grown on Si substrates,” *Optics Express*, vol. 19, no. 12, pp. 11 381–11 386, 2011.

[17] D. Liang and J. E. Bowers, “Recent progress in lasers on silicon,” *Nature Photonics*, vol. 4, no. 8, p. 511, 2010.

[18] J. C. Norman, Z. Zhang, D. Jung, C. Shang, M. Kennedy, M. Dumont *et al.*, “The importance of *p*-doping for quantum dot laser on silicon performance,” *IEEE Journal of Quantum Electronics*, vol. 55, no. 6, pp. 1–11, 2019.

[19] K. Li, Z. Liu, M. Tang, M. Liao, D. Kim, H. Deng *et al.*, “O-band InAs/GaAs quantum dot laser monolithically integrated on exact (001) Si substrate,” *Journal of Crystal Growth*, vol. 511, pp. 56–60, 2019.

[20] J. Kwoen, B. Jang, K. Watanabe, and Y. Arakawa, “High-temperature continuous-wave operation of directly grown InAs/GaAs quantum dot lasers on on-axis Si (001),” *Optics Express*, vol. 27, no. 3, pp. 2681–2688, 2019.

[21] D. Jung, J. Norman, Y. Wan, S. Liu, R. Herrick, J. Selvidge *et al.*, “Recent advances in InAs quantum dot lasers grown on on-axis (001) silicon by molecular beam epitaxy,” *Physica Status Solidi (a)*, vol. 216, no. 1, p. 1800602, 2019.

[22] D. Jung, R. Herrick, J. Norman, Y. Wan, A. C. Gossard, and J. E. Bowers, “High performance and reliable 1.3 μm InAs quantum dot lasers epitaxially grown on Si,” in *2018 23rd Opto-Electronics and Communications Conference (OECC)*, 2018, pp. 1–2.

[23] D. Jung, Z. Zhang, J. Norman, R. Herrick, M. Kennedy, P. Patel *et al.*, “Highly reliable low-threshold InAs quantum dot lasers on on-axis (001) Si with 87% injection efficiency,” *ACS Photonics*, vol. 5, no. 3, pp. 1094–1100, 2017.

[24] D. Jung, J. Norman, M. Kennedy, C. Shang, B. Shin, Y. Wan *et al.*, “High efficiency low threshold current 1.3 μm InAs quantum dot lasers on on-axis (001) GaP/Si,” *Applied Physics Letters*, vol. 111, no. 12, p. 122107, 2017.

[25] J. E. Bowers, J. Bovington, A. Liu, and A. Gossard, “A path to 300 mm hybrid silicon photonic integrated circuits,” in *2014 Optical Fiber Communications Conference and Exhibition (OFC)*, 2014, pp. 1–3.

[26] C. Cole, “Beyond 100G client optics,” *IEEE Communications Magazine*, vol. 50, no. 2, pp. s58–s66, 2012.

[27] X. Liu and F. Effenberger, “Emerging optical access network technologies for 5G wireless,” *IEEE/OSA Journal of Optical Communications and Networking*, vol. 8, no. 12, pp. B70–B79, 2016.

[28] V. Houtsma and D. van Veen, “Demonstration of symmetrical 25 Gbps TDM-PON with 31.5 dB optical power budget using only 10 Gbps optical components,” in *2015 European Conference on Optical Communication (ECOC)*, 2015, pp. 1–3.

[29] J. Gao, “Demonstration of the first 29dB power budget of 25-Gb/s 4-PAM system without optical amplifier for next generation access network,” in *2016 Optical Fiber Communication Conference and Exhibition (OFC)*, 2016, pp. Th1I–2.

[30] M. Tao, L. Zhou, S. Yao, D. Zou, S. Li, H. Lin, and X. Liu, “28-Gb/s/λ, TDM-PON with narrow filter compensation and enhanced FEC supporting 31.5 dB link loss budget after 20-km downstream transmission in the C-band,” in *2016 Optical Fiber Communications Conference and Exhibition (OFC)*, 2016, pp. 1–3.

[31] L. Yi, Z. Li, M. Bi, W. Wei, and W. Hu, “Symmetric 40-Gb/s TWDM-PON with 39-dB power budget,” *IEEE Photonics Technology Letters*, vol. 25, no. 7, pp. 644–647, 2013.

[32] C.-H. Yeh, C.-W. Chow, and C.-H. Hsu, “40-Gb/s time-division-multiplexed passive optical networks using downstream OOK and upstream OFDM modulations,” *IEEE Photonics Technology Letters*, vol. 22, no. 2, pp. 118–120, 2009.

[33] E. Agrell, M. Karlsson, A. Chraplyvy, D. J. Richardson, P. M. Krummrich, P. Winzer *et al.*, “Roadmap of optical communications,” *Journal of Optics*, vol. 18, no. 6, p. 063002, 2016.

[34] R. Blum, “Silicon photonics - the key to data centre connectivity,” *Optical Connection News*, vol. 10, no. Q3, pp. 33–34, 2017.

[35] C. Gunn, “CMOS photonics for high-speed interconnects,” *IEEE Micro*, vol. 26, no. 2, pp. 58–66, 2006.

[36] H. Liu, C. F. Lam, and C. Johnson, “Scaling optical interconnects in datacenter networks opportunities and challenges for WDM,” in *2010 18th IEEE Symposium on High Performance Interconnects*, 2010, pp. 113–116.

[37] Z. Haas and M. A. Santoro, “A mode-filtering scheme for improvement of the bandwidth-distance product in multimode fiber systems,” *Journal of Lightwave Technology*, vol. 11, no. 7, pp. 1125–1131, 1993.

[38] M. Nix, C. Qian, S. S.-H. Yam, and L. Huff, “Modal noise improvement in 10-Gb/s offset launch in multimode fiber link with multimode fiber taper,” in *2019 IEEE International Electromagnetics and Antenna Conference*, 2019, pp. 012–015.

[39] D. Patterson, I. De Sousa, and L.-M. Achard, “The future of packaging with silicon photonics,” *Chip Scale Review*, vol. 21, no. 1, pp. 1–10, 2017.

[40] M. Paniccia, M. Morse, and M. Saliv, “Integrated photonics,” in *Silicon photonics*, D. J. Lockwood and L. Pavesi, Eds. New York, USA: Springer-Verlag, 2004, vol. 94, pp. 51–88.

[41] T. Liljeberg, "Silicon photonics and the future of optical connectivity in the data center," in *2017 IEEE Optical Interconnects Conference*, 2017, pp. 1–2.

[42] C. Minkenberg and N. Kucharewki, "Integrated optics permeate datacenter networks," *Laser Focus World*, vol. 54, no. 10, pp. 27–30, 2018.

[43] C. V. Poulton, A. Yaacobi, D. B. Cole, M. J. Byrd, M. Raval, D. Vermeulen, and M. R. Watts, "Coherent solid-state LIDAR with silicon photonic optical phased arrays," *Optics Letters*, vol. 42, no. 20, pp. 4091–4094, 2017.

[44] P. Bhargava, T. Kim, C. Poulton, J. Notaros, A. Yaacobi, E. Timurdogan *et al.*, "Fully integrated coherent LiDAR in 3D-integrated silicon photonics/65nm CMOS," in *2019 Symposium on VLSI Circuits*, 2019, pp. C262–C263.

[45] B. Behroozpour, P. A. Sandborn, M. C. Wu, and B. E. Boser, "Lidar system architectures and circuits," *IEEE Communications Magazine*, vol. 55, no. 10, pp. 135–142, 2017.

[46] C. V. Poulton, D. B. Cole, A. Yaacobi, and M. R. Watts, "Frequency-modulated continuous-wave LIDAR module in silicon photonics," in *2016 Optical Fiber Communications Conference and Exhibition (OFC)*, 2016, pp. 1–3.

[47] Z. Wang, A. Abbasi, U. Dave, A. De Groote, S. Kumari, B. Kunert *et al.*, "Novel light source integration approaches for silicon photonics," *Laser & Photonics Reviews*, vol. 11, no. 4, p. 1700063, 2017.

[48] G. Girardin and S. Hallerau, "Photonics Applied: Biometric Security: The second wave of consumer biometrics is reshaping the VCSEL industry," *Laser Focus World*, vol. 55, no. 02, 2019.

[49] A. White, P. Khial, F. Salehi, B. Hassibi, and A. Hajimiri, "A silicon photonics computational lensless active-flat-optics imaging system," *Scientific Reports*, vol. 10, no. 1, pp. 1–9, 2020.

[50] C. Weimann, M. Lauermann, F. Hoeller, W. Freude, and C. Koos, "Silicon photonic integrated circuit for fast and precise dual-comb distance metrology," *Optics Express*, vol. 25, no. 24, pp. 30 091–30 104, 2017.

[51] J. T. Kirk, G. E. Fridley, J. W. Chamberlain, E. D. Christensen, M. Hochberg, and D. M. Ratner, "Multiplexed inkjet functionalization of silicon photonic biosensors," *Lab on a Chip*, vol. 11, no. 7, pp. 1372–1377, 2011.

[52] A. L. Washburn and R. C. Bailey, "Photonics-on-a-chip: recent advances in integrated waveguides as enabling detection elements for real-world, lab-on-a-chip biosensing applications," *Analyst*, vol. 136, no. 2, pp. 227–236, 2011.

[53] M. Hochberg, N. C. Harris, R. Ding, Y. Zhang, A. Novack, Z. Xuan, and T. Baehr-Jones, "Silicon photonics: the next fabless semiconductor industry," *IEEE Solid-State Circuits Magazine*, vol. 5, no. 1, pp. 48–58, 2013.

[54] J. Mendoza-Alvarez, F. Nunes, and N. Patel, "Refractive index dependence on free carriers for GaAs," *Journal of Applied Physics*, vol. 51, no. 8, pp. 4365–4367, 1980.

[55] B. R. Bennett, R. A. Soref, and J. A. Del Alamo, "Carrier-induced change in refractive index of InP, GaAs and InGaAsP," *IEEE Journal of Quantum Electronics*, vol. 26, no. 1, pp. 113–122, 1990.

[56] R. Soref and B. Bennett, "Electrooptical effects in silicon," *IEEE Journal of Quantum Electronics*, vol. 23, no. 1, pp. 123–129, 1987.

[57] J. McCaulley, V. Donnelly, M. Vernon, and I. Taha, "Temperature dependence of the near-infrared refractive index of silicon, gallium arsenide, and indium phosphide," *Physical Review B*, vol. 49, no. 11, pp. 7408–7417, 1994.

[58] S. Srinivasan, A. W. Fang, D. Liang, J. Peters, B. Kaye, and J. E. Bowers, "Design of phase-shifted hybrid silicon distributed feedback lasers," *Optics Express*, vol. 11, no. 10, pp. 9255–9261, 2011.

[59] N. Kobayashi, K. Sato, M. Namiwaka, K. Yamamoto, S. Watanabe, T. Kita *et al.*, "Silicon photonic hybrid ring-filter external cavity wavelength tunable lasers," *Journal of Lightwave Technology*, vol. 33, no. 6, pp. 1241–1246, 2015.

[60] M. A. Tran, D. Huang, T. Komljenovic, J. Peters, and J. E. Bowers, "A 2.5 kHz linewidth widely tunable laser with booster SOA integrated on silicon," in *2018 IEEE International Semiconductor Laser Conference (ISLC)*, Santa Fe, NM, USA, 2018, pp. 1–2.

[61] S. H. Macomber, "Design of high-power surface-emitting DFB lasers for suppression of filamentation," in *Proc. SPIE, High-Power Fiber and Semiconductor Lasers*, vol. 4993, San Jose, CA, USA, 2003, pp. 37–49.

[62] M. Radziunas and R. Čiegis, "Effective numerical algorithm for simulations of beam stabilization in broad area semiconductor lasers and amplifiers," *Mathematical Modelling and Analysis*, vol. 19, no. 5, pp. 627–646, 2014.

[63] W. W. Chow and S. W. Koch, "Free-carrier theory," in *Semiconductor-Laser Fundamentals: Physics of the Gain Materials.* Berlin, Heidelberg, New York: Springer Science & Business Media, 1999, pp. 36–71.

[64] S. Schneider, P. Borri, W. Langbein, U. Woggon, R. L. Sellin, D. Ouyang, and D. Bimberg, "Linewidth enhancement factor in InGaAs quantum-dot amplifiers," *IEEE Journal of Quantum Electronics*, vol. 40, no. 10, pp. 1423–1429, 2004.

[65] Y. Ohishi, A. Mori, T. Kanamori, K. Fujiura, and S. Sudo, "Fabrication of praseodymium-doped arsenic sulfide chalcogenide fiber for 1.3-μm fiber amplifiers," *Applied Physics Letters*, vol. 65, no. 1, pp. 13–15, 1994.

[66] T. Whitley, R. Wyatt, D. Szebesta, S. Davey, and J. R. Williams, "Quarter-watt output at 1.3 μm from a praseodymium-doped fluoride fiber amplifier pumped with a diode-pumped Nd:YLF laser," *IEEE Photonics Technology Letters*, vol. 5, no. 4, pp. 399–401, 1993.

[67] C. Tian and S. Kinoshita, "Analysis and control of transient dynamics of EDFA pumped by 1480-and 980-nm lasers," *Journal of Lightwave Technology*, vol. 21, no. 8, pp. 1728–1734, 2003.

[68] C. Hantschmann, P. P. Vasil'ev, S. Chen, M. Liao, A. J. Seeds, H. Liu *et al.*, "Gain switching of monolithic 1.3 μm InAs/GaAs quantum dot lasers on silicon," *Journal of Lightwave Technology*, vol. 36, no. 18, pp. 3837–3842, 2018.

[69] C. Hantschmann, P. P. Vasil'ev, A. Wonfor, S. Chen, M. Liao, A. J. Seeds *et al.*, "Understanding the bandwidth limitations in monolithic 1.3 μm InAs/GaAs quantum dot lasers on silicon," *Journal of Lightwave Technology*, vol. 37, no. 3, pp. 949–955, 2018.

[70] Z. Liu, C. Hantschmann, M. Tang, Y. Lu, J.-S. Park, M. Liao *et al.*, "Origin of defect tolerance in InAs/GaAs quantum dot lasers grown on silicon," *Journal of Lightwave Technology*, vol. 38, no. 2, pp. 240–248, 2019.

[71] C. Hantschmann, Z. Liu, M. Tang, A. Seeds, H. Liu, I. White, and R. Penty, "Impact of dislocations in monolithic III-V lasers on silicon: A theoretical approach," in *Proc. SPIE, Physics and Simulation of Optoelectronic Devices XXVIII*, vol. 11274, San Francisco, CA, USA, 2020.

[72] C. Hantschmann, Z. Liu, M. Tang, A. Seeds, H. Liu, I. White, and R. Penty, "Theoretical study on the effects of dislocations in monolithic III-V lasers on silicon," *Journal of Lightwave Technology*, 2020, published online (early access).

[73] C. Hantschmann, P. P. Vasil'ev, S. M. Chen, M. Liao, A. J. Seeds, H. Liu *et al.*, "Dynamic properties of monolithic 1.3 μm InAs/GaAs quantum dot lasers on silicon," in *2018 IEEE International Semiconductor Laser Conference (ISLC)*, 2018, pp. 1–2.

[74] C. Hantschmann, P. Vasil'ev, S. Chen, M. Liao, A. Seeds, H. Liu *et al.*, "Small-signal modulation and analysis of monolithic 1.3 μm InAs/GaAs quantum dot lasers on silicon," in *2018 European Conference on Optical Communication (ECOC)*, Rome, Italy, 2018, pp. 1–3.

[75] C. , P. Vasil'ev, S. Chen, M. Liao, A. Seeds, H. Liu *et al.*, "WC3.1 – Dynamics of quantum dot lasers on silicon," in *2019 IEEE Photonics Society Summer Topical Meeting Series (SUM)*, Fort Lauderdale, FL, USA, 2019, pp. 1–2.

[76] A. Einstein, "Zur Quantentheorie der Strahlung," *Physikalische Zeitschrift*, vol. 18, p. 124, 1917.

[77] T. H. Maiman, "Stimulated optical radiation in ruby," *Nature*, vol. 187, no. 4736, pp. 493–494, 1960.

[78] T. H. Maiman, "Ruby laser systems," Nov. 14 1967, US Patent 3,353,115.

[79] J. Hecht, "A short history of laser development," *Applied Optics*, vol. 49, no. 25, pp. F99–F122, 2010.

[80] L. Coldren and S. W. Corzine, "Ingredients," in *Diode Lasers and Photonic Integrated Circuits*, 1st ed. New York: John Wiley & Sons, Inc., 1995, pp. 1–27.

[81] L. Coldren and S. W. Corzine, "Gain and current relations," in *Diode Lasers and Photonic Integrated Circuits*, 1st ed. New York: John Wiley & Sons, Inc., 1995, pp. 111–184.

[82] G. P. Agrawal and N. K. Dutta, "Introduction," in *Semiconductor Lasers*, 2nd ed. Springer Science & Business Media, 2013, pp. 1–24.

[83] E. U. Rafailov, M. A. Cataluna, and E. A. Avrutin, “Semiconductor quantum dots for ultrafast optoelectronics,” in *Ultrafast Lasers Based on Quantum Dot Structures: Physics and Devices*. John Wiley & Sons, 2011, pp. 1–10.

[84] W. W. Chow, S. W. Koch, and M. I. Sargent, “Semiconductor laser diodes,” in *Semiconductor-Laser Physics*. Springer Science & Business Media, 2012, pp. 1–33.

[85] M. I. Nathan, W. P. Dumke, G. Burns, F. H. Dill Jr, and G. Lasher, “Stimulated emission of radiation from GaAs $p-n$ junctions,” *Applied Physics Letters*, vol. 1, no. 3, pp. 62–64, 1962.

[86] N. Holonyak Jr and S. Bevacqua, “Coherent (visible) light emission from $GaAs_{\mathbf{1-x}}P_x$ junctions,” *Applied Physics Letters*, vol. 1, no. 4, pp. 82–83, 1962.

[87] T. M. Quist, R. H. Rediker, R. Keyes, W. Krag, B. Lax, A. L. McWhorter, and H. Zeigler, “Semiconductor maser of GaAs,” *Applied Physics Letters*, vol. 1, no. 4, pp. 91–92, 1962.

[88] R. N. Hall, G. E. Fenner, J. Kingsley, T. Soltys, and R. Carlson, “Coherent light emission from GaAs junctions,” *Physical Review Letters*, vol. 9, no. 9, pp. 366–369, 1962.

[89] G. P. Agrawal and N. K. Dutta, “Laser structures and their performance,” in *Semiconductor Lasers*, 2nd ed. Springer Science & Business Media, 2013, pp. 180–230.

[90] Z. I. Alferov and R. Kazarinov, “Semiconductor laser with electric pumping,” *Inventor’s certificate 181737, application 950840, priority as of March 30*, 1963.

[91] H. Kroemer, “Semiconductor laser with electric pumping,” *US Patent 3,309,553 (filed Aug. 16, 1963)*, 1967.

[92] I. Hayashi, M. Panish, P. Foy, and S. Sumski, “Junction lasers which operate continuously at room temperature,” *Applied Physics Letters*, vol. 17, no. 3, pp. 109–111, 1970.

[93] Z. I. Alferov, V. Andreev, D. Garbuzov, Y. V. Zhilyaev, E. Morozov, E. Portnoi, and V. Trofim, “Investigation of the influence of the AlAs-GaAs heterostructure parameters on the laser threshold current and the realization of continuous emission at room temperature,” *Soviet Physysis – Semicond*, vol. 4, no. 9, pp. 1573–1575, 1971.

[94] J. Carroll, J. Whiteaway, and D. Plumb, “The semiconductor-diode laser,” in *Distributed Feedback Semiconductor Lasers*. London, United Kingdom: The Institution of Electrical Engineers, 1998, pp. 1–36.

[95] O. Hess, S. W. Koch, and J. V. Moloney, “Filamentation and beam propagation in broad-area semiconductor lasers,” *IEEE Journal of Quantum Electronics*, vol. 31, no. 1, pp. 35–43, 1995.

[96] S. L. Chuang, “Electromagnetics,” in *Physics of Optoelectronic Devices*. Wiley New York, 1995, pp. 200–111.

[97] G. P. Agrawal and N. K. Dutta, “Basic concepts,” in *Semiconductor Lasers*, 2nd ed. Springer Science & Business Media, 2013, pp. 25–73.

[98] L. Coldren and S. W. Corzine, “A phenomenological approach to diode lasers,” in *Diode Lasers and Photonic Integrated Circuits*, 1st ed. New York: John Wiley & Sons, Inc., 1995, pp. 28–64.

[99] M. Ettenberg, "Very low-threshold double-heterojunction $Al_xGa_{1-x}As$ injection lasers," *Applied Physics Letters*, vol. 27, no. 12, pp. 652–654, 1975.

[100] A. Cho, "Advances in molecular beam epitaxy (MBE)," *Journal of Crystal Growth*, vol. 111, no. 1-4, pp. 1–13, 1991.

[101] W. Tsang, "Advances in MOVPE, MBE, and CBE," *Journal of Crystal Growth*, vol. 120, no. 1-4, pp. 1–24, 1992.

[102] D. Bimberg, M. Kuntz, and M. Laemmlin, "Quantum dot photonic devices for lightwave communication," *Applied Physics A*, vol. 80, no. 6, pp. 1179–1182, 2005.

[103] R. Dingle and C. H. Henry, "Quantum effects in heterostructure lasers," Sep. 21 1976, US Patent 3,982,207.

[104] S. M. Sze and K. K. Ng, "Physics and properties of semiconductors - a review," in *Physics of Semiconductor Devices*, 3rd ed. Hoboken, New Jersey: John Wiley & Sons, Inc., 2006, pp. 7–78.

[105] S. L. Chuang, "Introduction," in *Physics of Optoelectronic Devices.* Wiley New York, 1995, pp. 1–20.

[106] M. Burt, "Gain spectra of quantum-well lasers," *Electronics Letters*, vol. 19, no. 6, pp. 210–211, 1983.

[107] Y. Arakawa and A. Yariv, "Quantum well lasers – Gain, spectra, dynamics," *IEEE Journal of Quantum Electronics*, vol. 22, no. 9, pp. 1887–1899, 1986.

[108] E. Yablonovitch and E. Kane, "Reduction of lasing threshold current density by the lowering of valence band effective mass," *Journal of Lightwave Technology*, vol. 4, no. 5, pp. 504–506, 1986.

[109] A. Adams, "Band-structure engineering for low-threshold high-efficiency semiconductor lasers," *Electronics Letters*, vol. 22, no. 5, pp. 249–250, 1986.

[110] P. J. Thijs, L. F. Tiemeijer, P. Kuindersma, J. Binsma, and T. Van Dongen, "High-performance 1.5 μm wavelength InGaAs-InGaAsP strained quantum well lasers and amplifiers," *IEEE Journal of Quantum Electronics*, vol. 27, no. 6, pp. 1426–1439, 1991.

[111] S. M. Sze and K. K. Ng, "LEDs and lasers," in *Physics of Semiconductor Devices*, 3rd ed. Hoboken, New Jersey: John Wiley & Sons, Inc., 2006, pp. 601–662.

[112] M. Asada, Y. Miyamoto, and Y. Suematsu, "Gain and the threshold of three-dimensional quantum-box lasers," *IEEE Journal of Quantum Electronics*, vol. 22, no. 9, pp. 1915–1921, 1986.

[113] M. Gioannini, P. Bardella, and I. Montrosset, "Time-domain traveling-wave analysis of the multimode dynamics of quantum dot Fabry-Perot lasers," *IEEE Journal of Selected Topics in Quantum Electronics*, vol. 21, no. 6, pp. 698–708, 2015.

[114] A. Markus and A. Fiore, "Modeling carrier dynamics in quantum-dot lasers," *Physica Status Solidi (a)*, vol. 201, no. 2, pp. 338–344, 2004.

[115] N. Ledentsov, "Long-wavelength quantum-dot lasers on GaAs substrates: from media to device concepts," *IEEE Journal of Selected Topics in Quantum Electronics*, vol. 8, no. 5, pp. 1015–1024, 2002.

[116] W. S. Rabinovich, G. C. Gilbreath, P. G. Goetz, R. Mahon, D. S. Katzer, K. Ikossi-Anastasiou *et al.*, "InGaAs multiple quantum well modulating retro-reflector for free-space optical communications," in *Proc. SPIE, Free-Space Laser Communication and Laser Imaging*, vol. 4489, San Jose, CA, USA, 2002, pp. 190–201.

[117] N. Kirstaedter, N. Ledentsov, M. Grundmann, D. Bimberg, V. Ustinov, S. Ruvimov *et al.*, "Low threshold, large T_0 injection laser emission from (InGa)As quantum dots," *Electronics Letters*, vol. 30, no. 17, pp. 1416–1417, 1994.

[118] H. Liu, I. Sellers, T. Badcock, D. Mowbray, M. Skolnick, K. Groom *et al.*, "Improved performance of 1.3 μm multilayer InAs quantum-dot lasers using a high-growth-temperature GaAs spacer layer," *Applied Physics Letters*, vol. 85, no. 5, pp. 704–706, 2004.

[119] H. Heidemeyer, S. Kiravittaya, C. Müller, N. Jin-Phillipp, and O. Schmidt, "Closely stacked InAs/GaAs quantum dots grown at low growth rate," *Applied Physics Letters*, vol. 80, no. 9, pp. 1544–1546, 2002.

[120] A. Y. Liu, S. Srinivasan, J. Norman, A. C. Gossard, and J. E. Bowers, "Quantum dot lasers for silicon photonics," *Photonics Research*, vol. 3, no. 5, pp. B1–B9, 2015.

[121] N. Kirstaedter, O. Schmidt, N. Ledentsov, D. Bimberg, V. Ustinov, A. Y. Egorov *et al.*, "Gain and differential gain of single layer InAs/GaAs quantum dot injection lasers," *Applied Physics Letters*, vol. 69, no. 9, pp. 1226–1228, 1996.

[122] T. W. Berg and J. Mørk, "Quantum dot amplifiers with high output power and low noise," *Applied Physics Letters*, vol. 82, no. 18, pp. 3083–3085, 2003.

[123] M. Sugawara, N. Hatori, M. Ishida, H. Ebe, Y. Arakawa, T. Akiyama *et al.*, "Recent progress in self-assembled quantum-dot optical devices for optical telecommunication: temperature-insensitive 10 Gbs^{-1} directly modulated lasers and 40 Gbs^{-1} signal-regenerative amplifiers," *Journal of Physics D: Applied Physics*, vol. 38, no. 13, p. 2126, 2005.

[124] K. Otsubo, N. Hatori, M. Ishida, S. Okumura, T. Akiyama, Y. Nakata *et al.*, "Temperature-insensitive eye-opening under 10-Gb/s modulation of 1.3-μm *p*-doped quantum-dot lasers without current adjustments," *Japanese Journal of Applied Physics*, vol. 43, no. 8B, p. L1124, 2004.

[125] A. Wilk, A. Kovsh, S. Mikhrin, C. Chaix, I. Novikov, M. Maximov *et al.*, "High-power 1.3 μm InAs/GaInAs/GaAs QD lasers grown in a multiwafer MBE production system," *Journal of Crystal Growth*, vol. 278, no. 1-4, pp. 335–341, 2005.

[126] A. Zhukov, M. Maksimov, and A. Kovsh, "Device characteristics of long-wavelength lasers based on self-organized quantum dots," *Semiconductors*, vol. 46, no. 10, pp. 1225–1250, 2012.

[127] S. Ghosh, S. Pradhan, and P. Bhattacharya, "Dynamic characteristics of high-speed $In_{0.4}Ga_{0.6}As$/GaAs self-organized quantum dot lasers at room temperature," *Applied Physics Letters*, vol. 81, no. 16, pp. 3055–3057, 2002.

[128] T. Kageyama, Q. Vo, K. Watanabe, K. Takemasa, M. Sugawara, S. Iwamoto, and Y. Arakawa, “Large modulation bandwidth (13.1 GHz) of 1.3 μm-range quantum dot lasers with high dot density and thin barrier layer,” in *2016 Compound Semiconductor Week (CSW)*, 2016, pp. 1–2.

[129] C. Wang, F. Grillot, and J. Even, “Impacts of wetting layer and excited state on the modulation response of quantum-dot lasers,” *IEEE Journal of Quantum Electronics*, vol. 48, no. 9, pp. 1144–1150, 2012.

[130] G. Liu, A. Stintz, H. Li, K. Malloy, and L. Lester, “Extremely low room-temperature threshold current density diode lasers using InAs dots in $In_{0.15}Ga_{0.85}As$ quantum well,” *Electronics Letters*, vol. 35, no. 14, pp. 1163–1165, 1999.

[131] T. Kageyama, K. Nishi, M. Yamaguchi, R. Mochida, Y. Maeda, K. Takemasa *et al.*, “Extremely high temperature (220°C) continuous-wave operation of 1300-nm-range quantum-dot lasers,” in *The European Conference on Lasers and Electro-Optics*, 2011, p. PDA_1.

[132] O. Shchekin, J. Ahn, and D. Deppe, “High temperature performance of self-organised quantum dot laser with stacked p-doped active region,” *Electronics Letters*, vol. 38, no. 14, pp. 712–713, 2002.

[133] M. Liao, S. Chen, Z. Liu, Y. Wang, L. Ponnampalam, Z. Zhou *et al.*, “Low-noise 1.3 μm InAs/GaAs quantum dot laser monolithically grown on silicon,” *Photonics Research*, vol. 6, no. 11, pp. 1062–1066, 2018.

[134] I. Joindot, “Measurements of relative intensity noise (RIN) in semiconductor lasers,” *Journal de Physique III*, vol. 2, no. 9, pp. 1591–1603, 1992.

[135] Y. Wan, S. Zhang, J. C. Norman, M. Kennedy, W. He, S. Liu *et al.*, “Tunable quantum dot lasers grown directly on silicon,” *Optica*, vol. 6, no. 11, pp. 1394–1400, 2019.

[136] D. O’Brien, S. Hegarty, G. Huyet, J. McInerney, T. Kettler, M. Laemmlin *et al.*, “Feedback sensitivity of 1.3 μm InAs/GaAs quantum dot lasers,” *Electronics Letters*, vol. 39, no. 25, pp. 1819–1820, 2003.

[137] G. P. Agrawal and N. K. Dutta, “Recombination mechanisms in semiconductors,” in *Semiconductor Lasers*, 2nd ed. Springer Science & Business Media, 2013, pp. 74–146.

[138] B.-S. Kim, Y. Chung, and J.-S. Lee, “An efficient split-step time-domain dynamic modeling of DFB/DBR laser diodes,” *IEEE Journal of Quantum Electronics*, vol. 36, no. 7, pp. 787–794, 2000.

[139] K. Williams, M. Thompson, and I. White, “Long-wavelength monolithic mode-locked diode lasers,” *New Journal of Physics*, vol. 6, no. 1, p. 179, 2004.

[140] A. Rae, *Monolithic mode-locked quantum-dot laser diodes: Experiment and simulation*. Cambridge, UK: Dissertation submitted at the University of Cambridge, 2009.

[141] T. W. Berg and J. Mørk, “Saturation and noise properties of quantum-dot optical amplifiers,” *IEEE Journal of Quantum Electronics*, vol. 40, no. 11, pp. 1527–1539, 2004.

[142] L. Coldren and S. W. Corzine, “Dynamic effects,” in *Diode Lasers and Photonic Integrated Circuits*, 1st ed. New York: John Wiley & Sons, Inc., 1995, pp. 185–261.

[143] A. Fiore and A. Markus, "Differential gain and gain compression in quantum-dot lasers," *IEEE Journal of Quantum Electronics*, vol. 43, no. 3, pp. 287–294, 2007.

[144] G. P. Agrawal and N. K. Dutta, "Rate equations and operating characteristics," in *Semiconductor Lasers*, 2nd ed. Springer Science & Business Media, 2013, pp. 231–318.

[145] P. P. Vasil'ev, "Ultrafast diode lasers in fiber optics communications," in *Ultrafast diode lasers.* Artech House Publishers, 1995, pp. 179–214.

[146] D. Gready, G. Eisenstein, M. Gioannini, I. Montrosset, D. Arsenijevic, H. Schmeckebier *et al.*, "On the relationship between small and large signal modulation capabilities in highly nonlinear quantum dot lasers," *Applied Physics Letters*, vol. 102, no. 10, p. 101107, 2013.

[147] R. Olshansky, P. Hill, V. Lanzisera, and W. Powazinik, "Frequency response of 1.3 μm InGaAsP high speed semiconductor lasers," *IEEE Journal of Quantum Electronics*, vol. 23, no. 9, pp. 1410–1418, 1987.

[148] S. Weisser, I. Esquivias, P. Tasker, J. Ralston, and J. Rosenzweig, "Impedance, modulation response, and equivalent circuit of ultra-high-speed $In_{0.35}Ga_{0.65}As/GaAs$ MQW lasers with p-doping," *IEEE Photonics Technology Letters*, vol. 6, no. 7, pp. 782–785, 1994.

[149] R. Nagarajan, M. Ishikawa, T. Fukushima, R. S. Geels, and J. E. Bowers, "High speed quantum-well lasers and carrier transport effects," *IEEE Journal of Quantum Electronics*, vol. 28, no. 10, pp. 1990–2008, 1992.

[150] H. Su and L. F. Lester, "Dynamic properties of quantum dot distributed feedback lasers: high speed, linewidth and chirp," *Journal of Physics D: Applied Physics*, vol. 38, no. 13, p. 2112, 2005.

[151] P. Bhattacharya, D. Klotzkin, O. Qasaimeh, W. Zhou, S. Krishna, and D. Zhu, "High-speed modulation and switching characteristics of In(Ga)As-Al(Ga)As self-organized quantum-dot lasers," *IEEE Journal of Selected Topics in Quantum Electronics*, vol. 6, no. 3, pp. 426–438, 2000.

[152] O. Kjebon, R. Schatz, S. Lourdudoss, S. Nilsson, and B. Stalnacke, "Modulation response measurements and evaluation of MQW InGaAsP lasers of various designs," in *Proc. SPIE, High-Speed Semiconductor Laser Sources*, vol. 2684, San Jose, CA, USA, 1996, pp. 138–152.

[153] A. Al-Omari, I. Al-Kofahi, and K. Lear, "Fabrication, performance and parasitic parameter extraction of 850 nm high-speed vertical-cavity lasers," *Semiconductor Science and Technology*, vol. 24, no. 9, p. 095024, 2009.

[154] M. Ishida, M. Matsuda, Y. Tanaka, K. Takada, M. Ekawa, T. Yamamoto *et al.*, "Temperature-stable 25-Gbps direct-modulation in 1.3-μm InAs/GaAs quantum dot lasers," in *CLEO: Science and Innovations*, 2012, pp. CM1I–2.

[155] W. Hofmann, N. Zhu, M. Ortsiefer, G. Bohm, J. Rosskopf, L. Chao *et al.*, "10-Gb/s data transmission using BCB passivated 1.55-μm InGaAlAs-InP VCSELs," *IEEE Photonics Technology Letters*, vol. 18, no. 2, pp. 424–426, 2006.

[156] Y.-G. Zhou, J. Duan, H. Huang, X.-Y. Zhao, C.-F. Cao, Q. Gong *et al.*, "Intensity noise and pulse oscillations of an InAs/GaAs quantum dot laser on germanium," *IEEE Journal of Selected Topics in Quantum Electronics*, vol. 25, no. 6, pp. 1–10, 2019.

[157] C. Cornet, Y. L'eger, and C. Robert, "Laser integration challenge," in *Integrated Lasers on Silicon.* London: ISTE Fress Ltd, 2016, pp. 1–30.

[158] R. D. Dupuis and C. J. Pinzone, "The growth of AlGaAs-GaAs lasers on Si substrates by metalorganic chemical vapor deposition," *Journal of Crystal Growth*, vol. 93, no. 1-4, pp. 434–442, 1988.

[159] T. Sasaki, H. Mori, M. Tachikawa, and T. Yamada, "Aging tests of InP-based laser diodes heteroepitaxially grown on Si substrates," *Journal of Applied Physics*, vol. 84, no. 12, pp. 6725–6728, 1998.

[160] D. L. Rode, "How much Al in the AlGaAs-GaAs laser?" *Journal of Applied Physics*, vol. 45, no. 9, pp. 3887–3891, 1974.

[161] B. Jalali and S. Fathpour, "Silicon Photonics," *Journal of Lightwave Technology*, vol. 24, no. 12, pp. 4600–4615, 2006.

[162] J. Wilson and J. Hawkes, "Fiber optical waveguides," in *Optoelectronics: An Introduction*, 3rd ed. Harlow, England: Prentice Hall, 1998, pp. 359–427.

[163] O. Boyraz and B. Jalali, "Demonstration of a silicon Raman laser," *Optics Express*, vol. 12, no. 21, pp. 5269–5273, 2004.

[164] H. Rong, R. Jones, A. Liu, O. Cohen, D. Hak, A. Fang, and M. Paniccia, "A continuous-wave Raman silicon laser," *Nature*, vol. 433, no. 17, pp. 725–728, 2005.

[165] H. Rong, Y.-H. Kuo, S. Xu, A. Liu, R. Jones, M. Paniccia *et al.*, "Monolithic integrated Raman silicon laser," *Optics Express*, vol. 14, no. 15, pp. 6705–6712, 2006.

[166] M. H. Nayfeh, S. Rao, N. Barry, J. Therrien, G. Belomoin, and a. C. S. Smith, A, "Observation of laser oscillation in aggregates of ultrasmall silicon nanoparticles," *Applied Physics Letters*, vol. 80, no. 1, pp. 121–123, 2002.

[167] J. Liu, X. Sun, R. Camacho-Aguilera, L. C. Kimerling, and J. Michel, "Ge-on-Si laser operating at room temperature," *Optics Letters*, vol. 35, no. 5, pp. 679–681, 2010.

[168] R. E. Camacho-Aguilera, Y. Cai, N. Pateil, J. T. Bessette, M. Romagnoli, L. C. Kimerling, and J. Michel, "An electrically pumped germanium laser," *Optics Express*, vol. 20, no. 10, pp. 11 316–11 320, 2012.

[169] C. Cornet, Y. L'eger, and C. Robert, "III-V lasers bonded on Si," in *Integrated Lasers on Silicon.* London: ISTE Press Ltd, 2016, pp. 52–77.

[170] E. A. Fitzgerald, M. T. Currie, S. B. Samavedam, T. A. Langdo, G. Taraschi, V. Yang *et al.*, "Dislocations in relaxed SiGe/Si heterostructures," *Physica Status Solidi A*, vol. 171, no. 1, pp. 227–238, 1999.

[171] C. Shang, J. C. Norman, N. Collins, I. MacFarlane, M. Dumont, S. Liu *et al.*, "Low-threshold epitaxially grown 1.3-µm InAs quantum dot lasers on patterned (001) Si," *IEEE Journal of Selected Topics in Quantum Electronics*, vol. 25, no. 6, p. 1502207, 2019.

[172] V. Yang, M. Groenert, C. Leitz, A. Pitera, M. Currie, and E. A. Fitzgerald, "Crack formation in GaAs heteroepitaxial films on Si and SiGe virtual substrates," *Journal of Applied Physics*, vol. 93, no. 7, pp. 3859–3865, 2003.

[173] M. Tachikawa and H. Mori, "Dislocation generation of GaAs on Si in the cooling stage," *Applied Physics Letters*, vol. 56, no. 22, pp. 2225–2227, 1990.

[174] Gourley, M. P L, Longerbone, S. L. Zhang, and H. Morko¸c, "Photoluminescence microscopy of epitaxial GaAs on Si," *Applied Physics Letters*, vol. 51, no. 8, pp. 599–601, 1987.

[175] A. Georgakilas, J. Stoemenos, K. Tsagaraki, P. Komninou, N. Flevaris, P. Panayotatos, and A. Christou, "Generation and annihilation of antiphase domain boundaries in GaAs on Si grown by molecular beam epitaxy," *Journal of Materials Research*, vol. 8, no. 8, pp. 1908–1921, 1993.

[176] Z. Zhou, B. Yin, and J. Michel, "On-chip light sources for silicon photonics," *Light: Science & Applications*, vol. 4, no. 11, p. e358, 2015.

[177] M. J. Wale, "Self aligned, flip chip assembly of photonic devices with electrical and optical connections," in *40th Conference Proceedings on Electronic Components and Technology*, 1990, pp. 34–41.

[178] S. Lindgren, H. Ahlfeldt, L. Backlin, L. Forssén, C. Vieider, H. Elderstig *et al.*, "24-GHz modulation bandwidth and passive alignment of flip-chip mounted DFB laser diodes," *IEEE Photonics Technology Letters*, vol. 9, no. 3, pp. 306–308, 1997.

[179] G. Lecarpentier, J. Mottet, J. Dumas, and K. Cooper, "High accuracy machine automated assembly for opto electronics," in *2000 Proceedings. 50th Electronic Components and Technology Conference*, 2000, pp. 1–4.

[180] R. Llorente, M. Morant, A. Brimont, and P. Sanchis, "The 5G fronthaul and enabling silicon photonics technology," in *Broadband Access Communication Technologies XIII*, vol. 10945, 2019, p. 1094508.

[181] G. Roelkens, L. Liu, D. Liang, R. Jones, A. Fang, B. Koch, and J. Bowers, "III-V/silicon photonics for on-chip and intra-chip optical interconnects," *Laser & Photonics Reviews*, vol. 4, no. 6, pp. 751–779, 2010.

[182] R. Blum, "Integrated silicon photonics for high-volume data center applications," in *Proc. SPIE, Optical Interconnects XX*, vol. 11286, San Francisco, CA, USA, 2020, p. 112860M.

[183] T. Komljenovic, D. Huang, P. Pintus, M. A. Tran, M. L. Davenport, and J. E. Bowers, "Photonic integrated circuits using heterogeneous integration on silicon," *Proceedings of the IEEE*, vol. 106, no. 12, pp. 2246–2257, 2018.

[184] P. A. Morton, M. J. Morton, C. Zhang, J. B. Khurgin, J. Peters, C. D. Morton, and J. E. Bowers, "High-power, high-linearity, heterogeneously integrated III-V on Si MZI modulators for RF photonics systems," *IEEE Photonics Journal*, vol. 11, no. 2, pp. 1–10, 2019.

[185] M. L. Davenport, S. Liu, and J. E. Bowers, "Integrated heterogeneous silicon/III-V mode-locked lasers," *Photonics Research*, vol. 6, no. 5, pp. 468–478, 2018.

[186] D. Huang, M. A. Tran, J. Guo, J. Peters, T. Komljenovic, A. Malik *et al.*, "High-power sub-kHz linewidth lasers fully integrated on silicon," *Optica*, vol. 6, no. 6, pp. 745–752, 2019.

[187] S. Uvin, S. Kumari, A. De Groote, S. Verstuyft, G. Lepage, P. Verheyen *et al.*, "1.3 µm InAs/GaAs quantum dot DFB laser integrated on a Si waveguide circuit by means of adhesive die-to-wafer bonding," *Optics Express*, vol. 26, no. 14, pp. 18 302–18 309, 2018.

[188] A. Abbasi, C. Spatharakis, G. Kanakis, N. S. André, H. Louchet, A. Katumba *et al.*, "High speed direct modulation of a heterogeneously integrated InP/SOI DFB laser," *Journal of Lightwave Technology*, vol. 34, no. 8, pp. 1683–1687, 2016.

[189] K. Van Gasse, R. Wang, and G. Roelkens, "27 dB gain III-V-on-silicon semiconductor optical amplifier with > 17 dBm output power," *Optics Express*, vol. 27, no. 1, pp. 293–302, 2019.

[190] R. Jones, P. Doussiere, J. B. Driscoll, W. Lin, H. Yu, Y. Akulova *et al.*, "Heterogeneously integrated InP/silicon photonics: Fabricating fully functional transceivers," *IEEE Nanotechnology Magazine*, vol. 13, no. 2, pp. 17–26, 2019.

[191] M. Fiorentino, D. Liang, G. Kurczveil, and R. G. Beausoleil, "Direct bandgap semiconductor bonded to silicon photonics," Jan. 29 2019, US Patent App. 10/192,857.

[192] D. Liang, X. Huang, G. Kurczveil, M. Fiorentino, and R. Beausoleil, "Integrated finely tunable microring laser on silicon," *Nature Photonics*, vol. 10, no. 11, pp. 719–722, 2016.

[193] A. Ramaswamy, J. E. Roth, E. Norberg, and B. Koch, "Thermal management for photonic integrated circuits," Jun. 7 2016, US Patent 9,360,620.

[194] B. R. Koch, E. J. Norberg, B. Kim, J. Hutchinson, J.-H. Shin, G. Fish, and A. Fang, "Integrated silicon photonic laser sources for telecom and datacom," in *National Fiber Optic Engineers Conference*, 2013, pp. PDP5C–8.

[195] J. M. Ramirez, H. Elfaiki, T. Verolet, C. Besancon, A. Gallet, D. Néel *et al.*, "III-V-on-silicon integration: From hybrid devices to heterogeneous photonic integrated circuits," *IEEE Journal of Selected Topics in Quantum Electronics*, vol. 26, no. 2, pp. 1–13, 2019.

[196] D. Liang, G. Roelkens, R. Baets, and J. E. Bowers, "Hybrid integrated platforms for silicon photonics," *Materials*, vol. 3, no. 3, pp. 1782–1802, 2010.

[197] J. E. Bowers and A. Y. Liu, "A comparison of four approaches to photonic integration," in *2017 Optical Networking and Communication Conference (OFC)*, 2017, p. M2B.4.

[198] C. A. Bower, E. Menard, S. Bonafede, J. W. Hamer, and R. S. Cok, "Transfer-printed microscale integrated circuits for high performance display backplanes," *IEEE Transactions on Components, Packaging and Manufacturing Technology*, vol. 1, no. 12, pp. 1916–1922, 2011.

[199] J. Justice, C. Bower, M. Meitl, M. C. Mooney, M. A. Gubbins, and B. Corbett, "Wafer-scale integration of group III-V lasers on silicon using transfer printing of epitaxial lasers," *Nature Photonics*, vol. 6, no. 9, pp. 610–614, 2012.

[200] M. A. Meitl, Z.-T. Zhu, V. Kumar, K. J. Lee, X. Feng, Y. Y. Huang *et al.*, "Transfer printing by kinetic control of adhesion to an elastomeric stamp," *Nature Materials*, vol. 5, no. 1, pp. 33–38, 2006.

[201] J. Zhang, B. Haq, J. O'Callaghan, A. Gocalinska, E. Pelucchi, A. J. Trindade *et al.*, "Transfer-printing-based integration of a III-V-on-silicon distributed feedback laser," *Optics Express*, vol. 26, no. 7, pp. 8821–8830, 2018.

[202] A. De Groote, P. Cardile, A. Z. Subramanian, A. M. Fecioru, C. Bower, D. Delbeke *et al.*, "Transfer-printing-based integration of single-mode waveguide-coupled III-V-on-silicon broadband light emitters," *Optics Express*, vol. 24, no. 13, pp. 13 754–13 762, 2016.

[203] M. Tang, S. Chen, J. Wu, Q. Jiang, K. Kennedy, P. Jurczak *et al.*, "Optimizations of defect filter layers for 1.3-μm InAs/GaAs quantum-dot lasers monolithically grown on Si substrates," *IEEE Journal of Selected Topics in Quantum Electronics*, vol. 22, no. 6, pp. 50–56, 2016.

[204] J. Yang, P. Jurczak, F. Cui, K. Li, M. Tang, L. Billiald *et al.*, "Thin Ge buffer layer on silicon for integration of III-V on silicon," *Journal of Crystal Growth*, vol. 514, pp. 109–113, 2019.

[205] J. Matthews, S. Mader, and T. Light, "Accommodation of misfit across the interface between crystals of semiconducting elements or compounds," *Journal of Applied Physics*, vol. 41, no. 9, pp. 3800–3804, 1970.

[206] R. Houdré and H. Morkoç, "Properties of GaAs on Si grown by molecular beam epitaxy," *Critical Reviews in Solid State and Material Sciences*, vol. 16, no. 2, pp. 91–114, 1990.

[207] C. Claeys, P. Hsu, L. He, Y. Mols, R. Langer, N. Waldron *et al.*, "Are extended defects a show stopper for future III-V CMOS technologies," in *Journal of Physics: Conference Series*, vol. 1190, no. 1, 2019, p. 012001.

[208] P. Petroff, O. Lorimor, and J. Ralston, "Defect structure induced during forward-bias degradation of GaP green-light-emitting diodes," *Journal of Applied Physics*, vol. 47, no. 4, pp. 1583–1588, 1976.

[209] Q. Feng, W. Wei, B. Zhang, H. Wang, J. Wang, H. Cong *et al.*, "O-band and C/L-band III-V quantum dot lasers monolithically grown on Ge and Si substrate," *Applied Sciences*, vol. 9, no. 3, p. 385, 2019.

[210] R. Roedel, A. Von Neida, R. Caruso, and L. Dawson, "The effect of dislocations in $Ga_{1-x}Al_xAs$:Si light-emitting diodes," *Journal of the Electrochemical Society*, vol. 126, no. 4, pp. 637–641, 1979.

[211] J. Selvidge, J. Norman, M. E. Salmon, E. T. Hughes, J. E. Bowers, R. Herrick, and K. Mukherjee, "Non-radiative recombination at dislocations in InAs quantum dots grown on silicon," *Applied Physics Letters*, vol. 115, no. 13, pp. 131 102–1–5, 2019.

[212] C. Andre, J. Boeckl, D. Wilt, A. Pitera, M. L. Lee, E. Fitzgerald *et al.*, "Impact of dislocations on minority carrier electron and hole lifetimes in GaAs grown on metamorphic SiGe substrates," *Applied Physics Letters*, vol. 84, no. 18, pp. 3447–3449, 2004.

[213] M. Yamaguchi and C. Amano, “Efficiency calculations of thin-film GaAs solar cells on Si substrates,” *Journal of Applied Physics*, vol. 58, no. 9, pp. 3601–3606, 1985.

[214] T. Liu, P. Petroff, and H. Kroemer, “Luminescence of GaAs/(Al,Ga)As superlattices grown on Si substrates, containing a high density of threading dislocations: Strong effect of the superlattice period,” *Journal of Applied Physics*, vol. 64, no. 12, pp. 6810–6814, 1988.

[215] S. Shutts, C. Allford, C. Spinnler, Z. Li, A. Sobiesierski, M. Tang *et al.*, “Degradation of III-V quantum dot lasers grown directly on silicon substrates,” *IEEE Journal of Selected Topics in Quantum Electronics*, 2019, published online.

[216] J. C. Norman, “III-V heteroepitaxy on silicon,” in *Quantum Dot Lasers for Silicon Photonics*. Santa Barbara, CA, USA: Dissertation submitted at the University of California, Santa Barbara, 2018, pp. 38–50.

[217] L. Kimerling, “Recombination enhanced defect reactions,” *Solid-State Electronics*, vol. 21, no. 11-12, pp. 1391–1401, 1978.

[218] P. Hutchinson, P. Dobson, S. O’hara, and D. Newman, “Defect structure of degraded heterojunction GaAlAs-GaAs lasers,” *Applied Physics Letters*, vol. 26, no. 5, pp. 250–252, 1975.

[219] P. Petroff and R. Hartman, “Rapid degradation phenomenon in heterojunction GaAlAs–GaAs lasers,” *Journal of Applied Physics*, vol. 45, no. 9, pp. 3899–3903, 1974.

[220] M. Liao, S. Chen, M. Tang, J. Wu, W. Li, K. Kennedy *et al.*, “Integrating III-V quantum dot lasers on silicon substrates for silicon photonics,” in *Proc. SPIE, Silicon Photonics XII*, vol. 10108, San Francisco, CA, USA, 2017, p. 101081A.

[221] Y. A. Biod, A. Boucherif, M. Myronov, A. Soltani, G. Patriarche, N. Braidy *et al.*, “Uprooting defect to enable high-performance III-V optoelectronic devices on silicon,” *Nature Communications*, vol. 10, no. 1, pp. 1–12, 2019.

[222] K. Linder, J. Phillips, O. Qasaimeh, X. Liu, S. Krishna, P. Bhattacharya, and J. Jiang, “Self-organized $In_{0.4}Ga_{0.6}As$ quantum-dot lasers grown on Si substrates,” *Applied Physics Letters*, vol. 74, no. 10, pp. 1355–1357, 1999.

[223] Z. Mi, P. Bhatttacharya, J. Yang, and K. Pipe, “Room-temperature self-organised $In_{0.5}Ga_{0.5}As$ quantum-dot lasers grown on silicon,” *Electronics Letters*, vol. 41, no. 13, pp. 742–743, 2017.

[224] Y. B. Bolkhovityanov and O. P. Pchelyakov, “GaAs epitaxy on Si substrates: Modern status of research and engineering,” *Physics–Uspekkhi*, vol. 51, no. 5, pp. 437–456, 2008.

[225] B. Kunert, Y. Mols, M. Baryshniskova, N. Waldron, A. Schulze, and R. Langer, “How to control defect formation in monolithic III/V hetero-epitaxy on (100) Si? A critical review on current approaches,” *Semiconductor Science and Technology*, vol. 33, no. 9, p. 093002, 2018.

[226] A. Y. Liu, J. Peters, X. Huang, D. Jung, J. Norman, M. L. Lee *et al.*, “Electrically pumped continuous-wave 1.3 μm quantum-dot lasers epitaxially grown on on-axis (001) GaP/Si,” *Optics Letters*, vol. 42, no. 2, pp. 338–341, 2017.

[227] S. Chen, M. Liao, M. Tang, J. Wu, M. Martin, T. Baron *et al.*, “Electrically pumped continuous-wave 1.3 μm InAs/GaAs quantum dot lasers monolithically grown on on-axis Si (001) substrates,” *Optics Express*, vol. 25, no. 5, pp. 4632–4639, 2017.

[228] J. Norman, M. Kennedy, J. Selvidge, Q. Li, Y. Wan, A. Y. Liu *et al.*, “Electrically pumped continuous wave quantum dot lasers epitaxially grown on patterned, on-axis (001) Si,” *Optics Express*, vol. 25, no. 4, pp. 3927–3934, 2017.

[229] Y. Wan, Q. Li, A. Y. Liu, A. C. Gossard, J. E. Bowers, E. L. Hu, and K. M. Lau, “Optically pumped 1.3 μm room-temperature InAs quantum-dot micro-disk lasers directly grown on (001) silicon,” *Optics Letters*, vol. 41, no. 7, pp. 1664–1667, 2016.

[230] B. Shi, Y. Han, Q. Li, and K. M. Lau, “1.55-μm lasers epitaxially grown on silicon,” *IEEE Journal of Selected Topics in Quantum Electronics*, vol. 25, no. 6, pp. 1–11, 2019.

[231] Q. Li, K. W. Ng, and K. M. Lau, “Growing antiphase-domain-free GaAs thin films out of highly ordered planar nanowire arrays on exact (001) silicon,” *Applied Physics Letters*, vol. 106, no. 7, p. 072105, 2015.

[232] B. Beaumont, P. Vennéguès, and P. Gibart, “Epitaxial lateral overgrowth of GaN,” *Physica Status Solidi (b)*, vol. 227, no. 1, pp. 1–43, 2001.

[233] Z. I. Kazi, P. Thilakan, T. Egawa, M. Umeno, and T. Jimbo, “Realization of GaAs/AlGaAs lasers on Si substrates using epitaxial lateral overgrowth by metalorganic chemical vapor deposition,” *Japanese Journal of Applied Physics*, vol. 40, no. 8R, pp. 4903–4906, 2001.

[234] H. Liu, T. Wang, Q. Jiang, R. Hogg, F. Tutu, F. Pozzi, and A. Seeds, “Long-wavelength InAs/GaAs quantum-dot laser diode monolithically grown on Ge substrate,” *Nature Photonics*, vol. 5, no. 7, p. 416, 2011.

[235] M. E. Groenert, A. J. Pitera, R. J. Ram, and E. A. Fitzgerald, “Improved room-temperature continuous wave GaAs/AlGaAs and InGaAs/GaAs/AlGaAs lasers fabricated on Si substrates via relaxed graded $\mathrm{Ge}_x\mathrm{Si}_{1-x}$ buffer layers,” *Journal of Vacuum Science & Technology B: Microelectronics and Nanometer Structures Processing, Measurement, and Phenomena*, vol. 21, no. 3, pp. 1064–1069, 2003.

[236] M. Currie, S. Samavedam, T. Langdo, C. Leitz, and E. Fitzgerald, “Controlling threading dislocation densities in Ge on Si using graded SiGe layers and chemical-mechanical polishing,” *Applied Physics Letters*, vol. 72, no. 14, pp. 1718–1720, 1998.

[237] M. L. Lee, E. A. Fitzgerald, M. T. Bulsara, M. T. Currie, and A. Lochtefeld, “Strained Si, SiGe, and Ge channels for high-mobility metal-oxide-semiconductor field-effect transistors,” *Journal of Applied Physics*, vol. 97, no. 1, pp. 011 101– – –27, 2005.

[238] G. Li, Y. Luo, X. Zheng, G. Masini, A. Mekis, S. Sahni *et al.*, “Improving CMOS-compatible Germanium photodetectors,” *Optics Express*, vol. 20, no. 24, pp. 26 345–26 350, 2012.

[239] A. Lee, Q. Jiang, M. Tang, A. Seeds, and H. Liu, “Continuous-wave InAs/GaAs quantum-dot laser diodes monolithically grown on Si substrate with low threshold current densities,” *Optics Express*, vol. 20, no. 20, pp. 22 181–22 187, 2012.

[240] A. Y. Liu, C. Zhang, A. Snyder, D. Lubyshev, J. M. Fastenau, A. W. Liu *et al.*, "MBE growth of *p*-doped 1.3 µm InAs quantum dot lasers on silicon," *Journal of Vacuum Science & Technology B, Nanotechnology and Microelectronics: Materials, Processing, Measurement, and Phenomena*, vol. 32, no. 2, p. 02C108, 2014.

[241] A. Y. Liu, C. Zhang, J. Norman, A. Snyder, D. Lubyshev, J. M. Fastenau *et al.*, "High performance continuous wave 1.3 µm quantum dot lasers on silicon," *Applied Physics Letters*, vol. 104, no. 4, p. 041104, 2014.

[242] "GaAs - Gallium Arsenide, Thermal properties," in *www.ioffe.ru/SVA/NSM/Semicond/GaAs/ thermal.html.* Ioffe Physico-Technical Institute Electronic Archive, Dec. 09 2019.

[243] "GaP - Gallium Phospide, Thermal properties," in *www.ioffe.ru/SVA/NSM/Semicond/GaP/thermal.html.* Ioffe Physico-Technical Institute Electronic Archive, Dec. 09 2019.

[244] "Si - Silicon, Thermal properties," in *www.ioffe.ru/SVA/NSM/Semicond/Si/ thermal.html.* Ioffe Physico-Technical Institute Electronic Archive, Dec. 09 2019.

[245] S. Liu, X. Wu, D. Jung, J. C. Norman, M. Kennedy, H. K. Tsang *et al.*, "High-channel-count 20 GHz passively mode-locked quantum dot laser directly grown on Si with 4.1 Tbit/s transmission capacity," *Optica*, vol. 6, no. 2, pp. 128–134, 2019.

[246] M. Tachikawa and M. Yamaguchi, "Film thickness dependence of dislocation density reduction in GaAs-on-Si substrates," *Applied Physics Letters*, vol. 56, no. 5, pp. 484–486, 1990.

[247] J. Ayers, "New model for the thickness and mismatch dependencies of threading dislocation densities in mismatched heteroepitaxial layers," *Journal of Applied Physics*, vol. 78, no. 6, pp. 3724–3726, 1995.

[248] J. R. Orchard, J. Wu, S. Chen, Q. Jiang, T. Ward, R. Beanland *et al.*, "Optimising the defect filter layer design for III/V QDs on Si for integrated laser applications," in *Prof. SPIE, Quantum Dots and Nanostructures: Synthesis, Characterization, and Modeling XII*, vol. 9373, San Francisco, CA, USA, 2015, p. 93730G.

[249] Z. Mi, J. Yang, P. Bhattacharya, P. Chan, and K. Pipe, "High performance self-organized InGaAs quantum dot lasers on silicon," *Journal of Vacuum Science & Technology B: Microelectronics and Nanometer Structures Processing, Measurement, and Phenomena*, vol. 24, no. 3, pp. 1519–1522, 2006.

[250] Z. Mi, J. Yang, P. Bhattacharya, G. Qin, and Z. Ma, "High-performance quantum dot lasers and integrated optoelectronics on Si," *Proceedings of the IEEE*, vol. 97, no. 7, pp. 1239–1249, 2009.

[251] Z. Mi, J. Yang, P. Bhattacharya, and D. Huffaker, "Self-organised quantum dots as dislocation filters: the case of GaAs-based lasers on silicon," *Electronics Letters*, vol. 42, no. 2, pp. 121–123, 2006.

[252] J. Yang, P. Bhattacharya, and Z. Mi, "High-performance $In_{0.5}Ga_{0.5}As$ quantum-dot lasers on silicon with multiple-layer quantum-dot dislocation filters," *IEEE Transactions on Electronic Devices*, vol. 54, no. 11, pp. 2849–2855, 2007.

[253] J. Kwoen, B. Jang, J. Lee, T. Kageyama, K. Watanabe, and Y. Arakawa, "All MBE grown InAs/GaAs quantum dot lasers on on-axis Si (001)," *Optics Express*, vol. 26, no. 9, pp. 11 568–11 576, 2018.

[254] D. Jung, P. G. Callahan, B. Shin, K. Mukherjee, A. C. Gossard, and J. E. Bowers, "Low threading dislocation density GaAs growth on on-axis GaP/Si (001)," *Journal of Applied Physics*, vol. 122, no. 22, p. 225703, 2017.

[255] J. Lee, H. Shichijo, H. Tsai, and R. Matyi, "Defect reduction by thermal annealing of GaAs layers grown by molecular beam epitaxy on Si substrates," *Applied Physics Letters*, vol. 50, no. 1, pp. 31–33, 1987.

[256] J.-M. Gerard and C. Weisbuch, "Semiconductor structure for optoelectronic components with inclusions," Dec. 24 1991, US Patent 5,075,742.

[257] V. Y. Aleshkin, N. Baidus, A. Dubinov, A. Fefelov, Z. Krasilnik, K. Kudryavtsev *et al.*, "Monolithically integrated InGaAs/GaAs/AlGaAs quantum well laser grown by MOCVD on exact Ge/Si (001) substrate," *Applied Physics Letters*, vol. 109, no. 6, p. 061111, 2016.

[258] J.-H. Kim, G. Radhakrishnan, A. Nouhi, J. K. Liu, R. J. Lang, and J. Katz, "High-power AlGaAs/GaAs DH stripe laser diodes on GaAs-on-Si prepared by migration-enhanced molecular beam epitaxy," *Japanese Journal of Applied Physics*, vol. 28, no. 5R, p. 791, 1989.

[259] T. C. Chong and C. G. Fonstad, "Low-threshold operation of AlGaAs/GaAs multiple quantum well lasers grown on Si substrates by molecular beam epitaxy," *Applied Physics Letters*, vol. 51, no. 4, pp. 221–223, 1987.

[260] J. Van der Ziel, R. Dupuis, R. Logan, R. Mikulyak, C. Pinzone, and A. Savage, "Low threshold pulsed and continuous laser oscillation from AlGaAs/GaAs double heterostructures grown by metalorganic chemical vapor deposition on Si substrates," *Applied Physics Letters*, vol. 50, no. 8, pp. 454–456, 1987.

[261] J.-H. Kim, R. J. Lang, G. Radhakrishnan, J. Katz, A. A. Narayanan, and R. R. Craig, "High-power low-threshold graded-index separate confinement heterostructure AlGaAs single quantum well lasers on Si substrates," *Applied Physics Letters*, vol. 55, no. 15, pp. 1492–1494, 1989.

[262] J. Van der Ziel, R. Dupuis, R. Logan, and C. Pinzone, "Degradation of GaAs lasers grown by metalorganic chemical vapor deposition on Si substrates," *Applied Physics Letters*, vol. 51, no. 2, pp. 89–91, 1987.

[263] D. P. Popescu, P. G. Eliseev, A. Stintz, and K. J. Malloy, "Carrier migration in structures with InAs quantum dots," *Journal of Applied Physics*, vol. 94, no. 4, pp. 2454–2458, 2003.

[264] S. A. Moore, L. O'Faolain, M. A. Cataluna, M. B. Flynn, M. V. Kotlyar, and T. F. Krauss, "Reduced surface sidewall recombination and diffusion in quantum-dot lasers," *IEEE Photonics Technology Letters*, vol. 18, no. 17, pp. 1861–1863, 2006.

[265] J. Huang, Y. Wan, D. Jung, J. Norman, C. Shang, Q. Li *et al.*, "Defect characterization of InAs/InGaAs quantum dot *pin* photodetector grown on GaAs-on-V-grooved-Si substrate," *ACS Photonics*, vol. 6, no. 5, pp. 1100–1105, 2019.

[266] N. El-Masry, J. Tarn, and N. Karam, "Interactions of dislocations in GaAs grown on Si substrates with InGaAs-GaAsP strained layered superlattices," *Journal of Applied Physics*, vol. 64, no. 7, pp. 3672–3677, 1988.

[267] A. Y. Liu, R. W. Herrick, O. Ueda, P. M. Petroff, A. C. Gossard, and J. E. Bowers, "Reliability of InAs/GaAs quantum dot lasers epitaxially grown on silicon," *IEEE Journal of Selected Topics in Quantum Electronics*, vol. 21, no. 6, pp. 690–697, 2015.

[268] S. Zhu, B. Shi, Q. Li, and K. M. Lau, "1.5 µm quantum-dot diode lasers directly grown on CMOS-standard (001) silicon," *Applied Physics Letters*, vol. 113, no. 22, p. 221103, 2018.

[269] Y. Xue, X. Wu, W. Luo, S. Zhu, H. K. Tsang, and K. M. Lau, "Characteristics of 1.3 µm electrically pumped InAs/AlGaInAs quantum dot lasers on (001) silicon," in *2019 IEEE Photonics Conference (IPC)*, 2019, pp. 1–2.

[270] B. Shi, Y. Han, Q. Li, and K. M. Lau, "1.55-µm lasers epitaxially grown on silicon," *IEEE Journal of Selected Topics in Quantum Electronics*, vol. 25, no. 6, pp. 1–11, 2019.

[271] J. Wu, S. Chen, A. Seeds, and H. Liu, "Quantum dot optoelectronic devices: lasers, photodetectors and solar cells," *Journal of Physics D: Applied Physics*, vol. 48, no. 36, p. 363001, 2015.

[272] S. Liu, D. Jung, J. Norman, M. Kennedy, A. Gossard, and J. Bowers, "490 fs pulse generation from passively mode-locked single section quantum dot laser directly grown on on-axis GaP/Si," *Electronics Letters*, vol. 54, no. 7, pp. 432–433, 2018.

[273] H. Huang, J. Duan, D. Jung, A. Y. Liu, Z. Zhang, J. Norman *et al.*, "Analysis of the optical feedback dynamics in InAs/GaAs quantum dot lasers directly grown on silicon," *JOSA B*, vol. 35, no. 11, pp. 2780–2787, 2018.

[274] A. Y. Liu, T. Komljenovic, M. L. Davenport, A. C. Gossard, and J. E. Bowers, "Reflection sensitivity of 1.3 µm quantum dot lasers epitaxially grown on silicon," *Optics Express*, vol. 25, no. 9, pp. 9535–9543, 2017.

[275] J. Orchard, S. Shutts, A. Sobiersierski, J. Wu, M. Tang, S. Chen *et al.*, "In situ annealing enhancement of the optical properties and laser device performance of InAs quantum dots grown on Si substrates," *Optics Express*, vol. 24, no. 6, pp. 6196–6202, 2016.

[276] D. Jung, R. Herrick, J. Norman, K. Turnlund, C. Jan, K. Feng *et al.*, "Impact of threading dislocation density on the lifetime of InAs quantum dot lasers on Si," *Applied Physics Letters*, vol. 112, no. 15, p. 153507, 2018.

[277] E. Gehrig and O. Hess, "Semiconductor laser theory: The Maxwell-Bloch equations," in *Spatio-Temporal Dynamics and Quantum Fluctuations in Semiconductor Lasers*. Berlin Heidelberg: Springer Verlag, 2003, pp. 14–24.

[278] E. Gehrig and O. Hess, "Mesoscopic spatiotemporal theory for quantum-dot lasers," *Physical Review A*, vol. 65, no. 3, pp. 033 804–1–033 804–16, 2002.

[279] D. W. Reschner, E. Gehrig, and O. Hess, "Spatio-temporal fluctuations and disorder in quantum dot lasers," in *Proc. SPIE Photonics Europe, Semiconductor Lasers and Laser Dynamics*, vol. 5452, Strasbourg, France, 2004, pp. 14–21.

[280] M. G. Thompson, *Ultra-Short Pulse Generation in Quantum Well and Quantum Dot Monolithic Mode-Locked Laser Diodes.* Cambridge: Dissertation submitted at the University of Cambridge, 2006.

[281] J. Carroll, J. Whiteaway, and D. Plumb, “Numerical modelling for DFB lasers,” in *Distributed Feedback Semiconductor Lasers.* London, United Kingdom: The Institution of Electrical Engineers, 1998, pp. 209–251.

[282] L. M. Zhang, S. F. Zu, M. C. Nowell, D. D. Marenac, J. E. Carroll, and R. G. S. Plumb, “Dynamic analysis of radiation and side-mode suppression in a second-order DFB laser using time-domain large-signal traveling wave model,” *IEEE Journal of Quantum Electronics*, vol. 30, no. 6, pp. 1389–1395, 1994.

[283] M. Gioannini and M. Rossetti, “Time-domain traveling wave model of quantum dot DFB lasers,” *IEEE Journal of Selected Topics in Quantum Electronics*, vol. 17, no. 5, pp. 1318–1326, 2011.

[284] T. W. Berg, J. Mørk, and J. M. Hvam, “Gain dynamics and saturation in semiconductor quantum dot amplifiers,” *New Journal of Physics*, vol. 6, no. 1, p. 178, 2004.

[285] C. Tong, S. Yoon, and C. Liu, “Rate equation model of the negative characteristic temperature of InAs/GaAs quantum dot lasers,” *Journal of Applied Physics*, vol. 101, no. 10, p. 104506, 2007.

[286] S. A. Gioannini, M. and I. Montrosset, “Simulations of differential gain and linewidth enhancement factor of quantum dot semiconductor lasers,” *Optical and Quantum Electronics*, vol. 38, no. 4-6, pp. 381–394, 2006.

[287] T. Müller, F. F. Schrey, G. Strasser, and K. Unterrainer, “Ultrafast intraband spectroscopy of electron capture and relaxation in InAs/GaAs quantum dots,” *Applied Physics Letters*, vol. 83, no. 17, pp. 3572–3573, 2003.

[288] K. Lüdge and E. Schöll, “Quantum-dot lasers - desynchronized nonlinear dynamics of electrons and holes,” *IEEE Journal of Quantum Electronics*, vol. 45, no. 11, pp. 1396–1403, 2009.

[289] D. McDonald and F. O’Dowd, “Comparison of two- and three-level rate equations in the modeling of quantum-well lasers,” *IEEE Journal of Quantum Electronics*, vol. 31, no. 11, pp. 1927–1934, 1995.

[290] P. Vankwikelberge, G. Morthier, and R. Baets, “CLADISS – A longitudinal multimode model for the analysis of the static, dynamic and stochastic behaviour of diode lasers with distributed feedback,” *IEEE Journal of Quantum Electronics*, vol. 26, no. 10, pp. 1728–1741, 2000.

[291] J. E. Carroll and L. M. Zhang, “Large-signal dynamic model of the DFB laser,” *IEEE Journal of Quantum Electronics*, vol. 28, no. 3, pp. 604–611, 1992.

[292] W. Li, W.-P. Huang, X. Li, and J. Hong, “Multiwavelength gain-coupled DFB laser cascade: design modeling and simulation,” *IEEE Journal of Quantum Electronics*, vol. 36, no. 10, pp. 1110–1116, 2000.

[293] J. Duan, H. Huang, D. Jung, Z. Zhang, J. Norman, J. Bowers, and F. Grillot, "Semiconductor quantum dot lasers epitaxially grown on silicon with low linewidth enhancement factor," *Applied Physics Letters*, vol. 112, no. 25, p. 251111, 2018.

[294] T. L. Koch and J. E. Bowers, "Nature of wavelength chirping in directly modulated semiconductor lasers," *Electronics Letters*, vol. 20, no. 25/26, pp. 1038–1040, 1984.

[295] C. H. Henry, R. A. Logan, and K. A. Bertness, "Spectral dependence of the change in refractive index due to carrier injection in GaAs lasers," *Journal of Applied Physics*, vol. 52, no. 7, pp. 4457–4461, 1981.

[296] M. Osinski and J. Buss, "Linewidth broadening factor in semiconductor lasers – an overview," *IEEE Journal of Quantum Electronics*, vol. QE-23, no. 1, pp. 9–29, 1987.

[297] C. H. Henry, "Theory of the linewidth of semiconductor lasers," *IEEE Journal of Quantum Electronics*, vol. QE-18, no. 2, pp. 259–264, 1982.

[298] S. Melnik, G. Huyet, and A. V. Uskov, "The linewidth enhancement factor α of quantum dot semiconductor lasers," *Optics Express*, vol. 14, no. 7, pp. 2950–2955, 2006.

[299] S. Murata, A. Tomita, , and A. Suzuki, "Influence of free carrier plasma effect on carrier-induced refractive index change for quantum-well lasers," *IEEE Photonics Technology Letters*, vol. 5, no. 1, pp. 16–19, 1993.

[300] M. Ishida, N. Hatori, T. Akiyama, K. Otsubo, Y. Nakata, H. Ebe *et al.*, "Photon lifetime dependence of modulation efficiency and K factor in 1.3 μm self-assembled InAs/GaAs quantum-dot lasers: Impact of capture time and maximum modal gain on modulation bandwidth," *Applied Physics Letters*, vol. 85, no. 18, pp. 4145–4147, 2004.

[301] W. W. Chow, A. Y. Liu, A. C. Gossard, and J. E. Bowers, "Extraction of inhomogeneous broadening and nonradiative losses in InAs quantum-dot lasers," *Applied Physics Letters*, vol. 107, no. 17, p. 171106, 2015.

[302] K. Sun, A. Kechiantz, B. Lee, and C. Lee, "Ultrafast carrier capture and relaxation in modulation-doped InAs quantum dots," *Applied Physics Letters*, vol. 88, no. 16, p. 163117, 2006.

[303] P. Bardella, M. Rossetti, and I. Montrosset, "Modeling of broadband chirped quantum-dot super-luminescent diodes," *IEEE Journal of Selected Topics in Quantum Electronics*, vol. 15, no. 3, pp. 785–791, 2009.

[304] K. Gündoğdu, K. Hall, T. F. Boggess, D. Deppe, and O. Shchekin, "Ultrafast electron capture into *p*-modulation-doped quantum dots," *Applied Physics Letters*, vol. 85, no. 20, pp. 4570–4572, 2004.

[305] S. Sauvage, P. Boucaud, F. Glotin, R. Prazeres, J.-M. Ortega, A. Lemaıtre *et al.*, "Saturation of intraband absorption and electron relaxation time in n-doped InAs/GaAs self-assembled quantum dots," *Applied Physics Letters*, vol. 73, no. 26, pp. 3818–3821, 1998.

[306] D. Bimberg, N. Kirstaedter, N. Ledentsov, Z. I. Alferov, P. Kop'Ev, and V. Ustinov, "InGaAs-GaAs quantum-dot lasers," *IEEE Journal of Selected Topics in Quantum Electronics*, vol. 3, no. 2, pp. 196–205, 1997.

[307] M. Ishida, M. Sugawara, T. Yamamoto, N. Hatori, H. Ebe, Y. Nakata, and Y. Arakawa, “Theoretical study on high-speed modulation of Fabry-Pérot and distributed-feedback quantum-dot lasers: K-factor-limited bandwidth and 10 Gbit/s eye diagrams,” *Journal of Applied Physics*, vol. 101, no. 1, p. 013108, 2007.

[308] “Rate equations for 1.3-μm dots-under-a-well and dots-in-a-well self-assembled InAs-GaAs quantum-dot lasers.”

[309] M. Gioannini and I. Montrosset, “Numerical analysis of the frequency chirp in quantum-dot semiconductor lasers,” *IEEE Journal of Quantum Electronics*, vol. 43, no. 10, pp. 941–949, 2007.

[310] F. Grillot, B. Dagens, J.-G. Provost, H. Su, and L. F. Lester, “Gain compression and above-threshold linewidth enhancement factor in 1.3-μm InAs-GaAs quantum-dot lasers,” *IEEE Journal of Quantum Electronics*, vol. 44, no. 10, pp. 946–951, 2008.

[311] A. Kovsh, N. Maleev, A. Zhukov, S. Mikhrin, A. Vasil’ev, E. Semenova *et al.*, “InAs/InGaAs/GaAs quantum dot lasers of 1.3 μm range with enhanced optical gain,” *Journal of Crystal Growth*, vol. 251, no. 1-4, pp. 729–736, 2003.

[312] D. L. Huffaker, G. Park, Z. Zou, O. Shchekin, and D. G. Deppe, “Continuous-wave low-threshold performance of 1.3-μm InGaAs-GaAs quantum-dot lasers,” *IEEE Journal of Selected Topics in Quantum Electronics*, vol. 6, no. 3, pp. 452–461, 2000.

[313] C. Tong, D. Xu, and S. F. Yoon, “Carrier relaxation and modulation response of 1.3-μm InAs-GaAs quantum dot lasers,” *Journal of Lightwave Technology*, vol. 27, no. 23, pp. 5442–5450, 2009.

[314] S. Kim, Y. Wang, M. Keever, and J. Harris, “High-frequency modulation characteristics of 1.3-μm InGaAs quantum dot lasers,” *IEEE Photonics Technology Letters*, vol. 16, no. 2, pp. 377–379, 2004.

[315] C. Xing and E. Avrutin, “Multimode spectra and active mode locking potential of quantum dot lasers,” *Journal of Applied Physics*, vol. 97, no. 10, p. 104301, 2005.

[316] E. Gehrig and O. Hess, “Dynamic amplitude-phase coupling in quantum-dot lasers,” *Applied Physics Letters*, vol. 86, no. 20, p. 203116, 2005.

[317] T. Newell, D. Bossert, A. Stintz, B. Fuchs, K. Malloy, and L. Lester, “Gain and linewidth enhancement factor in InAs quantum-dot laser diodes,” *IEEE Photonics Technology Letters*, vol. 11, no. 12, pp. 1527–1529, 1999.

[318] J. Carroll, J. Whiteaway, and D. Plumb, “Gain, loss and spontaneous emission,” in *Distributed Feedback Semiconductor Lasers*. London, United Kingdom: The Institution of Electrical Engineers, 1998, pp. 37–75.

[319] M. Sugawara and M. Usami, “Quantum dot devices: Handling the heat,” *Nature Photonics*, vol. 3, no. 1, pp. 30–31, 2009.

[320] A. Markus, J. X. Chen, O. Gauthier-Lafaye, J.-G. Provost, C. Paranthoën, and A. Fiore, “Impact of intraband relaxation on the performance of a quantum-dot laser,” *IEEE Journal of Selected Topics in Quantum Electronics*, vol. 9, no. 5, pp. 1308–1314, 2003.

[321] H. Schneider and K. V. Klitzing, “Thermionic emission and gaussian transport of holes in a GaAs/Al_xGa_{1-x}As multiple-quantum-well structure,” *Physical Review B*, vol. 38, no. 9, pp. 6160–6165, 1988.

[322] C. Y. Jin, T. J. Badcock, H.-Y. Liu, K. M. Groom, R. J. Royce, D. J. Mowbray, and M. Hopkinson, “Observation and modeling of a room-temperature negative characteristic temperature of 1.3-μm p-type modulation-doped quantum-dot laser,” *IEEE Journal of Quantum Electronics*, vol. 42, no. 12, pp. 1259–1265, 2006.

[323] C. Wang and Y. Zhou, “Dynamics of InAs/GaAs quantum dot lasers epitaxially grown on Ge or Si substrate,” *Journal of Semiconductors*, vol. 40, no. 10, p. 101306, 2019.

[324] J. R. Orchard, C. Woodhead, S. Shutts, J. Wu, A. Sobiesierski, R. J. Young *et al.*, “Analysing radiative and non-radiative recombination in InAs QDs on Si for integrated laser applications,” in *Proc. SPIE, Quantum Dots and Nanostructures: Growth, Characterization, and Modeling XIII*, vol. 9758, San Francisco, CA, USA, 2016, p. 975809.

[325] J. Wang, Y. Bai, H. Liu, Z. Cheng, M. Tang, S. Chen *et al.*, “Optimization of 1.3 μm InAs/GaAs quantum dot lasers epitaxially grown on silicon: Taking the optical loss of metamorphic epilayers into account,” *Laser Physics*, vol. 28, no. 12, p. 126206, 2018.

[326] S. Shutts, C. Allford, C. Spinnler, Z. Li, M. Tang, H. Liu, and P. Smowton, “Degradation studies of InAs/GaAs QD lasers grown on Si,” in *2018 IEEE International Semiconductor Laser Conference (ISLC)*, Santa Fe, NM, USA, 2018, pp. 1–2.

[327] P. Crump, G. Erbert, H. Wenzel, C. Frevert, C. M. Schultz, K.-H. Hasler *et al.*, “Efficient high-power laser diodes,” *IEEE Journal of Selected Topics in Quantum Electronics*, vol. 19, no. 4, p. 1501211, 2013.

[328] P. Crump, W. Dong, M. Grimshaw, J. Wang, S. Patterson, D. Wise *et al.*, “100-W+ diode laser bars show $> 71\%$ power conversion from 790-nm to 1000-nm and have clear route to $> 85\%$,” in *Proc. SPIE, High-Power Diode Laser Technology and Applications V*, vol. 6456, San Jose, CA, USA, 2007, p. 64560M.

[329] K. Nishi, H. Saito, S. Sugou, and J.-S. Lee, “A narrow photoluminescence linewidth of 21 meV at 1.35 μm from strain-reduced InAs quantum dots covered by $In_{0.2}Ga_{0.8}As$ grown on GaAs substrates,” *Applied Physics Letters*, vol. 74, no. 8, pp. 1111–1113, 1999.

[330] Z. Zhang, D. Jung, J. C. Norman, P. Patel, W. W. Chow, and J. E. Bowers, “Effects of modulation *p* doping in InAs quantum dot lasers on silicon,” *Applied Physics Letters*, vol. 113, no. 6, p. 061105, 2018.

[331] S. Liu, J. C. Norman, D. Jung, M. Kennedy, A. C. Gossard, and J. E. Bowers, “Monolithic 9 GHz passively mode locked quantum dot lasers directly grown on on-axis (001) Si,” *Applied Physics Letters*, vol. 113, no. 4, p. 041108, 2018.

[332] E. Le Ru, A. Bennett, C. Roberts, and R. Murray, “Strain and electronic interactions in InAs/GaAs quantum dot multilayers for 1300 nm emission,” *Journal of Applied Physics*, vol. 91, no. 3, pp. 1365–1370, 2002.

[333] M. Radziunas, J. Fuhrmann, A. Zeghuzi, H.-J. Wünsche, T. Koprucki, C. Brée *et al.*, *Efficient coupling of electro-optical and heat-transport models for broad-area semiconductor lasers.* Berlin: Weierstraß-Institut für Angewandte Analysis und Stochastik, 2018.

[334] K. Lüdge, E. Schöll, E. Viktorov, and T. Erneux, “Analytical approach to modulation properties of quantum dot lasers,” *Journal of Applied Physics*, vol. 109, no. 10, p. 103112, 2011.

[335] W. Li, X. Li, and W.-P. Huang, “A traveling-wave model of laser diodes with consideration for thermal effects,” *Optical and Quantum Electronics*, vol. 36, no. 8, pp. 709–724, 2004.

[336] X. Li and W.-P. Huang, “Simulation of DFB semiconductor lasers incorporating thermal effects,” *IEEE Journal of Quantum Electronics*, vol. 31, no. 10, pp. 1848–1855, 1995.

[337] M. Ettenberg, “Effects of dislocation density on the properties of liquid phase epitaxial GaAs,” *Journal of Applied Physics*, vol. 45, no. 2, pp. 901–906, 1974.

[338] T. L. Paoli and B. W. Hakki, “CW degradation at 300 °K of GaAs double-heterostructure junction lasers. I. Emission spectra,” *Journal of Applied Physics*, vol. 44, no. 9, pp. 4108–4112, 1973.

[339] M. Buffolo, F. Samparisi, C. De Santi, D. Jung, J. Norman, J. Bowers *et al.*, “Physical origin of the optical degradation of InAs quantum dot lasers,” *IEEE Journal of Quantum Electronics*, vol. 55, no. 3, p. 2000607, 2019.

[340] M. Buffolo, F. Samparisi, C. De Santi, D. Jung, J. Norman, J. Bowers *et al.*, “Investigation of current-driven degradation of 1.3 μm quantum-dot lasers epitaxially grown on silicon,” *IEEE Journal of Selected Topics in Quantum Electronics*, vol. 26, no. 2, p. 1900208, 2020.

[341] C. Donolato, “Modeling the effect of dislocations on the minority carrier diffusion length of a semiconductor,” *Journal of Applied Physics*, vol. 84, no. 5, pp. 2656–2664, 1998.

[342] W. Harding, I. Blenkinsop, and D. Wight, “Dislocation-limited minority-carrier lifetime in n-type GaP,” *Electronics Letters*, vol. 12, no. 19, pp. 503–504, 1976.

[343] H. Casey Jr, B. Miller, and E. Pinkas, “Variation of minority-carrier diffusion length with carrier concentration in GaAs liquid-phase epitaxial layers,” *Journal of Applied Physics*, vol. 44, no. 3, pp. 1281–1287, 1973.

[344] L. Aukerman, M. Millea, and M. McColl, “Diffusion lengths of electrons and holes in GaAs,” *Journal of Applied Physics*, vol. 38, no. 2, pp. 685–690, 1967.

[345] D. Ritter, E. Zeldov, and K. Weiser, “Steady-state photocarrier grating technique for diffusion length measurement in photoconductive insulators,” *Applied Physics Letters*, vol. 49, no. 13, pp. 791–793, 1986.

[346] T. Suzuki and Y. Matsumoto, “Effects of dislocations on photoluminescent properties in liquid phase epitaxial GaP,” *Applied Physics Letters*, vol. 26, no. 8, pp. 431–433, 1975.

[347] W. Nakwaski and M. Osinski, “On the thermal resistance of vertical-cavity surface-emitting lasers,” *Optical and Quantum Electronics*, vol. 29, no. 9, pp. 883–892, 1997.

[348] J. W. Scott, R. S. Geels, S. W. Corzine, and L. A. Coldren, “Modeling temperature effects and spatial hole burning to optimize vertical-cavity surface-emitting laser performance,” *IEEE Journal of Quantum Electronics*, vol. 29, no. 5, pp. 1295–1308, 1993.

[349] T. Windhorn, G. Metze, B.-Y. Tsaur, and J. C. Fan, “AlGaAs double-heterostructure diode lasers fabricated on a monolithic GaAs/Si substrate,” *Applied Physics Letters*, vol. 45, no. 4, pp. 309–311, 1984.

[350] M. E. Groenert, C. W. Leitz, A. J. Pitera, V. Yang, H. Lee, R. J. Ram, and E. A. Fitzgerald, “Monolithic integration of room-temperature cw GaAs/AlGaAs lasers on Si substrates via relaxed graded GeSi buffer layers,” *Journal of Applied Physics*, vol. 93, no. 1, pp. 362–367, 2003.

[351] S. Y. Karpov and Y. N. Makarov, “Dislocation effect on light emission efficiency in gallium nitride,” *Applied Physics Letters*, vol. 81, no. 25, pp. 4721–4723, 2002.

[352] T. Sugahara, H. Sato, M. Hao, Y. Naoi, S. Kurai, S. Tottori *et al.*, “Direct evidence that dislocations are non-radiative recombination centers in GaN,” *Japanese Journal of Applied Physics*, vol. 37, no. 4A, p. L398, 1998.

[353] L. Chernyak, A. Osinsky, and A. Schulte, “Minority carrier transport in GaN and related materials,” *Solid-State Electronics*, vol. 45, no. 9, pp. 1687–1702, 2001.

[354] S. Watanabe, Y. Kakuta, and O. Hashimoto, “Analytical study of rectangle wave propagation in electromangetic field using FDTD, CIP, and R-CIP methods,” *Microwave and Optical Technology Letters*, vol. 48, no. 10, pp. 1940–1943, 2006.

[355] K. Löhnert and E. Kubalek, “The cathodoluminescence contrast formation of localized non-radiative defects in semiconductors,” *Physica Status Solidi (a)*, vol. 83, no. 1, pp. 307–314, 1984.

[356] J. Duan, H. Huang, B. Dong, J. C. Norman, Z. Zhang, J. E. Bowers, and F. Grillot, “Dynamic and nonlinear properties of epitaxial quantum dot lasers on silicon for isolator-free integration,” *Photonics Research*, vol. 7, no. 11, pp. 1222–1228, 2019.

[357] G. Stringfellow, P. Lindquist, T. Cass, and R. Burmeister, “Dislocations in vapor phase epitaxial GaP,” *Journal of Electronic Materials*, vol. 3, no. 2, pp. 497–515, 1974.

[358] M. Sugo, H. Mori, Y. Sakai, and Y. Itoh, “Stable cw operation at room temperature of a 1.5-µm wavelength multiple quantum well laser on a Si substrate,” *Applied Physics Letters*, vol. 60, no. 4, pp. 472–473, 1992.

[359] B. Shi, H. Zhao, L. Wang, B. Song, S. T. S. Brunelli, and J. Klamkin, “Continuous-wave electrically pumped 1550 nm lasers epitaxially grown on on-axis (001) silicon,” *Optica*, vol. 6, no. 12, pp. 1507–1514, 2019.

[360] B. Shi, H. Zhao, L. Wang, S. T. Š. Brunelli, B. Song, and J. Klamkin, “Room temperature continuous wave electrically pumped 1.55 µm quantum well lasers epitaxially grown on (001) Si,” in *Asia Communications and Photonics Conference*, 2019, pp. S3H–5.

[361] B. Shi, S. Pinna, B. Song, H. Zhao, and J. Klamkin, “Thermal impedance and gain switching of 1550 nm room temperature continuous-wave electrically pumped laser diode monolithically grown on silicon,” in *Optical Fiber Communication Conference*, 2020, pp. T4H–1.

[362] F. J. Effenberger, “Industrial trends and roadmap of access,” *Journal of Lightwave Technology*, vol. 35, no. 5, pp. 1142–1146, 2016.

[363] M. Tao, J. Zheng, X. Dong, L. Zhou, H. Zeng, Y. Luo *et al.*, "Improved dispersion tolerance for 50G-PON downstream transmission via receiver-side equalization," in *Optical Fiber Communication Conference*, 2019, pp. M2B–3.

[364] P. P. Vasil'ev, "Gain and Q-switching in diode lasers," in *Ultrafast diode lasers.* Norwood, MA, USA: Artech House Publishers, 1995, pp. 53–94.

[365] S. Schuster and H. Haug, "Analysis of emission and gain saturation in gain-switched semiconductor lasers," *JOSA B*, vol. 13, no. 7, pp. 1605–1613, 1996.

[366] P. P. Vasil'ev, I. H. White, and J. Gowar, "Fast phenomena in semiconductor lasers," *Reports on Progress in Physics*, vol. 63, no. 12, pp. 1997–2042, 2000.

[367] D. Grischkowsky and A. Balant, "Optical pulse compression based on enhanced frequency chirping," *Applied Physics Letters*, vol. 41, no. 1, pp. 1–3, 1982.

[368] G. N. Pearson, K. D. Ridley, and D. V. Willetts, "Chirp-pulse-compression three-dimensional lidar imager with fiber optics," *Applied Optics*, vol. 44, no. 2, pp. 257–265, 2005.

[369] P. Anandarajah, R. Maher, Y. Xu, S. Latkowski, J. O'carroll, S. Murdoch *et al.*, "Generation of coherent multicarrier signals by gain switching of discrete mode lasers," *IEEE Photonics Journal*, vol. 3, no. 1, pp. 112–122, 2011.

[370] H.-F. Liu, M. Fukazawa, Y. Kawai, and T. Kamiya, "Gain-switched picosecond pulse ($<$ 10 ps) generation from 1.3 μm InGaAsP laser diodes," *IEEE Journal of Quantum Electronics*, vol. 25, no. 6, pp. 1417–1425, 1989.

[371] A. Sato, S. Kono, K. Saito, K.-i. Sato, and H. Yokoyama, "A high-peak-power UV picosecond-pulse light source based on a gain-switched 1.55 μm laser diode and its application to time-resolved spectroscopy of blue-violet materials," *Optics Express*, vol. 18, no. 3, pp. 2522–2527, 2010.

[372] T. Schönau, S. M. Riecke, K. Lauritsen, and R. Erdmann, "Amplification of ps-pulses from freely triggerable gain-switched laser diodes at 1062 nm and second harmonic generation in periodically poled lithium niobate," in *Nonlinear Frequency Generation and Conversion: Materials, Devices, and Applications X*, vol. 7917, 2011, p. 791707.

[373] B. M. Zhang, M. Liu, P. P. Shum, X. Li, and X. Cheng, "Design and fabrication of 100 kW peak power picosecond fiber laser for efficient laser marking and drilling," in *2015 IEEE Photonics Conference (IPC)*, 2015, pp. 70–71.

[374] J. Yang, Y. Zhao, and X. Zhu, "Transition between nonthermal and thermal ablation of metallic targets under the strike of high-fluence ultrashort laser pulses," *Applied Physics Letters*, vol. 88, no. 9, p. 094101, 2006.

[375] D. Auth, S. Liu, J. Norman, J. E. Bowers, and S. Breuer, "Passively mode-locked semiconductor quantum dot on silicon laser with 400 Hz RF line width," *Optics Express*, vol. 27, no. 19, pp. 27 256–27 266, 2019.

[376] D. Auth, S. Liu, J. E. Bowers, and S. Breuer, "Pulse timing and amplitude stability of a monolithic passively mode-locked quantum dot laser at 1310 nm directly grown on silicon," in *The European Conference on Lasers and Electro-Optics*, 2019, p. cb_8_1.

[377] S. Liu, X. Wu, J. Norman, D. Jung, M. Kennedy, H. K. Tsang *et al.*, "100 GHz colliding pulse mode locked quantum dot lasers directly grown on Si for WDM application," in *CLEO: Applications and Technology*, 2019, pp. ATu3P–5.

[378] M. G. Thompson, A. R. Rae, M. Xia, R. V. Penty, and I. H. White, "InGaAs quantum-dot mode-locked laser diodes," *IEEE Journal of Selected Topics in Quantum Electronics*, vol. 15, no. 3, pp. 661–672, 2009.

[379] G. Carpintero, M. G. Thompson, R. V. Penty, and I. H. White, "Low noise performance of passively mode-locked 10-GHz quantum-dot laser diode," *IEEE Photonics Technology Letters*, vol. 21, no. 6, pp. 389–391, 2009.

[380] W. Chow, "MC3.1 - Spontaneous mode locking and frequency comb generation in a quantum-dot laser," in *2019 IEEE Photonics Society Summer Topical Meeting Series (SUM)*, Fort Lauderdale, FL, USA, 2019, pp. 1–2.

[381] D. Inoue, D. Jung, J. Norman, Y. Wan, N. Nishiyama, S. Arai *et al.*, "Directly modulated 1.3 µm quantum dot lasers epitaxially grown on silicon," *Optics Express*, vol. 26, no. 6, pp. 7022–7033, 2018.

[382] D. Inoue, D. Jung, J. Norman, J. Wan, N. Nishiyama, S. Arai *et al.*, "NRZ and PAM-4 direct modulation of 1.3 µm quantum dot lasers grown directly on on-axis (001) Si," in *2018 European Conference on Optical Communication (ECOC)*, Rome, Italy, 2018, pp. 1–3.

[383] Z. Zhang, D. Jung, J. C. Norman, P. Patel, W. W. Chow, and J. E. Bowers, "Continuous tuning of gain peak linewidth enhancement factor from negative to positive with p doping in InAs QD laser on Si," in *2018 IEEE International Semiconductor Laser Conference (ISLC)*, Santa Fe, NM, USA, 2018, pp. 1–2.

[384] J. Duan, H. Huang, B. Dong, D. Jung, Z. Zhang, J. Norman *et al.*, "Thermally insensitive determination of the chirp parameter of InAs/GaAs quantum dot lasers epitaxially grown onto silicon," in *Proc. SPIE, Novel In-Plane Semiconductor Lasers XVIII*, vol. 10939, San Francisco, CA, USA, 2019, p. 109390S.

[385] F. Grillot, J. Duan, H. Huang, B. Dong, D. Jung, Z. Zhang *et al.*, "Linewidth broadening factor and optical feedback sensitivity of silicon based quantum dot lasers," in *Proc. SPIE, Novel In-Plane Semiconductor Lasers XVIII*, vol. 10939, San Francisco, CA, USA, 2019, p. 109390N.

[386] J. Duan, H. Huang, B. Dong, D. Jung, J. C. Norman, J. E. Bowers, and F. Grillot, "1.3-µm reflection insensitive InAs/GaAs quantum dot lasers directly grown on silicon," *IEEE Photonics Technology Letters*, vol. 31, no. 5, pp. 345–348, 2019.

[387] P. Downey, J. Bowers, R. Tucker, and E. Agyekum, "Picosecond dynamics of a gain-switched InGaAsP laser," *IEEE Journal of Quantum Electronics*, vol. 23, no. 6, pp. 1039–1047, 1987.

[388] I. White, D. Gallagher, M. Osiński, and D. Bowley, "Direct streak-camera observation of picosecond gain-switched optical pulses from a 1.5 µm semiconductor laser," *Electronics Letters*, vol. 21, no. 5, pp. 197–199, 1985.

[389] E. Göbel, G. Veith, J. Kuhl, H.-U. Habermeier, K. Lübke, and A. Perger, "Direct gain modulation of a semiconductor laser by a GaAs picosecond optoelectronic switch," *Applied Physics Letters*, vol. 42, no. 1, pp. 25–27, 1983.

[390] R. Nagarajan, T. Fukushima, M. Ishikawa, J. E. Bowers, R. S. Geels, and L. A. Coldren, "Transport limits in high-speed quantum-well lasers: Experiment and theory," *IEEE Photonics Technology Letters*, vol. 4, no. 2, pp. 121–123, 1992.

[391] J. Huang and L. W. Casperson, "Gain and saturation in semiconductor lasers," *Optical and Quantum Electronics*, vol. 25, no. 6, pp. 369–390, 1993.

[392] A. Zhukov, M. Maximov, A. Savelyev, Y. M. Shernyakov, F. Zubov, V. Korenev *et al.*, "Gain compression and its dependence on output power in quantum dot lasers," *Journal of Applied Physics*, vol. 113, no. 23, p. 233103, 2013.

[393] P. Bhattacharya, Z. Mi, J. Yang, D. Basu, and D. Saha, "Quantum dot lasers: From promise to high-performance devices," *Journal of Crystal Growth*, vol. 311, no. 7, pp. 1625–1631, 2009.

[394] M. Yamada and Y. Suematsu, "Analysis of gain suppression in undoped injection lasers," *Journal of Applied Physics*, vol. 52, no. 4, pp. 2653–2664, 1981.

[395] N. Hatori, M. Sugawara, K. Mukai, Y. Nakata, and H. Ishikawa, "Room-temperature gain and differential gain characteristics of self-assembled InGaAs/GaAs quantum dots for 1.1–1.3 μm semiconductor lasers," *Applied Physics Letters*, vol. 77, no. 6, pp. 773–775, 2000.

[396] T. S. McComb and D. McCal, "Pulsed bias current for gain switched semiconductor lasers for amplified spontaneous emission reduction," Dec. 26 2017, US Patent 9,853,411.

[397] D. Arsenijević and D. Bimberg, "Quantum-dot lasers for 35 Gbit/s pulse-amplitude modulation and 160 Gbit/s differential quadrature phase-shift keying," in *Proc. SPIE, Semiconductor Lasers and Laser Dynamics VII*, vol. 9892, San Francisco, CA, USA, 2016, p. 98920S.

[398] D. G. Deppe, H. Huang, and O. B. Shchekin, "Modulation characteristics of quantum-dot lasers: The influence of *p*-type doping and the electronic density of states on obtaining high speed," *IEEE Journal of Quantum Electronics*, vol. 38, no. 12, pp. 1587–1593, 2002.

[399] K. Takada, Y. Tanaka, T. Matsumoto, M. Ekawa, H. Song, Y. Nakata *et al.*, "Wide-temperature-range 10.3 Gbit/s operations of 1.3 μm high-density quantum-dot DFB lasers," *Electronics Letters*, vol. 47, no. 3, pp. 206–208, 2011.

[400] Y. Tanaka, M. Ishida, Y. Maeda, T. Akiyama, T. Yamamoto, H.-Z. Song *et al.*, "High-speed and temperature-insensitive operation in 1.3-μm InAs/GaAs high-density quantum dot lasers," in *2009 Conference on Optical Fiber Communication*, 2009, pp. 1–3.

[401] K. Kamath, J. Phillips, H. Jiang, J. Singh, and P. Bhattacharya, "Small-signal modulation and differential gain of single-mode self-organized $In_{0.4}Ga_{0.6}As$/GaAs quantum dot lasers," *Applied Physics Letters*, vol. 70, no. 22, pp. 2952–2953, 1997.

[402] R. Krebs, F. Klopf, S. Rennon, J. Reithmaier, and A. Forchel, "High frequency characteristics of InAs/GaInAs quantum dot distributed feedback lasers emitting at 1.3 μm," *Electronics Letters*, vol. 37, no. 20, pp. 1223–1225, 2001.

[403] M. Kuntz, G. Fiol, M. Lammlin, C. Schubert, A. Kovsh, A. Jacob *et al.*, "10 Gbit/s data modulation using 1.3 μm InGaAs quantum dot lasers," *Electronics Letters*, vol. 41, no. 5, pp. 244–245, 2005.

[404] M. Kuntz, G. Fiol, M. Lämmlin, D. Bimberg, M. Thompson, K. Tan *et al.*, "Direct modulation and mode locking of 1.3 μm quantum dot lasers," *New Journal of Physics*, vol. 6, no. 1, p. 181, 2004.

[405] A. Abdollahinia, S. Banyoudeh, A. Rippien, F. Schnabel, O. Eyal, I. Cestier *et al.*, "Temperature stability of static and dynamic properties of 1.55 μm quantum dot lasers," *Optics Express*, vol. 26, no. 5, pp. 6056–6066, 2018.

[406] E. P. Haglund, P. Westbergh, J. S. Gustavsson, and A. Larsson, "Impact of damping on high-speed large signal VCSEL dynamics," *Journal of Lightwave Technology*, vol. 33, no. 4, pp. 795–801, 2014.

[407] E. Malic, M. J. Bormann, P. Hovel, M. Kuntz, D. Bimberg, A. Knorr, and E. Scholl, "Coulomb damped relaxation oscillations in semiconductor quantum dot lasers," *IEEE Journal of Selected Topics in Quantum Electronics*, vol. 13, no. 5, pp. 1242–1248, 2007.

[408] J. Bowers, A. Gossard, S. Liu, J. Norman, Y. Wan, C. Zhang *et al.*, "Reflection insensitive quantum dot lasers grown on silicon substrates," in *ARPA-E - Changing what's possible*, 2019.

[409] A. Alduino and M. Paniccia, "Interconnects: Wiring electronics with light," *Nature Photonics*, vol. 1, no. 3, pp. 153–155, 2007.

[410] J. E. Bowers, T. Komljenovic, M. Davenport, J. Hulme, A. Y. Liu, C. T. Santis *et al.*, "Recent advances in silicon photonic integrated circuits," in *Next-Generation Optical Communication: Components, Sub-Systems, and Systems V*, vol. 9774, 2016, p. 977402.

[411] S. Feng, Y. Geng, K. M. Lau, and A. W. Poon, "Epitaxial III-V-on-silicon waveguide butt-coupled photodetectors," *Optics Letters*, vol. 37, no. 19, pp. 4035–4037, 2012.

[412] Y. Matsui, R. Schatz, T. Pham, W. A. Ling, G. Carey, H. M. Daghighian *et al.*, "55 GHz bandwidth distributed reflector laser," *Journal of Lightwave Technology*, vol. 35, no. 3, pp. 397–403, 2017.

[413] M. Smit, X. Leijtens, H. Ambrosius, E. Bente, J. Van der Tol, B. Smalbrugge *et al.*, "An introduction to InP-based generic integration technology," *Semiconductor Science and Technology*, vol. 29, no. 8, p. 083001, 2014.

[414] C. Wang, X.-L. Zhong, and Z.-Y. Li, "Linear and passive silicon optical isolator," *Scientific Reports*, vol. 2, no. 1, pp. 1–6, 2012.

[415] Y. Zhang, Q. Du, C. Wang, T. Fakhrul, S. Liu, L. Deng *et al.*, "Monolithic integration of broadband optical isolators for polarization-diverse silicon photonics," *Optica*, vol. 6, no. 4, pp. 473–478, 2019.

[416] Y. Arakawa and H. Sakaki, "Multidimensional quantum well laser and temperature dependence of its threshold current," *Applied Physics Letters*, vol. 40, no. 11, pp. 939–941, 1982.

[417] O. B. Shchekin, G. Park, D. L. Huffaker, and D. G. Deppe, "Discrete energy level separation and the threshold temperature dependence of quantum dot lasers," *Applied Physics Letters*, vol. 77, no. 4, pp. 466–468, 2000.

[418] J. Wei, Q. Cheng, R. V. Penty, I. H. White, and D. G. Cunningham, "400 Gigabit Ethernet using advanced modulation formats: performance, complexity, and power dissipation," *IEEE Communications Magazine*, vol. 53, no. 2, pp. 182–189, 2015.

[419] K. Zhang, Q. Zhuge, H. Xin, W. Hu, and D. V. Plant, "Performance comparison of DML, EML and MZM in dispersion-unmanaged short reach transmissions with digital signal processing," *Optics Express*, vol. 26, no. 26, pp. 34 288–34 304, 2018.

[420] F. Effenberger, "XG-PON1 versus NG-PON2: Which one will win?" in *2012 38th European Conference and Exhibition on Optical Communications*, 2012, pp. 1–3.

[421] H. Gupta, P. Gupta, P. Kumar, A. K. Gupta, and P. K. Mathur, "Passive optical networks: Review and road ahead," in *TENCON 2018-2018 IEEE Region 10 Conference*, 2018, pp. 0919–0924.

[422] D. Zhang, D. Liu, X. Wu, and D. Nesset, "Progress of ITU-T higher speed passive optical network (50G-PON) standardization," *Journal of Optical Communications and Networking*, vol. 12, no. 10, pp. D99–D108, 2020.

[423] Y. Matsui, D. Mahgerefteh, X. Zheng, C. Liao, Z. F. Fan, K. McCallion, and P. Tayebati, "Chirp-managed directly modulated laser (CML)," *IEEE Photonics Technology Letters*, vol. 18, no. 2, pp. 385–387, 2006.

[424] D. Mahgerefteh, Y. Matsui, X. Zheng, and K. McCallion, "Chirp managed laser and applications," *IEEE Journal of Selected Topics in Quantum Electronics*, vol. 16, no. 5, pp. 1126–1139, 2010.

[425] A. Abbasi, B. Moeneclaey, X. Yin, J. Bauwelinck, G. Roelkens, and G. Morthier, "10-/28-Gb chirp managed 20-km links based on silicon photonics transceivers," *IEEE Photonics Technology Letters*, vol. 29, no. 16, pp. 1324–1327, 2017.

[426] W.-H. Chu, H.-W. Chiang, C.-P. Liu, Y.-F. Lai, K.-Y. Hsu, and H.-C. Chung, "Defect-induced negative differential resistance of GaN nanowires measured by conductive atomic force microscopy," *Applied Physics Letters*, vol. 94, no. 18, p. 182101, 2009.

[427] V. M. Ustinov, N. A. Maleev, A. R. Kovsh, and A. E. Zhukov, "Quantum dot VCSELs," *Physica Status Solidi (a)*, vol. 202, no. 3, pp. 396–402, 2005.

[428] P. Moser, J. Lott, P. Wolf, G. Larisch, H. Li, and D. Bimberg, "Error-free 46 Gbit/s operation of oxide-confined 980 nm VCSELs at 85 C," *Electronics Letters*, vol. 50, no. 19, pp. 1369–1371, 2014.

[429] J. Lott, N. Ledentsov, V. Ustinov, N. Maleev, A. Zhukov, A. Kovsh *et al.*, "InAs-InGaAs quantum dot VCSELs on GaAs substrates emitting at 1.3 µm," *Electronics Letters*, vol. 36, no. 16, pp. 1384–1385, 2000.

[430] S. A. McHugo, A. Krishnan, J. J. Krueger, Y. Luo, N. Tan, T. Osentowski *et al.*, "Characterization of failure mechanisms for oxide VCSELs," in *Vertical-Cavity Surface-Emitting Lasers VII*, vol. 4994, 2003, pp. 55–66.

[431] J. M. Ostermann, F. Rinaldi, P. Debernardi, and R. Michalzik, "VCSELs with enhanced single-mode power and stabilized polarization for oxygen sensing," *IEEE Photonics Technology Letters*, vol. 17, no. 11, pp. 2256–2258, 2005.

You can leave Cambridge, but Cambridge will never leave you.